Instabilité globale linéaire et non linéaire d'écoulements de couche limite attachées ou décollées sur une plque plane

Stefania Cherubini

ParisTech
INSTITUT DES SCIENCES ET TECHNOLOGIES
PARIS INSTITUTE OF TECHNOLOGY

ARTS ET MÉTIERS ParisTech

2010-ENAM-0012

École doctorale n° 432 : Sciences des Métiers de l'Ingénieur

Doctorat ParisTech

T H È S E

pour obtenir le grade de docteur délivré par

l'École Nationale Supérieure d'Arts et Métiers

Spécialité " Mécanique "

présentée et soutenue publiquement par

Stefania CHERUBINI

le 04/06/2010

Linear and non-linear global instability of attached and separated boundary-layer flows over a flat plate

Directeur de thèse : **Pr. Alain LERAT**
Co-encadrement de la thèse : **Dr. Jean-Christophe ROBINET, Pr. Pietro DE PALMA, Pr. Michele NAPOLITANO**

Jury

M. Ulrich RIST, Professeur, IAG, Université de Stuttgart (Allemagne)	Président du jury
M. Jean-Marc CHOMAZ, Directeur de Recherche (CNRS), LadHyX, Ecole Polytechnique	Rapporteur
M. Uwe EHRENSTEIN, Professeur, IRPHE, Université de Provence	Rapporteur
M. Alessandro BOTTARO, Professeur, DICAT, Università di Genova (Italie)	Examinateur
M. Denis SIPP, Ingénieur de Recherche, DAFE, ONERA Meudon	Examinateur
M. Alain LERAT, Professeur, DynFluid, Arts et Métiers ParisTech	Directeur
M. Jean-Christophe ROBINET, Maître de Conférences, DynFluid, Arts et Métiers ParisTech	Co-directeur
M. Pietro DE PALMA, Professeur, DIMeG, Politecnico di Bari (Italie)	Co-directeur

T H È S E

Arts et Métiers ParisTech - Centre de Paris
Laboratoire DynFluid

Doctorat ParisTech

T H È S E

pour obtenir le grade de docteur délivré par

l'École Nationale Supérieure d'Arts et Métiers

Spécialité " Mécanique "

présentée et soutenue publiquement par

Stefania Cherubini

Linear and non-linear global instability of attached and separated boundary-layer flows over a flat plate*

* *Thèse en cotutelle entre le Politecnico di Bari (Italie) et Arts et Métiers ParisTech, co-financé par une bourse Vinci pour la mobilité de l'Université Franco-Italienne*

A mio padre

Aknowledgements

First of all I would like to express my appreciation to Professor Alain Lerat, chair of the DynFluid laboratory at Arts et Métiers ParisTech, and to Professor Michele Napolitano from the Polytechnical University of Bari, for making possible the cooperation between the two laboratories in which this PhD thesis has been carried out. My most sincere gratitude to Jean-Christophe Robinet who has been my supervisor since the beginning of my study, and whose long and fruitful discussions have provided me many helpful suggestions, important advices and constant encouragement during the course of this work. Special thanks are due to Prof. Pietro De Palma, who followed my thesis work closely during my 'italian' period, giving me many valuable suggestions and constructive advices. Sincere gratitude is due to Prof. Alessandro Bottaro, University of Genova, for taking intense academic interest in this study as well as providing valuable suggestions that improved the quality of this thesis.
I would also like to express my sincere thanks to the members of the DynFluid laboratory, who welcomed me in the kindest way when I first came from Italy. Most of all, special thanks go to Xavier and Fred, who contributed, with various songs and chatting, to keep me in a good mood with my thesis work.
I would like to express my gratitude to the referees of this thesis, Professor Uwe Ehrenstein and Professor Jean-Marc Chomaz, who accepted to revise my manuscript, and whose valuable suggestions and constructive criticisms have helped to improve the quality of this work.
Most of all I am grateful to my parents and sister, who always encouraged me to concentrate on my studies, even during the last year, when family issues could have diverted me from my thesis work. Finally, I would like to express my heartiest thanks to Luca for having supported me during the course of this work. Without his help and encouragement, this study would not have been the same.

Contents

List of Figures

List of Tables

Nomenclature

$\mathbf{u}$	Three-dimensional velocity perturbation vector	11
u	Streamwise velocity perturbation	12
v	Wall-normal velocity perturbation	12
w	Spanwise velocity perturbation	12
p	Pressure perturbation	12
$\mathbf{q}$	Three-dimensional velocity and pressure perturbation	12
α	Streamwise wavenumber of the perturbation	12
β	Spanwise wavenumber of the perturbation	12
x	Streamwise direction	33
y	Wall-normal direction	33
z	Spanwise direction	33
$\breve{\mathbf{u}}$	Three-dimensional istantaneous velocity	33
δ^*	Inflow boundary-layer displacement thickness	33
U_∞	Freestream velocity	33
Re	Reynolds number	33
ν	Kinematic viscosity coefficient	33
$\mathbf{Q}$	Three-dimensional base flow vector	36
U	Streamwise velocity component of the base flow	36
V	Wall-normal velocity component of the base flow	36
P	Pressure of the base flow	36
x_{out}	Outlet abscissa	36
$E(t)$	Disturbance energy density at time t	37
T	Target time	37
$\Im$	Objective function of the direct-adjoint optimization	37
$\mathcal{L}$	Lagrange functional	37
E_0	Given energy at $t = 0$	37
a	Lagrange multiplier for the continuity equation	37
b	Lagrange multiplier for the streamwise momentum conservation	37
c	Lagrange multiplier for the wall-normal momentum conservation	37
d	Lagrange multiplier for the spanwise momentum conservation	37
λ_0	Lagrange multiplier for the initial energy	37
$\mathbf{q}^\dagger$	Adjoint vector	38
ω	Eigenvalue of the global eigenvalue problem	38
$\hat{\mathbf{q}}$	Eigenvector of the global eigenvalue problem	38
N	Number of global modes	38
$\mathbf{A}$	Left hand side matrix of the global eigenvalue problem	39
$\mathbf{B}$	Right hand side matrix of the global eigenvalue problem	39
$\mathbf{u}_0$	Initial velocity vector	40
$G(t)$	Maximum energy gain at time t	40
$\mathcal{F}$	Harmonic forcing vector	40
σ_f	Forcing frequency	40
λ_ε	Pseudospectrum of the global linear operator	41
ω_r	Real part of the eigenvalue ω	41
ω_i	Imaginary part of the eigenvalue ω	41

ABBREVIATIONS

WKB	Wentzel–Kramers–Brillouin	13
PSE	Parabolized stability equations	13
LSB	Laminar separation bubble	27
BF, bf	Base flow	44
Wp	Wave packet	58
FFT	Fast Fourier transform	73

1 Introduction

1.1 Motivations

> *'I am an old man now, and when I die and go to heaven there are two matters on which I hope for enlightenment. One is quantum electrodynamics, and the other is the turbulent motion of fluids. And about the former I am rather optimistic.'*
> *- Horace Lamb -*

As Sir Horace Lamb had foreseen in 1932, transition to turbulence is still an open problem, especially concerning spatially developing boundary-layer flows (Schmid and Henningson, 2001). Transition in such kind of flows is crucial, since they are fundamental in several fields, for example in engineering and meteorology, as well as in physiology and biology. In fact, when a fluid moves over a solid surface, a thin region, the boundary layer, is created. In such regions the flow is decelerated from the freestream velocity to zero velocity at the wall. Boundary layers could be either laminar or turbulent. In the former case, the fluid motion is smooth and regular, whereas the latter case is characterized by an unsteady random behaviour in both time and space.
In many aerodynamic and industrial applications, as in airplane wings and gas turbine blades, the boundary layer is required to be laminar. For instance, on commercial aircraft about 50% of the total drag is due to the turbulent skin-friction associated with the boundary layers, and about 90% for submarines (Marusic (2009)).
In many cases, it could be crucial to predict time and location of boundary-layer transition. As an example, for the design of a spacecraft entering in the atmosphere, a detailed prediction of the transition of the hypersonic boundary layers bordering the aircraft is needed, since turbulence induces an higher drag and heat-transfer.
In other cases, a rapid transition to turbulence is required. Examples are combustion engines, where an optimal mixing is needed, and golf balls, where the goal is to delay separation and reduce the consequent pressure drag.

Transient energy growth: the optimal perturbations It is well–known that transition is triggered by exogeneous disturbances, namely wall roughness, acoustic waves, or freestream turbulence, but the understanding of the transition mechanism is still an open problem. For small amplitude disturbances, the linear stability analysis predicts the slow transition process due to the generation, amplification and secondary instability of

Tollmien–Schlichting (TS) waves. Recently, the small perturbation analysis has improved mainly due to the development of global modes concepts (Briggs (1964), Bers (1983)); it is now recognized that the impulse response of a boundary-layer flow is a wave packet which may either decay, grow algebraically or exponentially (depending on the Reynolds number) while travelling downstream at the group velocity. Even if the regime is subcritical (i.e. all eigenmodes are damped), there exist some disturbances which could induce a transient amplification. Transient growth arises from the constructive interference of damped non-orthogonal eigenmodes and results in a spatial amplification of the disturbances (Schmid and Henningson (2001)). If growth is sufficient, such amplified structures could induce secondary instability and breakdown, leading to a *by-pass* transition (see Schoppa and Hussain (2002), Brandt et al. (2004)).
The concept of "optimal perturbation" was introduced in the eighties (Landahl (1980, 1990)), generating much hope to fill the gap in the understanding of bypass transition. Since than, many works have focused on looking for an "optimal perturbation" characterized by a single wavenumber in the streamwise and spanwise direction (Farrell, 1988, Butler and Farrell, 1992, Luchini, 2000, Schmid, 2000, Corbett and Bottaro, 2000). In such studies, either a temporal or spatial optimization has been performed, under the hypothesis of a parallel or non-parallel flow, respectively. In both cases, the optimal perturbation in a boundary layer has been found to be characterized by a counter-rotating vortex pair without any modulation in the streamwise direction, and resulting at finite time in a pair of streamwise velocity streaks.
The results of such an analysis are very promising, since they bring into play some of the main ingredients present in transitional flow fields, namely streaks and vortices. Nevertheless, single-wavenumber optimal perturbations do not always induce transition efficiently (Biau et al. (2008)). Indeed, the drawbacks of such 'local' methods are that they focus onto a single wavenumber/frequency at a time and that they neglect non-linear and non-parallel effects.

Convective non-parallel amplification: the separated boundary layer In the past few years, a new light has been shed on the fundamental role in the transition process of the convective amplification due to the non-parallelism of the flows. The transient amplification of the disturbance energy, which is the primary cause of the by-pass transition, is due to the non-orthogonality of the eigenvectors associated with both the wall-normal and streamwise eigendirections of the linearized Navier-Stokes operator. If the former – the one responsible for inducing the 'lift-up' effect – is recovered in parallel and non-parallel flows, the latter is mostly promoted by the non-parallelism of the flow. Even though an attached boundary-layer flow could be supposed nearly non-parallel, in the case of a separated flow such an hypothesis is not adequate.
In many engineering applications the boundary layer could undergo separation and reattachment, thus forming recirculation bubbles whose stability and control may be crucial for the performance of the considered device. This may happen, for example, over the surface of turbomachinery blades or of airplane wings. Separation may be triggered by the geometry of the body or by the adverse pressure gradient. In both cases the aerodynamic load may be strongly affected by the behavior of the bubble which changes its

characteristics depending on the operating conditions.
Often, the presence of a bubble is associated with a laminar-turbulent transition of the boundary layer since flow separation occurs in the laminar part of the bubble and, after transition, the flow reattaches. Such a transition is governed by the amplification of flow perturbations which may be due to a linear process based on transient growth or to a non-linear one in the presence of high free-stream disturbance levels (see Schmid and Henningson (2001), Schmid (2007)). In Rist and Maucher (1994), a thorough analysis is provided of the different transition mechanisms with respect to two and three-dimensional initial perturbations, showing that several transition scenarios are possible and that, when small amplitudes perturbation are considered, two-dimensional disturbances are the most amplified ones.
For a separation induced by the wall geometry, such as a step (Barkley et al., 2002, Beaudoin et al., 2004, Blackburn et al., 2008, Marino and Luchini, 2009) or a bump (Marquillie and Ehrenstein, 2003, Gallaire et al., 2007, Ehrenstein and Gallaire, 2008), it has been established that the evolution of the perturbations leads to the formation of three-dimensional flow patterns (see also Williams and Baker (1997)) characterized by global steady and weakly growing eigenmodes. Such three-dimensional steady modes have been originally discovered by Theofilis et al. (2000) for a laminar separation bubble induced by an adverse pressure gradient. On the other hand, laminar separation bubbles show a strong two-dimensional instability mechanism known as "flapping" (Cherry et al., 1984, Pauley et al., 1990, Gallaire et al., 2007, Ehrenstein and Gallaire, 2008) and a high sensitivity to external noise (Marquet et al., 2008) whose basic features are still not fully understood. In particular, the role of all of these instability mechanisms in the transition process is still an open question.

1.2 Aims

The aim of this thesis is to describe the linear and non-linear dynamics of both attached and separated boundary-layer flows at low Reynolds numbers, focusing on the effects of non-normality of the differential Navier–Stokes (NS) operator. The linear dynamics, driven by the interactions among the non-orthogonal eigenvectors, is studied using two different approaches for the global stability analysis of the linearized NS equations: the global eigenvalue analysis and the direct-adjoint optimization. If in a 'local' eigenvalue analysis (Farrell, 1988, Butler and Farrell, 1992, Luchini, 2000, Schmid, 2000, Corbett and Bottaro, 2000) the perturbation is supposed sinusoidal in the streamwise and spanwise directions, in the global eigenvalue analysis no spatial structure is imposed to the perturbation in both the streamwise and wall-normal directions. Thus, the advantage is twofold: i) to take into account the convective effects due to the non-parallelism of the flow, which is crucial in the case of a separation bubble; ii) to allow the perturbation to be not single-wavenumber in such directions, which could be important for a real boundary-layer flow of finite streamwise extent. In the direct-adjoint optimization, a fully three-dimensional perturbation has been considered, so that the perturbation could be characterized by more than one frequency also in the spanwise direction, allowing one to compute spanwise-localized perturbations.
For the case of the adverse-pressure-induced separated boundary layer flows, the aim is

to clarify the role of the following features in the onset of unsteadiness: i) the strong two-dimensional convective amplification; ii) the non-normal effects such as the 'flapping' phenomenon; iii) the high sensitivity to external forcing; iv) the asymptotically unstable global mode triggering three-dimensional patterns into the flow. Indeed, even if the flow presents an unstable weakly-growing three-dimensional mode, the flow could by-pass the asymptotical mechanism and transition may occur via the transient amplification of disturbances impulsively injected in the flow or induced by the numerical noise. The global eigenvalue analysis has been used in a two-dimensional and three-dimensional framework to compute the global eigenmodes, the global optimal perturbations, and the maximum response to an external forcing.
Concerning the attached boundary layer, the aim is to identify localized optimal perturbations, characterized by more than one frequency in the streamwise direction, inducing a strong energy amplification. In fact, since in most practical cases boundary layers undergo transition by receptively selecting and amplifying external disturbances, such as those arising from the presence of localized roughness elements or gaps on the wall, it makes sense to inquire on the spatially localized flow patterns which most easily amplify and cause breakdown. Thus, the global eigenvalue analysis has been performed to identify localized optimal perturbations, together with a direct-adjoint approach which allows to perform a truly three-dimensional optimization of the perturbations. Indeed, even if the considered problem is homogeneous in the spanwise direction, so that the result of the optimization should always be characterized by a single wavenumber on that direction, real perturbations are often localized and characterized by more than a wavenumber in all the directions. Thus, a partially optimized localized *near-optimal* perturbation has been looked for by means of the direct-adjoint optimization.
In order to assess the effects of non-linearity on the instability mechanisms identified by the global linear stability analysis, direct numerical simulations (DNS) have been performed in a two- and three-dimensional framework for both the attached and separated boundary layers. Perturbations of different shapes, frequencies and amplitudes have been superposed to the considered base flows with the aim of identifing which kind of perturbation most easily brings the flows on the verge of turbulence. Different scenarios of transition have been observed, and the mechanisms leading the flow to turbulence have been analyzed in detail.

1.3 Main contributions

The transient and asymptotical dynamics of attached and separated boundary-layer flows over a flat plate have been studied in order to investigate the role of non-normality and non-linearity of the differential operator in the stability of such flows. In the following the main contributions of this thesis are described.

1.3.1 The two-dimensional separated boundary layer

Transient amplification of small amplitude perturbations: the convective Kelvin–Helmoltz (KH) mechanism Both linear eigenvalue analysis and numerical simulations with small amplitude perturbations, have shown that the non-normality of the convective modes of the NS operator allows the bubble to act as a strong amplifier of small disturbances, due to the Kelvin–Helmholtz-like convective instability acting over the separation streamline. Indeed, the front part of the bubble has been found to show a high sensitivity to external noise, as observed in simulations with white noise disturbances superposed upon the whole base flow or upon the inflow Blasius profile. The most responsive disturbance takes the form of Kelvin-Helmholtz-like vortices, which roll up and amplify themselves along the shear layer, until being advected and die away in the attached boundary layer.

Sensitivity to external forcing: the optimal forcing and response An analysis of the evolution of the optimal response to external forcing in function of the Reynolds number and the pressure gradient has clarified the strong influence of the shear layer on the maximum response. Once verified that such a separated flow acts as a strong selective noise amplifier, it has been investigated whether a connection exists between the global optimal response of the flow and the unsteadiness observed in experiments and direct numerical simulations. It has been shown that the selected frequencies recovered by a Fourier transform of the velocity signal recovered by a continuously perturbed DNS in the asymptotic regime are in agreement with the most amplified frequencies derived from the optimal response analysis. The most amplified frequency has been then compared with the shedding frequencies measured by many authors, and the Strouhal number recovered by such authors has been found consistent with the dimensionless most amplified frequency of the global optimal response, thus establishing a connection between the sensitivity response and the vortex shedding phenomenon.

Finite amplitude perturbations: non-linear effects For finite amplitude initial perturbations, due to nonlinear interactions between modes, a wave packet cycle has been observed within the bubble, similar to the one occurring at supercritical Reynolds numbers. It has been found that non-linear interactions contribute also to the excitation of a convectively unstable mode in the attached-flow region due to the high sensitivity of the boundary layer. This induces a further transient amplification of the finite amplitude perturbations as well as an asymptotical instability at slightly subcritical Reynolds numbers.

Supercritical Reynolds number: the flapping frequency In a two-dimensional framework, it has been observed that at supercritical Reynolds numbers the separated flow shows topological flow changes, supporting the hypothesis of some authors that the unsteadiness of separated flows could be due to structural changes within the bubble. Furthermore, non-normality effects have shown to play an active role also at large times.

In fact, due to the superposition of convective non-normal modes, a low-frequency oscillation known as 'flapping' frequency appears. Close to transition, when topological changes occur in the flow, a secondary flapping frequency appears as well. A possible explanation of such a behavior has been provided, in which it is assumed that the oscillations are due to the interaction of the main wave packet with the perturbations carried upstream by the backflow inside the bubble. A scaling law based on the previous assumption has been derived, which is able to predict accurately the dependence of the flapping frequency on the Reynolds number and the onset of the secondary frequency close to transition.

1.3.2 The three-dimensional separated boundary layer

Centrifugal modes and their role in the onset of unsteadiness In a three-dimensional framework, a steady, weakly-growing unstable mode has been found to grow asymptotically, once the transient amplifier phase has been passed (for two-dimensionally subcritical flows). By means of a Rayleigh instability analysis, it has been shown that such a mode is due to a centrifugal instability of the closed streamlines within the bubble. A homologous of such a mode has been recovered among the stable three-dimensional ones, which is characterized by a streamwise elongated structures amplifying themselves downstream due to a Gortler mechanism, as assessed by a Gortler analysis. Both modes have been observed during the slow energy growth phase following the early transient. Although for large amplitude perturbations the flow presents a K-type transition due to the secondary instability of TS modes, the centrifugal three-dimensional modes have a role on the onset of unsteadiness induced at two-dimensionally subcritical Reynolds numbers by small amplitude perturbations. In such a case, the flow has been observed to transition via secondary varicose instability of the Gortler vortices, due to the wall-normal interaction of high- and low-momentum streamwise streaks, inducing the formation of a series of hairpin vortices in streamwise succession.

1.3.3 The three-dimensional attached boundary layer

Localized optimal and near-optimal perturbations For an attached boundary layer, the spatially localized disturbances capable to effectively provoke breakdown to turbulence have been computed. The optimal initial perturbation is characterized by a pair of streamwise-modulated counter-rotating vortices, tilted upstream, resulting at optimal time in streak-like structures alternated in the streamwise direction. This indicates that perturbations with non-zero streamwise wavenumber have a role in the transient dynamics of a boundary layer; such a result is in contrast with the local theory, which predicts that the optimal dynamics of a boundary-layer flow is dominated by zero-streamwise-wavenumber waves. A scaling law is provided describing the variation of the streamwise modulation of the optimal initial perturbation with the streamwise domain length and the Reynolds number. For sufficiently large domains, a near-optimal spanwise-localized perturbation characterized by a large spectrum of frequencies has been extracted during the optimization process, resulting in a wave packet of elongated disturbances modulated in the spanwise and streamwise direction. This near-optimal initial disturbance attains a

gain which is less than 1% smaller than the true optimal disturbance.

Transition via optimal and near-optimal perturbations: hairpin vortices and turbulent spots The capability of the localized optimal perturbations to induce transition has been investigated by means of direct numerical simulations. It is shown that the global optimal disturbance is able to induce transition for lower levels of the initial energy than local optimal and suboptimal perturbations. Simulations are also carried out for the non-linear evolution of the near-optimal wave packet, which is found to evolve in a *turbulent spot* spreading out in the boundary layer. It has been shown that transition is initiated in a region of the flow close to the center of the packet, by means of a mechanism including features of both quasi-sinuous and quasi-varicose breakdown. A hairpin vortex has been observed in the region of interaction of the streaks prior to transition, generated by the inclined shear layer resulting from the front interaction of a low and a high-speed streak, and inducing secondary hairpins. The transition scenario presented here appears to connect two different views of transition, that based on transient growth and secondary instability of the streaks (Schoppa and Hussain (2002), Brandt et al. (2004)), and that which describes breakdown via the continuous regeneration of vortices (Adrian (2007), Wu and Moin (2009)).

1.4 Thesis organization

Chapter 2: Background The chapter provides a review of the main concepts used to study the linear instability of open flows. The local and global approaches to the instability analysis are presented and compared. A discussion of the modal and non-modal amplification of the perturbation is then provided. Finally, some results published in the literature about instability and transition of attached and separated boundary layer flows are briefly presented.

Chapter 3: Computational approach Chapter 3 describes the numerical tools and the methods employed to achieve the results discussed in the following sections. In particular, the problem formulation and the governing equations are provided; then, the numerical details of the direct numerical simulations are discussed. The Newton procedure, which has been used to compute the base flow at supercritical Reynolds numbers, and the direct-adjoint optimization are presented; both are derived from the existing DNS algorithm. The global eigenvalue analysis and the consequent optimization via global modes are then discussed. Finally, the sensitivity and optimal response analysis are provided.

Chapter 4: Non-normal dynamics of a two-dimensional separated boundary layer The chapter presents the results about the two-dimensional dynamics of separated gradient-pressure-induced boundary-layer flows. In particular, for subcritical and supercritical Reynolds numbers, the linear dynamic is investigated by means of the global eigenvalue analysis. The results about the global optimal perturbation are generalized by means of a DNS for small amplitude perturbations. The non-linear effects are investigated

by superposing large amplitude perturbations on the base flows. In supercritical conditions, a scaling law is provided for the onset of a low-frequency beating characterizing the separated flow.

Chapter 5: The response to a harmonic forcing of a two-dimensional separated boundary layer In Chapter 5 the sensitivity of the flow to an external forcing is investigated. A pseudospectrum is computed, assessing the high sensitivity of the flow. An optimal response analysis is performed, which allows to identify the most sensitive frequencies. Such frequencies are then compared to the ones obtained asymptotically by a DNS continuously forced by a random noise at the inlet points. A Strouhal number is thus computed and compared to the one recovered by many authors in DNS and experiments.

Chapter 6: The onset of three-dimensional centrifugal global modes in a separated boundary layer Chapter 6 presents the three-dimensional dynamics of the separated boundary-layer flow. The global eigenvalue analysis is employed in order to identify the most amplified three-dimensional modes. A Rayleigh and a Gortler analysis are used in order to shed light on the centrifugal mechanisms characterized the family of the steady modes. By means of DNS the small and large amplitude perturbation dynamics is studied, and many of the modes recovered by global eigenvalue analysis are identified. Finally, the late stages of unsteadiness are analyzed in detail, in order to assess the role of such modes in the destabilization of the flow.

Chapter 7: Three-dimensional optimal localized perturbations in an attached boundary layer In this chapter the three-dimensional optimal and near-optimal dynamics of an attached boundary layer of finite streamwise extent are investigated. Localized optimal perturbations are computed by means of both global eigenvalue analysis and direct-adjoint optimization. A scaling law is derived which describes the streamwise modulation of the optimal perturbations with respect to the Reynolds number and the streamwise extent of the considered domain. Near-optimal perturbations, which are localized also in the spanwise direction, are computed for domains of large spanwise extent. DNS are performed by superposing the optimal and near-optimal disturbances to the base flow, in order to assess their effectiveness in inducing transition. Finally, the late stages of transition, characterized by the generation of hairpin vortices and turbulent spots, are analyzed in detail.

Chapter 8: Conclusions and outlook In Chapter 8, conclusions are drawn, and a discussion of the results presented in the previous sections is provided. Finally, the future works are presented.

1.5 Conferences and journal articles

The content of this thesis has been published, or proposed for publication, in the following journals or conferences (in chronological order):

1. F. Alizard, S. Cherubini, J.-C. Robinet and P. De Palma, *Sensitivity and forcing response in a separated boundary-layer flow* , ICTAM '08, Adelaide, Australia, August 2008, Springer eds.

2. S. Cherubini, F. Alizard, J.-C. Robinet and P. De Palma, *Linear and non linear transient behaviour of a separated flow*, EMFC7 '08, Manchester, UK, September, 2008

3. S. Cherubini, J.-C. Robinet and P. De Palma, *Recovering flapping frequency in a separated flow*, ERCOFTAC Flubio SIG 33 '08, Genova, Italy, October, 2008

4. S. Cherubini, J.-C. Robinet, A. Bottaro and P. De Palma, *Global three-dimensional optimal perturbations in a Blasius boundary layer*, in Proceedings of the IUTAM Symposium on Laminar-Turbulent Transition, Stockholm, Sweden, June 2009, Springer eds.

5. S. Cherubini, J.-C. Robinet, A. Bottaro and P. De Palma, *The global optimal wave packet in a boundary layer and its non-linear evolution*, Global Flow Instability and Control Symposium IV, Creta Maris, Hersonissos, Greece, Sept. 29 - Oct. 2, 2009, V. Theofilis et al. (eds.), ISBN-13: 978-84-692-6247-4

6. S. Cherubini, J.-C. Robinet and P. De Palma, *Low-frequency dynamics of separated boundary- layer*, in Colloque GDR 'Controle Des Décollements', Nov. 24-25 2009, Cépadues eds.

7. F. Alizard, S. Cherubini and J.-C. Robinet, *Sensitivity and optimal forcing response in separated boundary layer flows*, Physics of Fluids, Vol. 21 (6), 064108-064108-13 (2009).

8. S. Cherubini, J.-C. Robinet and P. De Palma, *The effects of non-normality and non-linearity of the Navier-Stokes operator on the dynamics of a large laminar separation bubble*, Physics of Fluids, Vol. 22 (1), 014102 (2010).

9. S. Cherubini, J.-C. Robinet, A. Bottaro and P. De Palma *Optimal wave packets in a boundary layer and initial phases of a turbulent spot*, published on line on Journal of Fluid Mechanics, 28 may 2010, doi:10.1017/S002211201000114X

10. S. Cherubini, F. Alizard, J.-C. Robinet and P. De Palma, *The onset of three-dimensional centrifugal global modes and their non-linear development in a recirculating flow over a flat surface*, submitted to Physics of Fluids in February 2010.

2 Background

2.1 Linear stability concepts

2.1.1 Asymptotical instability

Linear stability analysis in hydrodynamics aims at studing the evolution of an infinitesimal perturbation, $\mathbf{u}$, of a steady solution of the Navier–Stokes equations, the base flow $\mathbf{U}$. Since perturbations are supposed infinitesimal, their evolution is governed by the Navier–Stokes equations linearized about $\mathbf{U}$. Following Joseph (1976), one could consider the kinetic energy of the perturbations in a volume V,

$$E_v = \frac{1}{2}\int_V u_i u_i dV, \tag{2.1}$$

where u_i is the i^{th} component of the perturbation velocity and the Einstein summation has been used. The base flow $\mathbf{U}$ could be defined linearly stable, if the perturbation energy satisfies:

$$\lim_{t\to\infty} \frac{E_v(t)}{E_v(0)} \to 0. \tag{2.2}$$

Generally speaking, if infinitesimal perturbations grow in time, the base flow is said to be linearly unstable.

The inviscid and viscous local stability problems The beginning of modern hydrodynamic stability is attributed to the first controlled scientific experiment of Reynolds (1883), in which the Reynolds number, Re, was introduced as a critical nondimensional parameter distinguishing stable from unstable flows. From the theoretical point of view, the seminal work of Rayleigh (1880) had set the ground of inviscid theory. The inviscid Rayleigh's criterion related the presence of an unstable mode to the occurrence of an inflection point on the base flow profile.
A number of theoretical efforts followed such work in the past century, including the temporal formulation of the viscous stability problem for parallel shear flows (Orr (1907), Sommerfeld (1908)). These works are based on the hypothesis that the base flow evolves on the streamwise direction very slowly with respect to the wall-normal direction. Such hypothesis of *weakly non-parallelism* of the flow leads to a *local* approach to the instability problem: the instability problem is solved locally, at each streamwise location, by

supposing that the base flow is parallel for each streamwise point.
In the work by Orr (1907) and Sommerfeld (1908), the linearized NS equation were thus taken into account for the parallel base flow $\mathbf{U} = (U, 0, 0)$; wavelike solutions were introduced such as

$$\mathbf{q}(x, y, z, t) = \hat{\mathbf{q}}(y) \exp(i(\alpha x + \beta z - \omega t)), \tag{2.3}$$

where $\mathbf{q} = (u, v, w, p)^T$ is the perturbation vector (u, v, and w being the streamwise, wall-normal, and spanwise components of the velocity perturbation vector, and p is the pressure disturbance), α the streamwise wavenumber, β the spanwise wavenumber and ω the temporal pulsation. By introducing the normal vorticity:

$$\eta = \frac{\partial u}{\partial z} - \frac{\partial w}{\partial x}$$

and eliminating the pressure, this results in the pair of equations:

$$\left[(-i\omega + i\alpha U)\left(\frac{\partial^2}{\partial y^2} - k^2\right) - i\alpha\frac{\partial^2 U}{\partial y^2} - \frac{1}{Re}\left(\frac{\partial^2}{\partial y^2} - k^2\right)^2\right]\hat{v} = 0 \tag{2.4}$$

$$\left[(-i\omega + i\alpha U) - \frac{1}{Re}\left(\frac{\partial^2}{\partial y^2} - k^2\right)\right]\hat{\eta} = -i\beta\frac{\partial U}{\partial y}\hat{v}, \tag{2.5}$$

with $k^2 = \alpha^2 + \beta^2$. These equations are called the Orr-Sommerfeld and Squire equations, after the authors who first derived them. Such an eigenvalue problem is used to determine the temporal instability of boundary layer flows.

The energy equation Some fundamental concepts about hydrodynamic stability are due to Prandtl (1935), who derived from the NS equations an expression for the kinetic energy transfer in two directions in space,

$$\frac{dE_v}{dt} = \int_V u_i u_j \frac{\partial U_i}{\partial x_j} dV - \frac{1}{Re}\int_V \frac{\partial u_i}{\partial x_j}\frac{\partial u_i}{\partial x_j} dV, \tag{2.6}$$

where the subscripts i and j represents the streamwise and wall-normal directions. From such equation the author concluded that the growth or damping of the perturbations energy depends on the balance between the two right-hand-side terms, namely, the exchange of energy with the base flow and the energy dissipation due to viscous effects, respectively. By means of a decomposition on a basis of normal modes,

$$u_i(y) = \hat{u}_i \exp(i\alpha(x - ct)), \tag{2.7}$$

where c is the phase velocity equal to ω/α, he derived an expression for the Reynolds tensor,

$$u_i u_j = \cos(\phi_i - \phi_j)|\hat{u}_i||\hat{u}_j| \exp(\Im(c)t), \tag{2.8}$$

where ϕ are the phasis of the i and j components of the velocity vector and $\Im(c)$ is the imaginary part of the phase velocity. On the basis of such equation, he concluded that the viscosity could have a destabilizing role due to a phase shift between the velocity components u_i and u_j, inducing an energy transfert between the base flow and the perturbation, via the Reynolds tensor.

The Tollmien-Schlichting waves The work of Prandtl (1935) has put the basis for the theoretical prediction (Schlichting (1933), Tollmien (1929)) and experimental observation of Tollmien-Schlichting (TS) waves (Schubauer and Skramstad (1948)), a class of eigenmodes which may grow exponentially due to viscous effects. Such modes are the most unstable ones for a boundary layer, when the spectrum is obtained by solving a local eigenvalue problem, as the Orr-Sommerfeld and Squire equations (see equations 2.4 and 2.5). The first experimental measures of TS waves induced by a vibrating ribbon (Schubauer and Skramstad (1948)) were in agreement with the theoretical predictions, once taken into account the spatial development of such waves. Since the theoretical studies of Schlichting (1933) were based on a temporal appoach, Schubauer and Skramstad (1948) traced a neutral curve by using a transformation relating the amplitude of the perturbation at a series of streamwise positions with the temporal pulsation, ω.

The spatial instability problem and the non-parallel corrections A mathematical framework for spatially growing disturbances was given by Gaster (1965), who solved the instability eigenvalue problem with respect to the spatial wavenumber, α, permitting a direct comparison with the experiments, and predicting a critical Reynolds number equal to 520. Nevertheless, the comparison with experiments showed that the critical Reynolds number was overestimated in the Gaster's work, due to the hypothesis of parallelism of the flow. Thus, a series of spatial instability studies were published in the seventies, based on the hypothesis that the envelope of the perturbation is characterized by a streamwise variation which is slower than the one associated with its oscillatory part. For instance, Gaster (1974) defined a slow spatial variable, $X = \varepsilon x$ (with $\varepsilon \ll 1$), affecting the amplitude of the velocity and pressure perturbations through the ansatz:

$$\mathbf{q} = \hat{\mathbf{q}}(X, y) \exp(\Theta(x, t)). \tag{2.9}$$

Developing the NS equations at the first order in ε, the author was able to estimate more accurately the critical Reynolds number.
Other methods were used to take into account the non-parallel effects. One of the most known is the one by Herbert (1997), who derived the parabolized stability equations (PSE). Such equations are derived by allowing the flow to grow mildly in the streamwise direction. Thus, at every specific streamwise location, the perturbation is supposed to be on the form:

$$\mathbf{q}(x, y, z, t) = \hat{\mathbf{q}}(x, y) \exp i(\int_{x_0}^{x} \alpha(d\zeta)d\zeta + \beta z - \omega t). \tag{2.10}$$

Such ansatz is based on the WKB-type assumption of the existence of two scales on which the instability problem is studied, a slow one related to the base flow, and a fast one on which the instability problem is considered. In particular, $\alpha(x)$ is supposed to vary slowly in the streamwise direction, in order to capture every streamwise variations of the disturbance on the fast scale. These parabolized equations could be solved by a simple space-marching algorithm, thus avoiding the solution of a large eigenvalue problem.
In the same period the development of the computational power allowed the comparison of such theoretical results with the ones of the first direct numerical simulations. Fasel (1976) was able to reproduce by means of DNS the results of the work by Gaster (1974),

simulating a vibrating ribbon within the boundary layer.

Secondary instability of Tollmien-Schlichting waves and the K-type transition According to the Squire's theorem (Squire (1933)), two-dimensional TS waves are less stable than three-dimensional ones. However, when the amplitude of the TS waves reaches a large enough value, they could experience secondary instability (Herbert (1988)) and turn to three-dimensional disturbances. The concept of secondary instability can be described as follows: when a disturbance grow up to a finite amplitudes, it could saturate to a steady state and establish a new mean flow which could become unstable. In the experiments by Klebanoff et al. (1962), it was observed that the initially two-dimensional Tollmien-Schlichting waves become three-dimensional when reaching an amplitude of the order of 1% of freestream velocity. The authors defined the three-dimensional pattern as *peaks* and *valleys*. Such a transition scenario, which is called K-type secondary instability (K for Klebanoff), would be described in more detail in section 2.5.1, together with the others scenarios such as the H-type, O-type and by-pass transition.

2.2 Absolute and convective instabilities

As it has been previously defined, whenever infinitesimal perturbations grow in time, the base flow is defined linearly unstable. However, different kind of instabilities could be defined. In the work by Huerre and Monkewitz (1985), a fundamental distintion between *absolute* and *convective* instability has been made.
The impulse response of a parallel shear flow is considered in a linear framework: if the infinitesimal perturbation generated by the impulse, initially localized in space, grows at that fixed spatial location, spreading both upstream and downstream of the location where it is originated, then the flow is defined *absolutely unstable*. An example of absolute instability is illustrated in Figure 2.1 (a) on a $x - t$ diagram. If on the other hand, the perturbation grows in magnitude but is convected by the base flow away from the point where it has been generated, so that at any streamwise location the perturbation ultimately decays to zero, then the flow is *convectively unstable*. Such concept is illustrated in Figure 2.1 (b).

Absolute instability for non-parallel flows By means of a WKB development, Chomaz et al. (1991) had demonstrated that in a weakly non-parallel flow the existence of a zone of absolute instability within the flow is a necessary but not sufficient condition for the *global instability* of the flow. For global instability one means an intrinsic behaviour of regeneration of the perturbations impulsively injected into the flow, leading to the formation of coherent structure at a certain frequency. The global eigenvector is written as:

$$\mathbf{q} = \hat{\mathbf{q}}(X, y) exp(i\omega_G t) \tag{2.11}$$

where X is the slow streamwise scale defined in the previous subsection, the real part of ω_G is the pulsation of the perturbation and its imaginary part is the amplification rate.

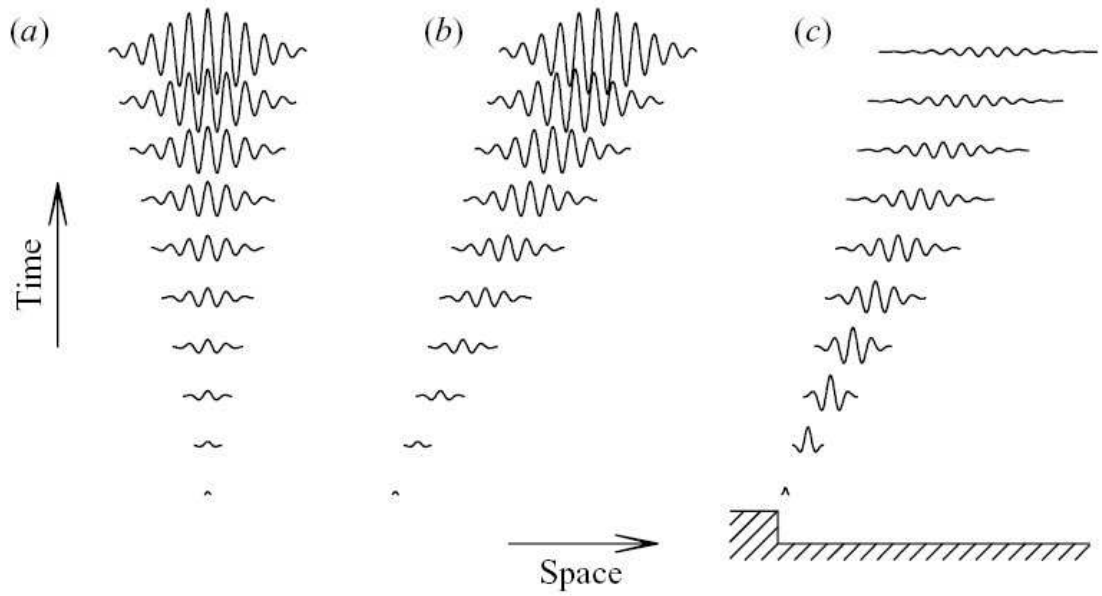

Figure 2.1: Schematic of absolute and convective instabilities and caption taken from Blackburn et al. (2008). An infinitesimal perturbation, localized in space, can grow at a fixed location leading to an absolute instability (a) or decay at a fixed points leading to a convective instability (b). In inhomogeneous, complex geometry flow we can also observe local regions of convective instability surrounded by regions of stable flow (c).

If we define $\omega_0(X)$ as the local absolutely unstable mode (at each streamwise location), it is possible to obtain ω_G as:

$$\omega_G \ll \omega_0(X_s) + \mathcal{O}(\varepsilon), \tag{2.12}$$

where X_S is the saddle point on the complex plane (X_r, X_i), such that

$$\left.\frac{d\omega_G}{dX}\right|_{X_s} = 0. \tag{2.13}$$

Such analysis, which have been extended to a non linear regime (Couairon and Chomaz (1997)), have been able to explain the onset of the Karman vortex street after a cylinder (Pier (2002)). Nevertheless, in such work, the strong hypothesis about the weakly non-parallelism of the flow does not allow accurate predictions for non-parallel flows such as boundary layers.

Resonator and amplifier dynamics The concept of absolute and convective instability could be related to a classification of the open flows carried out by Huerre and Monkewitz (1990) which characterizes the flows as *resonators* or *amplifiers* with respect to their dynamics.
For instance, a *resonator* dynamics could be recovered in a flow past a cylinder. For values of the Reynolds number larger than the critical one, the flow shows oscillations at a given frequency. Such a frequency is independent of the external noise and forcing, so that a Fourier spectrum of the perturbation signal within the flow always shows a well defined peak on such frequency. Often, a resonator dynamics is recovered in a flow due to the onset of an absolute instablity; in other cases, the resonator dynamics could be due to some intristic characteristics of the flow, namely a strong non-parallelism. Indeed, in such cases the hypothesis of weakly non-parallelism made by Chomaz et al. (1991) is ill-posed, so that absolute instability is no more a necessary condition for the global instability of the flow.
On the other hand, an *amplifier* is a flow which presents a convective instability mechanism inducing a strong spatial amplification of the disturbances, such as a shear layer. Due to convective amplification, such flows are very sensitive to external noise and forcing, even of weak amplitude. They present a wide spectrum, although the most sensitive frequencies are more amplified than the others. When the flow is forced at a certain frequency, the structures developing into the flow are strongly dependent on the forcing frequency.
In some cases, for inhomogeneous flow geometries, the flow is characterized by zones of convective instability surrounded upstream and downstream by regions of stability. An example could be found in Figure 2.1 (c) for the flow past a backward-facing step. Thus, an impulsively injected perturbation initially grows and then decays, due to the local features of the flow. The amplification or damping of the perturbation at a certain streamwise location is directly linked to the presence of a convective instability. Local convective modes could be computed by a spatial instability analysis at different streamwise positions within the flow, in order to predict whether the perturbation would grow or decay in space. Nevertheless, the presence of a local spatially unstable mode is not the

only reason for the occurring of a spatial amplification of the perturbations. A spatial growth of disturbances could also be due to the high non-normality of stable eigenmodes.

2.3 Non-normality and local optimal perturbations

The classical instability analysis briefly described in the previous subsections rely on the solution of an eigenvalue problem for the NS equations linearized about a steady state. For some flows, the predictions of the local eigenvalue analysis have been able to match the experimental findings, as for Rayleigh-Benard and Taylor-Couette flows. In other cases, the local eigenvalue analysis has been found to fail. For instance, the critical Reynolds number predicted by eigenvalue analysis for Poiseuille flow is approximately $Re = 5772$ (Orszag, 1971), but it has been experimentally observed that transition occurs earlier, at $Re \approx 1000$ (Patel and Head, 1969). Similarly, in the case of the Couette flow, eigenvalue analysis computations predict a critical Reynolds number tending to infinity, whereas, in an experimental framework, transition is observed for $Re \approx 350$ (Tillmark and Alfredsson, 1992). Discrepancies are also found for boundary layer flows, for which transition could be abrupt, not following the slow process of asymptotical growth of TS waves.

Non-normality and transient growth Farrell (1988) was the first author suggesting that the excitation of non-modal perturbations strongly amplified in the flow could facilitate transition from laminar to turbulent flows. The author computed by means a variational method based on the local Orr-Sommerfeld and Squire equations, the perturbation that attains the highest energy gain in a given time period, called *optimal perturbations*, for a plane channel flow. Such perturbations are able to reach, in a finite time, an energy amplification much larger than the one reached by the eigenvalues of the NS operator. In fact, as concluded by Butler and Farrell (1992):

> *"What makes the initial-value problem for viscous shear flow interesting is that the set of operators involved is not self-adjoint in the norms of physical interest [...] The eigenfuctions resulting from a non-self-adjoint system are not orthogonal. As a result, a perturbation may consist of modes that initially destructively interfere, then separate in time to reveal considerable growth in integral energy or rms amplitude before decay and the eventual domination of the least-damped mode set in."*

In the years following such works, other authors (Gustavsson, 1991, Reddy and Henningson, 1993, Trefethen et al., 1993) drew similar conclusions about the fact that even if all the eigenmodes associated with a particular flow are stable, some perturbations could be strongly amplified if the associated eigenvectors are non-orthogonal. Such mechanism of transient growth of perturbations induced by non-normality is sketched in Figure 2.2: the vector $\mathbf{f}$ represents the initial perturbation, whereas the vectors Φ_1 and Φ_2 represent the eigenvectors of the linear NS operator. The initial perturbation can be decomposed on the basis of the eigenvectors, which in the case under consideration are stable and non-orthogonal, as shown in Figure 2.2. Even if Φ_1 and Φ_2 decrease asymptotically, since their are associated with stable eigenmodes, their difference, which is here equal to $\mathbf{f}$,

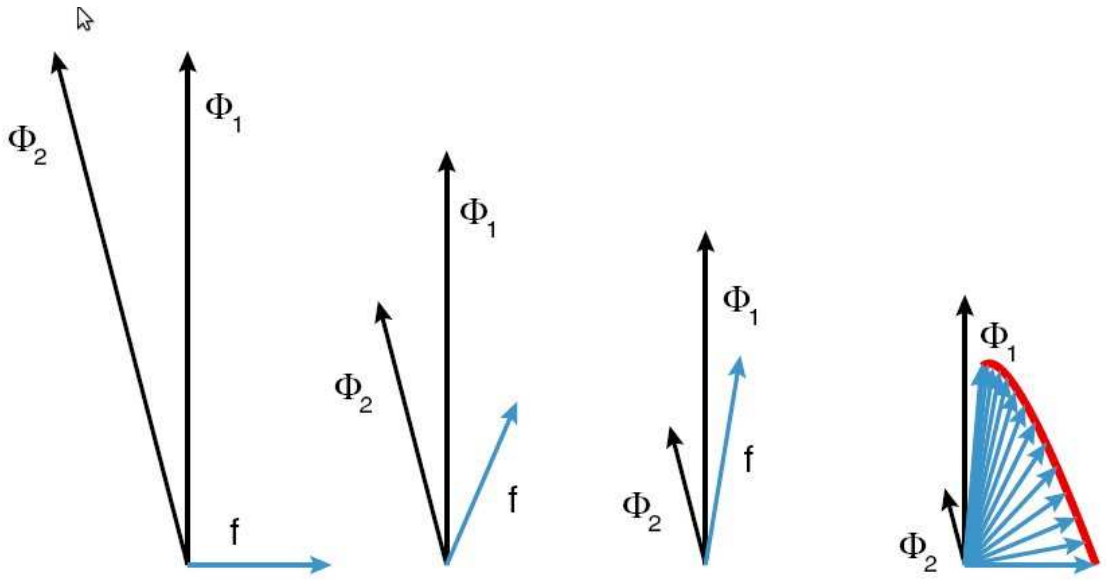

Figure 2.2: Schematic of non-normal transient growth and caption taken from Schmid (2007). Vector example of transient growth. Starting on the left, the vector **f** is defined as the difference between the nearly collinear vectors Φ_1 and Φ_2. During iteration (proceeding to the right of the figure), the vector Φ_1 decreases in length by 20% whereas vector Φ_2 shrinks by 50%. The vector **f** gradually turns into the direction of Φ_1 (sketch on the right), but increases substantially in length, before decaying to zero. Thus, the superposition of decaying nonorthogonal eigenfunctions can produce, in the short term, growth in the norm of a perturbation. The same scenario with orthogonal vectors Φ_1 and Φ_2 would have resulted in monotonic decay of the norm of **f**.

increases transiently. This transient growth is clearly shown by the red line in Figure 2.2, and is due to the non-orthogonality of the eigenvectors Φ_1 and Φ_2, but also to the initial perturbation chosen. For instance, an initial vector $\mathbf{f}$ parallel to Φ_1 or Φ_2 would have descreased monotonically.
For boundary-layer flows, the *optimal perturbations* were first computed by Luchini (2000), Schmid (2000), Corbett and Bottaro (2000), Andersson et al. (1999). In particular, Schmid (2000) used an eigenfunction expansion in discrete and (discretized) continuous modes. Corbett and Bottaro (2000) used a technique based on the direct and adjoint initial value problem in a temporal framework which avoids any modal representation. Luchini (2000) and Andersson et al. (1999) used a similar technique in a spatial framework. The results of their direct-adjoint space-marching technique showed a very good comparison with the results of the experiments by Westin et al. (1994), which were conducted on a boundary layer excited with grid-generated turbulence.
In all of these works the authors showed that, in a local framework, transient growth of optimal perturbations is essentially due to two amplification mechanisms: the *Orr* and the *lift-up* mechanism.

The Orr mechanism The inviscid Orr mechanism was first described by Orr (1907). The author observed that in a two-dimensional inviscid flow, having a constant shear in the plane $x-y$, the spanwise vorticity should be constant. When the vorticity perturbation is initially tilted opposing to the streamwise direction, the conservation of the vorticity induces a transient growth of the velocity components in the $x-y$ plane. Thus, the energy of the perturbation grows transiently as an effect of the non-normality of the operator. The optimal perturbations computed for shear flows is thus characterized by flow patterns that oppose the mean shear.

The *lift-up* mechanism Ellingsen and Palm (1975) and Landahl (1980) were the first authors to identify the so-called *lift-up* mechanism inducing a growth on the perturbations in a boundary-layer flow. By superposing a longitudinal vortex to a boundary layer having zero velocity components on the spanwise direction, low-momentum fluid is *lifted up* from the wall, whereas high-momentum fluid is deplaced down towards the wall. The physical mechanism inducing such a behaviour could be easily inferred by the structure of the boundary layer. Since the characteristic length of such flow in the streamwise direction is $\mathcal{O}(Re^{1/2})$ times larger than its thickness, the initial spanwise component of the initial longitudinal vortex would induce a streamwise velocity perturbation $\mathcal{O}(Re^{1/2})$ times larger.
The mechanism described is basically inviscid, but its viscous extention is the one inducing the transient growth of the perturbations discussed in the previous paragraph (Farrell (1988), Butler and Farrell (1992), Gustavsson (1991), Reddy and Henningson (1993), Trefethen et al. (1993)). In other words, such an amplification process, called the *lift-up* process (Landahl (1980)), is based on the generation of *streamwise streaks*, namely elongated regions of high and low perturbation velocity alternated in the spanwise direction, from *streamwise vortices*, namely regions of high vorticity on the crossflow plane.

The universality of optimal perturbations Streamwise streaks have been observed in experiments since the work of Klebanoff (1971). The author investigated the effect of freestream turbulence on the onset of transition, showing that low frequency (with respect with the higher-frequency TS–waves) fluctuations begins to grow at the plate leading edge and attained an amplitude of 5% the freestream velocity. They result in a spanwise oscillation of the layer inducing an alternating thickening or thinning of the layer. Kendall (1985) named such a disturbance Klebanoff mode, which is now known to be the result of the lift-up mechanism. Streamwise streaks are a fundamental feature of the boundary layer, cause they are responsible for the *by-pass* transition (Morkovin (1984)), so called because the slow transition scenario via TS-waves is by-passed by such a faster mechanism. They are also believed to be responsible for the energy transfer from the mean flow to the vortical structure present in developed turbulence (Hamilton et al., 1995).
Notably, even if streamwise streaks are the result of optimal initial perturbations, they are able to arise in the flow even when it is perturbed with freestream turbulence, or other exogeneous disturbances. Such a behaviour could be explained by the concept of *pseudo-resonance*, which was introduced by Trefethen et al. (1993). A flow is said to be capable of *pseudo-resonance* when it strongly amplifies time-dependent perturbations at various real frequencies forced in the flow. A self-adjoint (normal) operator is subjected to *pseudo-resonance* only when the forcing frequency is very close to one of the modes of the operator. For a non-normal operator, such a strong energy amplification occurs also for frequencies which are not close to an eigenmode of the considered operator.
As discussed in Luchini (2000), the universality of the output velocity profile no matter which perturbation is imposed, could also have an origin on the singular-value spectrum of the input-output transfer NS operator. Provided that the optimal perturbation is the first singular value of the perturbation, the separation between the first and the other singular values is an important feature of the flow; in fact, a random initial disturbance could be decomposed on the singular values basis, which is an ortho-normal basis (whereas the eigenmodes basis is non-orthogonal). When the first singular value is much larger than the others, the output of such initial perturbation would always consist almost entirely of the first singular vector, since the energies of the singular vectors are additive in an ortho-normal basis. This explains the observation of streamwise streaks in boundary layers in both experimental and numerical frameworks, and the consequent bypass transition.

2.4 Global instability analysis

In the two previous sections some fundamental concepts about open flows instability have been briefly described, in particular the concepts of *convective instability* and *transient growth*. Both mechanisms could be in part identified by means of a local eigenvalue analysis, by using a spatial analysis and a singular value analysis, respectively. Nevertheless, local methods do not allow an accurate prediction of the amount of integral energy in the flow at a certain time due to both the mechanisms of amplification, since the analysis performed at successive streamwise locations does not take into account the upstream effects or downstream propagation phenomena. Moreover, non-parallel effects are neglected by a local analysis, although they could contribute to a large part of the energy growth.

The convective instability due to the non-parallelism of the flow is a consequence of the non-normality of the operator in the streamwise direction, whereas the Orr and lift-up mechanism are induced by the so-called wall-normal non-normality of the NS operator. Convective non-parallel amplification could be large, and could cohexist with the Orr and lift-up mechanisms resulting in a large spatial growth in a limited part of the flow (see Figure 2.1 (c)).
A global eigenvalue analysis is able to accurately capture all of these mechanism, since it considers the real base flow, without any parallelism hypothesis. The first analysis of this kind was carried out by Pierrehumbert (1986), who reported the discovery of short-wavelength elliptic instability in inviscid vortex flows. Jackson (1987) and Zebib (1987) were the first authors proposing such a global approach in a viscous framework, for the case of the flow after a bluff body. Tatsumi and Yoshimura (1990) used such method some years later to study the flow in a rectangular duct driven by a constant pressure gradient, but a real development of the global approach has been seen only in the last decade, where it has been applied to several non-parallel flows (see Barkley and Henderson (1996), Theofilis et al. (2000), Ehrenstein and Gallaire (2005), for instance). Such a development is certainly due to the computing hardware improvements of the last years, as well as to the recent advances in algorithms for the numerical solution of large nonsymmetric generalized eigenvalue problems.
A two or three-dimensional base flow, $\mathbf{U}(x, y, x)$, is taken under consideration, and the global stability analysis is performed with respect to two or three-dimensional perturbations, $\mathbf{q}(x, y, z, t)$. Other than the initial linearization, no further approximation is required, whereas in the local instability analysis the perturbation is supposed sinusoidal in the streamwise and spanwise directions. Often, in spanwise homogeneous flows, the perturbation is supposed sinusoidal in the spanwise direction, and the problem is solved in a two-dimensional framework. In both cases, strong streamwise variations of the flow could be taken into account, differently from the local approaches with non-parallel corrections, like the PSE.
The perturbation is supposed to be of the following form:

$$\mathbf{q}(x, y, z, t) = \hat{\mathbf{q}}(x, y, z) \exp(\omega t), \tag{2.14}$$

or $\mathbf{q}(x, y, z, t) = \hat{\mathbf{q}}(x, y) \exp(i\beta z + \omega t)$ if the problem is homogeneous in the spanwise direction. Then, a large scale eigenvalue problem is solved for the global modal ω. In some cases, the eigenvalue problem is solved by means of eigenvalue algorithms (Theofilis, 2003). The classic QZ algorithm, which returns the full eigenvalue spectrum, was initially used to solve eigenvalue problems. However, the shortcoming of such an algorithm is that it requires the storage of four matrices having the dimension of the number of grid points used to discretize the two (or three) spatial directions. Thus, for most applications, the size of each of the four matrices would be of several *Gb*, and the required CPU time would scale with the cube of the matrices dimension, making this algorithm inappropriate for global instability analysis.
The development of the global approach was due, in the second half of the nineties, to the employement of the more efficient Krylov subspace iteration, which allows to recover only the most unstable part of the spectrum. The first authors adopting such a method were Ehrenstein (1996), Lin and Malik (1996) and Theofilis (1997), all of them using an Arnoldi's method together with a 'shift and invert' strategy. Instead of computing

the eigenvalues of the sparse matrix A, Arnoldi iteration computes the eigenvalues of the orthogonal projection of A onto a Krylov subspace. This projection is represented by an Hessenberg matrix which is of modest size, so that its eigenvalues can be computed efficiently.
Methods also exist which avoid storage of the matrix, as proposed in Barkley and Henderson (1996) and Tuckerman and Barkley (2000), which rely of the successive application of the operator A to an initial guess vector. Iterative matrix-free approaches are often used in order to compute the integral energy gain, without computing the eigenvalues of the operator. An example could be the so-called *direct optimal growth* method by Barkley et al. (2008), which evaluate the leading eigenmode of the operator AA^+ (where $^+$ identifies the adjoint), by the successive application of such an operator to an initial guess vector. Other methods are based on a Lagrange multipliers technique, leading to direct-adjoint iterations, as the one used in Corbett and Bottaro (2000) in a local framework.
However, global instability analysis has not been applied yet to flat plate boundary layer flows, either attached or separated. In the next section the state of the art on the instability dynamics and transition of attached and separated boundary layers is described.

2.5 State of the art

2.5.1 The attached boundary layer

As already discussed in section 2.1, the first authors proposing the existence of two-dimensional unstable waves in the Blasius boundary layer were Tollmien (1929) and Schlichting (1933). TS waves are the first modes becoming unstable as recovered by a local eigenvalue analysis based on the Orr-Sommerfeld and Squire equations. An experimental proof of their existence was found some years later by Schubauer and Skramstad (1948).
The stability of TS waves depends on their frequency in space and time, and on the Reynolds number, which for a boundary-layer flow is usually defined as $Re = U_\infty \delta^* / \nu$, where U_∞ is the freestream velocity, δ^* is the boundary-layer thickness, and ν is the viscosity. Since the boundary-layer thickness increases in the streamwise direction, the growth rate of the TS waves depends on the streamwise position along the flat plate. However, since the Orr-Sommerfeld and Squire equations are based on the hypothesis of parallel flow, the streamwise evolution of the boundary layer could be taken into account by performing the local eigenvalue analysis at different Reynolds numbers. A validation of such a local approach for low amplitude perturbations have been provided by DNS by Fasel and Konzelmann (1990), although different studies have aimed at including non-parallel effects into the instability analysis (see the discussion in section 2.1).

Natural transition The classical scenario of transition in a boundary layer involves the growth and secondary instability of TS waves. When a TS wave amplifies into the flow up to 1% of the freestream velocity, the flow could experience secondary instability (Herbert (1988)) and turn to three-dimensional disturbances.
Klebanoff et al. (1962) observed the amplification of three-dimensional waves, character-

ized by regions of spanwise alternating perturbations. The authors defined such pattern as *peaks* and *valleys*. The spanwise wavelength of such three-dimensional waves is of the same order of the streamwise one of the two-dimensional TS waves, so that such a transition scenario has been also called *fundamental* transition. In both peak and valley regions, the instantaneous velocity profiles have been found to show inflectional points, which could lead to inviscid instability. In the final phase of breakdown, when non-linear effects become important, rows of Λ-vortices aligned in the streamwise direction have been observed. Λ-vortices consists of pairs of streamwise counter-rotating vortices inducing the flow to *lift-up* towards the point in which they are connected. As a results, high amplitude peaks in the u velocity with a short duration in time are observed in the peak region prior to breakdown, which have been called *spikes* by the authors. The authors pointed out that the formation of spikes and Λ-vortices during the breakdown phase occurs on a smaller time scale than the one associated with the slow growth of TS waves.
Experimental and numerical validations of the Klebanoff's results were found by Kachanov and Levchenko (1984) and Rist and Fasel (1995), respectively. In the experiments by Kachanov and Levchenko (1984), TS waves were generated by a vibrating ribbon and three-dimensionality was introduced by a scotch tape, whereas in the simulations two- and three-dimensional perturbations were forced by blowing and suction at the wall. The results of such authors showed a good agreement, validating such a transition scenario.

A similar scenario of transition exists, which is called *H-type*, after Herbert, who performed a theoretical study of the secondary instability of TS waves. By a Floquet analysis, he found that TS waves are most likely to experience subharmonic secondary instability, since subharmonic modes has a larger growth rate than fundamendal ones. In the *H-type* transition, also called *subharmonic* scenario, the wavenumber of the secondary instability wave is half the streamwise wavenumber of the two-dimensional TS waves. The Λ vortices are observed also in this case, similarly to the previous case, but they present a staggered arrangement. In experiments, however, fundamental transition is observed more easily than subharmonic one, even if the latter is theoretically favored. In fact, low-amplitude streamwise vorticity perturbation in the mean flow are often present in an experimental framework, inducing the growth of fundamental modes. Indeed, H-type transition was first observed experimentally by Kachanov et al. (1977), fifteen years after the first observation of the K-type scenario. Some authors refers also to such a transition scenario as *N-type*, cause the experiments by Kachanov et al. (1977), were performed in Novosibirsk. Both K-type and H-type transitions are originating from the exponential growth of TS modes and their secondary instability. This is called *natural* transition, and is observed when the freestream turbulence is low, up to 1% the freestream velocity. For higher values of such parameter, instead, different mechanisms can set in, bypassing the *natural* transition scenario.

By-pass transition As already mentioned in section 2.3, in many flows transition occurs at Reynolds numbers lower than the critical one (the one for which the flow becomes asymptotically unstable). Such a behaviour is due to the non-normality of the NS operator, which induces a transient amplification of the perturbations. Farrell (1988) was the first author suggesting that the excitation of non-modal perturbations strongly amplified

in the flow could facilitate transition from laminar to turbulent flows. Thus, he computed the *optimal perturbations*, namely the perturbations inducing the maximal amplification of the energy, for a channel flow. For boundary layer flows, the *optimal perturbations* were first computed by Luchini (2000), Schmid (2000), Corbett and Bottaro (2000), Andersson et al. (1999). In all of these works the authors showed that, in a local framework, transient growth of optimal perturbations is mostly due to the *lift-up* mechanism. Ellingsen and Palm (1975) and Landahl (1980) were the first authors to propose that, by superposing a longitudinal vortex to a two-dimensional boundary layer, low-momentum fluid is *lifted up* from the wall, whereas high-momentum fluid is deplaced down towards the wall. As a result, *streamwise streaks*, namely elongated regions of high and low perturbation velocity alternated in the spanwise direction, are generated from *streamwise vortices*, namely regions of high vorticity on the crossflow plane.
Streamwise streaks could be observed in boundary layers when the freestream turbulence is higher than 1% the freestream velocity. Under such conditions, they have been observed in experiments since the work of Klebanoff (1971). Streaks are responsible for the *by-pass* transition (Morkovin (1984)), so called because the slow transition scenario via TS-waves is by-passed by such a faster mechanism. Indeed, growing downstream due to the lift-up mechanism, such elongated structures could experience secondary instability and breakdown, due to the inflection of the velocity profiles in their interaction zones (see Schoppa and Hussain (2002), Brandt et al. (2004)). In particular, Schoppa and Hussain (2002) performed an analysis of streaks extracted from fully developed near-wall turbulence showing that only about 20% of the streaks exceed the threshold for developing sinuous secondary instability. Brandt et al. (2004) showed that the most amplified secondary instability over a steady streak is an antisymmetric mode which induces spanwise oscillations on the low-speed streak. Such a scenario is called sinuous transition, and it has been observed in DNS more frequently than the varicose scenario, in which the secondary instability mode is symmetric.
The generation and breakdown of the streaks could be induced by the freestream turbulence. The investigations of Klebanoff (1971) and Kendall (1985), performed at low freestream turbulence levels, showed that streaky disturbances are the main features of the flow as the freestream turbulence level increases. Breakdown into turbulent spots occurs in regions where the streaks reach an high amplitude, and is often characterized by a wavy motion of the streak associated with the sinuous secondary instability. Similar results have been reported by Westin et al. (1994) in their study of boundary layer receptivity to localized freestream disturbances. Jacobs and Henningson (1999) observed that above the boundary layer the intensity of the turbulence slowly decays downstream, whereas inside the boundary layer it is highly damped, and the low-frequency disturbances, namely the streaks, appears.
Streaks could be induced in a boundary layer in other ways than by freestream turbulence. For instance, Klingmann (1992) generated streaks by means of a point-like disturbance. Acarlar and Smith (1987) forced a boundary-layer flow by a strong steady blowing in a streamwise oriented slit at the wall. They observed that the low-speed streaks developed a three-dimensional shear layer instability, due to a varicose secondary instability mode, which resulted in a periodic shedding of hairpin vortices. Singer and Joslin (1994) used blowing and suction to induce streamwise streaks and to excite a turbulent spot: hairpin vortices have also been observed when streaks are created with large blowing at the

boundary, whereas a smaller forcing is associated with a sinuous instability.
Another way for generating growing streaky structures in a boundary layer is the introduction of two finite-amplitude oblique waves having the same streamwise wavenumbers and spanwise wavenumber, but symmetric in the spanwise direction. The Fourier spectrum is thus dominated by the mode (1,1), where the digits refers to the streamwise and spanwise wavenumbers, respectively. The oblique waves experience transient growth while generating streamwise vortices due to the transfert of energy from the Fourier mode (1,1) to the (0, 2) one. Such streamwise vortices generate streaks by the lift-up effect. While the streaks are growing, the initial oblique waves decay until the flow field is dominated by the streaks. From this point on, the development is similar to the streak breakdown, as a fundamental secondary instability develops on the streak, inducing sinuous oscillations. This is called the *oblique transition* scenario. Such scenario was first proposed by Schmid and Henningson (1992) and verified experimentally by Elofsson and Alfredsson (1998) in plane Poiseuille flow and by DNS by Lundbladh and Henningson (1994) in Blasius boundary layer.

Turbulent spots For both *by-pass* and *oblique* transition, at large enough values of the Reynolds number, non-linear effects might kick in, and an impulse perturbation of sufficiently large amplitude could typically induce bypass transition by generating a turbulent *spot*. Such regions of randomized flow present a leading edge travelling at a velocity close to 90% the freestream velocity, and a trailing edge travelling at about 50% such velocity. As a result, the spot grows in size while travelling downstream. The lateral spreading is at a half-angle of about 10°, which is larger by an order of magnitude compared to the growth rate in the wall-normal direction which is about 1° (for a review, see Mathew and Das (2000)). If other spots are present, they could eventually merge one another leading the flow to a turbulent state. Since the early observations by Emmons (1951), many studies have been dedicated to the interior structure of turbulent spots, their shapes, spreading rates, and the mechanism of their rapid growth (Wygnanski et al. (1976), Perry et al. (1981), Gad-el Hak et al. (1981), Chambers and Thomas (1983), Barrow et al. (1984), Henningson et al. (1987), Sankaran et al. (1988), Lundbladh and Johansson (1991), Bakchinov et al. (1992), Henningson et al. (1993), Singer (1996), Matsubara and Alfredsson (2001)).
Turbulent spots are sustained by the self-regeneration character of the coherent structures present in wall bounded turbulent flows (Panton, 2001). Waleffe (1995) have described a simple cycle of events resulting in self-sustained turbulence in a turbulent boundary layer. The process consists of: (i) spanwise modulation of the streamwise velocity by the streamwise counter-rotating vortices, (ii) breakdown of the spanwise modulated flow from an inflectional wavelike instability; (iii) regeneration of the streamwise vortices from the nonlinear self-interaction of the growing instability. A possible mechanism for the regeneration of streamwise vortices from streaks, conjectured by Jimenez (1994), could be the following: the spanwise variation of the mean streamwise velocity, due to the streaks, induces a large wall-normal vorticity which is tilted into the streamwise direction by the normal shear of the streamwise velocity. As a result, streamwise vortices are formed again. Similarly, Schoppa and Hussain (2002) proposed that the streamwise vortices are

generated from the streaks which are not about to breakdown.

Hairpin vortices generation Recently, a new scenario of transition has emerged, based on vortex generation in wall bounded flows (Marusic (2009)). The relevance of hairpin vortices in the sustainment of wall turbulence has been proved in the past decades by a number of experimental (Head and Bandyopadhyay (1981)) and numerical (Adrian (2007)) studies. Before the first observations of hairpin vortices, Theodorsen (1952) conjectured its existence. He hypothized a vortex filament oriented spanwise to the mean flow, and perturbed by a wall-normal perturbation. The part of the filament away from the wall (the head of the structure) would experience higher mean flow velocity and be convected downstream faster than its lower part. Consequently, the legs of the vortex would be stretched, inducing the vortex to lift away from the wall and experience an higher mean velocity, resulting in a larger stretching. Such structures, inclined at 45° to the mean flow direction, are able to pump low-momentum fluid from the wall to the outer region of the boundary layer, inducing a low-speed streak, and to eject fluid outwards from the arch to the unperturbed flow. This ejection resembles the *bursting* phenomenon observed in turbulent boundary layer.
Swearingen and Blackwelder (1987) carried out experiments on Gortler counter-rotating streamwise vortices inducing streamwise streaks. They observed a scenario of transition inducing the generation of an hairpin vortex street, related with a varicose secondary instability. A different scenario is related to the spanwise oscillations induced by the sinous mode. They observed that the high frequency oscillations associated with the inflectional type inviscid instability are related with the velocity gradient in the spanwise direction rather than with the normal velocity gradient. Asai et al. (2002) experimentally investigated the secondary instability of low-speed streaks with respect to sinous and varicose modes, concluding that the latter leads to a train of hairpin vortices. Skote et al. (2002) conjectured that the generation of hairpin vortices in a turbulent boundary layer is related to a normal inflectional instability of the streaks.
On the other hand, some researchers proposed a different scenario for the occurrence of hairpin vortices. In Panton (1997) it is concluded that low-speed streaks are just the kinematic consequence of the passage of a hairpin vortex, since the spanwise spacing between streaks (100 viscous wall units) matches the one of the hairpin vortex legs. Similar conclusions are drawn by Adrian (2007). He studied the generation process of hairpin vortices in streamwise succession, observing that upstream and downstream hairpins are generated from a primary one, inducing a long low-speed region between the legs of the hairpins in the near-wall region. A clear evidence of the preponderance of hairpin vortices in the late stages of transition in a laminar boundary layer flow has been provided conclusively by Wu and Moin (2009). By means of a direct numerical simulation, they observed the onset of hairpin structures emerging from Λ-shaped vortices excited by the free-stream turbulence. They also concluded that low-speed streaks are just a kinematic feature induced by the passage of hairpin structures.
As it has been discussed, two different views of boundary layer transition could be identified, which are highlighted in the review by Panton (2001). Two schools could be identified, one based on instability and transient growth mechanisms (Schoppa and Hussain (2002)),

and the other based on vortex regeneration mechanisms (Adrian (2007)). However, a complete model for the generation and self-sustainement of such coherent structures in turbulent flows could be still not recovered in literature. Thus, an analysis of the instability dynamics and consequent transition in boundary layer flows is of interest.

2.5.2 The separated boundary layer

When a laminar boundary layer encounters a sufficiently large adverse pressure gradient, a laminar separation bubble (referenced as LSB hereafter) occurs. Many engineering applications such as low Reynolds number aerodynamics configurations of airfoils and turbomachineries involve typical structures of LSB. Since the first observations of Jones (1934), flow separation has been extensively studied, experimentally as well as numerically. Some of these researches deals with its steady structure, such as the experimental work of Gaster (1969), the first numerical attempt of Briley (1971) and the method of matched asymptotic expansions provided by the triple deck theory (Sychev et al., 2005). The first experimental and theoretical works by Gaster (1969) aimed at classifying separation bubbles over airfoils in *short* and *long* ones. The formers, characterized by a weak recirculation with a turbulent reattachment, show a slight step in the pressure distribution produced by the recirculation, which has a negligible effect on the forces acting on the aerofoil. However, a short bubble can enlarge, due to an increasing angle of incidence of the airfoil or a decreasing freestream velocity, becoming a long one. The pressure distribution associated with a long bubble is quite different from that of inviscid flow, and the forces acting on the aerofoil are therefore modified by the change in the reattachment point. Such a phenomenon has been called *bursting* by Gaster (1969), and it has been found to induce an increase in drag, a fall in lift and eventually a stall.
In order to define a criterion for bursting, the same author defined a non-dimensional pressure gradient parameter describing the pressure distribution in the region of the bubble, $P = (\Theta_s^2/\nu)(\Delta U/\Delta x)$ where ΔU is the rise in velocity over the length of the bubble Δx, Θ_s is the momentum thickness at the separation point and ν is the kinematic viscosity. Experimental data have showed that the critical bursting Reynolds numbers correlate with the Gaster's pressure-gradient parameter. In particular, in a series of experiments in which the flow is excited by means of acoustic waves, the same author recovered a different dynamics for short and long bubbles.
Short bubbles seem to transition via the amplification of two-dimensional waves due to an inviscid KH instability induced by the presence of an inflection point on the velocity profiles along the separation streamline. Instability is thus associated with the local features of the flow, so that it could be in part studied by the classical instability analysis. Rist and Maucher (2002) and Dovgal et al. (1994) both found a confirmation of such a behaviour by means of DNS and experiments, respectively.
On the other hand, long bubbles have shown to transition in a different way. In particular, Gaster (1969) observed the onset of a low-frequency oscillation, the *bursting*, charactering the bubble, which is not recovered by a local eigenvalue analysis. Several studies aimed at understanding the origin of such low-frequency oscillations. For instance, Pauley et al. (1990) found that bursting occurs under the same conditions as periodic shedding, suggesting that it is actually periodic shedding which has been time-averaged. The authors found a parameter, the Strouhal number based on the shedding frequency, the local free-

stream velocity, and the boundary-layer momentum thickness at separation which was independent of the Reynolds number and the pressure gradient, establishing a criterion for the onset of shedding.

Resonator dynamics A typical feature of LSB is its very unstable nature and its high sensitivity to background disturbances, even at low Reynolds numbers. This property is often synonymous of loss of aerodynamic performances such as increase of the drag or loss of lift on airfoils at angle of attack close to static stall values. As a consequence, many investigations have been carried out on the onset of unsteadiness in several configurations; for instance, the flat plate separated boundary layer has been studied by means of DNS (Rist and Maucher, 1994, 2002) and experiments (Dovgal et al., 1994), as well as the backward-facing-step flow (see Armaly et al. (1983) and Kaiktsis et al. (1996) for instance).
In particular, the self-sustained oscillatory behavior as well as the role of topological changes in the separated flows has received a lot of attention during the last two decades. More specifically, some analysis have been based on the theoretical results obtained in a weakly non-parallel framework by Huerre and Monkewitz (1985), stating that the onset of global instabilities observed in absence of external forcing is related to the existence of a local absolute instability. In particular, Hammond and Redekopp (1998) have studied the local instability of a model flow based on the Falkner-Skan velocity profiles, identifying a global instability arising as a result of a local absolute one. A criterion for absolute instability was derived, stating that the global mode associated with the inflection point at the separation streamline becomes unstable when the maximum backflow velocity approaches about 30% the freestream one. The dependence of such a threshold on the Reynolds number has been adjusted by considering an analytical velocity profile by Alam and Sandham (1999). Rist and Maucher (2002) analyzed the parameters which influence the onset of such an absolute instability, such as the maximum height of the separated region. Moreover, the non-linear selection criteria based on the local properties of the flow used by Marquillie and Ehrenstein (2003) has allowed to explain the global high frequency unsteadiness of a recirculation bubble confined between two bumps.
However, the connection between the dynamics of a long bubble and an absolute instability has not been demonstrated yet. Dallmann et al. (1995) have pointed out the role of topological changes on the instability of the flow. Some years later, such an hypothesis was corroborated by Theofilis et al. (2000). By means of a global eigenvalue analysis, the authors were able to recover an unstable global mode, which was not due to an absolute instability, but to the topological features of the separated flow. Such global mode was steady and three-dimensional; by superposing it to the base flow, a bifurcation was observed turning the two-dimensional flow into a three-dimensional one, in which the separation line remained unaffected while the reattachment line became three-dimensional. Such results confirmed the results of several experimental observations (Dovgal et al., 1994).
This global instability mechanism can thus be characterized by a resonator dynamics similar to the one observed in many open shear flows, for instance the self-sustained oscillations occurring in the wake of a cylinder (Pier, 2002). In such cases, the instability dynamics of the flow is due to the existence of an unstable global mode. A resonator

dynamics driven by a three-dimensional mechanism has been observed in a flat-plate separated flow by Theofilis et al. (2000), in a flow over a backward facing step by Barkley et al. (2002) or behind a bump by Gallaire et al. (2007). The same authors have identified a slowly amplified, steady and unstable global mode, not revealed by a local instability analysis.

Amplifier dynamics However, some authors has recently conjectured that the occurrence of self-sustained oscillations in separated flows observed numerically or experimentally may be attributed not only to a resonator dynamics, but should also take into account the influence of external forcing, such as discretization errors in numerical simulations or environment noise occuring in experiments. For instance, Kaiktsis et al. (1996) have reported discrepancies among various numerical simulations of the time asymptotic state of a two-dimensional flow over a backward facing step. Typically, the onset of global unsteadiness appears to be closely dependent on the numerical method and the grid resolution and well below the emergence of an unstable global mode as reported by Barkley et al. (2002). The response of the convective modes to the level of background noise due to the discretization errors is thus proposed by Kaiktsis et al. (1996) to explain such discrepancies in the asymptotic regime. A similar convective mechanism sustained by the presence of numerical noise is proposed by Wasistho et al. (1997) as an explanation of the onset of unsteadiness in a flat-plate separated flow. All these studies suggest that an inherent random background noise may generate unsteadiness in a separated flow. Therefore, the amplifier character of the flow which is due to the presence of a convectively unstable region may play a major role in the capability of the flow to self-sustain perturbations.
Since the seminal work of Cossu and Chomaz (1997) on the space-time dynamics of open flows, and the review of Chomaz (2005), it is well known that a global amplifier dynamics could derive from the convective instabilities due to the non-orthogonality of the set of global eigenmodes associated with the considered flow. Since then, this topic has received the attention of several researchers, turning into a vivid research field. In particular, in the previous works of Ehrenstein and Gallaire (2005), Alizard and Robinet (2007) and Åkervik et al. (2008) on a flat plate boundary layer, a large transient growth has been observed due to the optimal non-modal amplification of a localized perturbation. An appropriate superposition of global eigenmodes has shown that the optimal perturbation takes the form of a wave packet travelling along the flat plate and amplifying itself, leading to an increase of the kinetic energy of the perturbation.
Furthermore, similar global stability analysis have been performed in various configurations as a falling liquid curtain by Schmid & Henningson Schmid and Henningson (2002), an open cavity flow by Åkervik et al. (2007) and Henningson and Åkervik (2008) or a flow behind a bump by Ehrenstein and Gallaire (2008) and have pointed out new physical understandings on the low-frequency global unsteadiness of open-flows as the flapping effect occurring in separation bubbles (Dovgal et al., 1994), which has been explained in terms of an interaction of modes.
Furthermore, Blackburn et al. (2008) and Marquet et al. (2008) have studied the convective instability mechanism emerging in separated flow over a step by means of an optimization strategy involving the integration in time of the direct and adjoint linearized

Navier-Stokes equations. The results obtained by such a method have confirmed the large transient growth resulting from the convective amplification of a wave packet localized in space. Such studies have thus provided an attempt to relate the unsteadiness observed in numerical simulation and laboratory experiments in the considered flows with the noise amplifier dynamics derived from the optimal transient behaviour.
However, it is still not clear which instability mechanisms among the modal, non-modal and pseudo-resonance one, is selected by the separated flows and under which conditions such flows experience transition. Thus, a detailed study of the transient and asymptotical dynamics of optimal or random perturbation, which are impulsively injected or continuously forced in a separated boundary layer, is of interest.

2.6 A global approach to the boundary-layer flow problem

Global instability analysis has been applied to attached (Åkervik et al. (2008), Alizard and Robinet (2007)) and separated (Åkervik et al. (2007), Blackburn et al. (2008), Marquet et al. (2008)) boundary layer flows. A strong amplifier dynamics due to KH/TS waves has been recovered in both cases.
However, a fully three-dimensional global approach has still not been applied to the case of the attached boundary layer. Indeed, the spanwise dynamics in a boundary layer is crucial, since transition occurs often by means of a three-dimensional mechanism bypassing the TS waves amplification, as it has been previously discussed. Even if a local eigenvalue analysis is capable of recovering the transient amplification due to the lift-up phenomenon, it only take into account single-wavenumber perturbations in the streamwise direction. In other words, since in most practical cases boundary layers undergo transition by receptively selecting and amplifying exogenous disturbances, such as those arising from the presence of localized roughness elements or gaps on the wall, it makes sense to inquire on the initial spatially localized flow patterns which most easily amplify and cause breakdown. In fact, although the transition mechanism based on the local optimal perturbation concept brings into play some of the main ingredients present in transitional flow fields, namely streaks and vortices, it has the limitation of focusing onto a single wavenumber/frequency at a time, plus that of neglecting non-linear effects. When a direct simulation is performed to assess the effectiveness of linear optimal perturbations in triggering transition, the outcome is rather disappointing (Biau et al. (2008)), and suboptimal disturbances are found to be much more efficient than optimals. Indeed, in this thesis the optimal three-dimensional dynamics of an attached boundary layer would be studied by means of global eigenvalue analysis, direct-adjoint iterations and direct numerical simulations, in order to identify the initial, localized states which most easily bring the flow on the verge of turbulent transition via the formation of a spot.
Concerning the separated flow, several geometry-induced separation bubbles have been already studied by a global approach, as it has been discussed in the previous section. However, an adverse-pressure induced configuration has still not been analysed in detail, except for the seminal work of Theofilis et al. (2000), in which only the modal dynamics was studied. In particular, the following issues still need to be investigated in detail (i) the

role of the convective Kelvin–Helmholtz instability of the shear layer along the separation streamline with respect to the flapping phenomenon (ii) the influence of topological flow changes on the destabilization of the flow (iii) the connection of the high sensitivity of the flow to external forcing with the onset of unsteadiness (iv) the mechanism of transition from convective to global instability (v) the role of centrifugal steady modes on the transition to turbulence. A detailed study of the aforementioned issues could be performed by means of global eigenvalue analysis, together with direct numerical simulation in order to take into account non-linear effects.
In the present thesis such issues would be analysed in detail. In particular, in Chapter 4, the two-dimensional dynamics of a separated boundary layer would be analyzed with respect to the flapping phenomenon, the amplifier dynamics and the presence of topological changes in the flow. In Chapter 5, the sensitivity to external forcing and its role on the vortex shedding phenomenon would be discussed. In Chapter 6, the three-dimensional dynamics of the separated flow would be studied, and the role on transition of three-dimensional centrifugal stable and unstable modes would be clarified. Finally, in Chapter 7 the optimal localized perturbations leading an attached boundary layer flow to turbulence would be analyzed.

3
Computational approach

3.1 Governing equation and boundary conditions

The behaviour of a three-dimensional incompressible flow is governed by the Navier–Stokes equations,

$$\check{\mathbf{u}}_t + (\check{\mathbf{u}} \cdot \bigtriangledown)\check{\mathbf{u}} = -\bigtriangledown \check{p} + \frac{1}{Re} \bigtriangledown^2 \check{\mathbf{u}}, \tag{3.1}$$

$$\bigtriangledown \cdot \check{\mathbf{u}} = 0, \tag{3.2}$$

where $\check{\mathbf{u}} = (\check{u}, \check{v}, \check{w})^T$ is the velocity vector and $\check{p}$ is the pressure. Dimensionless variables are defined with respect to the inflow displacement thickness, δ^* , and to the freestream velocity, U_∞ , so that the Reynolds number is equal to $Re = U_\infty \delta^* / \nu$, where ν is the kinematic viscosity coefficient. A rectangular computational domain is employed, x, y and z being the streamwise, wall-normal and spanwise directions, respectively.

3.2 Direct numerical simulation (DNS)

The Navier–Stokes equations are integrated by a fractional step method using a staggered grid (see Verzicco and Orlandi (1996)). The viscous terms are discretized in time using an implicit Crank–Nicholson scheme, whereas an explicit third-order-accurate Runge–Kutta scheme is employed for the non-linear terms. The inversion of sparse matrices, typical of implicit numerical schemes, is avoided by means of a factorization which allows to reduce the problem to the inversion of three tri-diagonal matrices, one for every spatial direction. The *fractional step* method has been applied to the Navier-Stokes equations in a velocity-pression formulation, which have been integrated in the following form:

$$\frac{\check{\mathbf{u}}^* - \check{\mathbf{u}}^n}{\triangle t} + \left[\frac{3}{2} H\left(\check{\mathbf{u}}^n\right) - \frac{1}{2} H\left(\check{\mathbf{u}}^{n-1}\right)\right] = -\bigtriangledown \check{p}^n + \frac{1}{2Re} \bigtriangledown^2 \left(\check{\mathbf{u}}^* + \check{\mathbf{u}}^n\right) \tag{3.3}$$

where the Adams-Bashfort scheme has been reported as an example of the time discretization of non-linear terms for the sake of simplicity, and the nonsolenoidal velocity $\check{\mathbf{u}}^*$ does not satisfy the continuity equation (3.2). The following correction is thus applied:

$$\check{\mathbf{u}}^{n+1} = \check{\mathbf{u}}^* - \triangle t \bigtriangledown \pi \tag{3.4}$$

where π is the pressure correction computed from the continuity equation. We thus obtain:

$$\bigtriangledown^2 \pi = \frac{1}{\triangle t} \bigtriangledown \cdot \check{\mathbf{u}}^*, \tag{3.5}$$

representing a Poisson equation, which is solved by means of the *fishpack* routine for the solution of elliptics equations discretized with a second-order-accurate centered space discretization. Using the pressure correction obtained from equation (3.5), the value of the pressure is updated through the equation:

$$\check{p}^{n+1} = \check{p}^n + \pi - \frac{\triangle t}{2Re} \bigtriangledown^2 \pi; \tag{3.6}$$

the momentum equation (3.3) become:

$$(I - \Delta t \frac{1}{2Re} \bigtriangledown^2)(\check{\mathbf{u}}^* - \check{\mathbf{u}}^n) =$$

$$-\Delta t \left[\frac{3}{2} H\left(\check{\mathbf{u}}^n\right) - \frac{1}{2} H\left(\check{\mathbf{u}}^{n-1}\right) \right] - \Delta t \bigtriangledown \check{p}^n + (\frac{\Delta t}{Re} \bigtriangledown^2) \check{\mathbf{u}}^n \tag{3.7}$$

where the left hand side is known. This equation is solved using the factorization:

$$\left(I - a \bigtriangledown^2\right)\left(\check{\mathbf{u}}^* - \check{\mathbf{u}}^n\right) = \left(I - a \frac{\partial^2}{\partial x^2}\right)\left(I - a \frac{\partial^2}{\partial y^2}\right)\left(I - a \frac{\partial^2}{\partial z^2}\right)\left(\check{\mathbf{u}}^* - \check{\mathbf{u}}^n\right) \tag{3.8}$$

where x, y, z are the spatial directions and $a = \Delta t \frac{1}{2Re}$. Such a factorization introduces a third order error in time, making the algorithm second-order accurate, but allows a fast integration of the Navier–Stokes equations, being the inversion of a sparse matrix reduced to the integration of three tridiagonal matrices.
A second-order-accurate centered space discretization has been used for the linear terms. For the two-dimensional computations, a sixth-order-accurate space discretization has been implemented for the non-linear terms, based on a combined compact scheme for non-uniform grids (Chu and Fan (1999)). The basic idea of such a method is to relate the values of the unknown and of its first and second derivatives at three neighbouring grid points according to the following procedure. Consider the unknown, $\check{\mathbf{u}}_i$, and its first and second derivative, $\check{\mathbf{u}}'_i$ $\check{\mathbf{u}}''_i$ at any internal grid point with abscissa x_i, together with the corresponding values at the points $i-1$ and $i+1$. The scheme is based on the Hermite formula

$$\sum_{k=-1}^{1} (\alpha_k \check{\mathbf{u}}_{i+k} + \beta_k \check{\mathbf{u}}'_{i+k} + \gamma_k \check{\mathbf{u}}''_{i+k}) = 0. \tag{3.9}$$

In order to find the coefficients α_k, β_k and γ_k, the local Hermite polynomial is defined in the interval $[x_{i-1}, x_{i+1}]$,

$$\begin{aligned} H_i(x) \;=\; & \check{\mathbf{u}}_i + (\check{\mathbf{u}}_{i-1} - \check{\mathbf{u}}_i)\Phi_1(\eta) + (\check{\mathbf{u}}_{i+1} - \check{\mathbf{u}}_i)\Phi_2(\eta) + \\ & + \check{\mathbf{u}}'_{i-1} h_i \Phi_3(\eta) + \check{\mathbf{u}}'_{i+1} h_i \Phi_4(\eta) + \\ & + \check{\mathbf{u}}''_{i-1} h_i^2 \Phi_5(\eta) + \check{\mathbf{u}}''_{i+1} h_i^2 \Phi_6(\eta), \end{aligned} \tag{3.10}$$

where $h_i = x_i - x_{i-1}$, $\eta = (x - x_i)/h_i$ and

$$\begin{aligned} \Phi_j(\eta) \;=\; & a_j \eta + b_j \eta^2 + c_j \eta^3 + d_j \eta^4 + e_j \eta^5 + g_j \eta^6, \\ & j = 1, 2, ..., 6. \end{aligned} \tag{3.11}$$

Imposing the following boundary conditions:

$$\begin{aligned}
\Phi_1(-1) = 1, \quad \Phi_j(-1) = 0, \quad & j = 2,3,4,5,6, \\
\Phi_2(\frac{h_{i+1}}{h_i}) = 1, \quad \Phi_j(\tfrac{h_{i+1}}{h_i}) = 0, \quad & j = 1,3,4,5,6, \\
\Phi'_3(-1) = 1, \quad \Phi'_j(-1) = 0, \quad & j = 1,2,4,5,6, \\
\Phi'_4(\frac{h_{i+1}}{h_i}) = 1, \quad \Phi'_j(\tfrac{h_{i+1}}{h_i}) = 0, \quad & j = 1,2,3,5,6, \\
\Phi''_5(-1) = 1, \quad \Phi''_j(-1) = 0, \quad & j = 1,2,3,4,6, \\
\Phi''_6(\frac{h_{i+1}}{h_i}) = 1, \quad \Phi''_j(\tfrac{h_{i+1}}{h_i}) = 0, \quad & j = 1,2,3,4,5,
\end{aligned} \tag{3.12}$$

and taking $\check{\mathbf{u}}'_i = H'_i(x_i)$ and $\check{\mathbf{u}}''_i = H''_i(x_i)$, the coefficients in equation (3.9) are determined. Therefore, by solving a block-tridiagonal algebraic system the first and second derivatives are computed. The above procedure is employed along the horizontal and vertical directions to compute the derivatives of $\check{u}$ and $\check{v}$, respectively, at the cell faces. Moreover, since the Navier–Stokes equations are integrated on a staggered grid, a three-point sixth-order-accurate interpolation formula has also been employed to compute the values of the unknowns at the cell centers. The interpolation formula is obtained applying a procedure similar to the previous one by taking $\check{\mathbf{u}}_i = H_i(x_i)$, $\check{\mathbf{u}}_i$ indicating the value of the unknown to be interpolated at the cell center, whereas $\check{\mathbf{u}}_{i+1}$, $\check{\mathbf{u}}_{i-1}$,$\check{\mathbf{u}}'_{i+1}$, $\check{\mathbf{u}}'_{i-1}$, $\check{\mathbf{u}}''_{i+1}$, $\check{\mathbf{u}}''_{i-1}$ are evaluated at the faces of the cell. For the three-dimensional computations a second-order-accurate centered space discretization has been used also for the non-linear terms, in order to limit the computational cost.

3.3 Newton procedure for the base flow

The above DNS method has been used to perform all the non-linear simulations, and to compute the base flow for the global stability analysis at subcritical Reynolds number. However, using the DNS, the residual cannot be reduced to machine zero when computing the base flow at supercritical as well as at slightly subcritical Reynolds numbers since some frequencies present in the numerical noise are highly amplified. In these cases, several approaches may be employed to compute the base flow, based on filtering techniques (see Åkervik et al. (2006)) or on continuation methods. Here, a time-stepping continuation method has been employed. Therefore, following the procedure proposed by Tuckerman and Barkley (2000), the DNS method has been combined with a Newton steady-state solver. The steady-state Navier–Stokes equations are written as:

$$N(\check{\mathbf{q}}) + L(\check{\mathbf{q}}) = 0. \tag{3.13}$$

where $\check{\mathbf{q}} = (\check{\mathbf{u}}, \check{p})$ and

$$L(\check{\mathbf{q}}) = \frac{1}{Re} \bigtriangledown^2 \check{\mathbf{u}}, \quad N(\check{\mathbf{q}}) = -(\check{\mathbf{u}} \cdot \bigtriangledown)\check{\mathbf{u}} - \bigtriangledown \check{p} \tag{3.14}$$

are the linear and non-linear operators, respectively. In order to find the solution of equation (3.13), Newton's method is used. Starting from an initial solution, $\check{\mathbf{q}}_0$, the

variable $\check{\mathbf{q}}$ is iteratively updated by means of an increment, $\delta\check{\mathbf{q}}$, computed by solving the following equation:

$$(N_q + L)(\delta\check{\mathbf{q}}) = (N + L)(\check{\mathbf{q}}), \tag{3.15}$$

where N_q is the linearized operator N. By choosing the operator $\triangle t \left(I - \frac{\triangle tL}{2}\right)^{-1}$ as a preconditioner of the equation (3.15), one obtains the following equation:

$$\begin{aligned} \left[\left(I - \frac{\triangle tL}{2}\right)^{-1}(I + \triangle tN_q + \frac{\triangle tL}{2}) - I\right](\delta\check{\mathbf{q}}) &= \\ = \left[\left(I - \frac{\triangle tL}{2}\right)^{-1}(I + \triangle tN + \frac{\triangle tL}{2}) - I\right](\check{\mathbf{q}}). & \end{aligned} \tag{3.16}$$

It is noteworthy that the solution of equation (3.16) can be iteratively computed using the existing DNS algorithm with minor modifications since the fractional step operator, obtained by considering the implicit time discretization of the term $L(\check{\mathbf{q}})$, and the explicit discretization of $N(\check{\mathbf{q}})$,

$$\check{\mathbf{q}}^{n+1} = \left(I - \frac{\triangle tL}{2}\right)^{-1}\left[I + \triangle tN + \triangle t\frac{L}{2}\right]\check{\mathbf{q}}^{n}, \tag{3.17}$$

has been formally recovered.

3.4 Three-dimensional direct-adjoint optimization

The linear behaviour of a perturbation $\mathbf{q} = (u, v, w, p)^T$ evolving in a laminar incompressible flow past a flat plate is studied by employing the governing equations linearized around the two-dimensional steady state $\mathbf{Q} = (U, V, 0, P)^T$:

$$\left.\begin{aligned} u_x + v_y + w_z &= 0 \\ u_t + (uU)_x + U_y v + V u_y + p_x - \frac{u_{xx}}{Re} - \frac{u_{yy}}{Re} - \frac{u_{zz}}{Re} &= 0 \\ v_t + U v_x + (vV)_y + u V_x + p_y - \frac{v_{xx}}{Re} - \frac{v_{yy}}{Re} - \frac{v_{zz}}{Re} &= 0 \\ w_t + U w_x + V w_y + p_z - \frac{w_{xx}}{Re} - \frac{w_{yy}}{Re} - \frac{w_{zz}}{Re} &= 0. \end{aligned}\right\} \tag{3.18}$$

In order to close the system, a zero perturbation condition is chosen for the three velocity components at the x and y boundaries, whereas periodicity of the perturbation is imposed on the spanwise direction. The outlet zero perturbation condition is enforced by means of a fringe region, which lets the perturbation at the exit boundary vanish smoothly. The fringe region, of length L_f, is implemented by adding onto the equations a forcing term in a limited region with $x > x_{out}$. The forcing function applied in the fringe region is

defined as:

$$f = \begin{cases} \dfrac{A}{1+e^{(\frac{x_1-x_{out}}{x-x_{out}}-\frac{x_1-x_{out}}{x_1-x})}} & for \quad x_{out} < x < x_1 \\ A & for \quad x_1 < x < x_2 \\ \dfrac{A}{1+e^{(\frac{x_{out}+L_f-x_2}{x-x_2}-\frac{x_{out}+L_f-x_2}{x_{out}+L_f-x})}} & for \quad x_2 < x < x_{out}+L_f \end{cases} \tag{3.19}$$

where x_1 and x_2 are placed at the abscissae $x_{out} + L_f/3$ and $x_{out} + 2L_f/3$, respectively, and $A = 100$.
In order to identify the perturbation at $t = 0$ which is able to produce the largest disturbance growth at any given T, a Lagrange multiplier technique is used. Let us define the disturbance energy density as:

$$E(t) = \int_{-Z}^{Z}\int_{o}^{L_y}\int_{x_{in}}^{x_{out}} \left(u^2+v^2+w^2\right) dxdydz, \tag{3.20}$$

where the limits of integrations are the boundaries of the computational box, and would be defined in the next sections for the physical domains under consideration. The objective function of the procedure, $\Im$, is the energy of perturbations at time $t = T$, i.e. $E(T)$. The Lagrange multiplier technique consists in seeking extrema of the augmented functional $\mathcal{L}$ with respect to every independent variable. Such a functional is written as:

$$\begin{aligned} \mathcal{L} = \Im &+ \int_{-Z}^{Z}\int_{o}^{L_y}\int_{x_{in}}^{x_{out}}\int_{0}^{T} a\left(u_x+v_y+w_z\right) dtdxdydz \\ &+ \int_{-Z}^{Z}\int_{o}^{L_y}\int_{x_{in}}^{x_{out}}\int_{0}^{T} b\left(u_t+(uU)_x+U_y v+Vu_y+p_x-\frac{u_{xx}+u_{yy}+u_{zz}}{Re}\right) dtdxdydz \\ &+ \int_{-Z}^{Z}\int_{o}^{L_y}\int_{x_{in}}^{x_{out}}\int_{0}^{T} c\left(v_t+Uv_x+(vV)_y+uV_x+p_y-\frac{v_{xx}+v_{yy}+v_{zz}}{Re}\right) dtdxdydz \\ &+ \int_{-Z}^{Z}\int_{o}^{L_y}\int_{x_{in}}^{x_{out}}\int_{0}^{T} d\left(w_t+Uw_x+Vw_y+p_z-\frac{w_{xx}+w_{yy}+w_{zz}}{Re}\right) dtdxdydz \\ &+ \lambda_0\left[E(0)-E_0\right], \end{aligned} \tag{3.21}$$

where the linearized Navier-Stokes equations (3.18) and the value of the energy at $t = 0$, E_0 , have been imposed as constraints, and a, b, c, d and λ_0 are the Lagrange multipliers. Integrating by parts and setting to zero the first variation of $\mathcal{L}$ with respect to u, v, w, p allows us recover the adjoint equations:

$$\left.\begin{aligned} b_t + b_x U + (bV)_y - cV_x + a_x + \frac{b_{xx}}{Re} + \frac{b_{yy}}{Re} + \frac{b_{zz}}{Re} = 0, \\ c_t + (cU)_x + c_y V - bU_y + a_y + \frac{c_{xx}}{Re} + \frac{c_{yy}}{Re} + \frac{c_{zz}}{Re} = 0, \\ d_t + (dU)_x + (dV)_y + a_z + \frac{d_{xx}}{Re} + \frac{d_{yy}}{Re} + \frac{d_{zz}}{Re} = 0, \\ b_x + c_y + d_z = 0, \end{aligned}\right\} \tag{3.22}$$

where $\mathbf{q}^\dagger = (a, b, c, d)^T$ is now identified as the adjoint vector. By using the boundary conditions of the direct problem, one obtains:

$$\begin{array}{l} b = 0\,,\, c = 0\,,\, d = 0\,,\; for \quad y = 0 \quad and \quad y = L_y, \\ b = 0\,,\, c = 0\,,\, d = 0\,,\; for \quad x = x_{in} \quad and \quad x = x_{out}, \end{array} \tag{3.23}$$

and the optimality and compatibility conditions (see Corbett and Bottaro (2000)), respectively:

$$-b + 2\lambda_0 u = 0\,,\; -c + 2\lambda_0 v = 0\,,\; -d + 2\lambda_0 w = 0\,,\; for \quad t = 0, \tag{3.24}$$

$$b + 2u = 0\,,\; c + 2v = 0\,,\; d + 2w = 0\,,\; for \quad t = T. \tag{3.25}$$

The direct and adjoint equations are parabolic in the forward and backward time direction, respectively, so that they can be solved by a coupled iterative approach. The optimization procedure for a chosen objective time T can be summarized as follows:

1. An initial guess is taken for the initial state q_0 at $t = 0$, with an associated initial energy E_0.
2. The direct problem (3.18) is integrated from $t = 0$ to $t = T$.
3. At $t = T$ the initial state for the adjoint problem is provided by the compatibility condition (3.25).
4. The adjoint problem (3.22) is integrated backward in time from $t = T$ to $t = 0$, starting from the initial state of step (c).
5. At $t = 0$ the optimality condition (3.24) determines the new initial state q_0 for the direct problem and the Lagrange multiplier λ_0 is chosen in order to satisfy the constraint $E(0) = E_0$.
6. The objective function, $\Im$, is evaluated, in order to assess if its variation between two consecutive iterations is smaller than a chosen threshold. In such a case the loop is stopped, otherwise the procedure is restarted from step (b).

3.5 Global eigenvalue analysis

Once the base flows have been computed for several values of the Reynolds number, their global stability is studied by means of a perturbative technique, namely, by considering the instantaneous variables as a superposition of the base flow and of the perturbation $\mathbf{q}$. Such a perturbation is decomposed in temporal modes as:

$$\mathbf{q}(x, y, t) = \sum_{k=1}^{N} \kappa_k^0\, \hat{\mathbf{q}}_k(x, y) \exp\left(-i\omega_k t\right), \tag{3.26}$$

where N is the total number of modes, $\hat{\mathbf{q}}_k$ are the eigenvectors, ω_k are the eigenmodes (complex frequencies), and κ_k^0 represents the initial energy of each mode. A substitution

of such a decomposition in equations (3.1,3.2) and a successive linearization lead to the following eigenvalue problem

$$(\mathbf{A} - i\omega_k \mathbf{B})\,\hat{\mathbf{q}}_k = \mathbf{0}, \quad k = 1, \ldots, N_t. \tag{3.27}$$

where the operators $\mathbf{A}$ and $\mathbf{B}$ are defined as follows:

$$\mathbf{B} = \begin{pmatrix} 1 & 0 & 0 & 0 \\ 0 & 1 & 0 & 0 \\ 0 & 0 & 1 & 0 \\ 0 & 0 & 0 & 0 \end{pmatrix}, \tag{3.28}$$

$$\mathbf{A} = \begin{pmatrix} \mathcal{C}_1 - \mathcal{C}_2 + \dfrac{\partial U}{\partial x} & \dfrac{\partial U}{\partial y} & 0 & \dfrac{\partial}{\partial x} \\ \dfrac{\partial V}{\partial x} & \mathcal{C}_1 - \mathcal{C}_2 + \dfrac{\partial V}{\partial y} & 0 & \dfrac{\partial}{\partial y} \\ 0 & 0 & \mathcal{C}_1 - \mathcal{C}_2 & i\beta \\ \dfrac{\partial}{\partial x} & \dfrac{\partial}{\partial y} & i\beta & 0 \end{pmatrix} \tag{3.29}$$

with the term $\mathcal{C}_1 = U\partial/\partial x + V\partial/\partial y$ which represents the effect of the advection of the perturbation by the base flow and $\mathcal{C}_2 = \left(\partial^2/\partial x^2 + \partial^2/\partial y^2 - \beta^2\right)/\mathrm{Re}$ which models the viscous diffusion effects.
With the aim of simplifying the notation, the eigenvalue problem: $\mathbf{C}X = \lambda X$ is considered, where λ is the eigenvalue and X is the eigenvector. The matrix $\mathbf{C}$ has size n. Let us chose a Krylov sub space $\mathcal{K}$ having size k, generated by the vectors $\left(X_0, \mathbf{C}X_0, ..., \mathbf{C}^k X_0\right)$, with X_0 an initial guess vector. A Gram Schmidt orthonormal projection is carried out. On the orthonormal basis $\mathbf{V}_k$, one has:

$$\mathbf{C}\mathbf{V}_k = \mathbf{V}_k\mathbf{H}_k + f_k e_k^t \tag{3.30}$$

where $\mathbf{H}_k$ is the upper Hessenberg matrix, $f_k e_k^t$ the residual, and e_k is the k^{th} column vector of the identity matrix of size n, namely $\mathbf{I}$. The iterative process aims at nullify the residual $f_k e_k^t$. Moreover, the matrix $\mathbf{H}_k$ is able to give a good approximation of the leading eigenvalues.
The numerical algorithm is based on the ARPACK library (Lehoucq et al., 1997), using an "Implicitly Restarded Arnoldi" method, based on a careful choise of the initial guess vector X_0. In order to focus the computation on the frequencies of the dominant eigenvalues, the Arnoldi method is combined to a "shift and inverse" transformation. The eigenvalue problem is transformed as follows. Let us define μ the shift parameter, the problem $\mathbf{C}X = \lambda X$ could be written as:

$$\mathbf{C}X = (\lambda - \mu)\,X + \mu X. \tag{3.31}$$

Thus, the problem to be solved become:

$$\frac{1}{(\mathbf{C} - \mu\mathbf{I})} = \frac{1}{\lambda - \mu} X. \tag{3.32}$$

By means of the Arnoldi method, which is able to compute the dominant eigenvalues, one could obtain the spectrum in proximity of the chosen target.
The problem (3.27) is discretized with a Chebyshev/Chebyshev collocation spectral method employing up to $N = 1500$ modes (for more details on the discretization method, see Alizard (2007)).

3.5.1 Energy optimization via eigenvalue analysis

In order to optimize, by means of the global eigenvalue analysis, the disturbance energy density defined in equation 3.20, for a given initial value of the same, we define the maximum energy gain obtainable at the generic time t over all possible initial conditions $\mathbf{u}_0$ as

$$G(t) = \max_{\mathbf{u}_0 \neq 0} \frac{E(t)}{E(0)}. \tag{3.33}$$

By decomposing the perturbation into the basis of the eigenmodes, it is possible to rewrite equation (3.33) in the following form:

$$G(t) = ||\mathbf{F} \exp(-it\mathbf{\Lambda})\mathbf{F}^{-1}||_2^2, \tag{3.34}$$

where $\mathbf{\Lambda}$ is the diagonal matrix of the eigenvalues ω_k, and $\mathbf{F}$ is the Cholesky factor of the energy matrix $\mathbf{M}$ of components

$$M_{ij} = \int_o^{L_y} \int_{x_{in}}^{x_{out}} (\hat{u}_i^* \hat{u}_j + \hat{v}_i^* \hat{v}_j + \hat{w}_i^* \hat{w}_j)\, dxdy, \quad i,j = 1,\ldots,N, \tag{3.35}$$

where the superscript "*" denotes complex-conjugate. Finally, the maximum amplification at time t and the corresponding optimal initial condition, $\mathbf{u}_0$, are computed by a singular value decomposition of the matrix $\mathbf{F} \exp(-it\mathbf{\Lambda})\mathbf{F}^{-1}$ (Schmid and Henningson (2001)).

3.5.2 Sensitivity and optimal forcing

The global asymptotic response of a perturbation to a harmonic forcing $\mathcal{F}(\mathbf{x}) = \mathbf{f}e^{-i\sigma_f t}$, σ_f being a real frequency, can be formulated as a summation of temporal modes as in equation (7.2) (see Åkervik et al. (2008), Schmid and Henningson (2001)). The forcing term is expanded in a similar way:

$$\mathbf{f}(x,y) = \sum_k f_k \widehat{\mathbf{q}}_{f_k}(x,y), \tag{3.36}$$

The sensitivity of the flow has been thus studied by adding the forcing term $\hat{\mathbf{q}}_f e^{-i\sigma_f t}$ to the linear evolution equation (3.27) (Trefethen and Embree (2005)). The solution of the problem is:

$$\hat{\mathbf{q}} = \hat{\mathbf{q}}_0 e^{\mathbf{\Lambda} t} - \hat{\mathbf{q}}_f e^{-i\sigma_f t}/(i\sigma_f \mathbf{B} - \mathbf{A}), \tag{3.37}$$

where $\hat{\mathbf{q}}_0$ is the initial condition and $\mathbf{\Lambda}$ is the diagonal matrix, $\Lambda_{k,l} = -i\delta_{k,l}\omega_k$. When the flow is globally stable, the solution for long times is governed by the term $-\hat{\mathbf{q}}_f e^{-i\sigma_f t}/(i\sigma_f \mathbf{B} -$

$\mathbf{A}$). Moreover, since the influence of an exterior real harmonic forcing is determined for long times by $\hat{\mathbf{q}}_f$, it is possible to compute the sensitivity to a real exterior frequency through the analysis of the norm $\|(i\sigma_f\mathbf{B}-\mathbf{A})^{-1}\|$ (Trefethen and Embree (2005)). Such an analysis is performed through the evaluation of the pseudospectrum of the global linear operator, defined as

$$\lambda_\varepsilon = \left\{ \sigma \in \mathbf{C},\ \left\|(i\sigma_f\mathbf{B}-\mathbf{A})^{-1}\right\| \geq \varepsilon^{-1} \right\}. \tag{3.38}$$

The pseudospectrum is thus represented plotting the contours of ε on a (ω_r, ω_i) plane. At each point on the real axis ($\omega_i = 0$), the contour value represents the sensitivity of the flow to external forcing with the corresponding pulsation ω_r.
The pseudospectrum is able to give some insights on the sensitivity of the global modes to an harmonic forcing at large times. Moreover, the optimal response at small times to the same forcing could also be investigated. We introduce now the resolvent $R(\sigma_f)$ which characterizes the maximum response of the separated flow to a forcing:

$$R(\sigma_f) = \max_{\mathcal{F}} \frac{\|\mathbf{q}\|_E}{\|\mathcal{F}\|_E} \tag{3.39}$$

where the energy based norm $\|\cdot\|_E$ is derived from the scalar product

$$< \mathbf{q}, \mathbf{q} >_E = \int_0^{L_x}\int_0^{L_y} (u^*u + v^*v)\ \mathrm{d}x\ \mathrm{d}y \tag{3.40}$$

where only the two-dimensional case is considered. Under the assumption that all the temporal modes are damped temporally, in the asymptotic regime the flow's response to $\mathcal{F}$ reduces to:

$$\mathbf{q}(x,y,t) = \sum_k \frac{if_k}{(\sigma_f - \omega_k)}\widehat{\mathbf{q}}_k(x,y)e^{-i\sigma_f t}, \tag{3.41}$$

where the global modes decompositions of the forcing term in equation (3.36) has been used. In order to evaluate (3.39) we introduce the two-dimensional scalar product matrix $\mathbf{M}$ whose coefficients are defined by:

$$M_{i,j} = \int_0^{L_x}\int_0^{L_y} (\widehat{u}_i^*\widehat{u}_j + \widehat{v}_i^*\widehat{v}_j)\ \mathrm{d}x\ \mathrm{d}y \tag{3.42}$$

It is thus more convenient to compute (3.39) as:

$$R(\sigma_f) = \left\|\mathbf{F}\mathbf{D}_f\mathbf{F}^{-1}\right\|_2 \tag{3.43}$$

with $D_{f(l,p)} = \delta_{l,p}\dfrac{i}{(\sigma_f - \omega_l)}$ and $\mathbf{M} = \mathbf{F}^t\mathbf{F}$ the Cholesky decomposition of $\mathbf{M}$.
Finally, (3.43) can be computed for each σ_f by determining the largest singular value sv_1:

$$R(\sigma_f) = \mathrm{sv}_1\left(\mathbf{F}\mathbf{D}_f\mathbf{F}^{-1}\right) \tag{3.44}$$

The expression of the most responsive disturbance is represented in the temporal modes expansion by the vector $\mathbf{K}_{res}$ which is equal to the right singular vector of $\mathbf{F}\mathbf{D}_f\mathbf{F}^{-1}$ associated with the largest singular value sv_1. The components of the forcing term $\mathbf{K}_f = (f_1, f_2, ..., f_N)^t$ leading to such a response can thus be recovered by a simple matrix product $\mathbf{K}_f = \mathbf{F}^{-1}\mathbf{K}_{res}$.

4

Non-normal dynamics of a two-dimensional separated boundary layer

In this chapter, the two-dimensional dynamics of a separated adverse-pressure-induced boundary-layer flow is analyzed, with respect to the effects of non-normality of the associated NS operator. As discussed in section 2, laminar separation bubbles show a high amplification of external disturbances (Marquet et al., 2008, Blackburn et al., 2008), and a strong two-dimensional instability mechanism known as *flapping* (Cherry et al., 1984, Pauley et al., 1990, Ehrenstein and Gallaire, 2008), whose basic features are still not fully understood. In particular, the following issues need to be investigated: (i) the role of the convective Kelvin–Helmholtz instability of the shear layer along the separation streamline with respect to the flapping phenomenon; (ii) the mechanism of transition from convective to global instability; (iii) the influence of topological flow changes on the stability behavior; (iv) the influence of non-linearity on the dynamics of the flow.
This chapter provides a detailed analysis of the previous issues for five recirculation bubbles induced by suction-and-blowing wall-normal velocity profiles of different intensity. The global eigenvalue analysis described in the previous section has been carried out for all of the considered separated flows at low (subcritical or supercritical) Reynolds number. By means of the global mode decomposition, the energy optimization has been performed with the aim of identifying the effects of the non-orthogonality of the eigenvectors of the differential operator on the flow dynamics. Two-dimensional direct numerical simulations are employed as a complementary tool for validating the results obtained by the eigenvalue analysis in the linear case and for studying the nonlinear dynamics of separated flows. By means of the global eigenvalue analysis and DNS, the amplifier dynamics of the considered flows has been analyzed for optimal and random perturbations, at small and large amplitudes; the roles of topological changes, non-linear effects, KH waves and low-frequency oscillations on the destabilization of the flow have been clarified.
This part of the thesis has been published on Physics of Fluids Volume 22, Issue 01, pp. 014102, (2010).

4.1 Problem formulation

A rectangular computational domain with dimensions $L_x = 420$, $L_y = 30$ is employed, the inlet being placed at $x_{in} = 65$ displacement thickness units from the leading edge of the bottom wall. For the base flow computations, as well as the DNS, at inlet points a

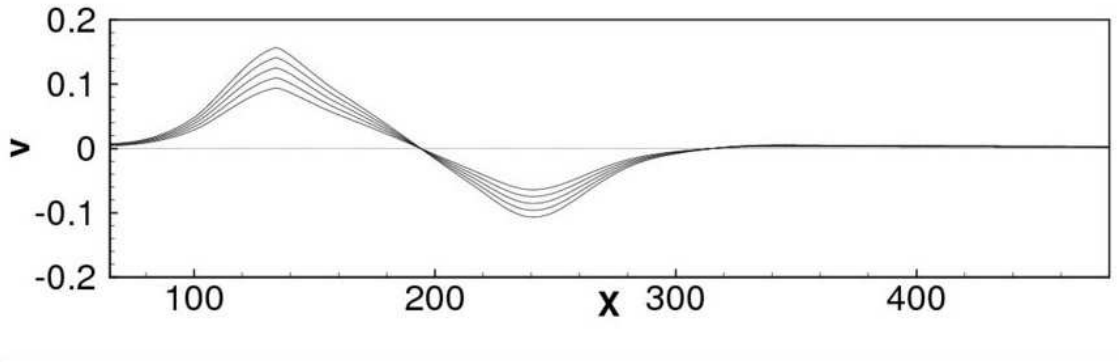

Figure 4.1: Suction-and-blowing profiles imposed at the upper boundary for the v-component of the velocity.

Blasius boundary-layer profile is imposed for both the streamwise, u, and wall-normal, v, components of the velocity vector, whereas, at outlet points, a standard convective condition is employed. At the bottom wall, the no-slip boundary condition is prescribed. Finally, at the upper-boundary points, a suction-and-blowing profile for the v-component of the velocity (Na and Moin, 1998) is imposed, and the vorticity is set to zero. Five profiles with different magnitude have been considered, see Figure 4.1, the one having the largest magnitude being imposed for obtaining the base flow 1 (BF1), the ones with smaller magnitude being associated with base flows BF2, BF3, BF4, BF5, respectively. Such base flows have been obtained for $Re = 200$. All numerical simulations have been performed discretizing the computational domain by a 501×150 Cartesian grid stretched in the wall-normal direction, the height of the first cell close to the wall being equal to 0.1. A numerical grid-convergence study is also provided.
The Newton method discussed in the previous section has been used for the computation of the base flows at supercritical Reynolds numbers and at slightly subcritical ones ($Re \geq 207$). In the subcritical case, the residual has been reduced to 10^{-12} in three up to ten Newton's iterations, whereas, in the supercritical case, the iterations have been stopped when a residual level of 10^{-10} has been achieved, due to a slower convergence of the algorithm.
Concerning the global model, at upper and inlet boundaries, a zero perturbation condition is imposed. A Robin condition based on the approximation of the local dispersion relation is prescribed at the outflow (Ehrenstein and Gallaire, 2005, Alizard and Robinet, 2007), being the flow locally unstable. For the subcritical flow computations the modes are discretized using $N_x = 250$ collocation points in the x-direction and $N_y = 48$ collocation points in the y-direction; a numerical study for the grid-sensitivity of the solution is provided. For supercritical flow simulations, a slightly finer grid with $N_x = 270$ and $N_y = 50$ has been chosen, due to the reduction of the boundary-layer displacement thickness. For energy gain computation, $N = 600$ have been used; a numerical study of the sensitivity of the energy gain curve with respect to the number of modes is also provided.

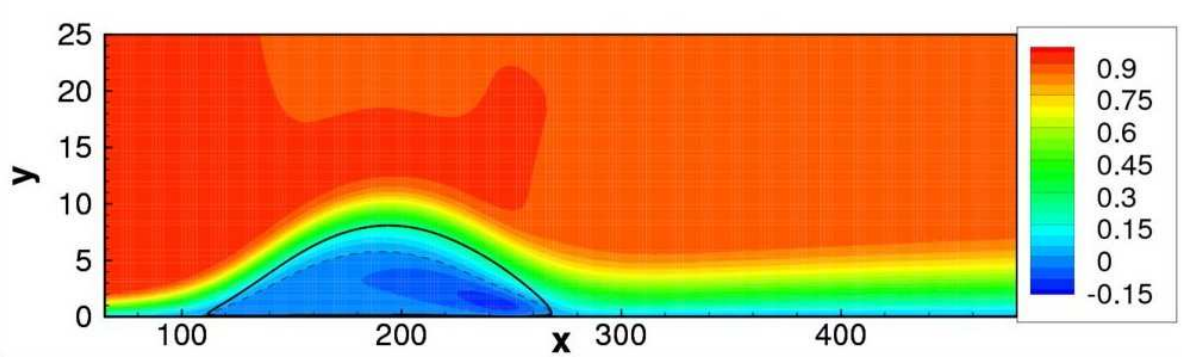

Figure 4.2: Streamwise velocity contours of the base flow BF1 at Reynolds number $Re = 200$. The black line is the separation streamline, whereas the dashed line represents the $u = 0$ contour.

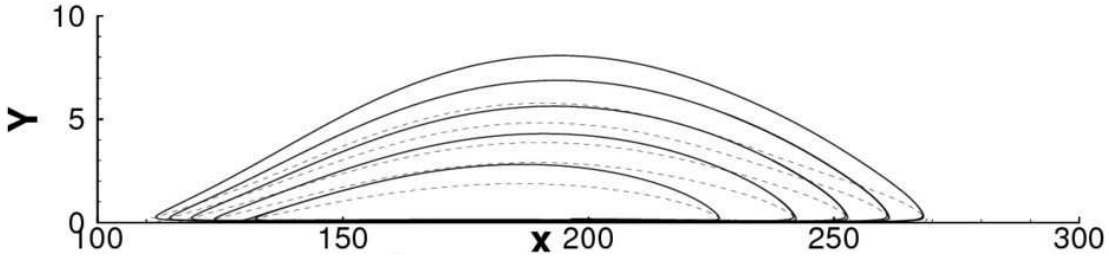

Figure 4.3: Separation streamlines (solid lines) and streamwise zero-velocity contour (dashed lines) of the base flows (from top to bottom) BF1, BF2, BF3, BF4, and BF5 at Reynolds number $Re = 200$.

4.2 Asymptotically stable dynamics: transient growth and convective instabilities

4.2.1 Linear dynamics

Figure 6.1 shows the streamwise velocity contours of the base flow 1 (BF1) at Reynolds number $Re = 200$, which has been obtained by imposing at the upper boundary the suction-and-blowing velocity profile, V_{top} , with maximum magnitude shown in Figure 4.1. Base flows BF2, BF3, BF4, and BF5 have been obtained by scaling such a profile by factors $0.9, 0.8, 0.7, 0.6$, respectively. A blow-up of the separated zone is provided in Figure 4.3 for all of the base flows, showing the decrease of the bubble size for decreasing values of the v velocity imposed at the upper boundary.
For such base flows the global eigenvalue analysis has been performed. Figure 4.4 shows the spectra for BF1, BF3, and BF5. All the spectra are found to be stable, although it can be noticed that for an increasing bubble size the eigenmodes rise up towards the $\omega_i = 0$ axis. By inspecting the spectra, three families of temporal modes, referenced as F1, F2 and F3 and described briefly hereafter, could be recovered.
The asymptotic behavior of the flows is driven by the family of the most unstable modes, F1, represented by diamonds in Figure 4.5 for the base flow BF1. The eigenvalues of the two most unstable modes, labelled ω_1 and ω_2, located on the upper branch of the spectrum, are shown in Figures 4.6 (a) and (b). They are reminiscent of classical KH waves along the shear layer, and relax to TS waves predicted by a local approach (Schmid and Henningson, 2001) on the attached boundary layer. This is in agreement with previous results obtained by a global analysis for an attached laminar boundary-layer flow (Ehrenstein and Gallaire, 2005, Alizard and Robinet, 2007, Åkervik et al., 2008), and for a cavity-induced separated boundary-layer flow (Åkervik et al., 2007).
A second family referenced as F2 and represented by squares in Figure 4.5 is characterized by modes having a spatial distribution reaching the outflow boundary as depicted in Figures 4.6 (c) and (d) which show the modes labelled ω_{49} and ω_{55} in Figure 4.5 (the modes are ordered by their amplification rate, so that for instance ω_{49} is the 49^{th} less stable mode).
Finally, the highly damped modes represented by circles in Figure 4.5 are classified into F3. These modes are reminiscent of the so-called continuous branch obtained by a local analysis (Schmid and Henningson, 2001). Indeed, a part of the energy of the corresponding eigenvectors is concentrated at high values of y. Furthermore, one may observe that KH waves are present on the shear layer as shown in Figures 4.6 (e) and (f), providing the modes ω_{202} and ω_{204}, respectively.
Looking at Figure 4.6, one can notice the strong similarity in terms of spatial structure of the eigenmodes of the same family, characterized by comparable frequencies. Such a property reveals the strong non-orthogonality of the eigenvectors associated with the considered flow, which seems to be a typical feature of open flows and in particular of separated flows (Åkervik et al., 2007, Ehrenstein and Gallaire, 2008). In the following we would investigate how the non-normality of the temporal modes could affect the linear transient dynamics of the flow as well as its asymptotic instability, when it is subject to a harmonic forcing.

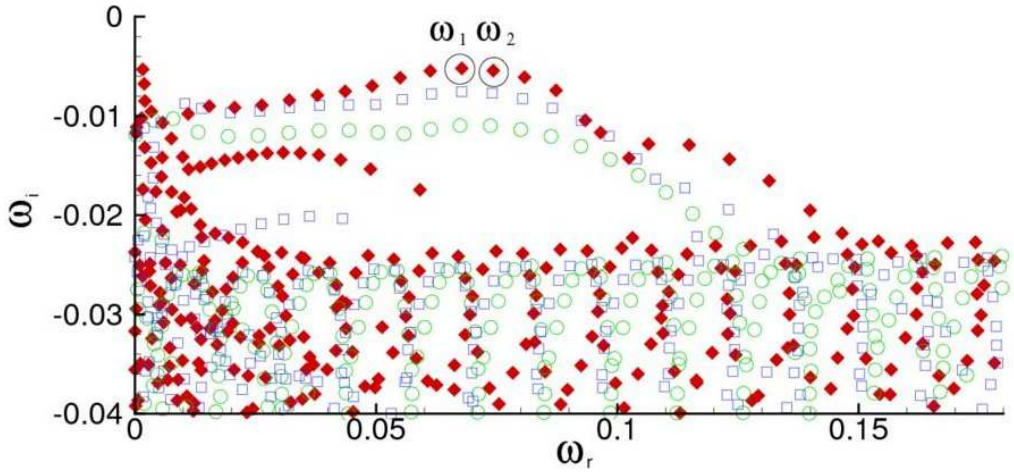

Figure 4.4: Eigenvalue spectrum for the flows BF1 (diamonds), BF3 (squares), and BF5 (circles) at $Re = 200$. The modes labelled ω_1 and ω_2 are the most unstable ones.

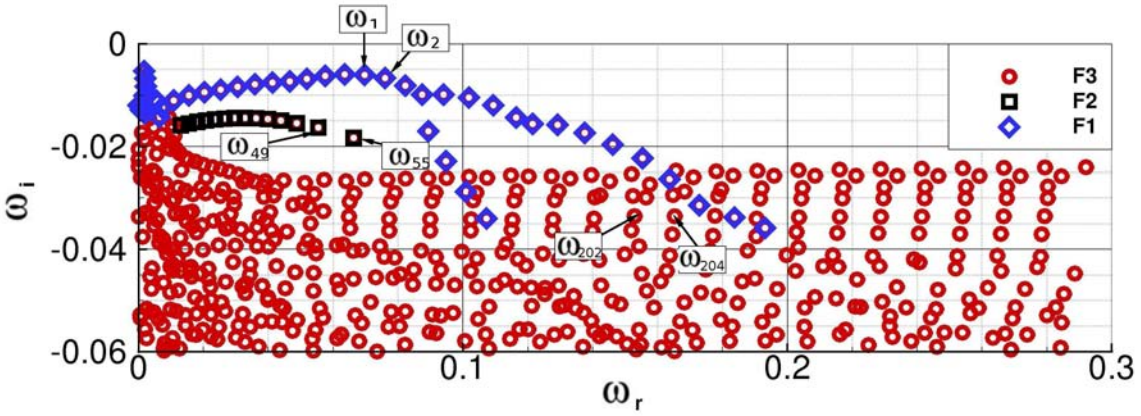

Figure 4.5: Eigenvalue spectrum for the flow BF1 at $Re = 200$. The three families of modes are identified by diamonds (F1), squares (F2) and circles (F3).

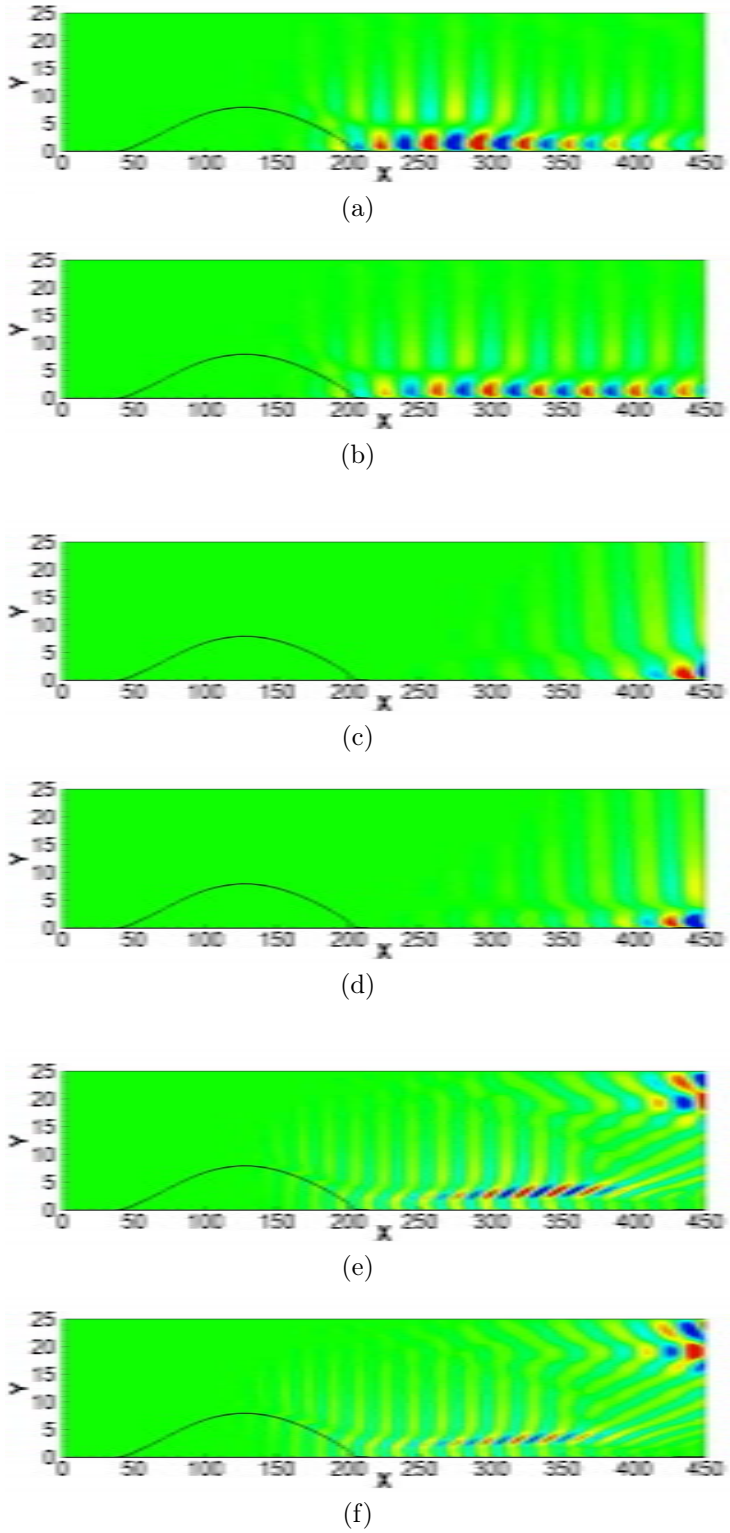

(a)

(b)

(c)

(d)

(e)

(f)

Figure 4.6: Streamwise velocity components of the real part of the eigenvectors corresponding to the eigenvalues labelled ω_1 (a) ω_2 (b), ω_{49}, (c) ω_{55} (d), ω_{202} (e), ω_{204} (f) in Figure 4.4. The black line is the separation streamline.

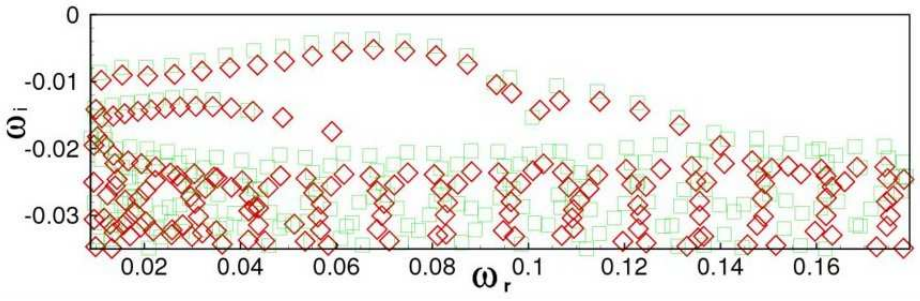

Figure 4.7: Global spectrum obtained for BF1 at $Re = 200$ with a (200×40) grid (squares), and a (250 × 48) grid (diamonds).

In order to validate the global model results, the spectrum has been computed also with a coarser grid. Figure 4.7 shows the spectra obtained for the separated flow BF1 at $Re = 200$ using two grids with 200×40 and 250×48 collocation points, respectively (computations with a considerably finer grid are not possible due to memory requirements). The shape of the spectra computed with the two grids does not show remarkable differences, although the modes are found to slightly change their position. Nevertheless, it is well known that a pointwise convergence of the global spectra with respect to grid resolution for highly non parallel flows cannot be reached due to the high non-normality of the operator (Trefethen and Embree, 2005), see, for instance, the sensitivity study provided by Ehrenstein and Gallaire (2008).

Although all of the modes have been found asymptotically stable, they are likely to interact leading to a transient amplification of the perturbations, due to the non-orthogonality of the corresponding eigenvectors. Figure 4.8 provides the maximum energy gain, $G(t)$, obtained for BF1, BF2, BF3, BF4, and BF5 by choosing $N = 600$ modes for the global eigenvalue analysis. The sensitivity of the optimal energy gain, $G(t)$, with respect to the number of modes chosen for its evaluation (see equation (3.35)) has been investigated for BF1. Figure 4.9 shows the optimal energy gain curves obtained by choosing $N = 300$ (dashed-dotted line), $N = 500$ (dashed line), and $N = 600$ modes for the global eigenvalue analysis. The solution shows a clear tendency towards convergence.
The energy gain curves for the five base flows here considered show a similar shape (see Figure 4.8), although the maximum value of the energy gain, G_{max}, as well as the time at which such a value is achieved, t_{max}, increase with the bubble size. Figure 4.10 provides the variation of G_{max} with respect to three features of the base flows, namely: the maximum value of the suction velocity at the upper boundary, v_{max}; the maximum value of the shape factor $H = \delta^*/\Theta$ (where Θ is the momentum thickness of the boundary layer); and the aspect ratio of the bubble, which is defined as the ratio between the maximum height of the separated region, h, (measured at the zero-streamwise-velocity line) and the length of the bubble. Figure 4.10 shows an approximatively linear increase of the G_{max} with respect to all of the three parameters. It is noteworthy that the aspect ratio of the smallest bubble is close to the ones experimentally measured for laminar separation bubbles on the suction surface of aerofoils at a large angle of attack (Watmuff, 1999, Haggmark et al., 2000); whereas, the largest bubble has a shape factor which is comparable to the

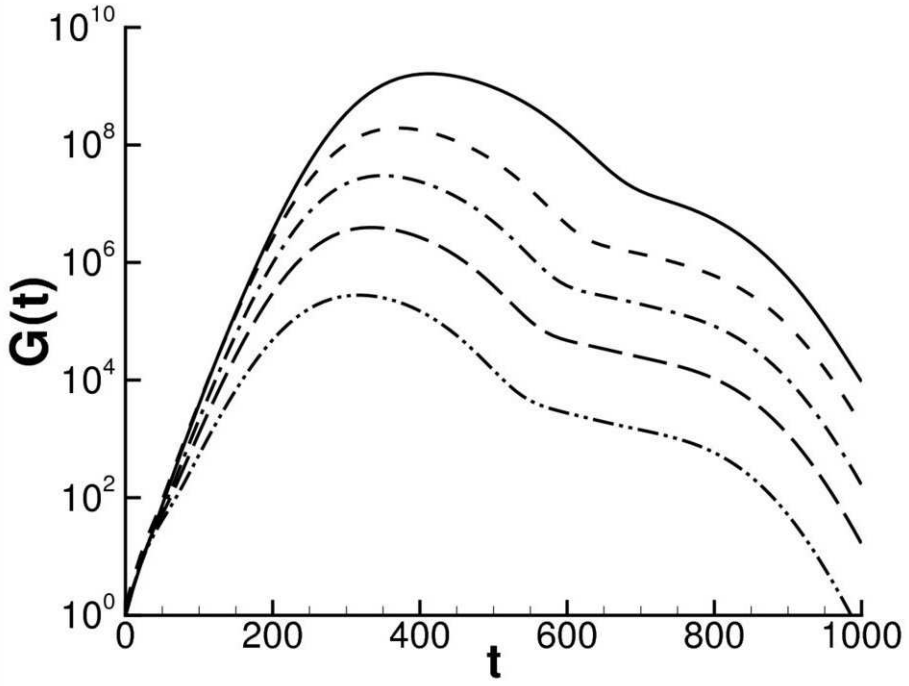

Figure 4.8: Optimal energy gain curves at $Re = 200$ computed by the global eigenvalue analysis for the base flows BF1 (solid line), BF2 (dashed line), BF3 (dashed-dotted line), BF4 (long-dashed line), and BF5 (dashed-dotted-dotted line).

one analyzed in Rist and Maucher (1994) and Marxen et al. (2003).
The dashed line in Figure 4.11 shows the linear transient time evolution of the energy gain, $E(t)/E(0)$, obtained by global eigenvalue analysis using the initial perturbation, ${\mathbf{u}_0}^{max}$, which provides the maximum peak value at $Re = 200$ for BF1. Such a curve is almost coincident with the $G(t)$ one, shown by the solid line in Figure 4.11 for the same number of modes, $N = 600$. Both curves reach a maximum value of order of magnitude 10^9 at $t = 410$, meaning that the linearized operator related to the considered flow has a high degree of non normality.

In order to get some insight into the amplification mechanism, the evolution of such an optimal perturbation in time is analyzed. Figure 4.12(a) shows that at time $t = 0$ the energy of the optimal perturbation is concentrated in the upstream part of the bubble. At $t = 200$ (Figure 4.12(b)), the disturbance has been convected downstream by the base flow along the separation streamline through a Kelvin-Helmholtz mechanism, and it has been amplified before reaching the reattachment point. Such an amplification is due to the local convective instability of the velocity profiles within the bubble, which leads to a global growth of the perturbations, as theoretically demonstrated in Cossu and Chomaz (1997) using the Ginzburg-Landau equation for non-parallel flows. After the reattachment point (Figure 4.12(c)), the perturbation is convected through the attached boundary layer, where it is damped. The same convective mechanism has been recovered for base flows BF2, BF3, BF4, and BF5, explaining the linear increase of G_{max} and of the

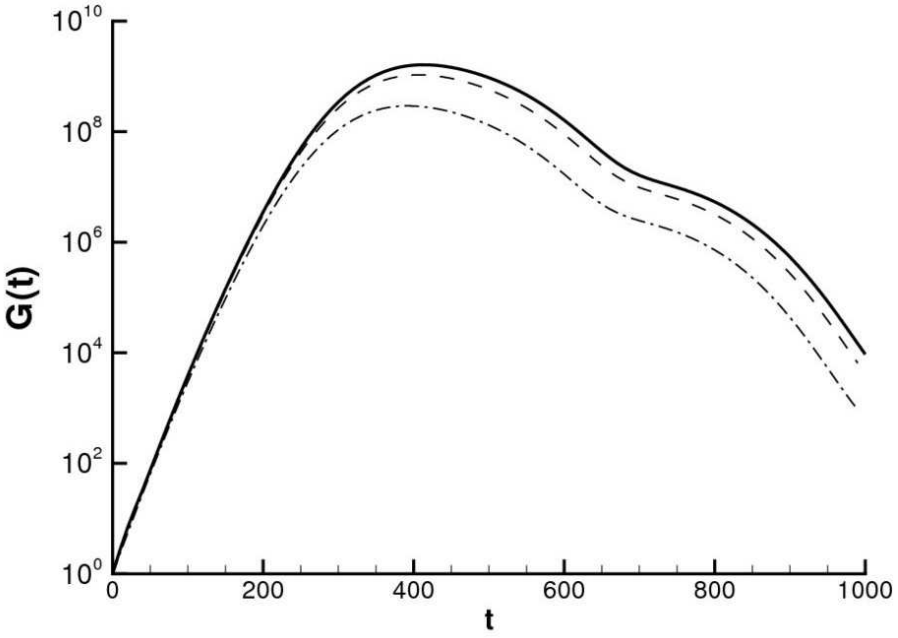

Figure 4.9: Optimal energy gain curve for BF1 at $Re = 200$ computed with $N = 600$ modes (solid line, reference case), $N = 500$ modes (dashed line), and $N = 300$ modes (dashed-dotted line).

time at which it is reached for an increase of the bubble size.
It is worth to notice that the energy gain values recovered by the global eigenvalue analysis are quite high. Nevertheless, one has to consider that these are optimal values, therefore the amplification for a real perturbation could be much lower. It is anticipated that, for small bubbles, the amplification of the disturbances could be too low to induce non-linear effects. For this reason, an investigation will be performed of the amplification of a random white-noise disturbance, forced at the inlet or in the whole domain.
Due to the similarities recovered in the transient behaviour of the different base flows, the following analysis will be carried out only for the separated flow BF1.

4.2.2 Weakly non-linear dynamics

In order to validate the results of the linear stability analysis and to study the weakly non-linear behavior of the considered separated flow, the DNS has been performed initializing the simulation by superposing the optimal perturbation upon the base flow. In order to satisfy the hypothesis of small perturbations, thus allowing a comparison with the results of the global eigenvalue analysis, the optimal disturbance, ${\mathbf{u}_0}^{max}$, has been scaled by a factor $A_0 = 10^{-8}$, which is 4 orders of magnitude greater than the residual noise. The energy of the disturbance, defined in equation (3.20), normalized by the value at $t = 0$, has been computed at each time step and is reported in Figure 4.13 using the dashed line. In order to verify that a perturbation of order of magnitude $A_0 = 10^{-8}$ is small enough

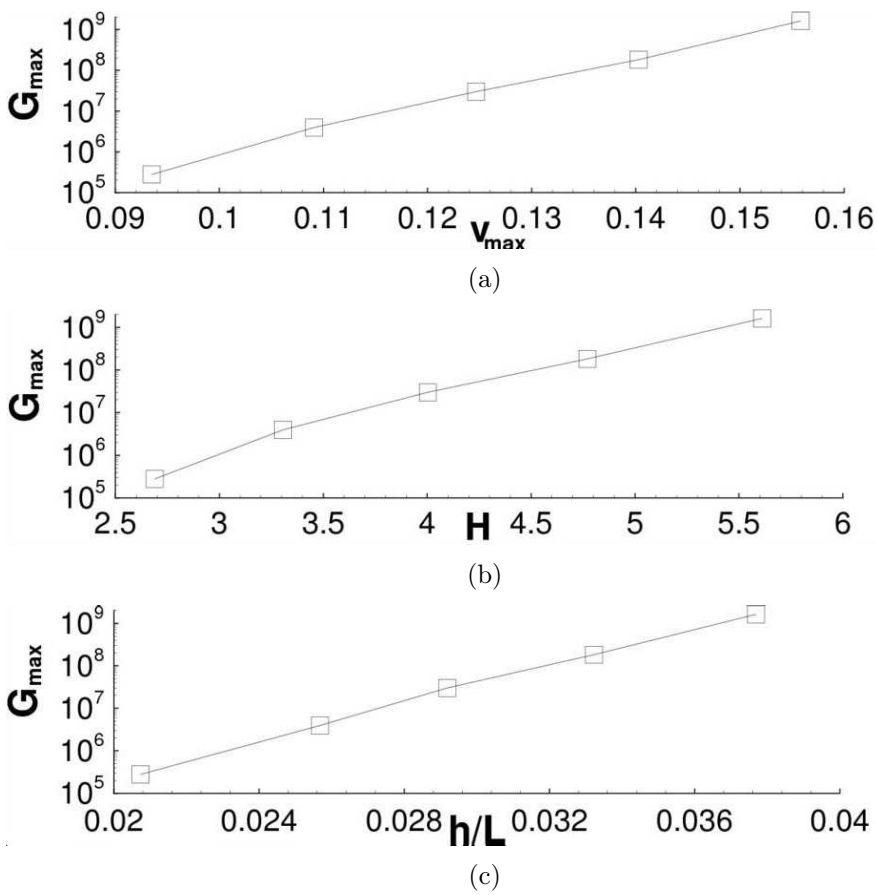

Figure 4.10: Maximum value of the optimal energy gain computed by the global eigenvalue analysis at $Re = 200$ versus the maximum suction velocity at the upper boundary (a), the shape factor (b) and the aspect ratio (c) for the base flows BF1, BF2, BF3, BF4, and BF5 (from right to left).

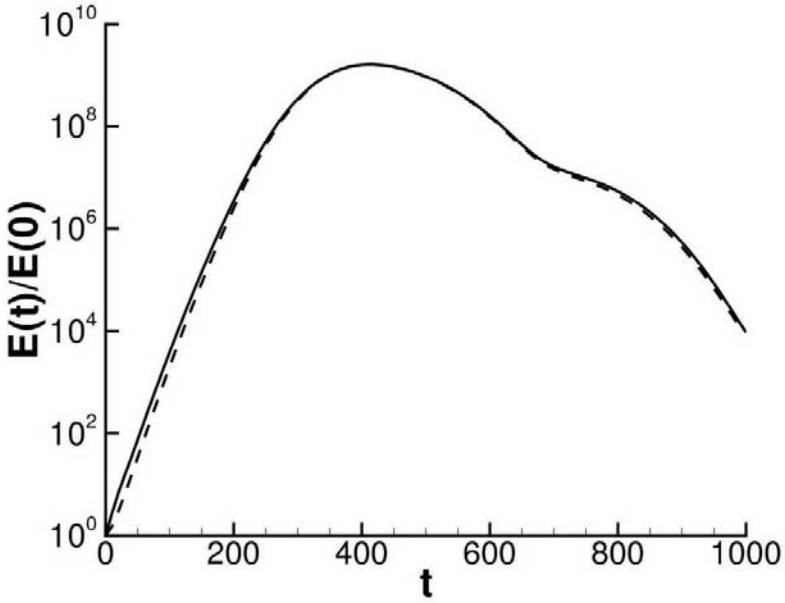

Figure 4.11: Optimal energy gain curve (solid line) and evolution of the normalized energy corresponding to the initial perturbation giving the optimal energy peak (dashed line) at $Re = 200$, both computed by the global eigenvalue analysis for BF1.

to allow a meaningful comparison with the linear model, a linearized DNS has been performed as well, whose result, shown by the dotted line in Figure 4.13, has been found identical to the one obtained by the DNS. Indeed, by injecting an initial perturbation with order of magnitude 10^{-8}, which corresponds to an initial energy of order of magnitude 10^{-16}, such a perturbation amplifies itself up to a factor 10^9, reaching an energy level about equal to 10^{-7}, which is low enough for non-linear effects to be negligible. Moreover, Figure 4.13 shows that the optimal perturbation energy growth curve obtained with the global eigenvalue analysis, provided by the solid line, is very close to the one computed by the DNS (dashed line), validating the capability of the global model to predict the linear transient mechanism.

A grid convergence study for the DNS has been performed by computing the energy growth of the optimal perturbation for the separated flow at $Re = 200$ using three grids with 251×75, 501×150, and 1001×300 cells, respectively. As shown in Figure 4.14, the results obtained using the second and the third grids are very close each other, so that the 501×150 grid, which has been used in all of the computations, can be considered adequate to capture the energy growth of the disturbances accurately.

Although the DNS has confirmed the convective amplifier character of the considered separated flow for an optimal initial perturbation, there is no evidence that such a flow would behave similarly in a real case. For this reason, simulations have been performed in which the base flow is perturbed using a time-varying pseudo-random zero-mean Gaussian white-noise disturbance. The flow has been perturbed in two different ways. In the first case (A), a disturbance field is impulsively injected in the whole domain. In the second case (B), the perturbation is superposed upon the inlet velocity profile, as it may happen in real experiments, where the inlet flow may be affected by some noise. In both cases a

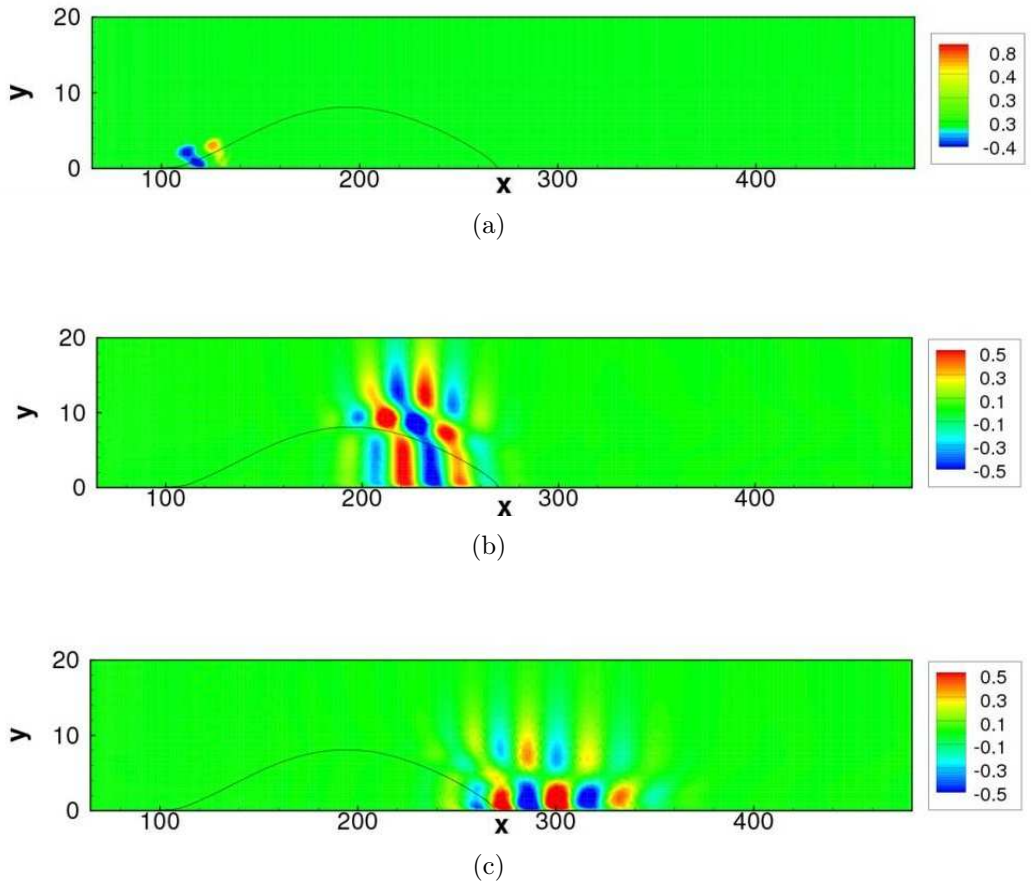

Figure 4.12: Streamwise velocity contours of the optimal perturbation obtained by the global eigenvalue analysis for BF1 at time $t = 0$ (a), $t = 200$ (b) and $t = 400$ (c). The streamwise perturbation has been normalized by its maximum value.

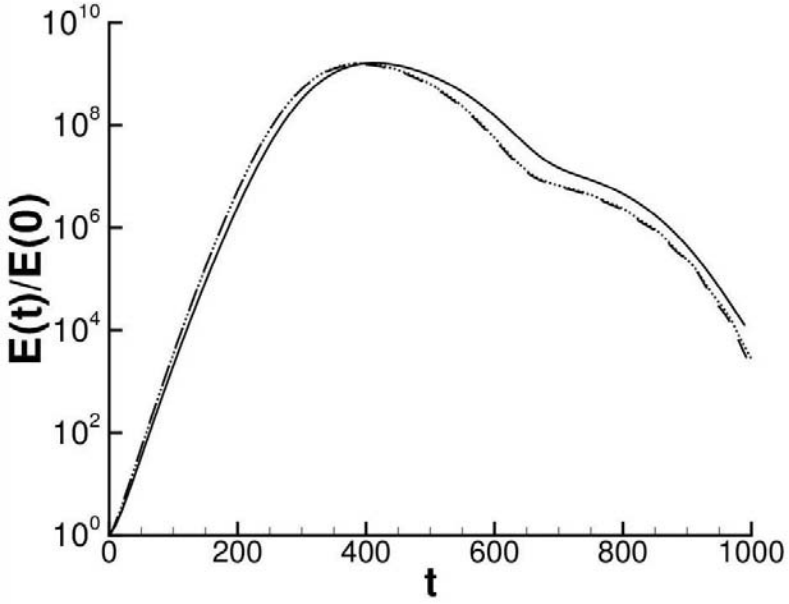

Figure 4.13: Time evolution of the energy gain of the optimal initial perturbation obtained by the global eigenvalue analysis (solid line), by the DNS (dashed line), and by the linearized DNS (dotted line).

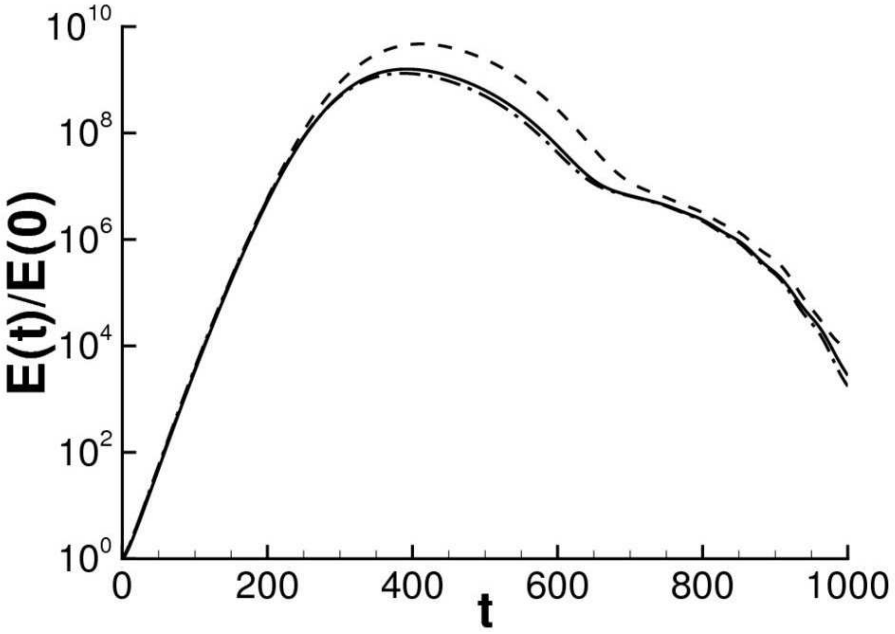

Figure 4.14: Energy gain curves obtained by DNS by a (251×75) grid (dashed line), a (501×150) grid (solid line) and a (1001×300) grid (dashed-dotted line).

strong energy gain has been observed, which is approximatively two order of magnitude lower than the optimal one. As shown in Figure 4.15, the shape of the amplification curves is not far from the optimal one, although some differences can be noticed. In particular, the algebraic growth phase is delayed with respect to the optimal case. This is due to the fact that the perturbation is damped until it is convected by the base flow along the separation streamline, where it begins to be amplified. Due to such an initial delay, the time instant at which the amplification peak occurs ($t_{max_A} = 460$, for case A, and at $t_{max_B} = 490$, for case B) is greater with respect to the optimal case. It is noteworthy that, for case B in which the inflow perturbation is continuously injected into the flow, the normalized energy does not decay for $t < 150$ and $t > 1100$, but assumes a value slightly greater than one. Indeed, for $t > 1100$, after the first wave packet has been advected through the separated zone, a statistically steady state is established, so that the continuously injected perturbations do not experience more transient amplification. Nevertheless, some highly sensitive frequencies are excited by the random forcing at the inlet (Kaiktsis et al., 1996), and are slightly amplified also after the transient has passed, so that the energy gain maintains asymptotically a value close to one. Therefore, it is possible to conclude that, even though the base flow is continuously perturbed, its response to a small amplitude perturbation is comparable to the response to an impulsive perturbation, which could mean that the strong transient amplification of the perturbations is a robust feature of separated flows. Such results are in agreement with previous ones obtained for a flow over a backward-facing step perturbed by an inflow random disturbance (Kaiktsis et al., 1996, Blackburn et al., 2008).
Finally, in order to understand the role of the separated region on such a dynamics, several DNS have been performed in which the perturbation is respectively placed upstream ($70 < x < 100$), downstream ($280 < x < 340$) and within the bubble, in its first half ($120 < x < 180$) or in its second half ($200 < x < 260$). Figure 4.16 shows that a perturbation placed upstream or within the bubble is amplified, whereas a disturbance initially located downstream of the bubble is damped. In particular, the dynamics of a perturbation placed in the first half of the bubble is comparable to the dynamics of case A, whereas a perturbation placed in the second half of the bubble is only weakly amplified, confirming that the amplification mechanism is based on the convection of perturbations along the separation streamline.

4.2.3 Non-linear dynamics

In order to study the role of non-linear effects in the dynamics of a separated flow, non-linear simulations have been performed increasing the amplitude of the initial perturbation, $\mathbf{u}_0{}^{max}$. Figure 4.17 provides the energy gain curves obtained scaling the optimal perturbation by a factor A_0 equal to 10^{-8}, 10^{-6}, 10^{-5}, and 10^{-4}, respectively. All of the curves initially follow the algebraic growth phase, but, for amplitudes greater than 10^{-6} they show a reduced peak value with respect to the linear case. For $A_0 = 10^{-4}$, a saturation plateau starts immediately after the initial algebraic growth phase around a value about equal to 10^7. For all cases, the perturbations eventually decay. It is worth to notice that, for $A_0 \geq 10^{-6}$, the decaying rate is lower than the linear one, due to the capability of the non-linear terms to transfer the energy back in the upstream part of the bubble. It is possible to visualize such a mechanism by inspecting, at a fixed wall normal position,

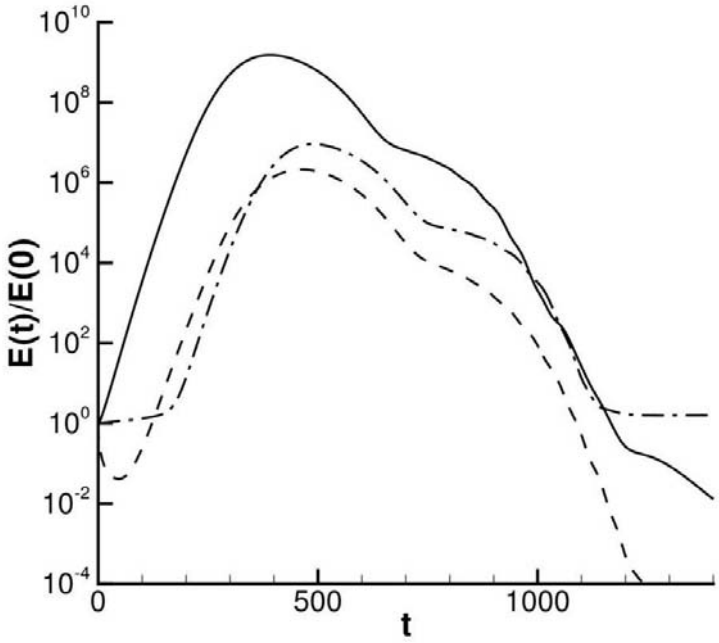

Figure 4.15: Time evolution of the energy gain computed by the DNS for an optimal initial perturbation (solid line); for a disturbance field injected in the whole domain (case A, dashed line); and for a time-varying disturbance superposed upon the inlet velocity profile (case B, dashed-dotted line).

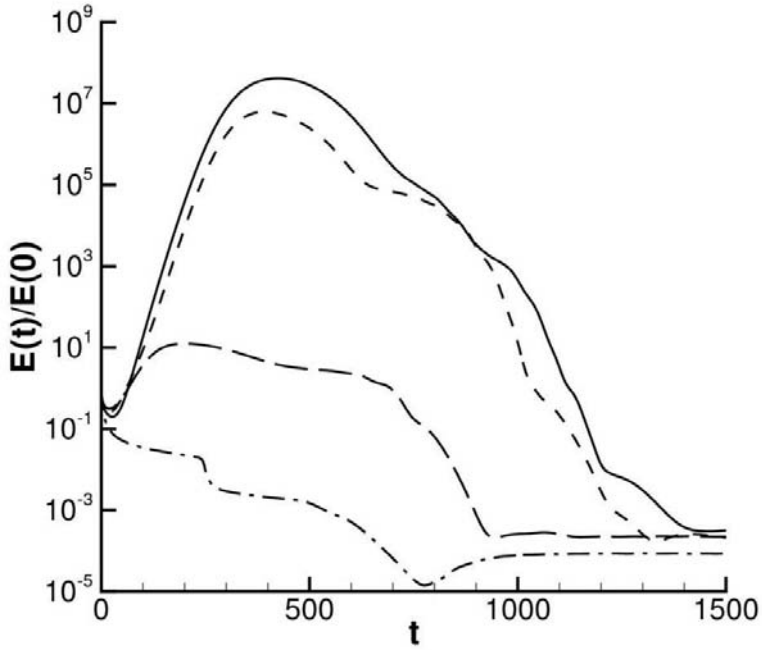

Figure 4.16: Time evolution of the energy gain computed by the DNS for an initial perturbation placed upstream (solid line), downstream (dashed-dotted line) or within the bubble in its first half (short-dashed line) or in its second half (long-dashed line).

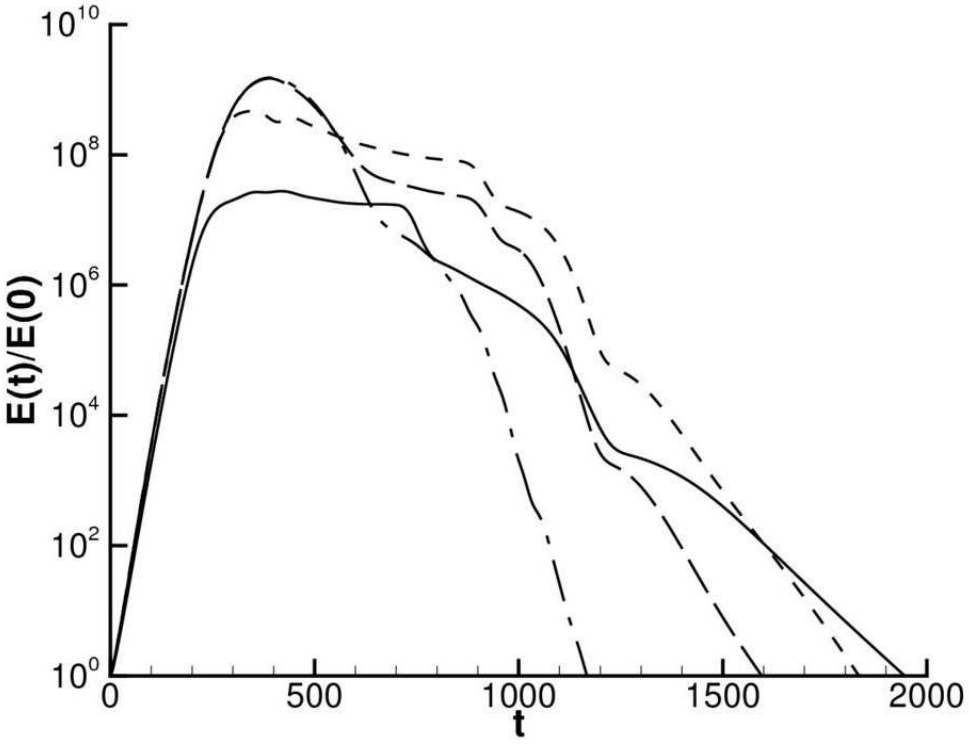

Figure 4.17: Time evolution of the energy gain computed by the DNS for an optimal initial perturbation with order of magnitude $A_0 = 10^{-4}$ (solid line), $A_0 = 10^{-5}$ (short-dashed line), $A_0 = 10^{-6}$ (long-dashed line), and $A_0 = 10^{-8}$ (dashed-dotted line).

the evolution in time of the perturbation that propagates along the streamwise direction. Indeed, comparing the evolution of the linear and non-linear wave packets shown in Figure 4.18, one can see that, in the second case (Figure 4.18 (b)), part of the perturbation is driven back in the separated region, where it interacts with the main part of the wave packet (WpI) which is being convected downstream. As a result, a second wave packet (WpII) appears in the bubble, which is convected in the attached-flow region. Looking at Figure 4.19, which shows the evolution in time of the vorticity perturbation, ω_z, at wall at a fixed streamwise position ($x = 400$), it is possible to notice that the amplitude of the two wave packets convected downstream is comparable, meaning that a wave packet cycle starts to be established within the bubble, but it is eventually damped.

In order to study the development of the wave packet downstream of the bubble, a longer computational domain has been considered, $L_{x_1} = 5\,L_x$. As shown in Figure 4.20, for $A_0 = 10^{-4}$ and $1000 < t < 4000$, the perturbation is amplified, whereas, for $A_0 = 10^{-8}$ and t>1000, it is damped, when the same domain length is used. Looking at the evolution of the wave packet in time, provided in Figure 4.21, it is possible to notice that the perturbation is amplified while it is convected through the attached-flow region, causing a further transient global growth of the energy until it leaves the domain. Such a result indicates that the flow downstream of the bubble is *convectively non-linearly unstable*

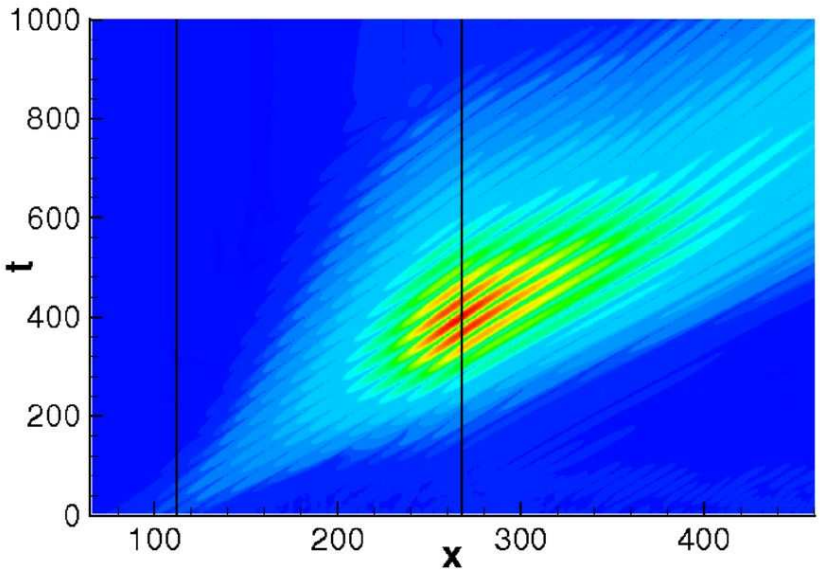

(a)

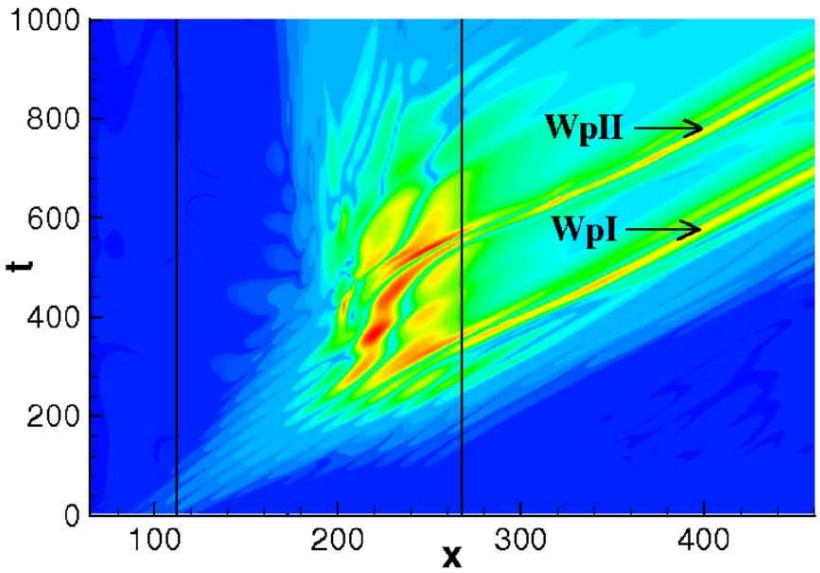

(b)

Figure 4.18: Evolution in time and in the streamwise direction of the vorticity perturbation at wall, ω_z, computed by DNS for an optimal initial perturbation normalized by a factor $A_0 = 10^{-8}$ (a) and $A_0 = 10^{-4}$ (b). The black lines indicate the separation and reattachment points of the base flow, whereas, the arrows point at the two wave packets shed by the bubble (WpI and WpII).

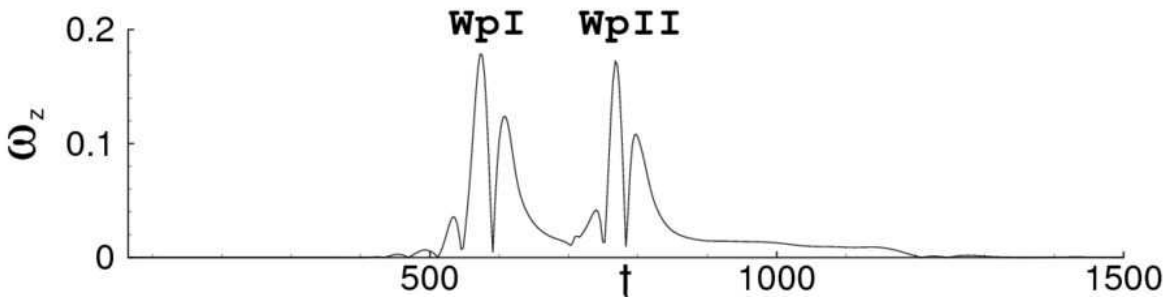

Figure 4.19: Evolution in time of the vorticity perturbation at wall computed by DNS for an optimal initial perturbation with order of magnitude $A_0 = 10^{-4}$ at the streamwise location $x = 400$.

though linearly globally stable. In order to understand the mechanism inducing such an amplification, the Fourier transform in time of the streamwise-velocity fluctuation at two different abscissae, $x = 380$ and $x = 455$, has been computed. Figure 4.22 shows that, immediately downstream of the bubble, the leading mode corresponds to the less stable eigenvalue of the global spectrum, labelled ω_1 in Figure 4.4, whose real part is $\omega_r \approx 0.08$. Thus, at such a location the behavior of the flow is driven by the global dynamics. However, for increasing abscissae, the dynamics is driven by a different mode whose real part is close to $\omega_r \approx 0.045$. A local spatial stability analysis, which solves the Orr-Sommerfeld and Squire eigenvalue problem with respect to a streamwise wavenumber α, has been performed on the velocity base flow profiles at the above streamwise locations. Such an analysis indicates that such a mode lies in the range of the local spatially unstable frequencies for $x = 455$, as shown in Figure 4.23. The same analysis has been performed at several streamwise locations downstream of the bubble confirming such a result. Thus, one can infer that the wave packet is spatially amplified while it is convected downstream as a consequence of the excitation of a locally unstable mode. In order to find the "critical perturbation" triggering such a mode, several simulations have been performed with increasing initial perturbation amplitudes. The streamwise velocity perturbations have been extracted as they have passed beyond the location $x = 455$, at two time instants, $t = 900$ and $t = 1000$. As shown in Figure 4.24, a spatial amplification begins to be noticed for amplitudes equal to 10^{-6}. Such a strong influence of the perturbation amplitude on the behaviour of the flow could be due to a high sensitivity to real forcing. Indeed, although the flow is not directly forced with a specific mode, different frequencies are present in the perturbed flow due to the initial impulsive forcing, which could eventually be damped or not depending on the sensitivity of the flow.

The sensitivity of the flow has been studied by following the method described in Section 3.5.2. The forcing term $\hat{\mathbf{q}}_f e^{-i\sigma_f t}$, has been added to the linear evolution equation (3.27), σ_f being a real frequency. This leads to recover a pseudospectrum, defined as in equation (3.38), provided for BF1 in Figure 4.25, represented plotting the contours of $-log_{10}(\varepsilon)$. At each point on the real axis ($\omega_i = 0$), the contour value represents the sensitivity of the flow to external forcing with the corresponding pulsation ω_r. The response to a real frequency is dominated by the global KH/TS-like modes, the most sensitive one corresponding to the most unstable one. Concerning the locally unstable mode with

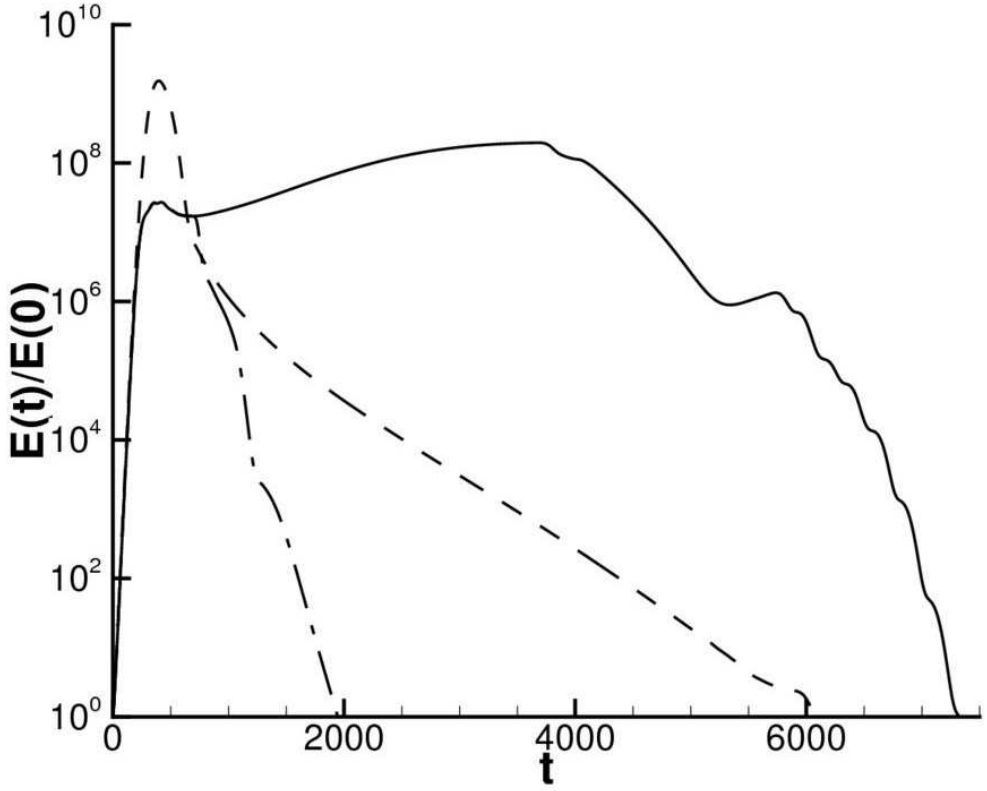

Figure 4.20: Time evolution of the energy gain computed by the DNS for an initial optimal perturbation with order of magnitude $A_0 = 10^{-4}$ with domain length $L = L_x$ (dashed-dotted line) and $L = 5\,L_x$ (solid line); and for an initial optimal perturbation with order of magnitude $A_0 = 10^{-8}$, and domain length $L_{x_1} = 5\,L_x$ (dashed line)

.

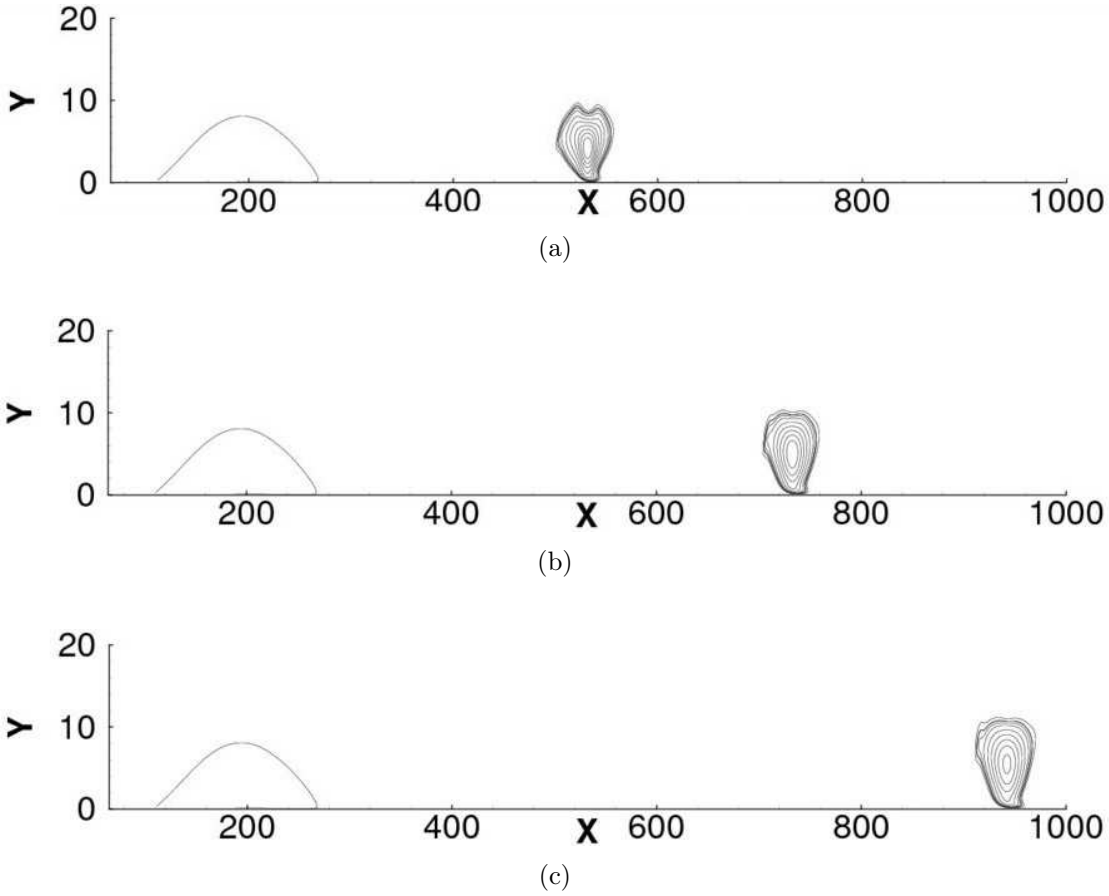

Figure 4.21: Contours of the streamwise velocity perturbation, u, computed by the DNS at three time instants, $t = 2200$, $t = 2600$ and $t = 3000$. The line on the left indicates the separation streamline.

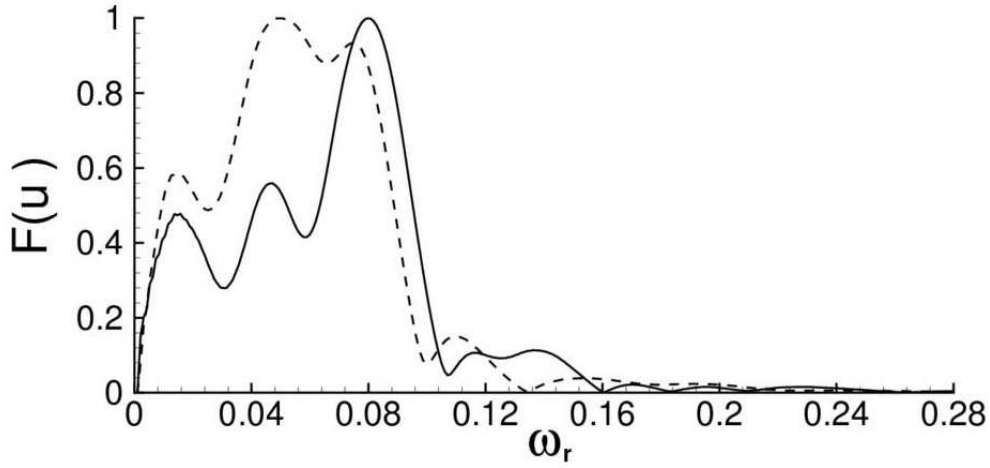

Figure 4.22: Fourier spectrum in time of the streamwise velocity perturbation at the first grid point in the wall normal direction computed by the DNS for two streamwise locations, $x = 380$ (solid line) and $x = 455$ (dashed line).

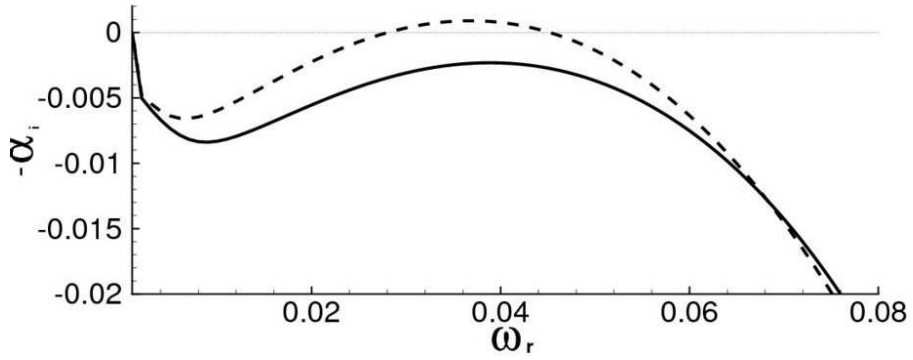

Figure 4.23: Spatial amplification rate, $-\alpha_i$, versus the real pulsation, ω_r, computed by local instability analysis at two streamwise locations, $x = 380$ (solid line) and $x = 455$ (dashed line).

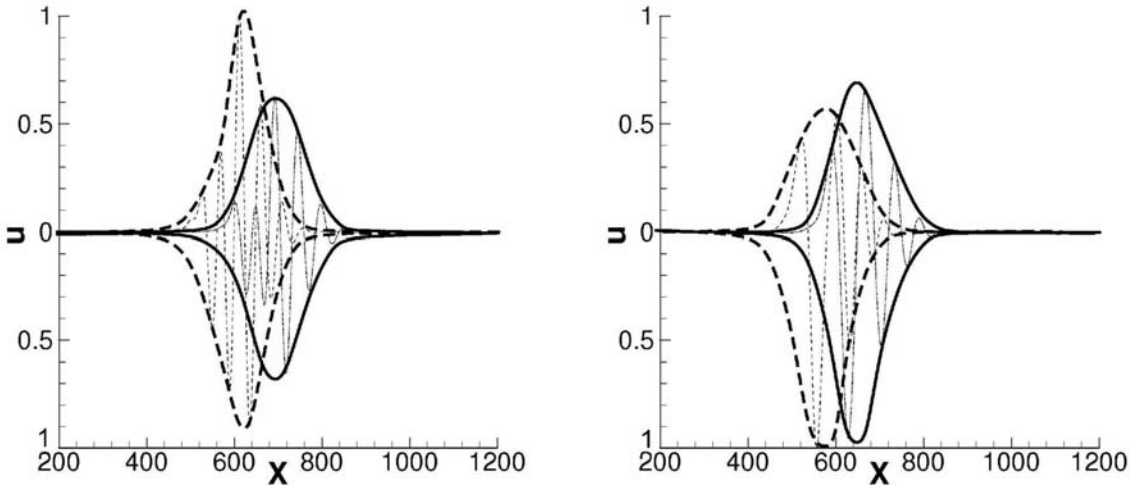

(a) (b)

Figure 4.24: Evolution in the streamwise direction of the streamwise perturbation velocity, u, computed by the DNS at a fixed wall normal position, $y = 1.49$, for two time values, $t = 900$ (dashed line) and $t = 1000$ (solid line), for initial perturbations scaled by a factor $A_0 = 10^{-7}$ (a) and $A_0 = 10^{-6}$ (b), respectively.

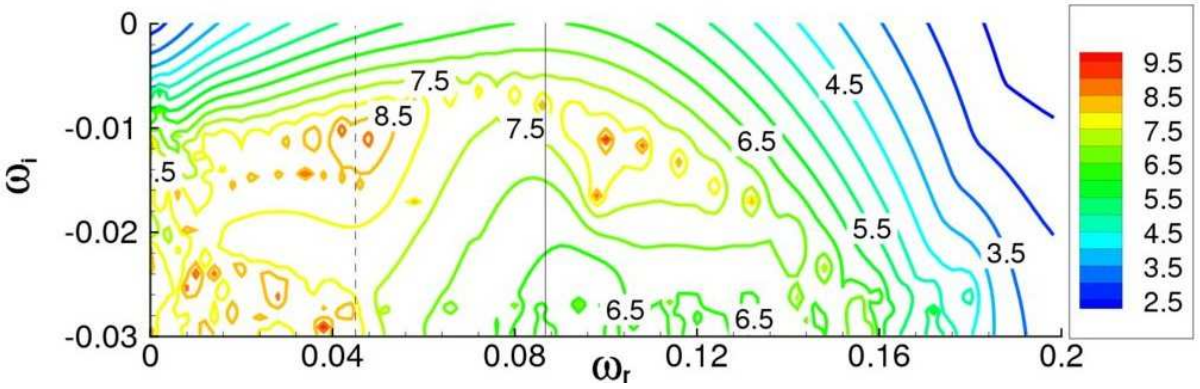

Figure 4.25: Pseudospectrum contours for BF1, represented using a logarithmic scale, $-log_{10}(\varepsilon)$. The vertical solid line indicates the most sensitive pulsation ($\omega_r \approx 0.085$), whereas the vertical dashed line indicates the sensitivity value to a forcing of pulsation $\omega_r \approx 0.045$.

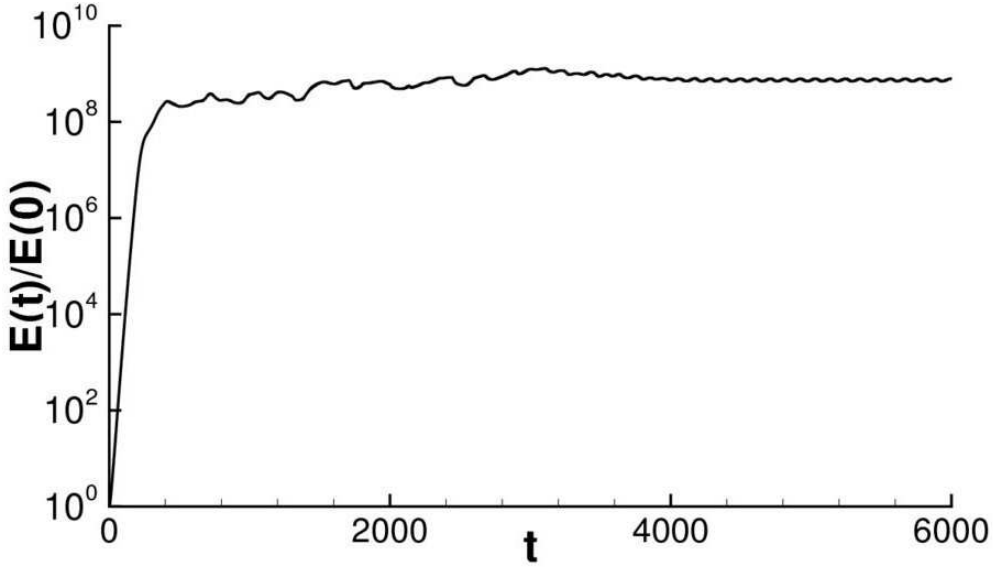

Figure 4.26: Time evolution of the energy gain computed by the DNS of an initial optimal perturbation of order of magnitude $A_0 = 10^{-4}$ at $Re = 223$.

$\omega_r \approx 0.045$, it lies in the range of the highly sensitive modes. As shown in Figure 4.25, the minimal perturbation amplitude triggering the real frequencies around $\omega_r \approx 0.045$ is approximatively 10^{-6}, which matches the value previously found by DNS (see Figure 4.24).
Finally, in order to investigate if such a mechanism linking sensitivity and convective instability may be found also in other flow configurations, several DNS with increasing Reynolds number have been performed. At $Re = 223$, an asymptotically unstable dynamics is recovered by superposing upon the base flow a perturbation of order of magnitude $A_0 = 10^{-4}$, while asymptotic stability is obtained with a smaller perturbation. As shown in Figure 4.26, the normalized energy saturates at a value of 10^9 which is maintained asymptotically, leading to a periodic self-sustained state. Since the period of the oscillations is about $T \approx 110$, it is possible to identify the locally unstable pulsation $\omega \approx 0.055$, which is very close to the one previously found for $Re = 200$. Therefore, it is likely that the generation of such a self-sustained state is due to the high sensitivity of the flow to that locally unstable frequency, which leads the flow to a subcritical transition. Such results show that the convective modes are a relevant feature of a separated boundary layer flow, being able to arise from different mechanisms (such as non-normality and sensitivity) in both a linear and a non-linear framework, and are able to play an active role in subcritical transition.

4.3 Asymptotically unstable dynamics: the origin of unsteadiness and the flapping frequency.

4.3.1 Linear dynamics

The supercritical dynamics of the flow has been investigated by performing the global eigenvalue analysis with increasing Reynolds numbers. Transition has been found to occur at $Re = 225$; Figure 4.27 shows the corresponding streamwise velocity contours of the base flow. The structure of the spectrum at such a Reynolds number, provided in Figure 4.28, is quite similar to the one at $Re = 200$. The spectrum is marginally unstable, since there are seven slightly unstable modes placed on the convective branch, their eigenvectors being reminiscent of the TS waves. Comparing Figure 4.27 with Figure 6.1, it is possible to notice that, for increasing Reynolds numbers, not only the bubble size (defined as the length of the separation region at the wall) increases, but some topological changes occur in the base flow. Looking at the separation streamline, one can observe a smoother reattachment and, most importantly, the presence of a secondary separation zone within the primary one, which is identified by a change of sign of the skin friction coefficient within the primary bubble. Such observations support the hypothesis of Dallmann et al. (1995) and Theofilis et al. (2000) that topological changes in the base flow could be at the origin of the onset of the unsteadiness in separation bubbles. As suggested in Marquillie and Ehrenstein (2003), it is likely that the primary instability of the considered bubble would be of structural type, meaning that for a supercritical Reynolds number the flow cannot exhibit any single-bubble state, instead it is characterized by a multiple separation which induces the vortex formation and shedding, leading to asymptotical instability.

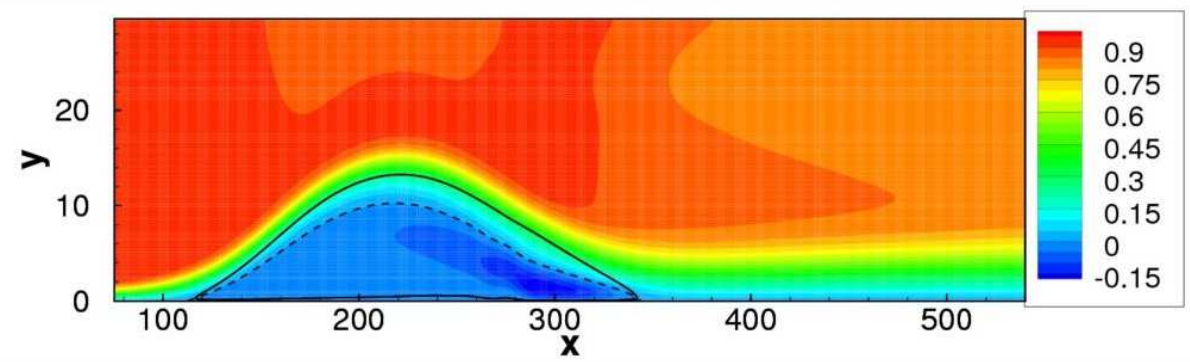

Figure 4.27: Streamwise velocity contours of the base flow BF1 at Reynolds number $Re = 225$. The solid line is the separation streamline, whereas the dashed line represents the $u = 0$ contour.

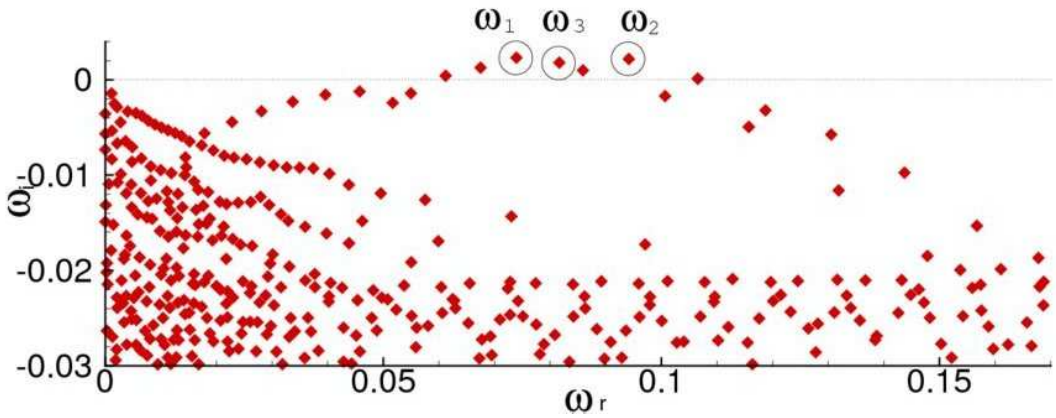

Figure 4.28: Eigenvalue spectrum for the flow BF1 at $Re = 225$ with $N_x = 270$ and $N_y = 50$ grid points. The modes labelled ω_1, ω_2 and ω_3 are the most unstable ones.

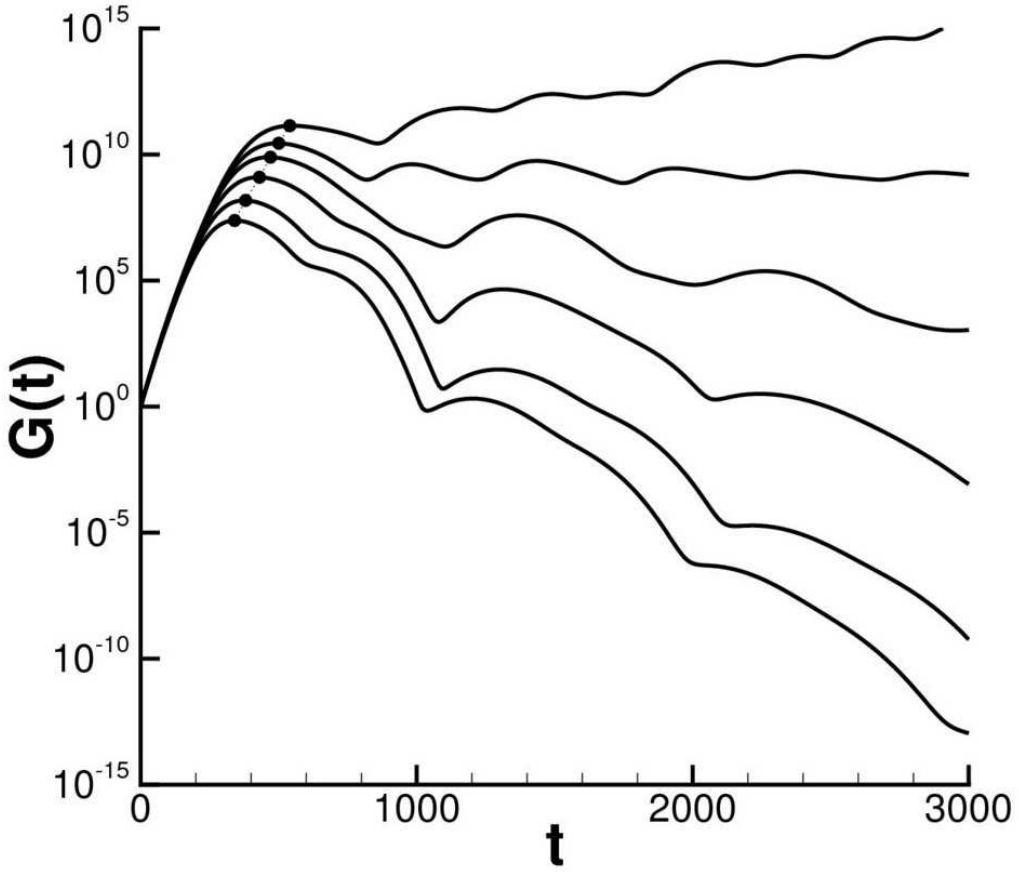

Figure 4.29: Optimal energy gain curves obtained by the global eigenvalue analysis with $N = 400$ modes for increasing Reynolds numbers: from the bottom curve to the top one, $Re = 190, 200, 207, 213, 219, 225$, respectively.

The linear energy growth has been studied using the global eigenvalue analysis for increasing Reynolds numbers. The behavior of the corresponding energy-gain curves, reported in Figure 4.29, shows that: i) the first peak value increases linearly with respect to Re; ii) the time at which the first peak occurs increases linearly with respect to Re. Recalling that the transient energy growth in the considered case is due to the Kelvin-Helmholtz amplification along the separation streamline, one can assume that the increase of $G(t)$ is due to the increase of the size of the bubble with the Reynolds number. Indeed, plotting the bubble size versus the Reynolds number, a linear dependence is recovered as shown in Figure 4.30.

In the slightly unstable case ($Re = 225$), a linear energy gain equal about to 10^{12} has been found, as shown by the top curve in Figure 4.29, which is a very high amplification with respect to the data available in the literature for other flow configurations. For instance, in Ehrenstein and Gallaire (2008), for a separated flow over a bump the authors found a peak value about equal to 10^9 for the critical Reynolds $Re = 590$, whereas here a growth of order of magnitude 10^{12} is observed for $Re = 225$. Such a difference is clearly

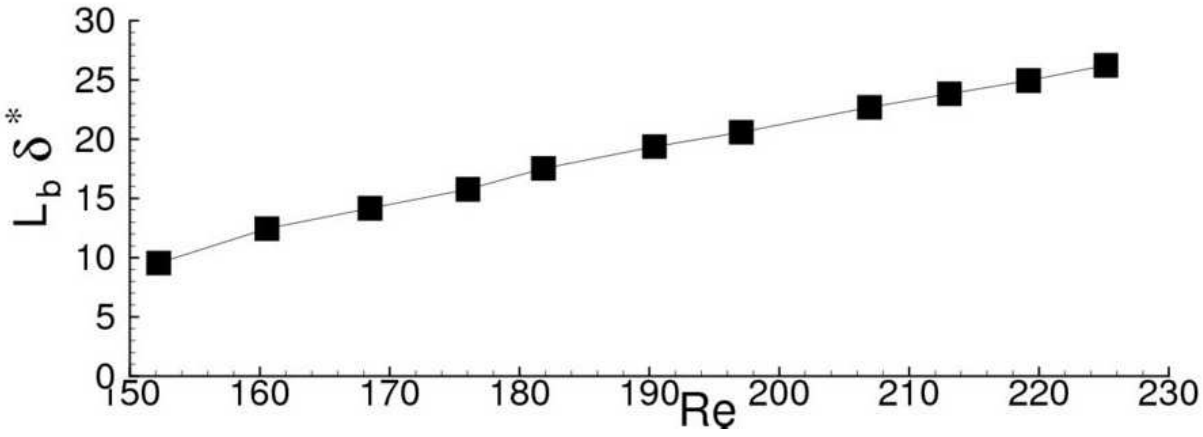

Figure 4.30: Dimensional bubble size $L_b\delta^*$ versus Re.

dependent on the bubble size and could also be due to the absence of solid boundaries bordering the bubble which allows the perturbation to amplify itself along the separation streamline from the separation point to the reattachment one.
In order to further investigate the linear unstable dynamics of an initial perturbation, the evolution of the optimal perturbation at $Re = 225$ has been studied. As shown in Figure 4.31, the perturbation is initially convected downstream by the mean flow as a localized wave packet. However, unlike the stable case previously analyzed, a second wave packet is generated due to the amplification of the disturbances carried back by the recirculation bubble. Such a disturbance shedding cycle is not due to an absolute instability of the velocity profiles within the bubble, as assessed by a local eigenvalue analysis, but to the global characteristics of the flow. It is worth to notice that the subcritical transient growth mechanism in a non-linear framework analyzed in Section 4.2.3 seems to be not far from the asymptotically unstable mechanism shown here. In the subcritical case, the non-linear terms being able to transfer energy among different modes, a wave packet cycle begins to be established until it decays due to the asymptotical damping of the perturbation. Thus, the generation of wave packets by the cyclic transfer of energy from the upstream part to the downstream part of the bubble and vice-versa seems to be a feature of the stability dynamics of such a separated flow.
Focusing now on the asymptotic behavior of the flow at different Reynolds numbers, one can observe in Figure 4.29 that each energy gain curve is affected by a modulation. Such a modulation, also named beating or flapping frequency, is a well-known feature of separated flows (Åkervik et al., 2007, Ehrenstein and Gallaire, 2008), although it has been found for the first time in a falling curtain flow by Schmid and Henningson (2002). Such a phenomenon is due to the interaction of the most unstable modes of the spectrum. In Figure 4.4 ($Re = 200$), one can observe two modes, labelled ω_1 and ω_2, having comparable amplification rate. Since such modes are associated to similar eigenvectors, they are able to interact resulting in the low frequency modulation observed for the energy gain curve at $Re = 200$. In fact, since the real parts of these eigenmodes differ of about $\delta\omega_r = 0.006$, their interaction results in a wave packet of period $T = 2\pi/\delta\omega_r \approx 1000$, which corresponds to the modulation shown in Figure 4.32 by the energy gain curve for $Re = 200$ (dashed

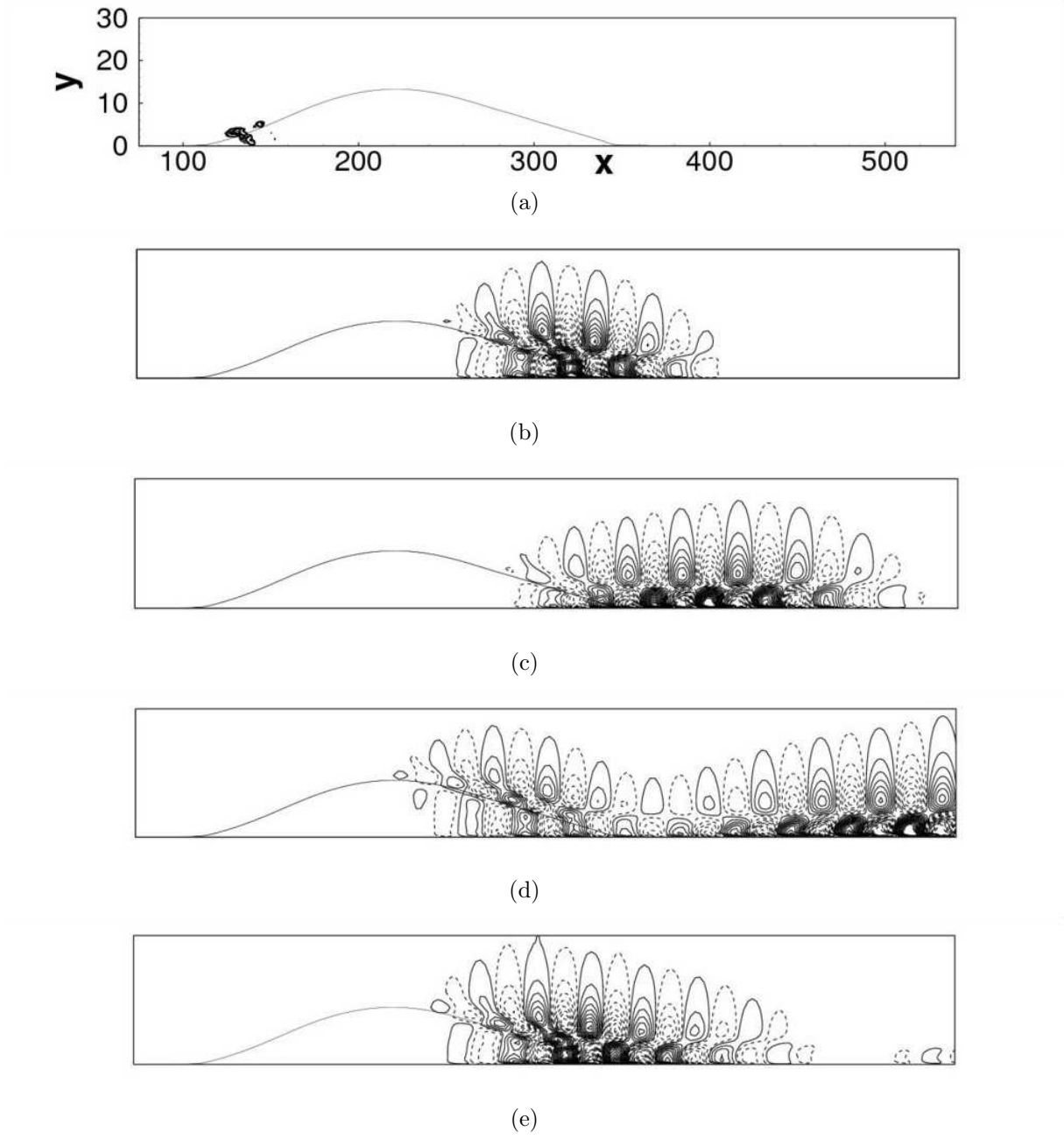

(a)

(b)

(c)

(d)

(e)

Figure 4.31: Streamwise perturbation velocity contours of the optimal perturbation obtained by the global eigenvalue analysis for $Re = 225$ at $t = 0$, $t = 450$, $t = 650$, $t = 850$, $t = 1050$. Solid-line contours indicate positive velocities; dashed-line ones are associated with negative velocities.

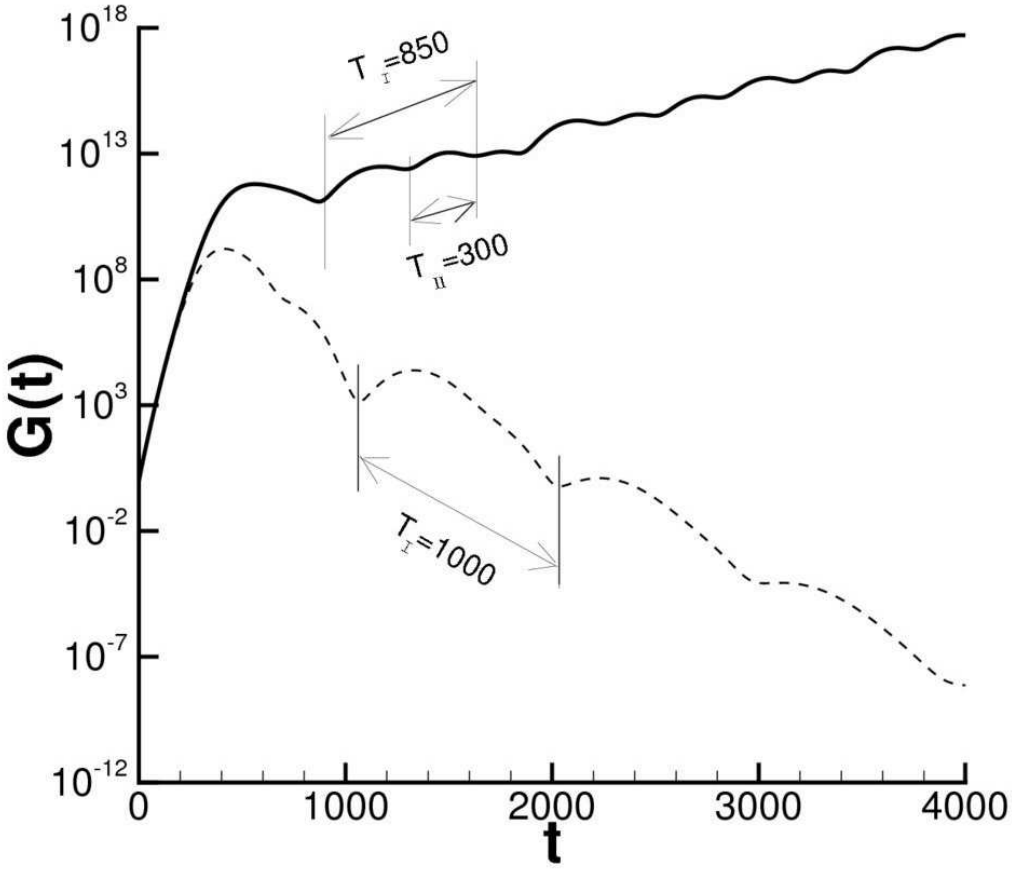

Figure 4.32: Optimal energy gain curves obtained by the global eigenvalue analysis with $N = 600$ modes for $Re = 225$ (solid line) and $Re = 200$ (dashed line).

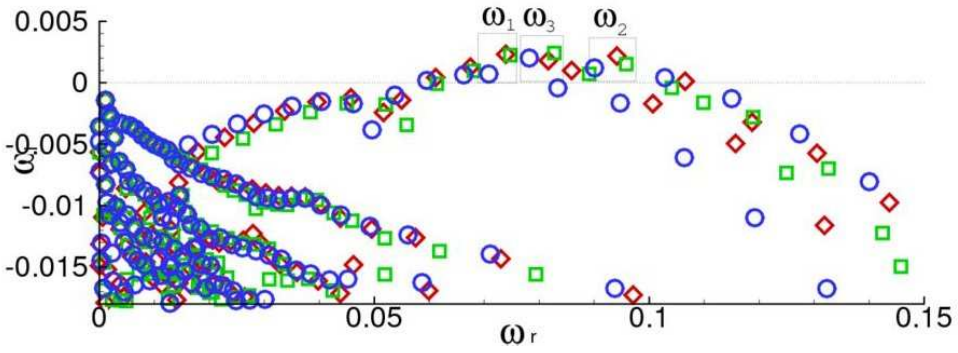

Figure 4.33: Spectra obtained at $Re = 225$ for three domain lengths, $L_1 = 430$ (diamonds), $L_2 = 480$ (squares), $L_3 = 530$ (circles).

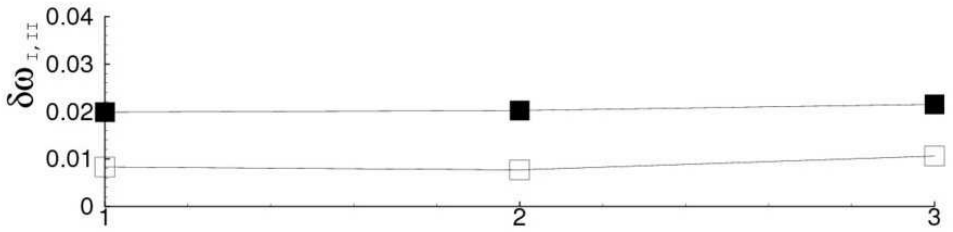

Figure 4.34: Sensibility of the value of the flapping frequencies I (white squares) and II (black squares) to the grid resolution: $N_x = 260$, $N_y = 48$ (point 1); reference case, $N_x = 270$, $N_y = 50$ (point 2); $N_x = 300$, $N_y = 56$ (point 3).

line). Moreover, it appears from Figure 4.29 that two frequencies can be identified for each energy gain curve with $Re \geq 213$. For instance, at $Re = 225$, the first frequency (labeled as I) corresponds to the low-frequency beating found in the previous case, having a period of about $T \approx 850$ (see the solid line in Figure 4.32). The second frequency (labeled as II) is slightly higher than the first one, having a period of about $T \approx 300$. Indeed, by looking at the spectrum at $Re = 225$, provided in Figure 4.28, one can notice that the three most unstable modes have very similar amplification rate, leading to cancellation as in the stable case. Since their real parts differ of about $\delta\omega_{r_I} = \omega_{r_3} - \omega_{r_1} \approx 0.0075$, and $\delta\omega_{r_{II}} = \omega_{r_2} - \omega_{r_3} \approx 0.02$, they result respectively in two wave packets of period $T_I = 2\pi/\delta\omega_{r_I} \approx 850$ and $T_{II} = 2\pi/\delta\omega_{r_{II}} \approx 300$. It is worth to notice that, due to the linearity of the global eigenvalue analysis, for large values of t the beating induced by the two most unstable modes (frequency II) dominates the other one, as reported in Figure 4.32.

The sensitivity of the computed flapping frequencies with respect to the grid resolution and the domain length has been studied. It is noteworthy that, although the spectra corresponding to different domain lengths do present some differences, as shown in Figure 4.33, due to the different streamwise extention of the modes, the global model is able to accurately predict the overall stability features of the flow. In fact, the computations demonstrate that the same two distinct frequencies are always recovered for different grid

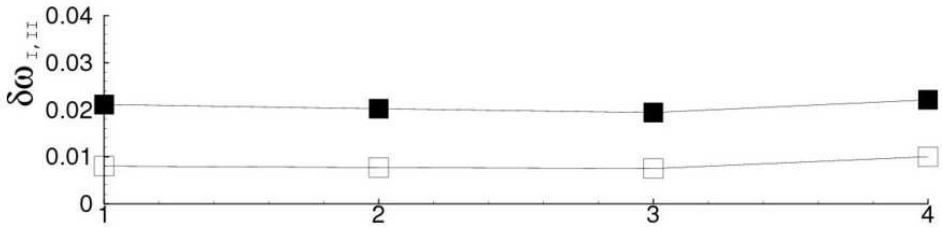

Figure 4.35: Sensibility of the value of the flapping frequencies I (white squares) and II (black squares) to the domain length: $N_x = 270$, $N_y = 50$, $L_x = 430$ (point 1); reference case, $N_x = 270$, $N_y = 50$, $L_x = 480$ (point 2); $N_x = 270$, $N_y = 50$, $L_x = 530$ (point 3), $N_x = 300$, $N_y = 50$, $L_x = 580$ (point 4).

resolutions (see Figure 4.34) and domain lengths (see Figure 4.35), the influence of such parameters on $\delta\omega_{r_I}$ and $\delta\omega_{r_{II}}$ being negligible.

4.3.2 Non-linear dynamics

The physical mechanism governing the beating phenomenon has been studied by performing several numerical simulations with increasing Reynolds numbers. DNS predicts transition for BF1 at $Re = 230$, which is close but not exactly equal to the critical Reynolds number obtained by the linear analysis, namely $Re = 225$. Such a discrepancy might be due to a stabilizing effect of the convective outflow boundary conditions, as conjectured in Ehrenstein and Gallaire (2008), or to an imperfect convergence of the convective branch of the eigenvalue spectrum, which is very sensitive to numerical parameters, or to the different numerical discretizations used in the global eigenvalue analysis and DNS. Superposing the optimal perturbation obtained by the transient growth analysis upon the base flow at $Re = 225$, the time evolution of the energy gain has been computed by DNS. In Figure 4.36 it is possible to observe that two modulations affect the energy gain curve after the transient has passed, with periods $T_I \approx 1200$ and $T_{II} \approx 350$. Such results are in good agreement with the ones found by using the global eigenvalue analysis.
It is worth to notice that the linear peak value of the energy gain, 10^{12} (see Figure 4.32), is not reached in the non-linear case shown in Figure 4.36, the predicted optimal growth being so high that the energy saturates before. In the considered case, by injecting an initial perturbation with order of magnitude 10^{-6}, which corresponds to an initial energy of order of magnitude 10^{-12}, such a perturbation amplifies itself up to a factor 10^{11}, reaching amplitudes about equal to 10^{-1}, so that the non-linear effects are not negligible. However, as the amplitudes of the perturbations begin to decrease due to asymptotic stability, a linear dynamics is eventually recovered.

At supercritical Reynolds numbers, saturation occurs earlier due to the interactions of exponentially growing wave packets and it is maintained asymptotically. The flow shows an unsteady, randomized behaviour within the separation region, which results in a continuous shedding of wave packets in the attached zone, as shown in a space-time diagram in Figure 4.37. In order to assess if the two flapping frequencies are a feature of the considered flow also at supercritical conditions, the power spectrum in time of the evolving

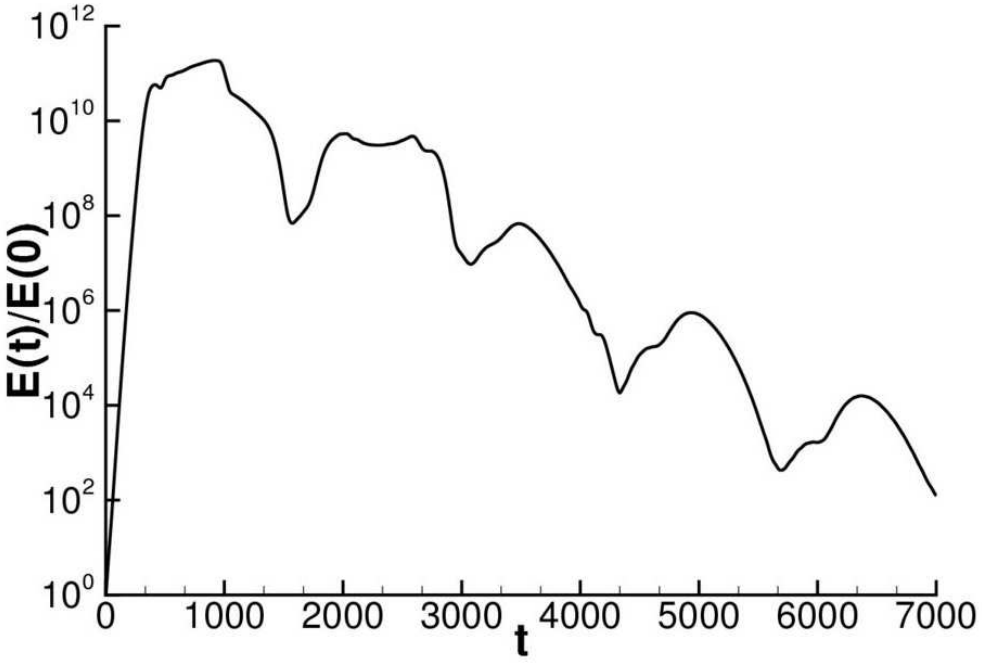

Figure 4.36: Time evolution of the energy gain of an initial optimal perturbation of order of magnitude $A_0 = 10^{-6}$ computed by the DNS at $Re = 225$.

perturbation, u, at a point within the bubble ($x = 339$, $y = 1.4$) has been computed for $Re = 230$. Figure 4.38 shows the power density spectrum of u obtained by the Welch periodogram/FFT method on a sampling period of $T = 40000$ divided in eight partially overlapped windows. A Hamming window-function has been used on each data segment. Two frequency ranges where the energy is mostly located are found. The higher frequency range corresponds to TS waves, since the pulsations in the range $0.06 < \omega_r < 0.12$ correspond to the globally unstable modes of Figure 4.28. Moreover, in the low-frequency region it is possible to recover three leading pulsations which are close to the flapping frequencies I and II and to their difference, respectively ($\omega_I \approx 0.005$, $\omega_{II} \approx 0.014$ and $\omega_{III} = \omega_{II} - \omega_I \approx 0.009$). It is worth to notice that, unlike the linear model predictions, there is not a dominant frequency, due to the non-linear effects.
In order to shed light on the onset of the beating phenomenon, the dependence of such modulations on the Reynolds number has been investigated. The primary flapping frequencies have been computed by means of the global eigenvalue analysis at several Reynolds numbers lying in the range $150 \leq Re \leq 225$. In order to eliminate the dependence of the frequencies on δ^*, a Reynolds number based on the reference length $L = 0.05m$, $Re_L = U_\infty L/\nu$, has been employed, the corresponding dimensionless frequency being $F = L/\delta^* f$. Plotting the frequency values versus Re_L, as shown in Figure 4.39, it appears that $F \approx 1$ for $Re_L \leq 33000$ ($Re \leq 207$), whereas, for $Re_L \geq 35000$ ($Re \geq 213$), that is the threshold for the onset of the secondary flapping frequency, the frequency F slightly increases. A possible explanation of such a behavior is here provided, which concerns the physical mechanism governing the onset of the flapping frequencies in

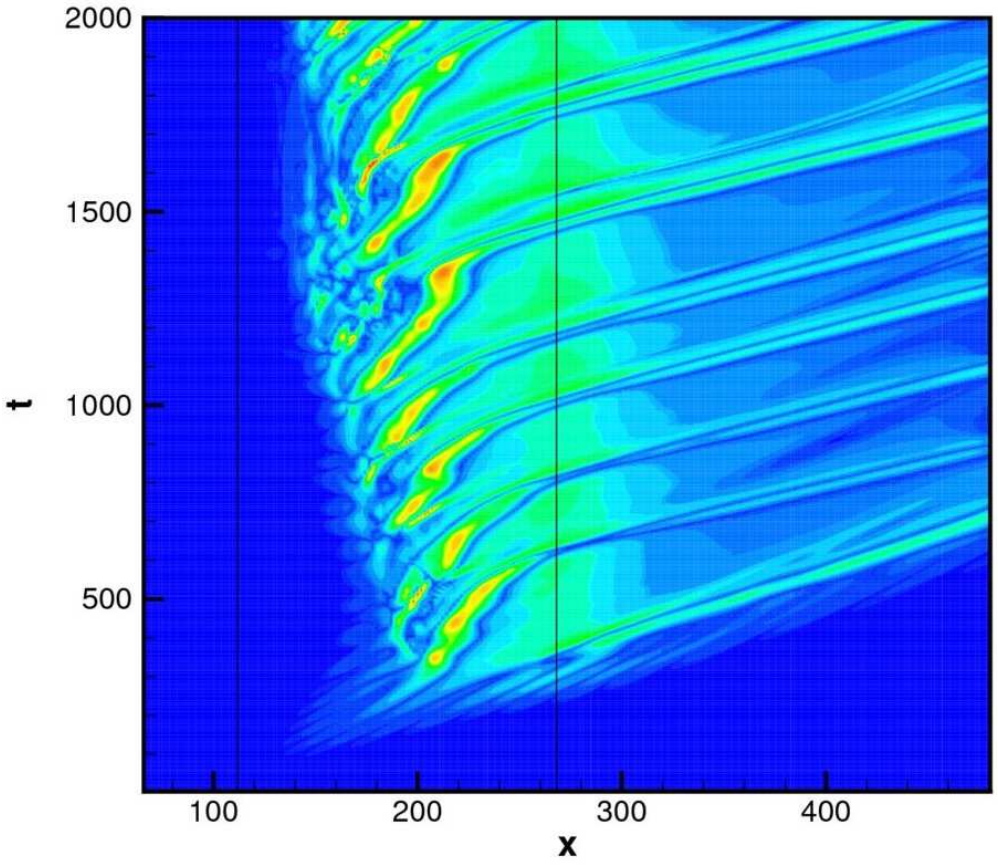

Figure 4.37: Space-time diagram of the perturbation vorticity at the wall for $Re = 230$ and an initial perturbation of amplitude $A_0 = 10^{-4}$. The solid lines identify the separation and reattachment points.

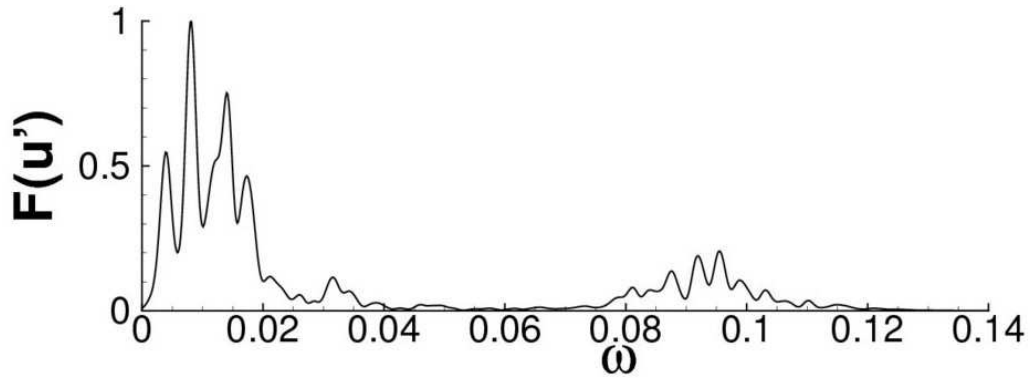

Figure 4.38: Power density spectrum in time of the evolving streamwise perturbation velocity, u, obtained by a Welch method on a sampling period of $T = 40000$ divided in eight partially overlapped windows for $Re = 230$ at $x = 339$, $y = 1.4$.

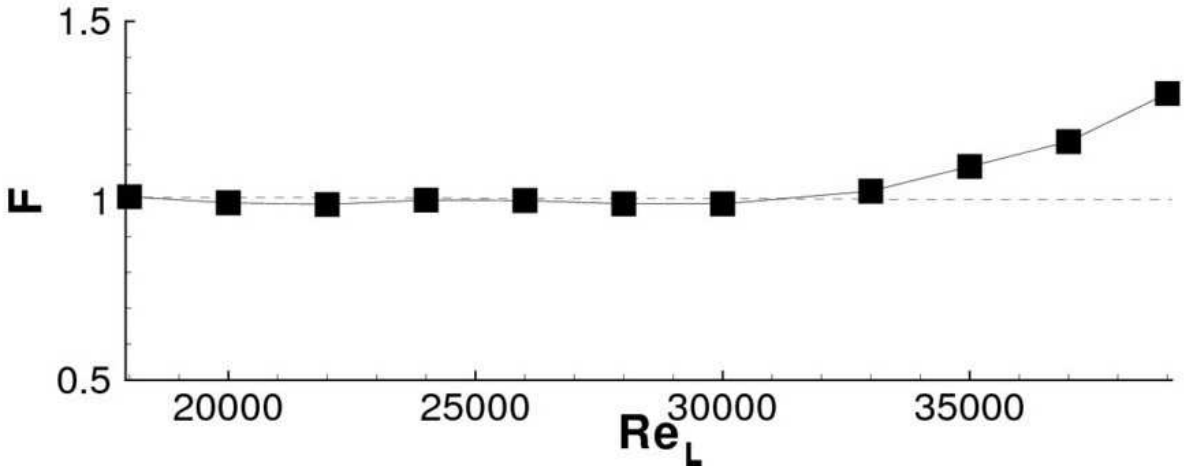

Figure 4.39: Values of the dimensionless flapping frequencies, F, versus Re_L. The value of Re at the black square points are: 152, 160, 168, 176, 182, 191, 200, 207,213, 220, 225, respectively.

separated flows over a flat plate.
Recalling that the beating is due to the interaction of two modes presenting similar eigenvectors, and that such an interaction has been observed in several separated flows, such as cavity-induced and bump-induced separation (Åkervik et al., 2007, Ehrenstein and Gallaire, 2008), it can be argued that a separated region, which is able to carry back the perturbation, could play an active role in the generation of the interaction between modes. In fact, a part of the perturbation located in the separated region could be convected upstream within the bubble, where it is likely to interact with the main part of the wave packet which is being convected downstream along the separation streamline. Therefore, one may assume that the beating frequency would be proportional to $1/t_b$, where t_b is the time needed by the mean flow to carry back such a wave packet from the reattachment point to the separation streamline:

$$F \propto 1/t_b \propto U_b/L_b, \tag{4.1}$$

where L_b is the size of the bubble and U_b the velocity of the base flow within the bubble. By measuring the variation of the bubble size and of the velocity of the flow at two points within the bubble at different Reynolds numbers, it appears that both L_b and U_b vary linearly with respect to Re_L when $Re_L < 35000$ ($Re < 213$, see Figures 4.30 and 4.40, respectively). Such a linear dependence is broken when $Re_L \geq 35000$, due to some topological changes of the base flow. Thus, as long as $Re_L < 35000$, the ratio between two frequencies F_1 and F_2 at two Reynolds numbers Re_{L_1} and Re_{L_2} could be written as:

$$\frac{F_2}{F_1} = \frac{t_{L_1}}{t_{L_2}} = \frac{U_{b_2}}{U_{b_1}}\frac{L_{b_1}}{L_{b_2}} = \frac{Re_{L_2}}{Re_{L_1}}\frac{Re_{L_1}}{Re_{L_2}} = 1\,, \tag{4.2}$$

meaning that the flapping frequency F remains constant when the Reynolds number varies, confirming the results shown in Figure 4.39 for $Re_L < 35000$.
Concerning the dynamics at $Re_L = 35000$ ($Re = 213$), looking at the corresponding base

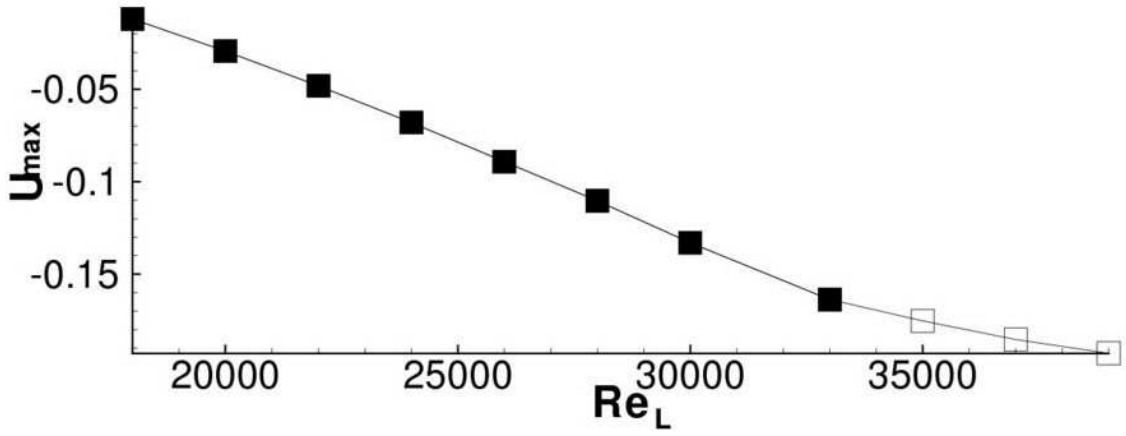

Figure 4.40: Values of the maximum backflow velocity within the bubble versus Re_L. The value of Re at the black square points are: 152, 160, 168, 176, 182, 191, 200, 207, respectively; whereas at the empty square points $Re = 213, 220, 225$, respectively.

flow in Figure 4.41(a), one can see an inflection of the streamlines within the bubble, which is not observed for smaller values of the Reynolds number (see Figure 4.41(b) corresponding to $Re = 207$). The DNS shows that when the flow is perturbed or when the Reynolds number is increased, such a topological change originate a small separation which splits the bubble in two smaller ones, labeled as part A and part B in Figure 4.42. It is possible to assume that the onset of the flapping frequency II at such a Reynolds number is a consequence of the splitting of the bubble in two smaller ones, which could carry back the perturbations at two different rates generating two distinct modulations of the energy gain curve. Indeed, one can notice that the ratio of the size of bubble A with respect to the size of the bubble B ($L_B/L_A \approx 2.5$) is very close to the ratio of the two flapping frequencies ($\omega_{II}/\omega_I \approx 2.8$), supporting such an assumption. Moreover, the bubble splitting would also explain why a higher value of the flapping frequency I is recovered for $Re_L \geq 35000$. Indeed, assuming that the beating I is generated by the part B of the bubble (while the beating II is generated by the part A), one can argue that such a bubble, which is smaller than the original one, would be able to carry back disturbances in a smaller time, originating a higher primary beating frequency.
In order to validate such a model for the case of smaller bubbles, the onset of the flapping frequency has been investigated for the base flows BF2, BF3, BF4, BF5. Figure 4.43 provides the energy gain curves computed by the global eigenvalue analysis for BF1, BF2, BF3, BF4, and BF5 (from top to bottom), showing that a low-frequency modulation is recovered for all of the considered separated flows. The dependence of the flapping frequency, F, on the ratio U_b/L_b has been investigated, where U_b, representing the upstream convection velocity of the base flow, has been measured within the bubble at the first grid point from the wall where the maximum backflow is recovered. Figure 4.44 shows that F has approximatively a linear variation versus the ratio U_b/L_b, validating the conjecture of equation 4.1. Finally, it should be noticed that the onset of the flapping modulation in the energy gain curve for BF5 (see the bottom curve in Figure 4.43) is associated with very low levels of the normalized energy, namely, of order 10^{-5}. Therefore, it is likely

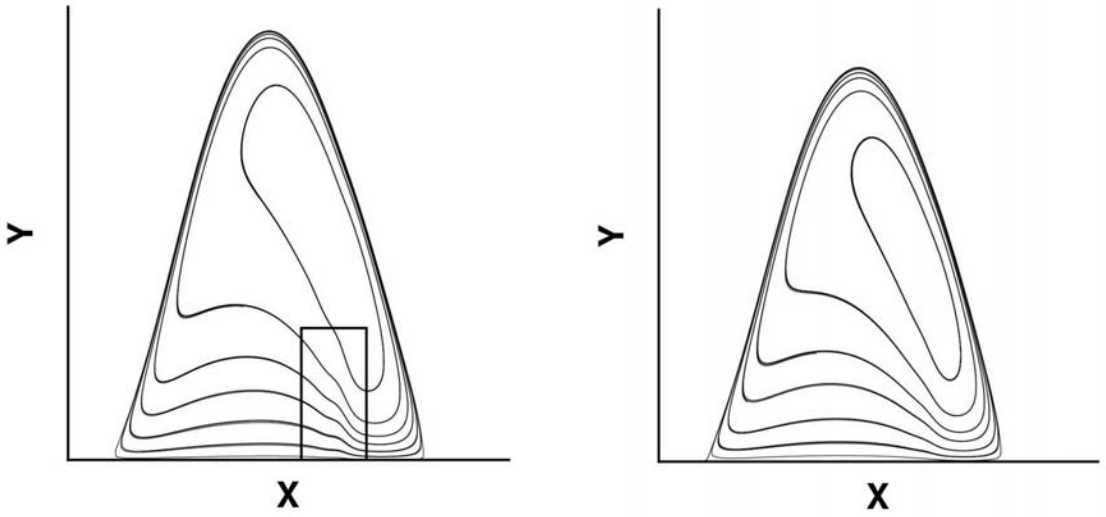

(a) (b)

Figure 4.41: Streamlines within the separated region for two base flows, at $Re = 213$ (a) and $Re = 207$ (b). Within the panel, the inflections of the streamlines for $Re = 213$ are shown.

that the beating could not be observed in an experimental framework for small size bubbles. Moreover, it has been verified that for a smaller bubble, having an aspect ratio of about $h/L \approx 0.01$, the flapping phenomenon is inhibited, probably due to the very narrow shape of the separated zone. For larger bubbles the flapping phenomenon is associated with higher levels of the energy, in some cases affecting the dynamics of the separated flow also in the presence of non-linear effects, and becoming observable in experimental measurements (Dovgal and Sorokin, 2009).

4.4 Discussion of the results

The transient and asymptotical dynamics of a large separation bubble over a flat plate has been studied in a two-dimensional framework in order to investigate the role of non-normality and non-linearity of the differential operator in the stability of such a flow. Linear eigenvalue analysis as well as numerical simulations with weakly non-linear perturbations have shown that the non-normality of convective modes of the Navier–Stokes operator allows the bubble to act as a strong amplifier of small disturbances, due to a Kelvin-Helmholtz mechanism acting over the separation streamline. Indeed, the front part of the bubble shows a high sensitivity to perturbations, as observed in simulations with white noise disturbances superposed upon the whole base flow or upon the inflow Blasius profile.
For finite amplitude initial perturbations, the strong linear transient amplification saturates, due to non-linear interactions between modes. Furthermore, such an energy exchange between modes induces the bubble to establish a wave packet cycle, characterized

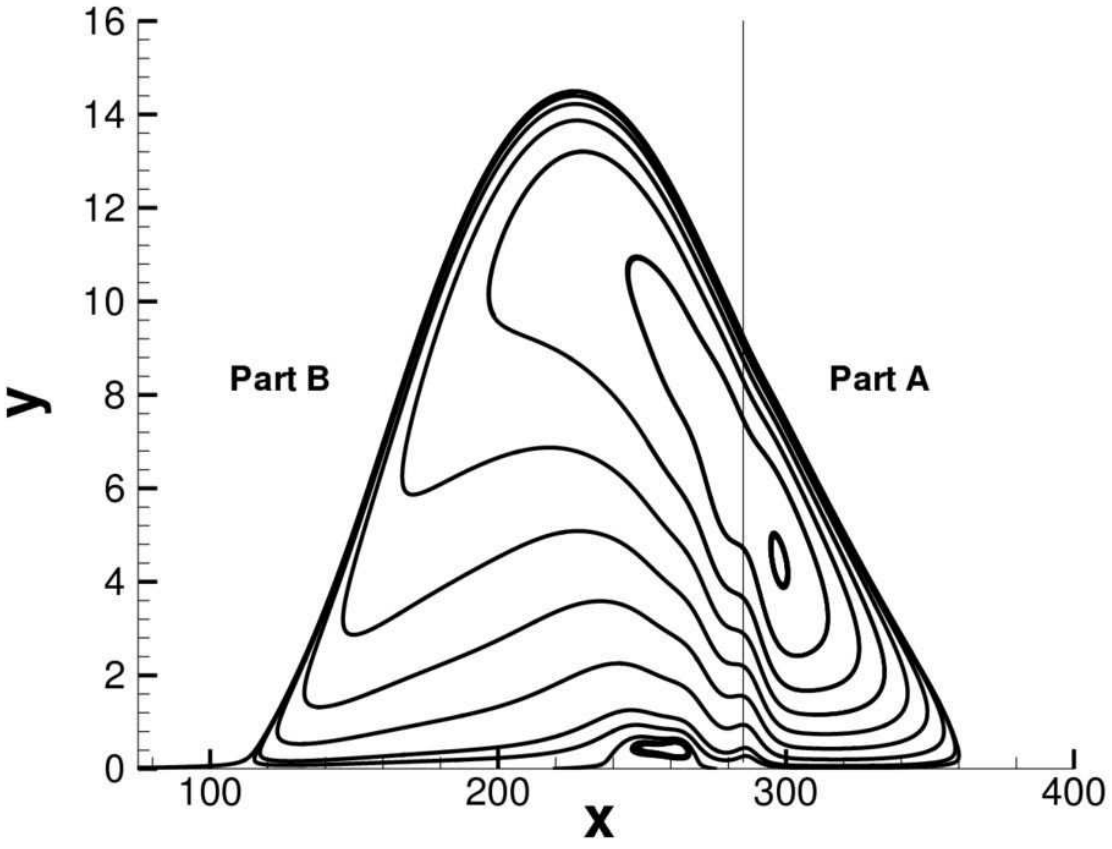

Figure 4.42: Streamlines within the separated region for the base flow at $Re = 230$. The presence of a secondary bubble within the first one divides the bubble in two parts, labelled A and B.

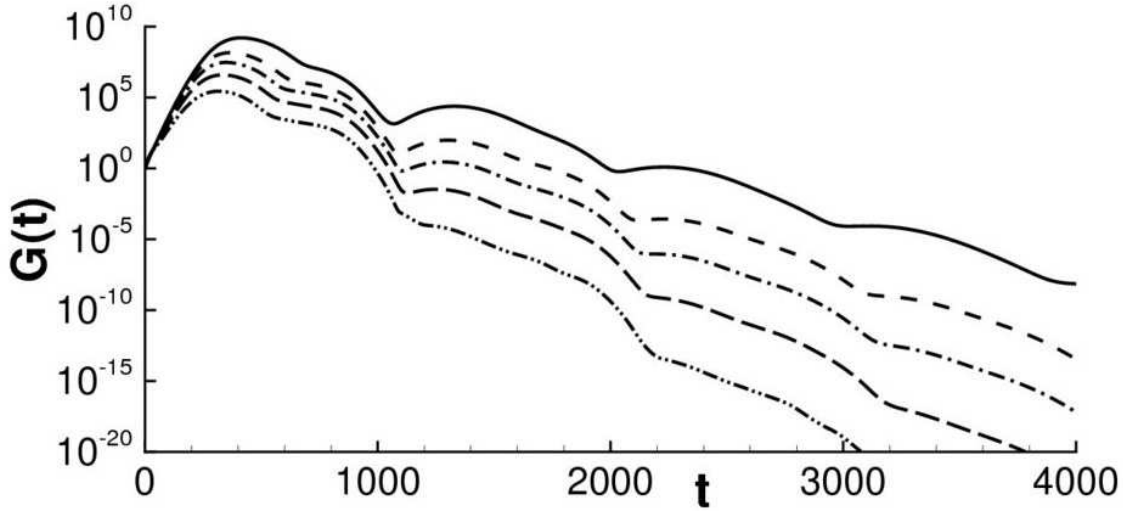

Figure 4.43: Energy gain curves computed by the global eigenvalue analysis for base flows BF1, BF2, BF3, BF4, and BF5 (from top to bottom).

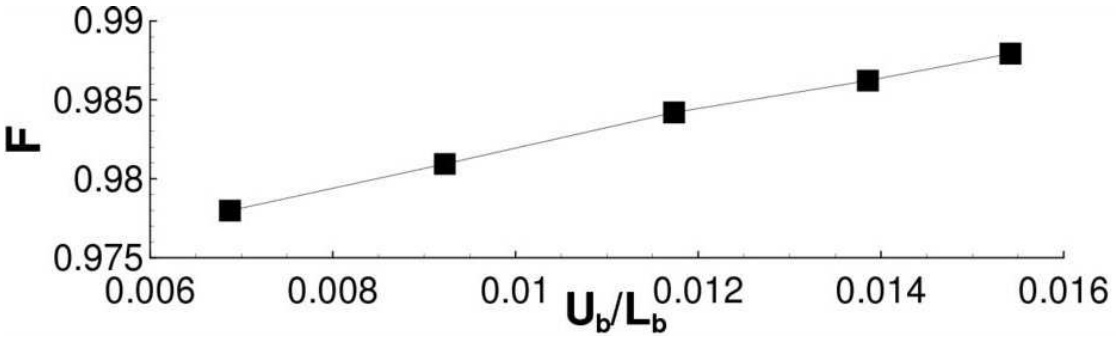

Figure 4.44: Value of the flapping frequency, F, versus the ratio U_b/L_b, computed by the global eigenvalue analysis for base flows BF1, BF2, BF3, BF4, and BF5 (from right to left).

by the shedding of two wave packets of comparable amplitude. Such a cycle is similar to the one occurring at supercritical Reynolds numbers, but it is eventually damped when the flow is asymptotically stable. Non-linear interactions contribute also to the excitation of a convectively unstable mode in the attached-flow region due to the high sensitivity of the boundary layer, inducing a further transient amplification of finite amplitude perturbations as well as an asymptotical instability at slightly subcritical Reynolds numbers.
Topological flow changes on the base flow have been found to occur close to transition, supporting the hypothesis of some authors (Dallmann et al., 1995, Theofilis et al., 2000) that the unsteadiness of separated flows could be due to structural changes within the bubble. Furthermore, non-normality effects have shown to play an active role also at large times. In fact, due to the superposition of two convective non-normal modes, a low-frequency oscillation, known as flapping frequency, appears. Close to transition, when topological changes occur in the flow, a secondary flapping frequency appears as well. A possible explanation of such a behavior has been provided, in which it is assumed that the oscillations are due to the interaction of the main wave packet with the perturbations carried upstream by the backflow inside the bubble. A scaling law based on the previous assumption is able to predict accurately the dependence of the flapping frequency on the Reynolds number and the onset of the secondary frequency close to transition.
Thus, in this part of the thesis the effects of non-normality and non-linearity on the instability dynamics of a separated boundary layer flow have been studied; the mechanisms of strong amplification of localized two-dimensional perturbations, the low-frequency oscillations known as flapping, as well as the role of topological changes in the onset of global instability have been clarified and explained in detail.

5

The response to a harmonic forcing of a two-dimensional separated boundary layer

In the previous chapter it has been shown that flat-plate two-dimensional separated boundary-layer flows are affected by strong non-normality effects at both small and large times, such as the high amplification of disturbances and the flapping phenomenon. Such features suggest that, due to the high non-normality of the NS operator, such a flow may also act as a selective noise amplifier (Trefethen and Embree (2005)). In fact, the response of the flow to forcing at a certain frequency is driven by the pseudo-resonance of the temporal modes, which is due to the non-normality of the underlying linearized evolution operator. Although many authors have studied the amplifier dynamics of separated flows by means of a global approach, (for instance, see Blackburn et al. (2008) and Marquet et al. (2008)), an investigation of the global response to external forcing of a separated flow is still not available in the literature.
In order to investigate whether and how the flow may select and amplify certain frequencies from a background or induced noise, the sensitivity of the flow and its optimal response to an external forcing are studied by means of the sensitivity analsys discussed in Section 3.5.2. The study of the resolvent is performed for different base flows, obtained for different Re or suction-and-blowing velocity profiles, in order to identify the most responsive disturbance and the underlying amplification mechanism. The connection of the optimal response to the onset of self-excited vortices observed in literature is investigated. For that purpose, direct numerical simulations perturbed with a small level of random noise, are also performed. The results of the DNS are then compared with the ones of the sensitivity analysis, and with the ones obtained in the literature about the most amplified frequencies in separated boundary-layer flows.
This part of the thesis has been developed in cooperation with Dr. F. Alizard (Arts et Métiers ParisTech, France), and it has been published on Physics of Fluids, Volume 21, Issue 6, pp. 064108 (2009).

5.1 Problem formulation

Five separated flows are computed, by imposing different suction-and blowing velocity profiles or Reynolds numbers. The base flows bf1, bf2 and bf3 are computed at a Reynolds number $Re = 200$ for the three suction profiles provided in Figure 5.1. The separated flows bf4 and bf5 are obtained by using the same upper boundary velocity distribution

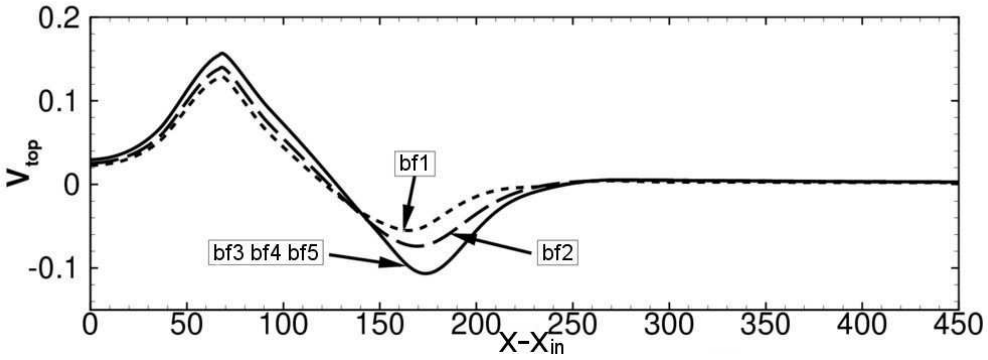

Figure 5.1: Suction profiles prescribed for base flows bf1 (short-dashed line), bf2 (long-dashed line), bf3, bf4 and bf5 (solid line).

as bf3, for the Reynolds numbers $Re = 215$ and $Re = 220$, respectively. It is noteworthy that the separated flows bf3 corresponds to one denoted as BF1 in the previous chapter. The Reynolds number Re varies from 200 to 220, which is below the critical Reynolds number for convective instabilities, as shown in the previous chapter. For the DNS, the boundary conditions are identical to the ones used in the previous chapter. The dimension of the computational box are $L_x = 450$ and $L_y = 30$, discretized by a (501×150) grid, which has been found adequate for the present computations, as it has been shown in the previous chapter.
For the global model computations, a (270×55) grid and $N = 1300$ modes have been chosen. The boundary conditions are identical to the ones used in the previous chapter. The lengths of the computational domains have proved to be large enough to not influence the stability results.

5.2 Response to a localized harmonic forcing: a selective noise amplifier.

The five considered separated flows, bf1, bf2, bf3, bf4 and bf5, are depicted in Figures 5.2 (a), (b), (c), (d), (e), respectively. One may observe the influence of the Reynolds number and the suction-and blowing velocity profile on the resulting base flows. An increasing intensity of the suction implies a larger separated zone as well as a displacement of the center of the bubble near the reattachment point. A slight increase of the Reynolds number induces an increase of the bubble size and of the recirculation close to the reattachment point. Moreover, under the same adverse pressure gradient, the location of the separation point is only slightly affected by the increasing of Re (Table 5.1).

5.2.1 Asymptotical sensitivity analysis

In this section, the sensitivity of the linearized NS operator to a harmonic forcing with an imposed frequency, and its consequences on the asymptotic behavior of the separated flows, are investigated. Even if all the modes are damped temporally, the flow, being

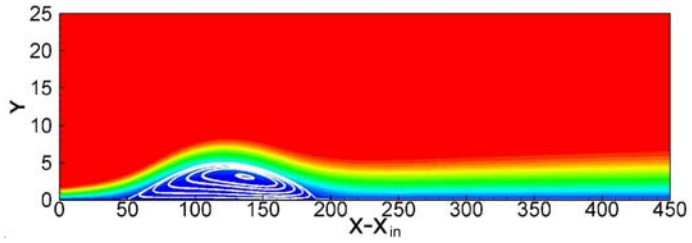

(a)

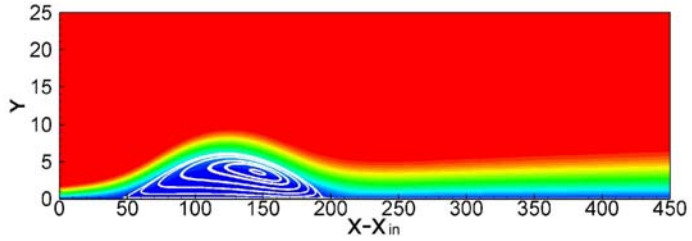

(b)

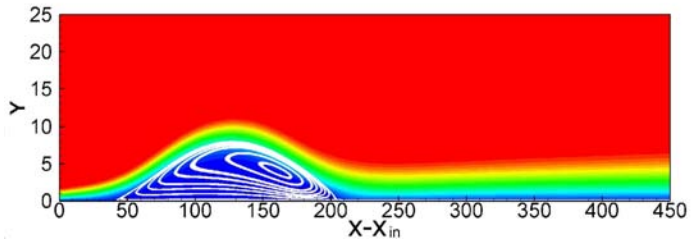

(c)

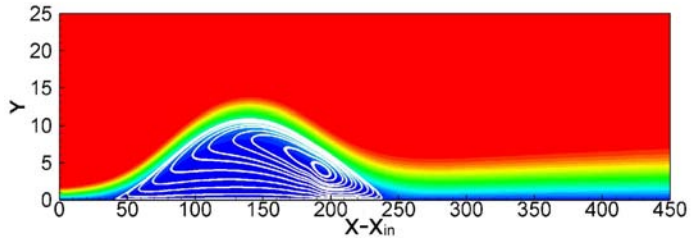

(d)

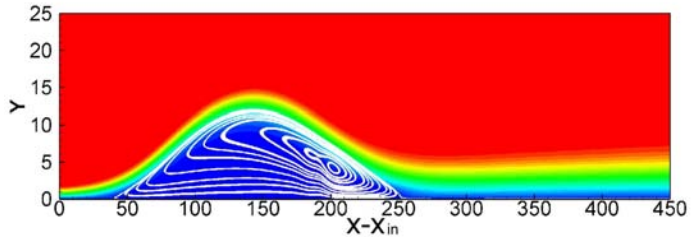

(e)

Figure 5.2: Streamwise component of the perturbation (shaded contours) and streamlines (white lines) for base flows bf1 (a), bf2 (b), bf3 (c), bf4 (d) and bf5 (e). The first three base flow have been obtained for $Re = 200$ and the three suction profiles in Figure 5.1, whereas the fourth and the fifth have been computed for the same suction profile as bf3, with $Re = 215$ and $Re = 220$, respectively.

X	bf1	bf2	bf3	bf4	bf5
X_s	49.5	45.8	40.8	39.8	39
X_r	189	194	204	238	253

Table 5.1: Distance from x_{in} of the separation and reattachment points, referenced as X_s and X_r respectively, for the five base flows.

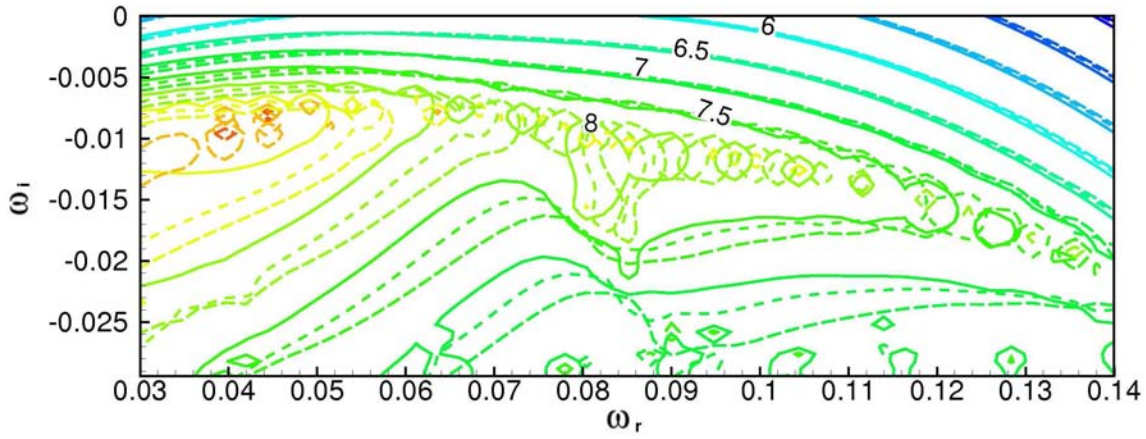

Figure 5.3: Pseudo-spectrum of the separated flow bf1. The iso-levels $-\log_{10}(\varepsilon)$ are shown for three domain sizes: $L_1 = 450$ (solid line), $L_2 = 425$ (dashed line) and $L_3 = 400$ (long-dashed line) discretized by $N_x = 270$, 265, and 260 grid points, respectively.

strongly separated, is subject to convective instabilities. Thus, the existence of convective waves as a response to a harmonic forcing $\mathcal{F} = \mathbf{f}e^{-i\sigma_f t}$ is investigated in a global framework.

The separated flow bf1 is considered first. Figure 5.3 provides its pseudospectrum (defined in equation (3.38)), represented by plotting the contours of $-log_{10}(\varepsilon)$. At each point on the real axis ($\omega_i = 0$), the contour value represents the sensitivity of the flow to external forcing with the corresponding pulsation $\sigma_f = \omega_r$; a high value of such parameter ($\approx 10^{-6}$ for the case here considered) means that the flow is able to get a large response to an external real forcing at a selected frequency σ_f. Furthermore, it is worth to notice that such a value does not depend on the domain size as shown by the ε levels in Figure 5.3, so that one can argue that it is an intrinsic property of the separated flow. As shown in Figure 5.3, large sensitivity areas appear around each temporal mode. A pseudo-resonance, resulting from the high non-orthogonality of the eigenvectors, may thus occur even far away from the considered modes. The response to a real frequency is dominated by the global KH/TS-like modes, the most sensitive one corresponding to the most unstable one. The separated flows bf2, bf3, bf4 and bf5 are found to show as well an high sensitivity to external forcing, although the pseudospectrum associated with such base flows is not shown here for brevity (the one for bf3 is shown in Figure 4.25).

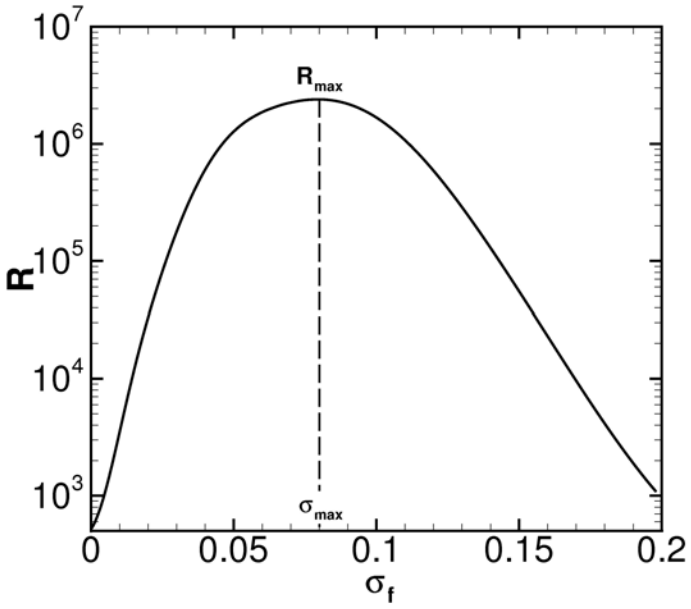

Figure 5.4: Curve of the resolvent R versus the forcing frequency σ_f for bf1 ($N = 1300$ modes are considered). The dashed line indicates the maximum value of the resolvent, R_{max}, and the frequency for which such value is reached, σ_{max}.

5.2.2 Optimal response to a localized harmonic forcing

Once the high sensitivity of the flow to an external forcing has been proved, it would be useful to investigate which perturbation is able to induce an optimal response to a harmonic forcing at a given frequency. Thus, the resolvent R, which has been defined in section 3 as the maximum response of the flow to a given forcing, has been computed. The base flow bf1 is considered, although similar results have been found for the different base flows. The resolvent R computed for such a base flow is plotted in Figure 5.4 for $N = 1300$. As it is suggested by the pseudospectrum analysis, one observes a strong amplification of the value of R which reaches a maximum value for $\sigma_f = 0.08$. Two quantities characterizing the intensity of the optimal response and the associated forcing frequency, denoted by $R_{\max}$ and $\sigma_{\max}$, are introduced, which are defined as

$$\begin{cases} R_{\max} = \max_{\sigma_f} \left(R\left(\sigma_f\right)\right) \\ \\ \sigma_{\max} = \{\sigma_f \ni R\left(\sigma_f\right) = R_{\max}.\} \end{cases} \tag{5.1}$$

Such parameters are sketched in Figure 5.4. The dependence of such quantities on the number of modes used in the computation of $R\left(\sigma_f\right)$ is shown in Figures 5.5 (a) and (b). One could observe a good convergence of the most amplified frequency which reaches an almost constant value for $N = 800$. The value of $R_{\max}$ exhibits a fast increase for moderate values of N and a slow convergence when $N \to \infty$.

Therefore, $N = 1300$ modes are here considered sufficient to capture the optimal response and its associated frequency. The streamwise distribution of the optimal forcing

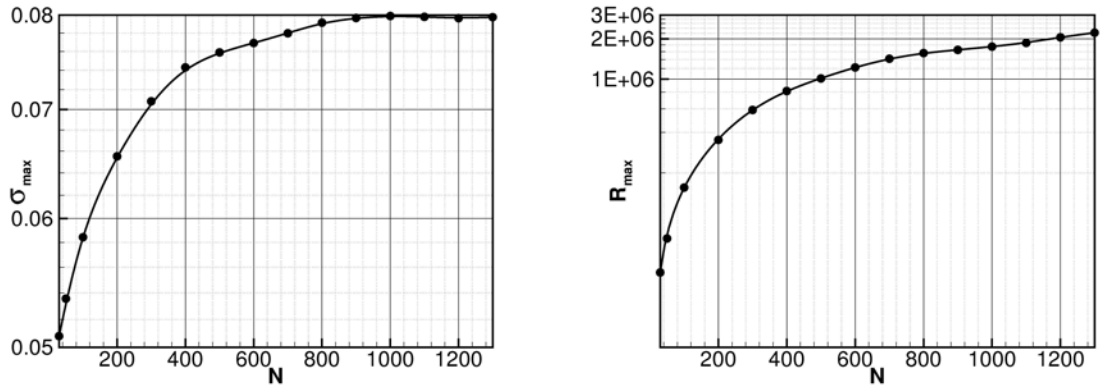

(a) (b)

Figure 5.5: Evolution of $\sigma_{\max}$ (a) and $R_{\max}$ (b) with the number of modes for bf1 and $L_x = 450$.

and its respective response, both represented by the following variable:

$$U_x(x) = \int_0^{L_y} u^2(x, y)\, \mathrm{d}y, \tag{5.2}$$

are shown in Figures 5.6 (a) and (b), where $U_x(x)$ has been normalized by the quantity $\max_x(U_x(x))$. It appears that a number of modes greater than $N = 800$ leads to a quite converged spatial distribution of the optimal response and forcing, whose streamwise components are shown in Figures 5.7 (a) and (b). One can observe that, for $N = 1300$, the optimal forcing is localized close to the separation point of the bubble leading to a response which is amplified along the shear layer and reaches a maximum after the reattachment point. Consequently, it could be argued that the optimal frequency and the corresponding response are well described by a limited number of modes despite the slow convergence of $R_{\max}$. In particular, such a slow convergence may be ascribed to the difficulty to recover the tilting of the initial perturbation upstream of the bubble by means of a reduced model based on a global modes expansion. Indeed, the action of the shear on structures tilted at $t = 0$ in the direction opposed to the mean flow may lead, through an Orr-mechanism, to an increase of the energy gain, as observed by Blackburn et al. (2008) by means of a direct optimal growth strategy. On the other hand, such a mechanism is not perfectly observed in the works by Åkervik et al. (2007) and Ehrenstein and Gallaire (2008), where a global modes expansion strategy is used. Furthermore, in the work by Åkervik et al. (2008) on a flat plate boundary layer it is demonstrated that the Orr-mechanism doesn't affect the value of the optimal response frequency but only the value of the maximum energy gain.

A further validation is also carried out with respect to the domain length. Although Figure 5.8 shows that the eigenvalue spectrum for base flow bf1 is influenced by the streamwise domain size, namely $L_x = 400$ (triangles), $L_x = 425$ (diamonds) and $L_x = 450$ (circles), the resulting resolvent is not. Figure 5.9 shows that the resolvent curves do not depend on the streamwise domain size, meaning that the overall sensitivity features of the flow are not influenced by the computational box.

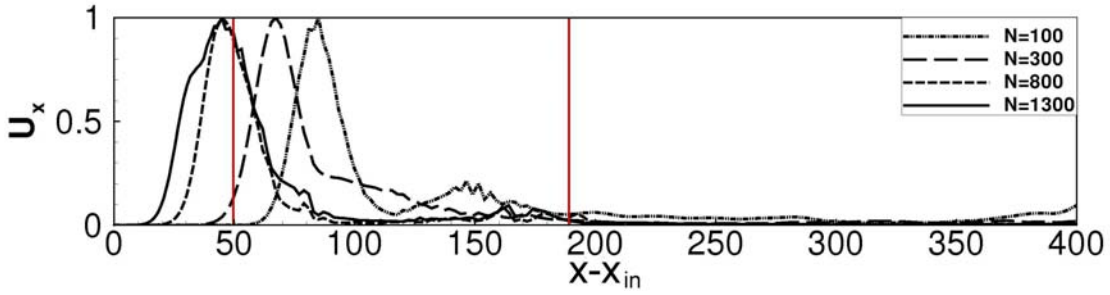

(a)

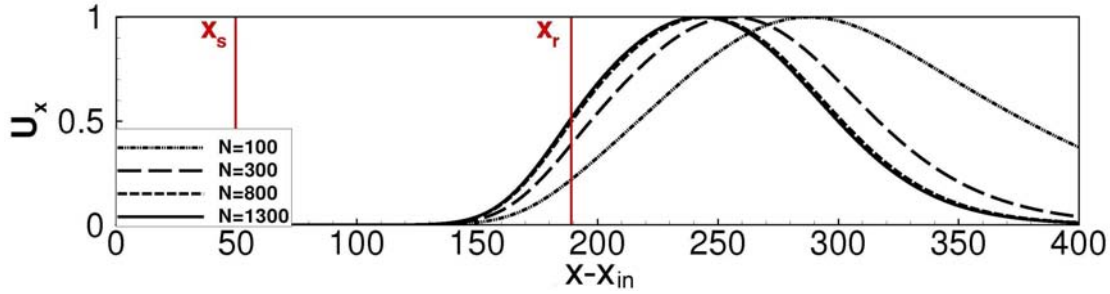

(b)

Figure 5.6: Influence of the number of modes N on the streamwise distribution of the optimal forcing (a) and the optimal response (b), represented by the variable $U_x(x)$ computed for bf1 and $L_x = 450$ with $N = 1300$ (solid line), $N = 800$ (dashed line), $N = 300$ (long-dashed line) and $N = 100$ (dashed-dotted line). The vertical lines correspond to the separation point and the reattachment point denoted by X_s and X_r, respectively.

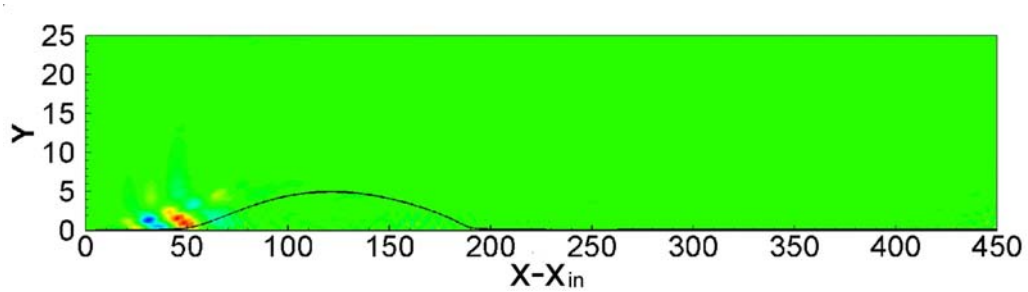

(a)

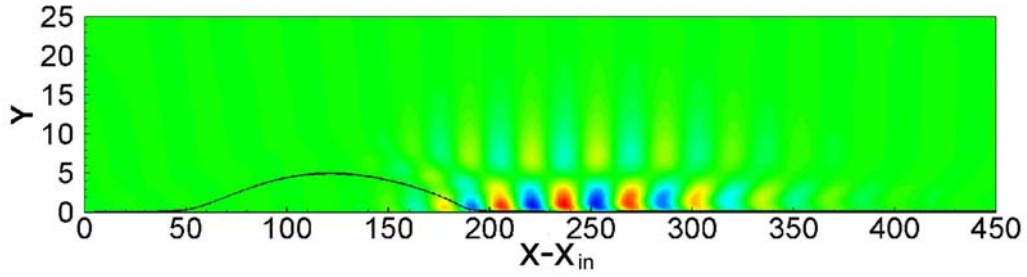

(b)

Figure 5.7: Streamwise component u of the optimal forcing (a) and response (b) computed for base flow bf1. The black line is the separation streamline.

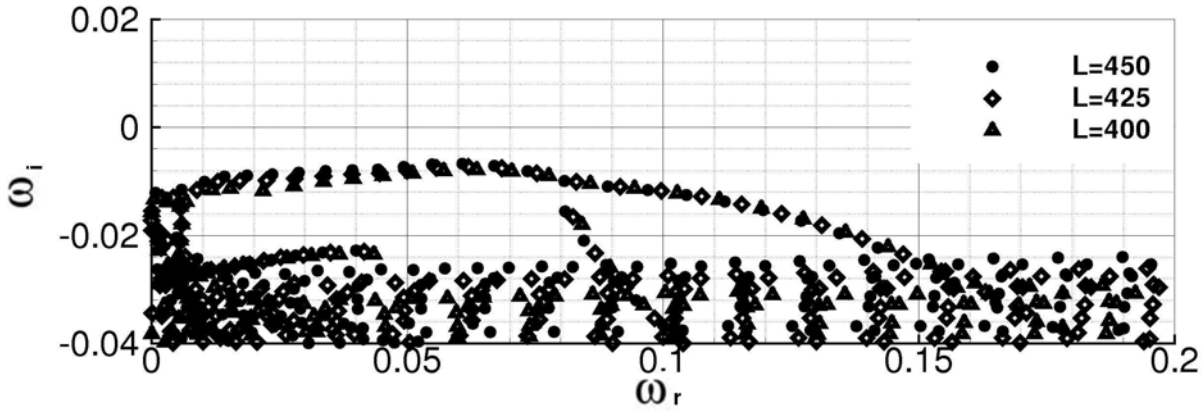

Figure 5.8: Influence of the computational box on the spectrum associated with bf1, for three different streamwise domain length, namely $L_x = 450$ (circles), $L_x = 425$ (diamonds) and $L_x = 400$ (deltas), discretized by $N_x = 270$, $N_x = 265$ and $N_x = 260$ grid points in the streamwise direction, respectively.

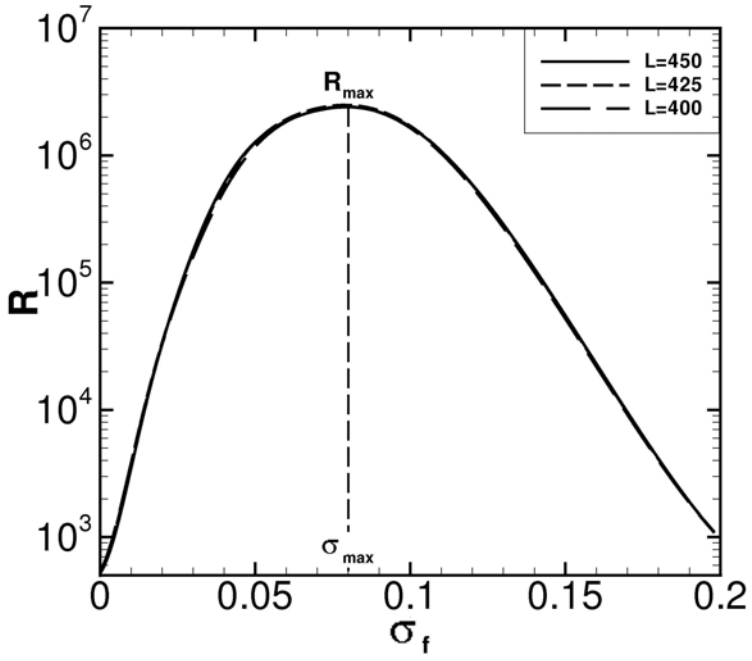

Figure 5.9: Resolvent $R(\sigma_f)$ obtained for bf1 with 1300 modes and for three different streamwise domain lengths, namely $L_x = 450$ (solid line), $L_x = 425$ (short-dashed line) and $L_x = 400$ (long-dashed line), discretized by $N_x = 270$, $N_x = 265$ and $N_x = 260$ grid points in the streamwise direction, respectively.

Finally, a validation of the previously discussed results is carried out by means of a perturbative linearized version of the NS equations in 3.1. The equations are written as follows:

$$\begin{aligned} \mathbf{u}_t + (\mathbf{U}\cdot\bigtriangledown)\mathbf{u} + (\mathbf{u}\cdot\bigtriangledown)\mathbf{U} &= -\bigtriangledown p + \frac{1}{Re}\bigtriangledown^2\mathbf{u} + \mathcal{F}, \\ \bigtriangledown\cdot\mathbf{u} &= 0, \end{aligned} \tag{5.3}$$

where $\mathcal{F}$ represents the forcing term, $\mathbf{U} = (U, V)^T$ is the two-dimensional base flow and $\mathbf{q} = (u, v, p)^T$ is the perturbation vector in the two-dimensional case. The boundary conditions which close the system (5.3) are identical to the ones used in the previous chapter.
The system has been forced with the optimal forcing field computed by the global model at two circular frequencies: $\sigma_f = 0.08$ and $\sigma_f = 0.13$. The instantaneous perturbation has been extracted from the DNS after the transient, and compared with the one resulting from the temporal modes expansion with $N = 1300$. Figures 5.10 (a) and (b) show that the linearized simulation results are in a very good agreement with the ones of the global eigenvalue analysis. Such a computation is a good validation of the temporal modes expansion which has been found to be an appropriate reduced model for the description of the optimal response to external forcing in the asymptotic regime. Being confident about the results derived from the present method, the physical destabilizing mechanism associated with the optimal response has been investigated.

Physical mechanism associated with the optimal response

In Figure 5.11 it is plotted the vector perturbation field (u, v) for $\sigma_{\max}$ in the asymptotic regime for bf3. One may observe that the action of the perturbation on the base flow originates a series of counter-rotating vortices along the shear layer and the decelerated zone. A visualization of the instantaneous vorticity field of the optimal response, $\breve{\omega}_z = \Omega_z + \varepsilon\omega_z$, where Ω_z is the vorticity of the base flow and where ε is fixed arbitrarily to 10% of the maximum value of U, is provided in Figure 5.12. The destabilizing mechanism associated with the most responsive disturbance described above leads to the formation of rolling vortices amplified along the shear layer which are advected in the attached boundary layer and dies away. Such process seems to be a specific feature underlying the optimal behaviour of separated flows, similar to the counter-rotating structures observed by Blackburn et al. (2008) in a flow over a backward facing step resulting from the optimal amplification of a localized wave packet.

In order to determine the effects of the size of the recirculation area on the values of $R(\sigma_f)$, the response curves are performed for the different base flows previously defined, as provided in Figure 5.13. One can observe the strong increase of the optimal response value $R_{\max}$ with the size of the recirculation zone which reaches a very high maximum energy gain of order $\approx 10^9$ for bf5. In particular, the most responsive frequency range is found to reduce when the Reynolds number and/or the pressure gradient at the upper boundary increases, leading to a more defined peak around $\sigma_{\max}$. Furthermore, Figures 5.14 (a), (b) and (c) show that the most responsive disturbance moves toward the end of the separated zone until reaching a maximum for bf4 at the reattachment point. An inviscid-type Kelvin-Helmholtz mechanism, similar to the one observed in separated flows

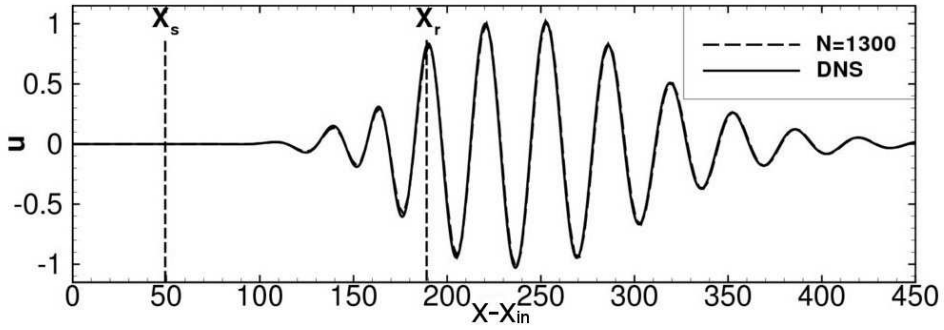

(a)

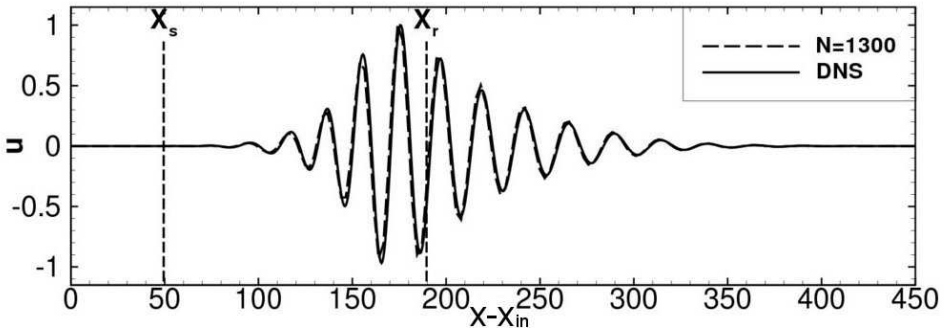

(b)

Figure 5.10: Values of the streamwise velocity u at $y = 8$, obtained by linearized DNS (solid line) and temporal modes expansion with $N = 1300$ (dashed line) for bf1, with a forcing of frequency $\sigma_f = 0.08$ (a) and $\sigma_f = 0.13$ (b). The vertical lines correspond to the separation point and the reattachment point denoted by X_s and X_r, respectively.

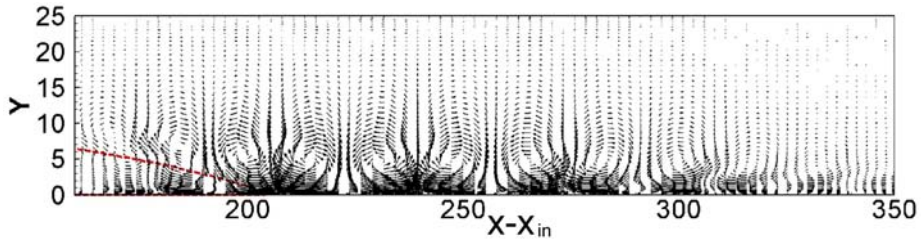

Figure 5.11: Perturbation vectors (u, v) obtained for bf3 and a forcing frequency $\sigma_{\max}$. The separation streamline is represented by the dashed line.

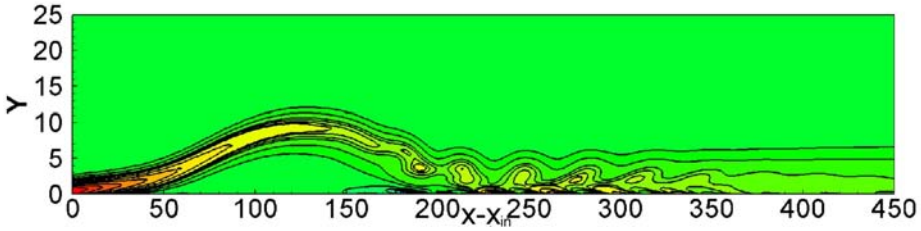

Figure 5.12: Snapshot of the instantaneous vorticity obtained asymptotically for bf3 and $\sigma_{\max}$ for a value of the perturbation equal to 10% of the maximum value of U.

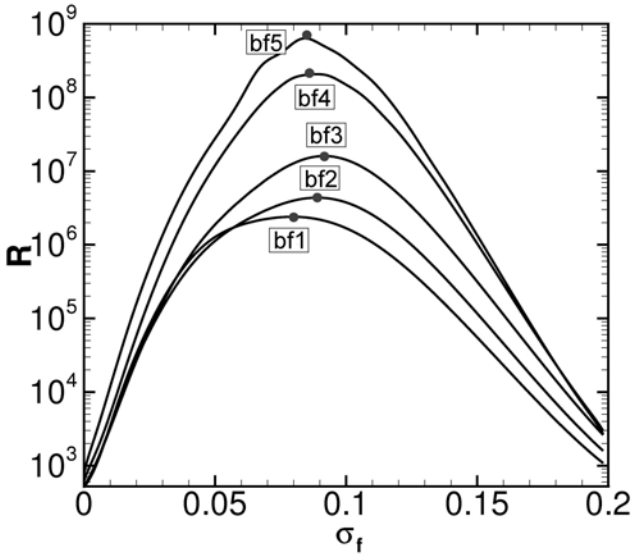

Figure 5.13: Evolution of $R(\sigma_f)$ for bf1, bf2, bf3, bf4 and bf5 (from bottom to top). The values of $\sigma_{\max}$ are sketched by the black dots.

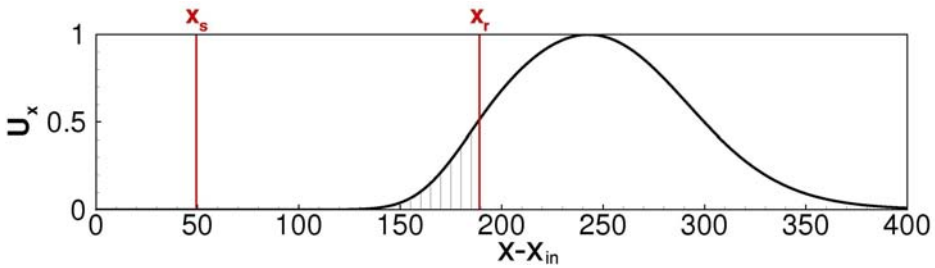

(a)

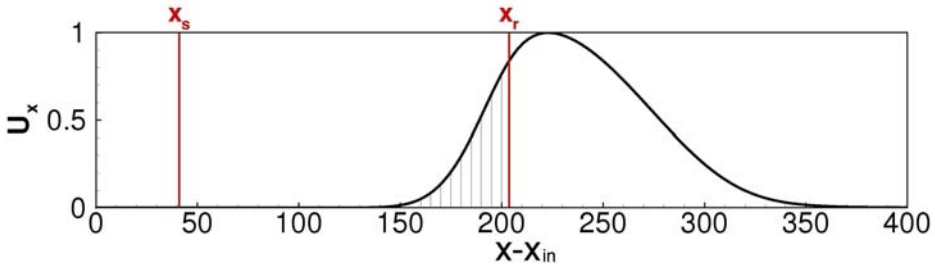

(b)

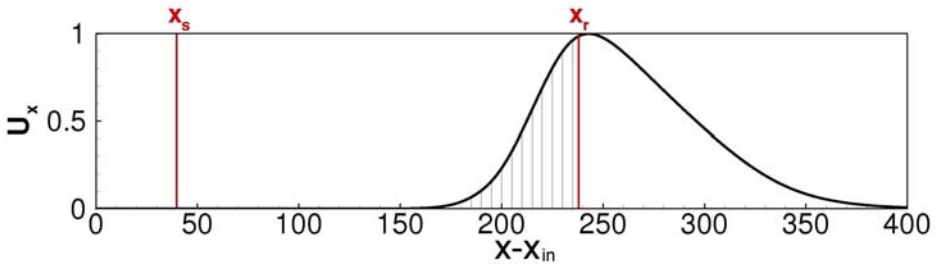

(c)

Figure 5.14: Streamwise distribution of the optimal response U_x for bf1 (a), bf3 (b) and bf4 (c).

by Lin and Pauley (1996) for instance, which results in the roll-up of the shear layer, appears to be the cause of the increase of the optimal response with respect to the bubble size.

5.2.3 The relation between the global optimal response and the onset of unsteadiness.

The analysis of the global response of the five flows has assessed that flat plate separated flows may exhibit a large response to a harmonic forcing for a range of frequencies at moderate Reynolds number. Indeed, the bubble may act as a selective amplifier of frequencies, due to the strong convectively unstable character of the flow.
A typical feature of recirculation bubbles is the onset of self-sustained oscillations characterized by the triggering of shedded vortices, as shown by the numerical simulations of Pauley et al. (1990), Ripley and Pauley (1993) and Wasistho et al. (1997), and by the experiments of Haggmark et al. (2000). Moreover, such flows are subject to a certain level of noise in experiments as well as in numerical simulations due to the discretization errors. Therefore, it is worth to investigate whether a connection exist between the emergence of coherent structures in the considered flow subject to noise and the amplifier dynamics related to the optimal response to forcing, which leads to the generation of counter-rotating structures, as previously discussed.
With this aim, the two-dimensional Navier-Stokes equations have been integrated by superposing a random noise with small amplitude (10^{-6}) to the base flow inlet velocities. Simulations are carried out for bf3 and bf5. First, the analysis has been focused on bf3. Figures 5.15 and 5.16 show a time series and a Fourier analysis of the vorticity component at the wall extracted at two different locations, the reattachment point $x = 204$ and $x = 262$, after that the simulation has reached a statistically stationary state. Although a white noise perturbation is imposed at the inflow, the Fourier spectra shown in Figures 5.16 (a) and (b) provide a narrow banded response whose peak is localized around $\sigma = 0.092$. This behavior is in agreement with the optimal response analysis realized in section 5.2.2. In particular, the peak and the range of excited pulsations are close to the predictions of the theoretical analysis based on a temporal modes summation.
The Fourier spectra relative to the largest bubble denoted by bf5 are shown in Figures 5.17 (a) and (b). Again, the corresponding spectral densities as well as the peak of intensity are consistent with the frequencies leading to an optimal response in the asymptotic regime provided in Figure 5.13. Thus, it could be hypothized that the amplification mechanism provided by the optimal response analysis is able to describe a possible scenario for the onset of unsteadiness in the considered separated flow. Under a sufficiently large pressure gradient and/or Reynolds number, even a two-dimensional globally stable separated flow, is able to select by means of sensitivity an optimal range of frequencies out of the existing numerical noise, generating optimal-like counter-rotating structures which can trigger a self-excited vortex shedding. This selective noise amplifier mechanism can be compared to the unsteadiness taking the form of Kelvin-Helmholtz-like shedded vortices observed in the asymptotic regime in numerical simulations of similar configurations by Pauley et al. (1990), Ripley and Pauley (1993) and Wasistho et al. (1997). Indeed, such authors have observed that under a sufficiently large pressure gradient, a strong unsteady behavior taking the form of self-excited vortex shedding occurs even at low Reynolds number

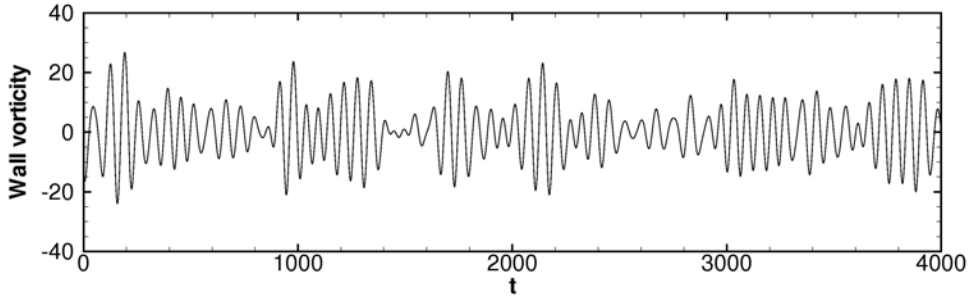

Figure 5.15: Evolution of the wall vorticity in time at the reattachment point $x = 204$ extracted from the DNS for bf3.

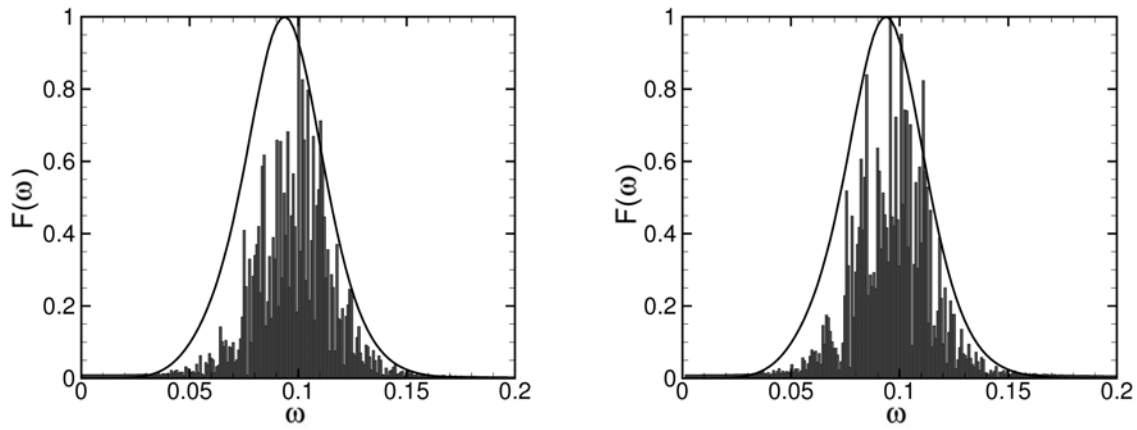

(a) (b)

Figure 5.16: Fourier spectrum in time of the wall-vorticity perturbation at the reattachment point, $x = 204$, (a) and at $x = 262$ (b) computed for bf3 by a DNS continuously perturbed at the inflow by a random noise with amplitude equal to 10^{-6}. The optimal response to a localized forcing for bf3 is represented by the black line.

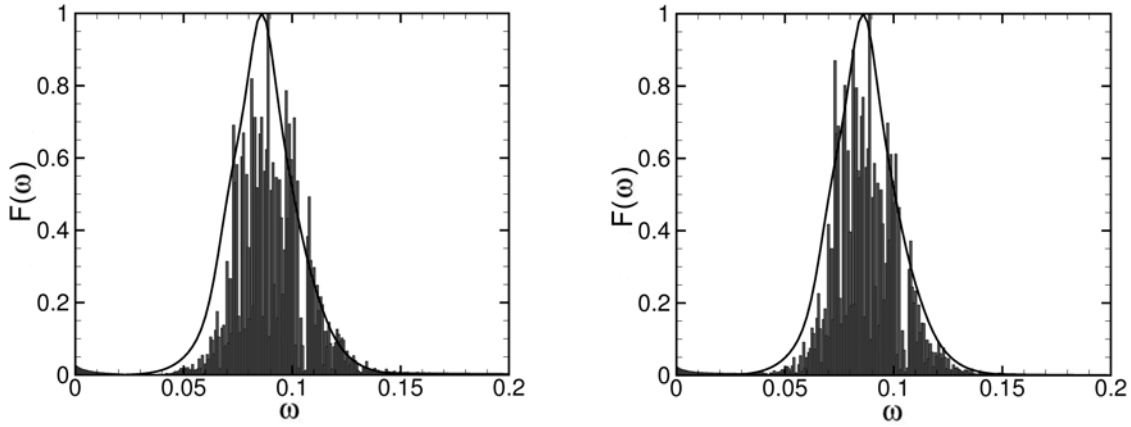

(a) (b)

Figure 5.17: Fourier spectrum in time of the wall-vorticity perturbation at the reattachment point, $x = 253$ (a), and at $x = 282$ (b) computed for bf5 by a DNS continuously perturbed at the inflow by a random noise with amplitude equal to 10^{-6}. The optimal response to a localized forcing for bf5 is represented by the black line.

($Re = 300$ for Pauley et al. (1990), and from 400 to 800 for Wasistho et al. (1997)). A natural generation of convective waves from the existing numerical noise is thus suggested by Wasistho et al. (1997) as an explanation.
Focusing on the relation between optimal response and the vortex shedding observed in previous investigations, a typical parameter characterizing the unsteadiness behavior has been computed. In particular, the shedding frequency non-dimensionalized by the boundary layer momentum thickness θ_s and the local freestream velocity U_∞ at the separation point with no applied gradient pressure has been considered, namely the Strouhal number:

$$S_{t\theta} = f\left(\frac{\theta_s}{U_\infty}\right) \tag{5.4}$$

where f denotes the shedding frequency. According to Pauley et al. (1990), Ripley and Pauley (1993) and Pauley (1994b) for flat plate separated flows or Lin and Pauley (1996) in an airfoil configuration, a typical Strouhal number associated with unsteadiness varies in the range 0.0055 to 0.008. It is worth to notice that such a value is not constant in the different configurations due to the dependence of the shedding frequency to the pressure distribution along the flat plate (Ripley and Pauley (1993)). Therefore, the shedding frequency is slightly geometry dependent.

The Strouhal numbers associated with the frequency leading to an optimal response are computed and summarized in table 5.2. Such values are found to be consistent with the ones obtained by the authors previously mentioned. In order to verify that the optimal response is able to trigger unsteadiness in the nonlinear regime, a larger white noise amplitude is superposed at inflow points in a direct numerical simulation. The base flow bf3 and an inflow perturbation of amplitude 10^{-5} are considered. After the transient, nonlinear saturation occurs. Figure 5.18 provides an instantaneous vorticity field showing the vortex-shedding behavior resulting from the selective noise amplifier

	θ_s	$\sigma_{\max}$	St_θ
bf1	0.508	0.08	0.00647
bf2	0.500	0.089	0.00708
bf3	0.489	0.092	0.00716
bf4	0.480	0.088	0.00673
bf5	0.477	0.084	0.00638

Table 5.2: Values of θ_s, σ_{max} and $S_{t\theta}$ at X_s for the five separated flows.

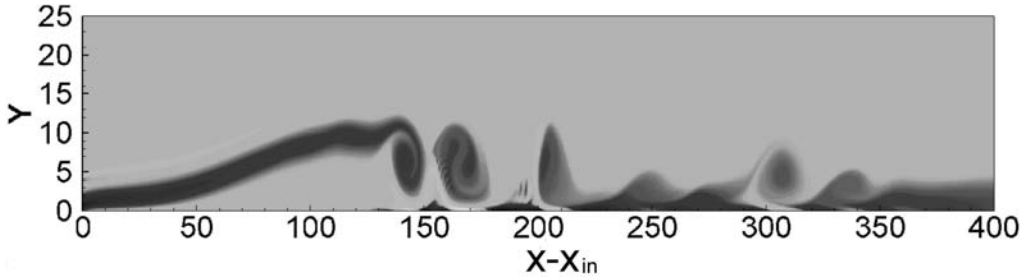

Figure 5.18: Instantaneous vorticity field from DNS subject to a random white noise at the inflow of amplitude 10^{-5} for bf3 at $T = 2000$.

mechanism at $t = 2000$. It is worth to notice the strong similarity between the resulting two-dimensional structures and the computations of previous investigations by Pauley et al. (1990), Ripley and Pauley (1993) and Wasistho et al. (1997).
Such results support the hypothesis that flat plate separated flows could act as a selective noise amplifier, whose selected frequencies could be recovered by an optimal response analysis; such amplifier behaviour leads to the onset of a self-excited vortex shedding phenomenon.

5.3 Discussion of the results

As argued by Marquet et al. (2008) and Blackburn et al. (2008), the amplifier dynamics predicted by an optimal growth analysis could yield a possible scenario explaining the onset of unsteadiness in separated flows under the influence of localized disturbances. Nevertheless, in this chapter a different point of view has been adopted, with the purpose of investigating whether a connection exists between the triggering of unsteadiness in the asymptotic regime and the selective noise amplifier behavior of the separated flows under consideration. For that purpose, the global linear response to a localized forcing leading to a maximum energy gain in the asymptotic regime has been studied, as well as the associated amplification mechanism and its connection with the onset of unsteadiness, for five different flat plate separated flows.
The global temporal modes approach has been found able to identify the instability mechanism related to the linear response to a harmonic forcing introduced into a laminar flat plate separated flow. In particular, it has been outlined a destabilizing mechanism involving the shear layer and inducing a strong amplification of disturbances at the selected fre-

quencies. Indeed, the most responsive disturbance takes the form of Kelvin-Helmholtz-like vortices, which roll up and amplify themselves along the shear layer, until being advected and die away in the attached boundary layer. The strong amplification of such harmonic perturbations could be explained by the pseudo-resonance of the temporal modes due to the high non-normality of the temporal evolution operator of the linearized Navier-Stokes equations. Moreover, an analysis of the evolution of the response, for an increase of the Reynolds number and/or the suction at the upper boundary, have clarified the strong influence of the shear layer on the maximum response.
Such elements suggest that flat plate separated flows may act as a strong selective noise amplifier. In order to find out if a connection exists between the global optimal response of the flow and the unsteadiness observed in experiments and direct numerical simulation, a DNS has been performed in which the base flow is continuously perturbed at inlet points with a random noise. The DNS results have shown that the selected frequencies recovered by Fourier transform in the asymptotic regime are in agreement with the amplified frequencies derived from the optimal response analysis. The most amplified frequency has been then compared with the shedding frequencies measured by Pauley et al. (1990), Ripley and Pauley (1993), Lin and Pauley (1996) and Wasistho et al. (1997). The Strouhal number recovered by the authors previously mentioned has been found consistent with the most amplified frequency of the global optimal response.
Thus, in this part of the thesis a connection has been established between the global optimal response to external forcing and the onset of vortex shedding and unsteadiness at subscritical Reynolds numbers in presence of low-level noise in a separated boundary layer flow.

6

The onset of three-dimensional centrifugal global modes in a separated boundary layer

In the previous chapter it has been demonstrated that flat plate separated flows may act as a strong selective noise amplifier. Moreover, a connection has been established between the response of the flow to an external forcing (either induced or present in the background noise) and the onset of unsteadiness and vortex shedding observed in experiments and direct numerical simulations (see Pauley et al. (1990) and Wasistho et al. (1997), for instance). Nevertheless, as discussed in Chapter 2, a resonator dynamics could occur in separated flows, which is associated with a three-dimensional global steady unstable mode. This global mode has been observed for the first time in a flat plate separated flow by Theofilis et al. (2000), and in an experimental framework for a flow past a backward-facing step by Beaudoin et al. (2004). Thus, it can be supposed that such three-dimensional mechanism could appear in the considered flow and dominate its asymptotic space-time dynamics.

Altough many studies have been devoted to the primary three-dimensional instability of separated flow in a linear framework (see Barkley et al. (2002), Gallaire et al. (2007) and Marquet et al. (2009) for instance), none of them has clarified whether this asymptotical mechanism would dominate the dynamics of the flow or if it would be bypassed by the transient one due to the high sensitivity of the flow to disturbances. Therefore, an analysis of the onset and origin of such unstable three-dimensional mode and of its interaction with the KH/TS mechanism of amplification of the disturbances along the shear layer, is of interest.

Thus, by means of the three-dimensional global eigenvalue analysis, the steady unstable mode is recovered, together with several stable three-dimensional ones affecting the dynamics of the flow. Such modes are analyzed by means of two different centrifugal instability analysis (the Rayleigh criterion and the Gortler equations). Finally, direct numerical simulations are carried out aiming at identifying the onset of such global modes in the instability dynamics of the flow, and at understanding their role in the transition process at small and large times.

This part of the thesis has been developed in cooperation with Dr. F. Alizard (Arts et Métiers ParisTech, France), and it has been submitted for publication to Physics of Fluids in February 2010.

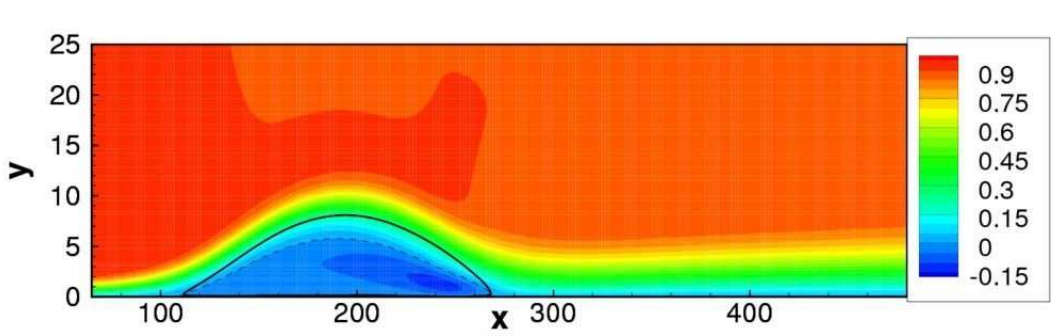

Figure 6.1: Streamwise velocity contours for the base flow bf3 at $Re = 200$. The solid line is the separation streamline, whereas the dashed line represents the $u = 0$ contour.

6.1 Problem formulation

A rectangular computational domain is employed, having dimensions $L_x = 425$, $L_y = 30$, $L_z = 62.8$. For the base flow computation and the DNS, at inlet points, placed at $x_{in} = 65$ from the leading edge of the bottom wall, a Blasius boundary-layer profile is imposed for the streamwise and wall-normal components of the velocity vector, and the spanwise component is set to zero. At outlet points, a standard convective condition is employed. At the bottom wall, the no-slip boundary condition is prescribed. At the upper boundary, three different suction-and-blowing profiles have been imposed on the wall-normal velocity component, and the spanwise component and the vorticity are set to zero. Three base flows, bf1, bf2 and bf3, have been obtained by imposing the three suction-and-blowing profiles of Chapter 5, shown in Figure 5.1. Most of the computations would be performed on the base flow bf3. Finally, in the spanwise direction, periodicity is imposed for the three velocity components. All numerical simulations have been performed discretizing the computational domain by a Cartesian grid stretched in the wall-normal direction. The computational domain contains $501 \times 150 \times 81$ grid points, the height of the first cell close to the wall being equal to 0.1.
The three-dimensional global eigenvalue analysis is employed, where β and the spanwise component of the perturbation are chosen to be different from zero. At upper and inlet boundary points, a zero perturbation condition is imposed, whereas at the outflow a Neumann condition is prescribed. The base flow is discretized using $N_x = 230$ collocation points in the x-direction and $N_y = 47$ collocation points in the y-direction. For the transient growth computations, $N = 1500$ modes have been employed.

6.2 Linear dynamics using the three-dimensional global eigenvalue analysis

6.2.1 Spectrum analysis

Figure 6.1 shows the streamwise velocity contours for bf3 at $Re = 200$. For such a base flow and $\beta = 0.1$, the three-dimensional global eigenvalue analysis provides the spectrum

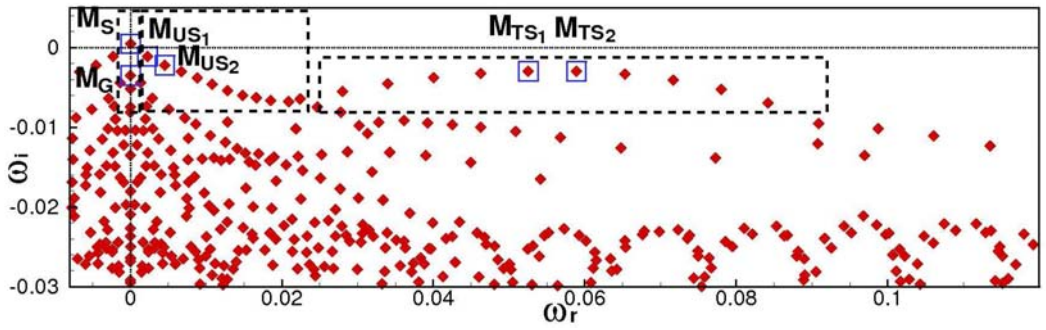

Figure 6.2: Spectrum associated with the base flow bf3 for $\beta = 0.1$. The dashed rectangles identify the different families of modes.

shown in Figure 6.2, which is found to be unstable. The spectrum is different from the two-dimensional one provided in Figure 4.4. Different families of modes can be detected, some of them having a very low growth rate. The three most amplified families, enclosed in the dashed rectangles in Figure 4.4, are here considered. Two modes for each family are analyzed, namely, M_S and M_G for the steady-modes family; M_{US_1} and M_{US_2}, placed on the branch of the unsteady low-frequency modes; M_{TS_1} and M_{TS_2}, placed on the convective branch. All of these modes are found to be relevant in the dynamics of the flow, as shown in the following sections.

The asymptotic behavior of the flow is driven by the most unstable mode, labelled M_S in Figure 4.4, which is a three-dimensional steady mode ($\omega_r = 0$), similar to the unstable weakly growing mode found in Theofilis et al. (2000) for a three-dimensional separated flow induced by an adverse pressure gradient. The contours of the streamwise and spanwise velocity components of such a mode can be observed in Figures 6.3 (a) and (b), respectively, showing that a great part of the perturbation is concentrated within the bubble. Figure 6.3 (c) provides the contours of the local energy, defined as $e = u^2 + v^2 + w^2$; one could notice that the energy is concentrated within the recirculation zone. In the spanwise direction, such a mode take the form of alternated flat roll structures, which follow the curvature of the streamlines of the base flow, as shown by the spanwise vorticity iso-surfaces in Figure 6.4 (a). Similar modes have been recovered in several separated flows induced by the geometry of the flow, such as a step (Barkley et al., 2002, Marquet et al., 2009, Marino and Luchini, 2009) or a bump (Gallaire et al., 2007).

The less stable steady mode is the one labelled M_G in Figure 4.4. Figure 6.4 (b) shows that its spanwise vorticity distribution presents some similarities with the one of mode M_S, being characterized by flat roll structures following the curvature of the streamlines. Therefore it can be supposed that both these three-dimensional global modes could have a common origin, which could be linked to a centrifugal instability (Gallaire et al., 2007), being both strongly affected by the curvature of the streamlines. On the other hand, the two modes present some differences, as shown in Figure 6.5, which provides the local energy contours of mode M_G. By comparing such a Figure with Figure 6.3 (c), one can observe that a great part of the energy is concentrated in the attached zone and in the shear layer; not within the bubble as it has been previously found for mode M_S. Thus,

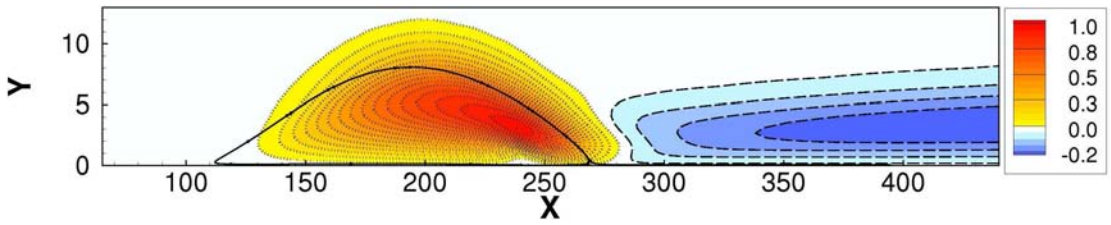

(a)

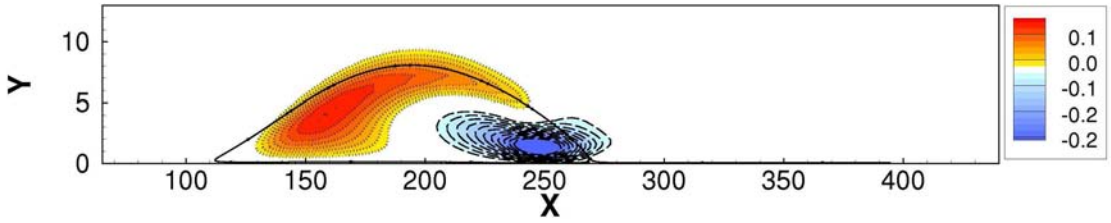

(b)

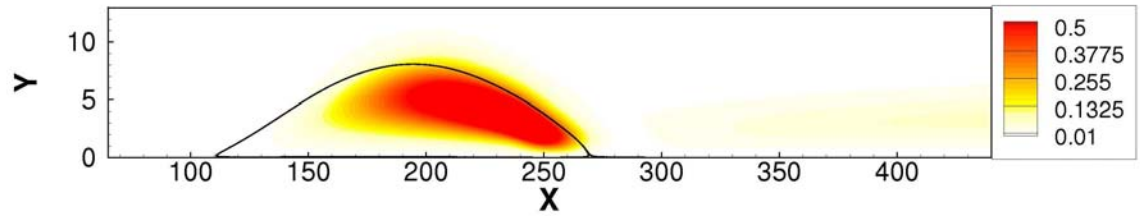

(c)

Figure 6.3: Contours of the streamwise (a) and spanwise (b) velocity perturbation normalized by the maximum value of the streamwise velocity, and of the local energy, e, (c) normalized by its maximum value, for the unstable steady mode (M_S) at $Re = 200$. The black line is the separation streamline, whereas dashed contours represent positive velocities and dotted contours represent negative velocities.

M_S is mainly located inside the bubble, whereas M_G has a strong spatial development, as one can also observe by comparing Figures 6.4 (a) and (b).
The second family of modes is characterized by the low-frequency unsteady eigenvalues shown in the second (from left to right) dashed rectangle of Figure 4.4. The spanwise velocity component of the modes labeled as M_{US1} and M_{US2} are provided in Figures 6.6 (a) and (b), respectively. Such modes are characterized by streamwise-alternated sickle-shaped packets, which are localized within the separation bubble, mostly in its upstream part. One can notice that the two modes have a similar shape, but the second one is characterized by structures of smaller wavelength. It is noteworthy that, in the two-dimensional spectrum computed for the same base flow, shown in Chapter 4 (see Figure 4.4), the first two families of modes are not recovered. Thus, it is possible to infer that modes M_S, M_G, M_{US1}, and M_{US2} are purely three-dimensional, since they are not

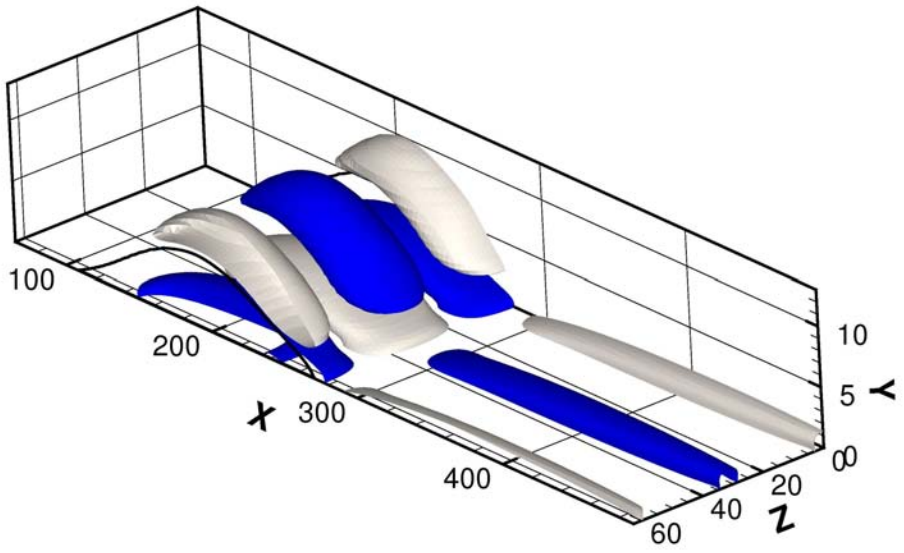

(a)

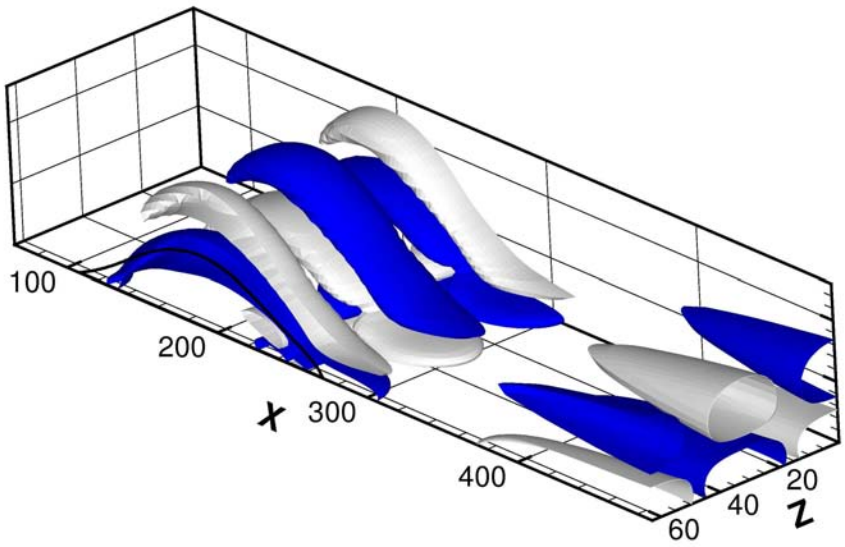

(b)

Figure 6.4: Iso-surfaces of spanwise vorticity for the most amplified steady modes M_S (a) and M_G (b) at the Reynolds number $Re = 200$. The black line is the separation streamline, whereas the dark and light surfaces represent the 0.15 and -0.15 values of spanwise vorticity, respectively. The perturbations have been normalized by their maximum value.

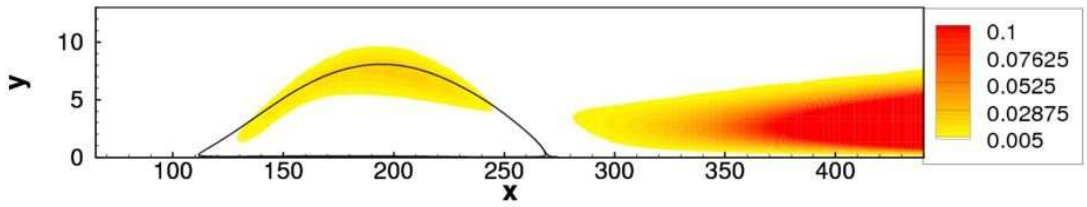

Figure 6.5: Local energy e of the second most amplified steady mode, M_G, at the Reynolds number $Re = 200$. The black line is the separation streamline.

recovered by a two-dimensional analysis which does not take into account the spanwise dynamics.
The third family of modes, which is recovered also in a two-dimensional case, is characterized by the high-frequency unsteady modes placed on the 'convective branch', shown in the third (from left to right) dashed rectangle of Figure 4.4. Such eigenvalues are reminiscent of the classical KH/TS modes predicted by a local approach (Schmid and Henningson, 2001), although they appear to be slightly tilted in the streamwise direction, as one can observe in Figure 6.7, providing the streamwise velocity contours of mode M_{TS_1}. The dynamics of such highly non-normal modes, which are the ones responsible for the strong amplifier dynamics of the bubble, has been extensively studied in the two previous Chapters for a two-dimensional case.

6.2.2 Analysis of centrifugal modes

In the previous subsection it has been conjectured that modes M_S and M_G could both have a centrifugal origin, due to the flat roll structure they show. However, the mechanism of their generation could differ, since they are characterized by a different distribution of the energy. In particular, M_S could be originated by an intrinsic centrifugal instability, due to the curvature of the streamlines within the separated zone, as conjectured by previous authors such as Barkley et al. (2002) and Gallaire et al. (2007), in the case of a geometry-induced separation bubble, whereas the stable mode M_G seems to have a convective nature similar to a Gortler instability. Indeed, some authors (see Inger (1987)) have conjectured that a weak concave streamline curvature occurring around a separation bubble may give rise to a Gortler instability despite the absence of curved walls. Moreover, Pauley (1994a) and Wilson and Pauley (1998) observed the onset of Gortler vortices in the case of the flow past a laminar separation bubble over a flat plate. In order to verify such conjectures about the origin of modes M_S and M_G, two different analysis are here proposed. Concerning mode M_S, a generalized form of the Rayleigh criterion provided by Sipp and Jacquin (2000) is used, whereas for mode M_G, a Gortler stability study is performed.

Rayleigh's criterion (see Drazin and Reid (1981), Bayly (1987)) is an inviscid condition for centrifugal instability. Such a criterion is based on the physical consideration that in a

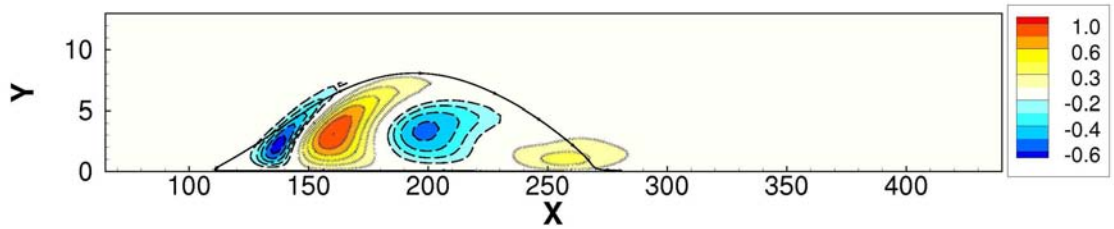

(a)

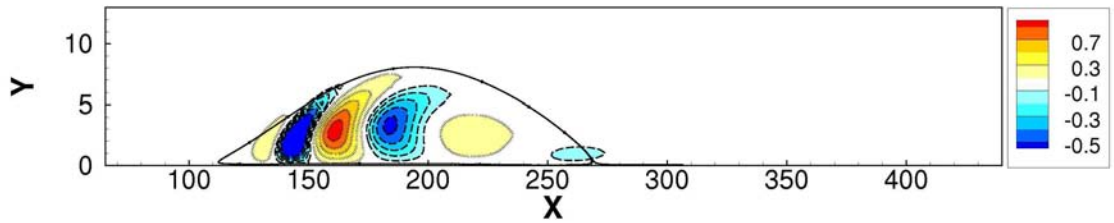

(b)

Figure 6.6: Spanwise velocity contours of the most amplified non-steady modes (M_{US1} and M_{US2}) at the Reynolds number $Re = 200$. The black line is the separation streamline, whereas dashed contours represent positive velocities and dotted contours represent negative velocities.

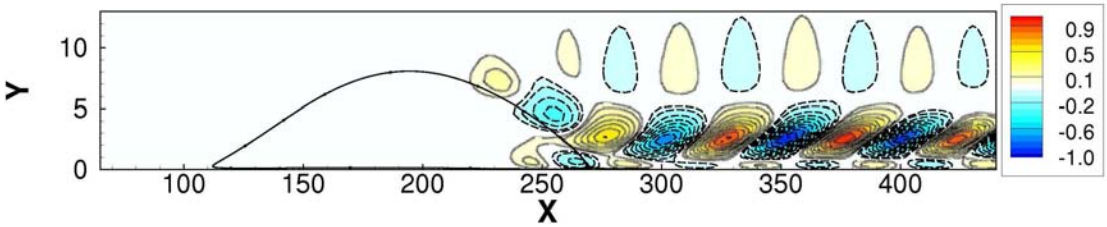

Figure 6.7: Streamwise velocity contours of mode M_{TS1} on the convective branch, at the Reynolds number $Re = 200$. The black line is the separation streamline, whereas dashed contours represent positive velocities and dotted contours represent negative velocities.

flow with closed streamlines, instability could be originated if there is an outward decrease in the angular momentum of the base flow. A sufficient condition for instability, based on a generalization of such a criterion to generic closed streamlines, has been provided by Sipp and Jacquin (2000) for a two-dimensional inviscid flow. In order to identify the centrifugal zones inside the recirculation region, the Rayleigh discriminant $\Delta(\mathbf{x})$ is defined as follows:

$$\Delta(\mathbf{x}) = 2\left(\frac{|\mathbf{U}(\mathbf{x})|}{\varrho(\mathbf{x})}\right)\varpi(\mathbf{x}), \tag{6.1}$$

where $\mathbf{x}$ is a point of the considered streamline, ϕ; $|\mathbf{U}(\mathbf{x})|$ is the norm of the base flow velocity; $\varpi(\mathbf{x}) = V_x - U_y$ is the spanwise base flow vorticity; and $\varrho(\mathbf{x})$ is the local algebraic radius of curvature of the streamline, defined as:

$$\varrho(\mathbf{x}) = \frac{|\mathbf{U}(\mathbf{x})|^3}{(\bigtriangledown\phi)\cdot(\mathbf{U}(\mathbf{x})\cdot\bigtriangledown\mathbf{U}(\mathbf{x}))}. \tag{6.2}$$

The flow is unstable if a closed streamlines, ϕ_0, exists such that:

$$\max_{\phi_0}(\Delta(\mathbf{x})) < 0, \tag{6.3}$$

where $\max_\phi$ denotes the maximum over the streamline ϕ . It is worth to notice that such a criterion compares the sign of the absolute angular velocity of the particle ($|\mathbf{U}(\mathbf{x})|/\varrho(\mathbf{x})$) to the sign of its vorticity $\varpi(\mathbf{x})$, so that the flow is unstable if these quantities have opposite signs along a whole streamline ψ_0 (Sipp and Jacquin, 2000).

The Rayleigh discriminant has been computed for the base flow here considered and is shown in Figure 6.8. Five centrifugal zones are recovered, defined by the negative values of the Rayleigh discriminant; the three of them which are placed within the bubble, namely, Z_1, Z_2, and Z_3, are analyzed. Recalling that criterion (6.3) is only a sufficient condition for instability, it is possible to point out that, even if no closed streamline has been recovered along which the Rayleigh discriminant remains negative, the fluid particles which follow closed streamlines within the recirculation zone, would periodically pass through these centrifugal zones, so that they could feel the effect of the instability, especially close to the wall where the lowest values of the Rayleigh discriminant are recovered (in Z_2). The large curvature of the streamlines would cause the perturbation to be displaced away from the centre of the bubble, where the presence of the wall would force it to move in the spanwise direction, inducing the formation of the roll structures observed in Figure 6.4 (a).

The Rayleigh discriminant has been computed also for base flows bf2 and bf1, which have the same Reynolds number of bf3 and a blowing and suction wall-normal velocity of smaller intensity (see Figure 5.1). The Rayleigh's discriminant contours for the base flows bf2 and bf1 are shown in Figure 6.8 (b) and (c), respectively. By comparing Figures 6.8 (a), (b) and (c), one could notice that for smaller bubbles, the spatial extent of the centrifugal zones Z_1, Z_2 and Z_3 decreases, and the minimal value of $\Delta(x)$ within the bubble is found to increase from $-3.8\cdot10^{-5}$ (for bf3) to $-6.9\cdot10^{-6}$ (for bf1). The amplification rate of mode M_S has been computed for all of the base flows, and is provided in Figure 6.9 as a function of the minimum value of the Rayleigh discriminant within the bubble. One can observe that the amplification rate decreases when the Rayleigh discriminant increases, meaning that a correlation exists between the intensity of the centrifugal mechanism and

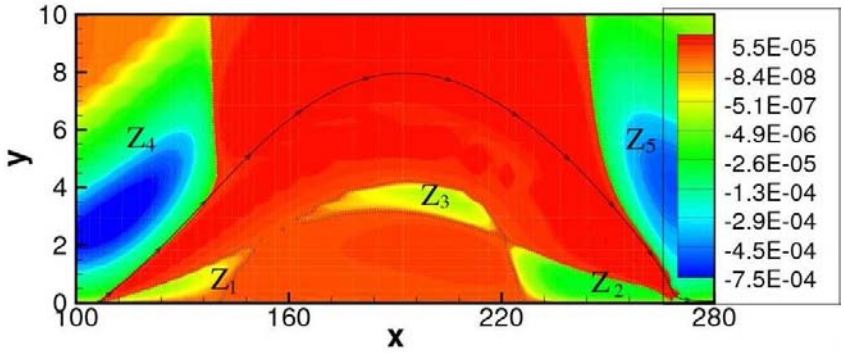

(a)

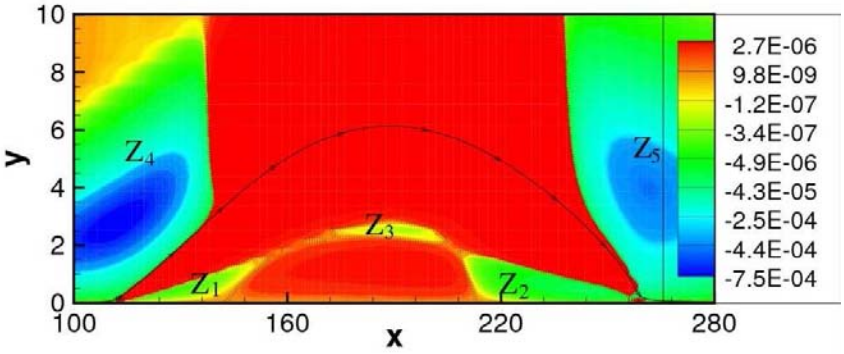

(b)

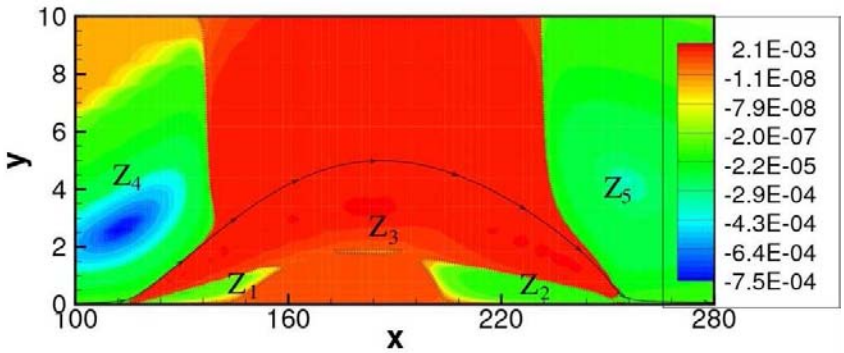

(c)

Figure 6.8: Rayleigh's discriminant contours for bf3 (a), bf2 (b) and bf1 (c). The black line is the separation streamline, whereas the dotted line is the zero discriminant contour. The three centrifugal zones within the bubble are labelled as Z_1, Z_2 and Z_3, whereas the centrifugal zones outside the bubble are labelled as Z_4 and Z_5.

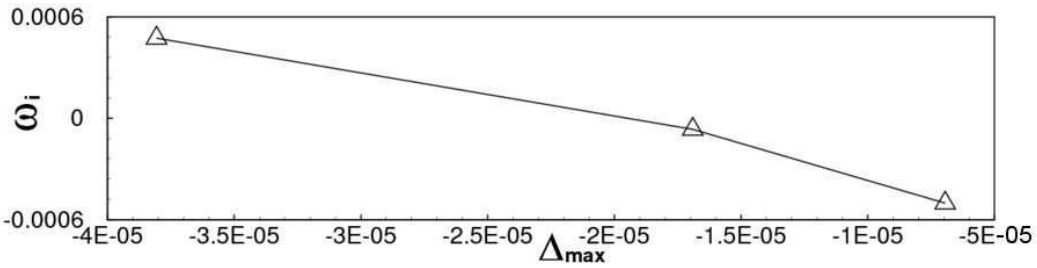

Figure 6.9: Values of the amplification rate of mode M_S versus the minimal value of the Rayleigh discriminant for base flows bf3, bf2 and bf1, from left to right.

the onset of mode M_S. Finally, it is worth to point out that Gallaire et al. (2007) have given a proof of the centrifugal origin of the three-dimensional primary instability affecting the separated flow over a bump. In such a work the authors have computed, by means of a viscous extention of the WKB method, the net amount of growth rate along the closed streamline within a separation bubble presenting three centrifugal zones inside the bubble not satisfying the Rayleigh's criterion. Indeed, it is likely that the same instability mechanism could act in the separated flow here considered, whose centrifugal zones strongly resemble in shape and location the ones described by Gallaire et al. (2007).

Concerning mode M_G, a Gortler analysis has been performed for the streamlines past the bubble. At this purpose, the formalism of Hall (1982) has been followed, which was proposed to study the influence of the curvature of the wall on the instability dynamics of a three-dimensional boundary layer. It is straightforward that, in the case under consideration, no curved wall is present, but it has been conjectured that the curvature of the streamlines past the separation bubble could have a similar effect on the instability of the boundary layer. Thus, a local cylindrical coordinate system $(\bar{x};\ \bar{y};\ \bar{z})$ has been defined along a streamline, ϕ_G, past the separated zone (see Figure 6.10 (a)), namely:

$$\begin{cases} \bar{x} &= \Theta\varrho \\ \bar{y} &= (r-\varrho)\sqrt{Re} \\ \bar{z} &= z\sqrt{Re} \end{cases}, \tag{6.4}$$

where ϱ is the local radius of curvature, Θ is the azimuthal coordinate, and r is the radial one. The variables $\bar{y}$ and $\bar{z}$ have been scaled with the square root of the Reynolds number in order to account for the different scaling of the boundary layer coordinates; for the same reason, the following non dimensional velocities have been defined:

$$(\bar{u},\bar{v},\bar{w}) = (u_\Theta, v_r\sqrt{Re}, w\sqrt{Re}), \tag{6.5}$$

where u_Θ and v_r are the velocities along the azimuthal and radial coordinates Θ and r, respectively. Since the instability is expected to be steady and three-dimensional, the perturbation has been considered sinusoidal in the spanwise direction, namely:

$$(\bar{u},\bar{v},\bar{w},\bar{p}) = (\tilde{u}cos(\beta z), \tilde{v}cos(\beta z), \tilde{w}sin(\beta z), \tilde{p}cos(\beta z)). \tag{6.6}$$

By assuming that the instability has an inviscid nature and that the curvature is small, one can obtain the linearized equations governing the evolution of a perturbation evolving on the base flow $(\bar{U}, \bar{V}, 0)$ as follows:

$$\frac{\partial \tilde{u}}{\partial \bar{x}} + \frac{\partial \tilde{v}}{\partial \bar{y}} + \beta \tilde{w} = 0 \tag{6.7a}$$

$$\bar{U}\frac{\partial \tilde{u}}{\partial \bar{x}} + \frac{\partial \bar{U}}{\partial \bar{x}}\tilde{u} + \bar{V}\frac{\partial \tilde{u}}{\partial \bar{y}} + \frac{\partial \bar{U}}{\partial \bar{y}}\tilde{v} = \frac{\partial^2 \tilde{u}}{\partial \bar{y}^2} - \beta^2 \tilde{u} \tag{6.7b}$$

$$\bar{U}\frac{\partial \tilde{v}}{\partial \bar{x}} + \frac{\partial \bar{V}}{\partial \bar{x}}\tilde{u} + \bar{V}\frac{\partial \tilde{v}}{\partial \bar{y}} + \frac{\partial \bar{V}}{\partial \bar{y}}\tilde{v} + \frac{\partial \tilde{p}}{\partial \bar{y}} + G\bar{U}\tilde{u} = \frac{\partial^2 \tilde{v}}{\partial \bar{y}^2} - \beta^2 \tilde{v} \tag{6.7c}$$

$$\bar{U}\frac{\partial \tilde{w}}{\partial \bar{x}} + \frac{\partial \bar{U}}{\partial \bar{x}}\tilde{w} + \bar{V}\frac{\partial \tilde{w}}{\partial \bar{y}} + \frac{\partial \bar{V}}{\partial \bar{y}}\tilde{w} - \beta \tilde{p} = \frac{\partial^2 \tilde{w}}{\partial \bar{y}^2} - \beta^2 \tilde{w} \tag{6.7d}$$

where $G = 2\delta^* \sqrt{R}e/\varrho$ is the Gortler number, characterizing the influence of the curvature with respect to the viscous effects. For computational purposes, the variables $\bar{p}$ and $\bar{w}$ have been eliminated. Following Hall (1982), an equation for $\bar{u}$ and $\bar{v}$ has been recovered from equations (6.7a), (6.7c), and (6.7d), whereas equation (6.7b) has been left untouched. The system has been thus reduced to a pair of equations for the variables $\bar{u}$ and $\bar{v}$, which have been integrated marching in the $\bar{x}$ direction by a fourth-order-accurate Runge–Kutta scheme. The space marching has been initialized at $x_{0_G} = 200$. Previous studies (Saric (1994), Goulpié et al. (1996)) have shown that, in the space marching problem under consideration, the spatial evolution of the perturbation is strongly dependent on the initial velocity profile imposed at the inlet points. Thus, in order to allow a meaningful comparison with the results of the global eigenvalue analysis, the inlet wall-normal and streamwise components of the perturbations have been chosen to be equal to the velocity profile extracted at $x = 200$ from mode M_G computed by the global eigenvalue analysis.

The Gortler equations have been integrated for different values of β, Figure 6.10 (b) showing the streamwise component of the perturbation for $\beta = 0.17$. Such a perturbation has been found very similar to the global mode M_G, which is provided in Figure 6.10 (a) for $\beta = 0.17$, for comparison. The spanwise vorticity perturbation, provided in Figure 6.11, shows that the perturbation obtained by the Gortler model presents the same flat roll structure of the global mode M_G, indicating that the mechanism underlying the onset of such longitudinal vortex is of the Gortler type. As a further validation, the spatial amplification of the perturbation has been analyzed by computing the streamwise local energy

$$E_x(\bar{x}) = \int_0^{\bar{L}_z} \int_0^{\bar{y}_{max}} \left(\bar{u}^2 + \bar{v}^2 + \bar{w}^2\right) d\bar{y} d\bar{z}. \tag{6.8}$$

following the streamline ϕ_G. For both the Gortler approximation and the global analysis, the largest value of the spatial energy gain $E_x(\bar{x})/E_x(x_{0_G})$ is recovered slightly downstream of the reattachment point, close to the point where the maximum value of G is attained, reaching a value close to 5.6. Moreover, both solutions present a positive slope at the outlet of the domain, namely $\partial E_x(\bar{x})/\partial \bar{x} \approx 0.0345$ for the Gortler approximation and $\partial E_x(\bar{x})/\partial \bar{x} \approx 0.0234$ for the global perturbation, with $\beta = 0.17$. Such a spatial amplification of the energy on the attached boundary layer induces the generation of

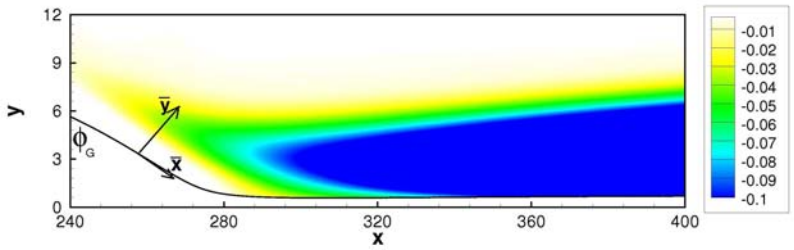

(a)

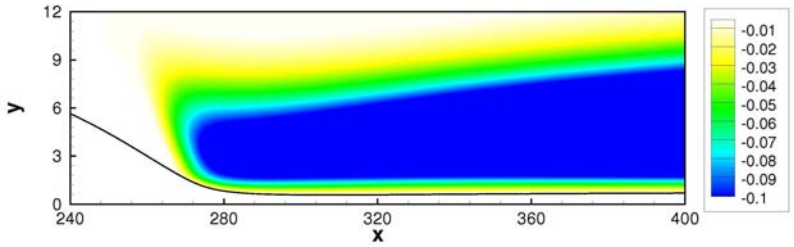

(b)

Figure 6.10: Streamwise component of velocity represented over the streamline ϕ_G for the global mode M_G (a) and for the perturbation resulting from the space integration of the Gortler equations (b).

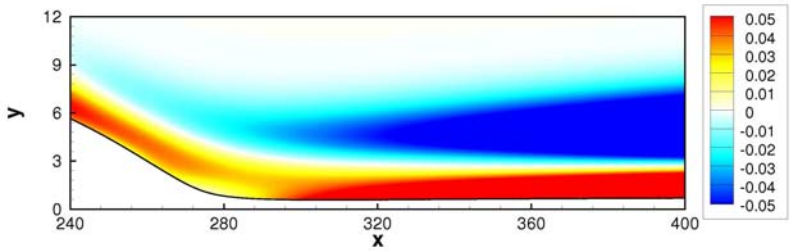

(a)

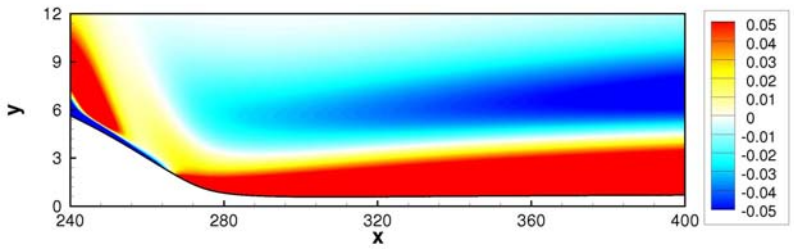

(b)

Figure 6.11: Spanwise vorticity perturbation represented over the streamline ϕ_G for the global mode M_G (a) and for the perturbation resulting from the space integration of the Gortler equations (b).

the streamwise vortices shown in Figure 6.10 and 6.11. The maximum value of such an amplification has been measured at $\beta = 0.19$ for the spatially developing perturbation computed with the Gortler approximation.

6.2.3 Spanwise analysis

Once clarified the physical mechanisms connected to the onset of the two steady global modes under consideration, M_S and M_G, the influence of the spanwise wavenumber, β, on the amplification rate of such modes is investigated. Several spectra have been computed for the base flow BF1, for different values of β. Figures 6.12 (a), (b), (c) and (d) show the curves of the amplification rate, ω_i, versus the spanwise wavenumber, β, for modes M_S, M_{US1}, M_G and M_{TS_1}, respectively. The amplification rate of the modes M_S and M_{US_1} is shown only for $0.03 \leq \beta \leq 0.28$, whereas, for M_G, it is shown for $0.03 \leq \beta \leq 0.22$. This is due to the fact that the steady three-dimensional modes change their nature becoming a complex pair of unsteady modes, when the spanwise length of the domains becomes too narrow or too large (see Barkley et al. (2002)). It is noteworthy that the amplifications rates of such unsteady modes is considerably lower than the ones of their steady homologus.
In Figure 6.12 (a), one can notice that mode M_S is unstable for $0.038 \leq \beta \leq 0.22$. Such a mode reaches the maximum amplification rate for $\beta = 0.1$ (hereafter called the most amplified spanwise wavenumber for mode M_S, $\beta_{S_{max}}$). The amplification rate of mode M_{US1} achieves its maximum for the same value of β but, unlike mode M_S, it is always stable, as shown in Figure 6.12 (b). Finally, mode M_G presents an higher value of the most amplified spanwise wavenumber, namely $\beta_{G_{max}} = 0.17$. Such a discrepancy could be a consequence of the different nature of the two steady modes, the first one (M_S) having an intrinsic origin, the second one (M_G) arising from a convective mechanism. Indeed, it is worth to point out that the peak of the spatial amplification of the perturbation computed with the Gortler approximation was recovered for $\beta = 0.19$, which is not far from the value of β providing the maximal temporal amplification of mode M_G. This is a further validation of the Gortler convective nature of mode M_G. Concerning the growth rate of the most amplified Tollmienn-Schlichting mode M_{TS_1}, Figure 6.12 (d) provides its variation with β: as expected, the amplification rate of such mode decreases with β, confirming the statements of the Squire theorem (Schmid and Henningson (2001)).

The influence of the spanwise wavenumber β on the transient amplification of the perturbations is now analyzed. Figure 6.13 shows the curves of the optimal energy gain, $G(t)$, for $\beta = 0$, $\beta = 0.1$, $\beta = 0.2$ and $\beta = 0.3$. The energy gain, which reaches a value of order $3 \cdot 10^8$ in the two-dimensional case, as shown by the solid line in Figure 6.13, has been found to decrease with β, as shown by the dashed, dotted and dashed-dotted lines providing the optimal energy gain curves computed by the global model for $\beta = 0.1$, $\beta = 0.2$ and $\beta = 0.3$. One could also observe the presence of the flapping phenomenon (which has been extensively analyzed in Chapter 4) for $\beta = 0$ and $\beta = 0.1$, as well as the asymptotical instability of the steady mode M_S for the curves at $\beta = 0.1$ and $\beta = 0.2$, the second one showing a lower amplification rate. It is noteworthy that the flapping phenomenon is not recovered for high values of β, due to the lowering of the convective TS branch of

the spectrum for increasing spanwise wavenumber. In Figure 6.14 (a) the dependence of the maximum value of the optimal energy gain on the spanwise wavenumber β is shown. Although such a parameter decreases with β, the decrease has been found to be very slow for $\beta < 0.1$. Such a behaviour could be due to the coexistence of the convective amplification of KH/TS waves, of the lift-up mechanism and of the energy growth due to the asymptotical instability of mode M_S. In particular, for such a large separation bubble, the energy gain is mostly due to the amplification of KH/TS waves, which reaches the highest value of spatial amplification when $\beta = 0$ (Schmid and Henningson (2001)). On the other hand, the amplification due to the *lift-up* mechanism, which is active only when $\beta \neq 0$ and increases with the spanwise wavenumber up to $\beta = 0.6$ (see Corbett and Bottaro (2000), as well as the spanwise analysis in the next Chapter), is able to reach an energy gain of order 10^2 for an attached boundary layer at the same Reynolds number. An even lower amplification is reached at short time by the weakly growing unstable mode M_S, reaching at $t \approx 400$ (close to the time at which the maximum value of the energy gain is reached, t_{max}) a value of the $G(t)$ of about order 10^1. Such amplification values are very low with respect to the one due to KH/TS waves, so that an optimal dynamics is recovered for the KH/TS optimal wavenumber, $\beta = 0$. It is worth to notice that, for a separation bubble in which the two-dimensional amplification reaches a maximum value of the energy gain comparable to the one due to the *lift-up* mechanism, an optimal wavenumber greater than zero would be recovered (see the results in Marquet et al. (2008), for a separation bubble after a backward facing step).
A similar explanation could be provided concerning the dependence of t_{max} on the spanwise wavenumber. Figure 6.14 (b) shows that t_{max} increases for $\beta \leq 0.1$ and decreases for greater values of the spanwise wavenumber. Such a trend recalls the one of the amplification rate of mode M_S, suggesting that the increase of t_{max} for $\beta \leq 0.1$ could be due to the amplification factor of mode M_S, which reaches its maximum for $\beta = 0.1$. On the other hand, t_{max} decreases for $\beta > 0.1$ due to the increasing effect of the lift-up mechanism with respect to the energy growth of KH/TS waves. Indeed, the lift-up mechanism is associated with lower values of t_{max}, its optimal time being around 250 for an attached boundary layer at $\beta = 0.6$, as it would be shown in the next Chapter.
In the following section it will be investigated the occurrence of the global modes here discussed in the non-linear dynamics of the separated flow under consideration, the flow being perturbed by disturbances of different shape and amplitude.

6.3 Dynamics of small amplitude perturbations: the onset of centrifugal global modes

6.3.1 Two-dimensional perturbations

This section aims at verifying the existence of the modes identified by the global eigenvalue analysis in a non-linear framework and at investigating their role in the transition mechanism. Non-linear simulations have been performed initializing the computation by superposing to the base flow the two-dimensional optimal perturbation with amplitude $A_0 = 10^{-8}$. The length of the domain in the spanwise direction has been chosen equal to the most amplified wavelength of mode M_S ($L_z = 2\pi/\beta_{S_{max}} = 62.8$). Figure 6.15 shows

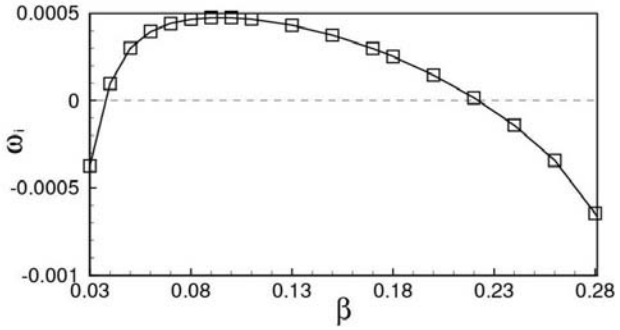

(a)

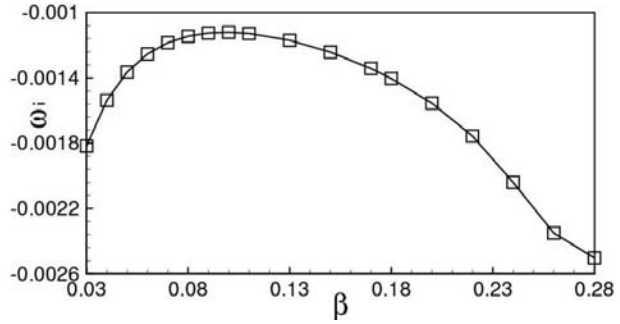

(b)

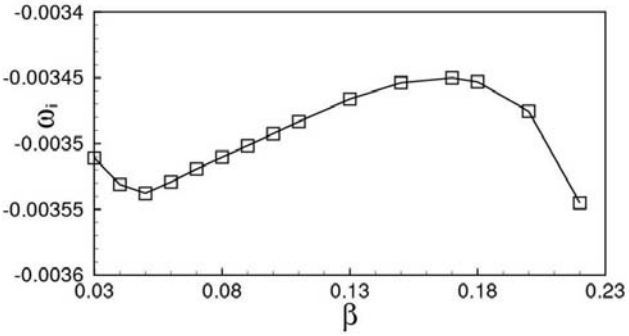

(c)

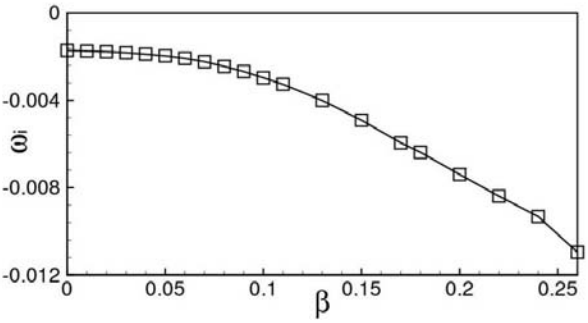

(d)

Figure 6.12: Amplification rate of the unstable mode M_S (a), of the unsteady mode M_{US1} (b), of the Gortler mode M_G (c), and of the Tollmien–Schlichting mode M_{TS_1} (d) versus the spanwise wavenumber β.

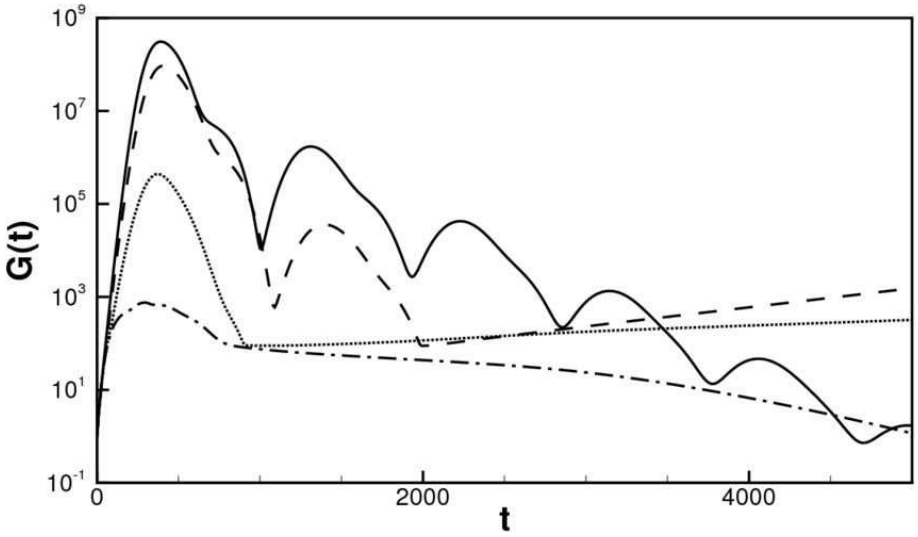

Figure 6.13: Energy gain curves computed by the global model for $\beta = 0$ (solid line), $\beta = 0.1$ (dashed line), $\beta = 0.2$ (dotted line) and $\beta = 0.3$ (dashed-dotted line).

on a semi-logarithmic scale the time evolution of the normalized energy obtained by the three-dimensional DNS (solid line) and by a two-dimensional one (dashed-dotted line), performed with the same parameters. It is worth to notice that for $t < 1500$ the two energy gain curves are overlapped, meaning that the amplification dynamics of the perturbation remains quasi two-dimensional. In both cases the disturbance initially placed close to the separation point of the bubble is amplified and convected downstream, resulting in a packet of TS waves in the attached zone, as shown in the two previous Chapters. Some differences are recovered in the asymptotic regime, due to the appearance of the three-dimensional steady weakly-growing mode which has been found to become unstable at $Re = 200$. Indeed, looking at the energy gain curve, one can observe that, after the transient has passed, the perturbation begins to be amplified with an exponential growth rate. By computing

$$\sigma_i(T) = \frac{1}{2E(T)} \frac{dE(t)}{dt}\bigg|_T \tag{6.9}$$

at a large time T, one obtains a growth rate of about $\sigma_i = 0.000463$, which is very close to the one recovered by the global model for mode M_S, $\omega_i = 0.000474$ (the dotted line in Figure 6.15 shows the growth of the energy theoretically associated with such an amplification rate). Furthermore, a similar behaviour is recovered by a linearized DNS, whose results are shown in Figure 6.15 by the dashed line. In such a case, the appearance of the three-dimensional mode (characterized by the same amplification rate of the weakly non-linear case) is delayed of about 1000 time units, so that the perturbation is continuously damped until $t = 2600$, except for a weak increase of the energy gain at $t \approx 1600$ due to the flapping effect. Such a discrepancy between the linear and non-linear simulation is due to the fact that non-linear interactions of the perturbation at different frequencies contribute to the onset of the wavenumber associated with mode M_S, despite

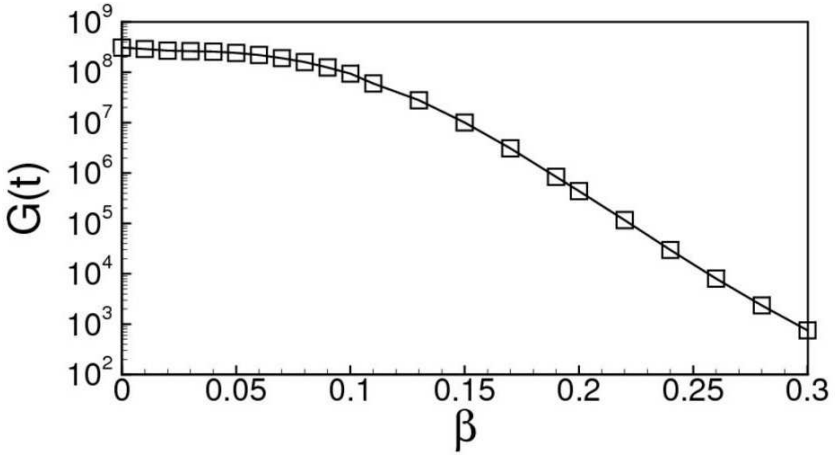

(a)

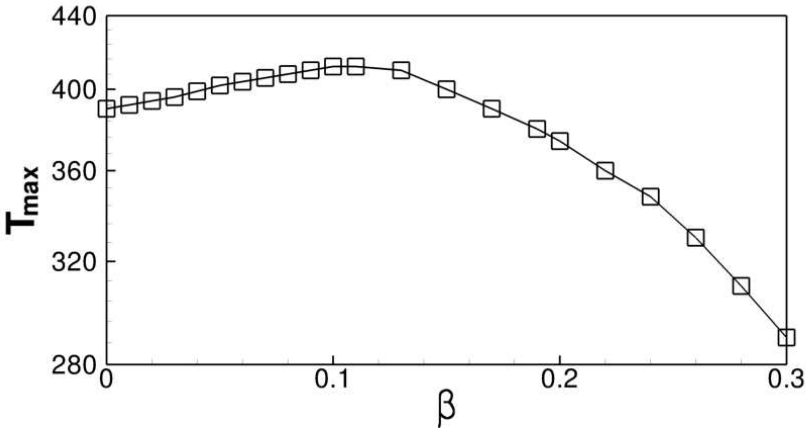

(b)

Figure 6.14: Maximum value of the energy gain (a) and time at which such a value is reached (b) obtained by the global model versus the spanwise wavenumber β.

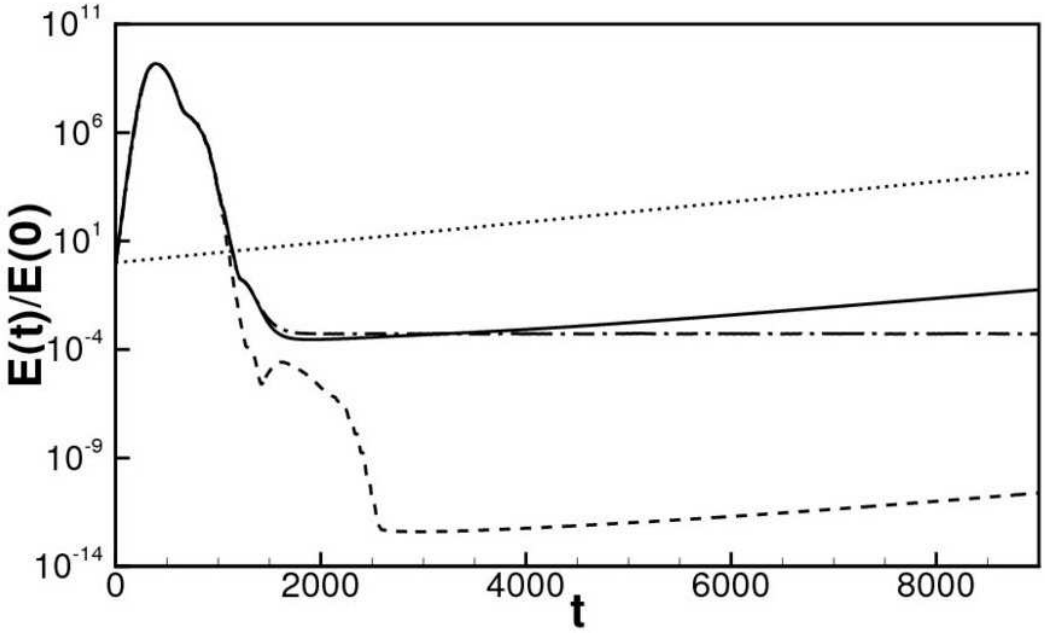

Figure 6.15: Time evolution of the normalized energy computed by a three-dimensional DNS (solid line), a two-dimensional one (dashed-dotted line), and a the linearized three-dimensional DNS (dashed line) initialized with the optimal perturbation obtained at $Re = 200$ and $A_0 = 10^{-8}$. The dotted line represent the theoretical trend of the amplification rate of mode M_S computed by the global model.

the flow has been forced with a perturbation having $\beta = 0$. It can be argued that, altough the appearance of the three-dimensional unstable mode is not directly due to a non-linear mechanism, non-linear interactions seem to accelerate its onset. Such a behaviour will be investigated in detail in section 6.4.

The perturbation has been extracted from the DNS at several times. Figure 6.16 shows the spanwise perturbation vorticity iso-surfaces at a very large time, $t = 12000$. Vorticity rolls, very similar to the ones of mode M_S, can be observed, confirming that the flow perturbed by a small amplitude disturbance tends towards the linearly most amplified three-dimensional mode, asymptotically. Nevertheless, at small times, the dynamics is more complex, as it can be observed in Figure 6.17, providing the spanwise velocity contours in the plane at $z = 26$. Figure 6.17 (a) shows at $t = 600$ the spanwise component of the KH and TS waves being convected downstream by the mean flow. At this time the dynamics is almost two-dimensional, so that the spanwise component of the velocity is very small with respect to the wall-normal and streamwise ones. Nevertheless, the dynamics begins to differ qualitatively from the purely two-dimensional one when a small amount of perturbation is "left behind" in the separated zone close to the reattachment point. Such a spanwise perturbation is convected upstream by the recirculation base flow increasing its extension due to the strong non-parallel effects which are present in this region (see Figure 6.17 (b)). Therefore, when the KH/TS wave packet leaves the separated zone, a residual perturbation is present inside the bubble, which is characterized by two

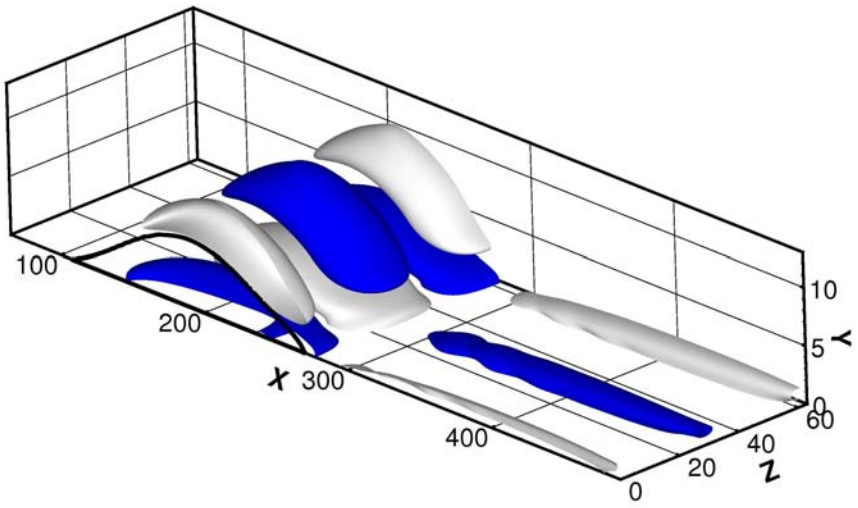

Figure 6.16: Iso-surfaces of the spanwise vorticity at $t = 12000$ extracted by a three-dimensional DNS with $L_z = 62.8$ perturbed with the two-dimensional optimal disturbance of amplitude $A_0 = 10^{-8}$. The solid line is the separation streamline, whereas dark and light surfaces represent the 0.15 and -0.15 values of spanwise vorticity, respectively. The perturbation has been normalized by its maximum value.

sickle-shaped packets with alternating sign, as shown in Figure 6.17 (c). The shape of such perturbations could be due to the presence of a negative shear close to the wall, which stretches the perturbation upstream, as well as a positive shear close to the separation streamline, stretching the perturbation downstream. Moreover, it is worth to point out that the shape of such wave packets recalls the one of the most unstable unsteady global mode, provided in Figure 6.6 (a). The further evolution of the spanwise perturbation in Figure 6.17 (d) shows that the main part of the wave packet continues to be convected upstream, whereas a residual part remains close to the reattachment point, although being stretched upstream. It is noteworthy that this part of the perturbation is placed in the strong centrifugal zone Z_2 (shown in Figure 6.8 (a)); therefore, it is likely that such a spanwise perturbation increases in size under the effect of the outward decrease of the momentum close to the wall. At $t = 2100$ (see Figure 6.17 (e)) the wave packet placed upstream has decreased its size in the wall-normal direction and has approached the separation point, whereas the downstream part of the perturbation continues to be stretched in the streamwise direction, increasing in size. Again, it is worth to point out that the upstream part of the perturbation is very similar to the second most unstable unsteady global mode provided in Figure 6.6 (b). Finally, one can observe in Figure 6.17 (f) that at $t = 2900$ the upstream negative spanwise perturbation has been stretched along the first half of the separation streamline, so that it takes the form of the unstable three-dimensional mode M_S (see Figure 6.3 (b)).

Therefore, it has been found that several global modes appear on the plane $x - y$ during the changeover of the early transient towards the asymptotical dynamics. The influence of the spanwise shape of the perturbation on its time evolution is now inves-

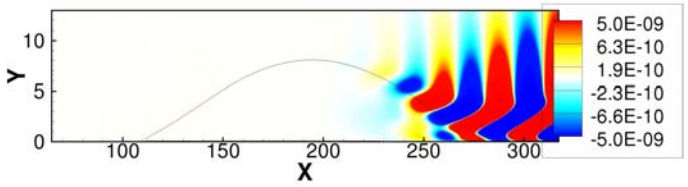

(a)

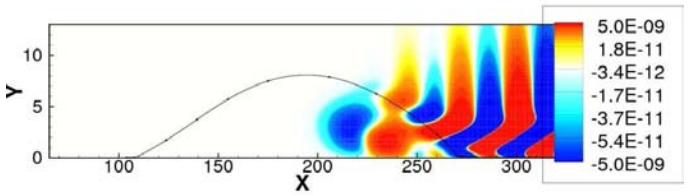

(b)

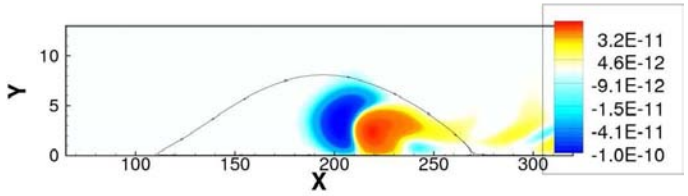

(c)

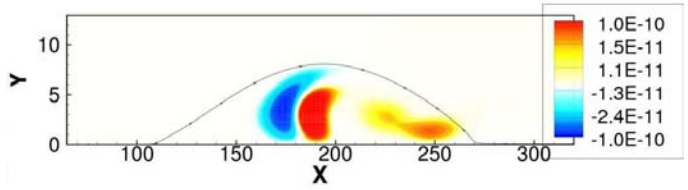

(d)

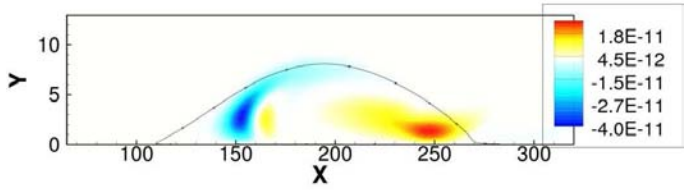

(e)

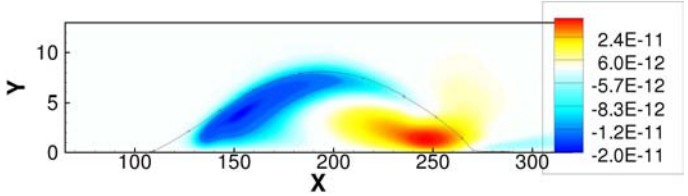

(f)

Figure 6.17: Evolution of the spanwise vorticity in the separated region at the time instants: $t = 600$ (a), $t = 700$ (b), $t = 900$ (c), $t = 1500$ (d), $t = 2100$ (e), $t = 2900$ (f) on the plane $z = 26$. The black line is the separation streamline.

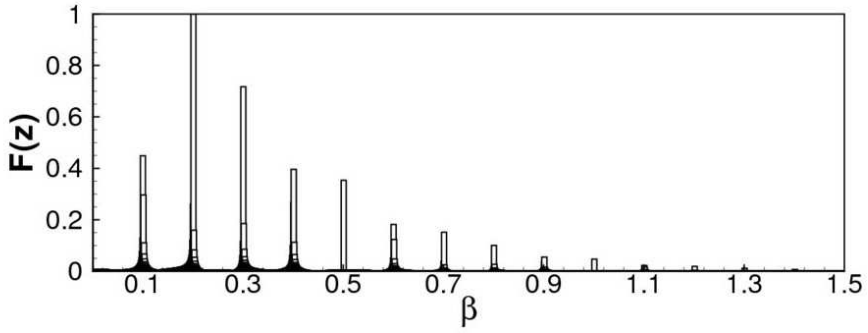

(a)

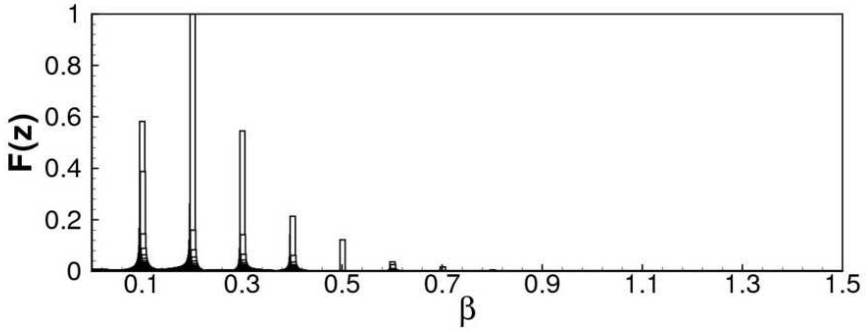

(b)

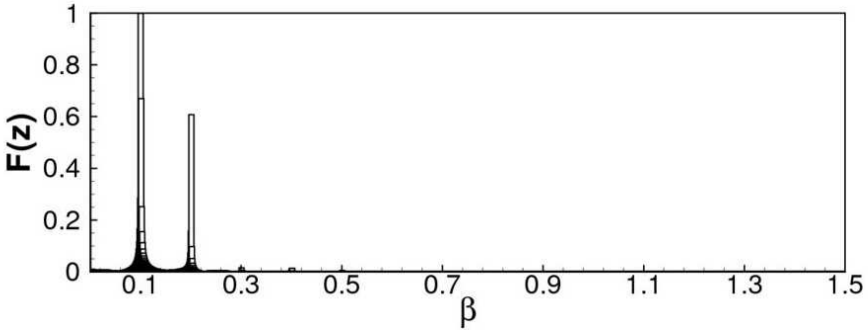

(c)

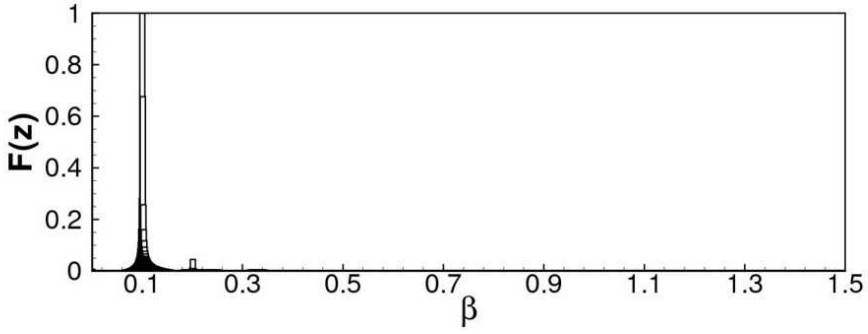

(d)

Figure 6.18: Fourier transform in z of the streamwise velocity extracted from a DNS initialized by the two-dimensional optimal initial perturbation at the point of greater amplification within the separated region at the time instants: $t = 700$ (a), $t = 1700$ (b), $t = 2500$ (c), $t = 12000$ (d).

tigated. Indeed, being the spanwise length of the domain chosen as the one giving the largest amplification rate of the most unstable global mode, one could infer that the dominant spanwise frequency would be equal to $\beta_{S_{max}}$ ($\beta = 0.1$) when non-linear effects are weak, as in the present computations. In order to verify such a possibility, the Fourier transform in the spanwise direction has been performed at different instants of time at the streamwise and wall-normal position whithin the separated region where the perturbation of highest amplitude is localized. Figures 6.18 (a) and (b) show a wide spectrum of frequencies for small times ($t = 700$ and $t = 1700$, respectively), due to the interactions of the several modes affecting the dynamics of the flow, as previously shown. At larger times (see Figures 6.18 (c) and (d) for $t = 2500$ and $t = 12000$, respectively), the spectrum results to be narrower, and dominated by the most amplified wavenumber $\beta_{S_{max}}$, since the asymptotical dynamics is dominated by the occurence of the unstable mode M_S. Most importantly, one can notice in Figures 6.18 (a) and (b) that for $t < 2500$ the dominant frequency is not $\beta_{S_{max}}$ but its double, $\beta = 0.2$. Such a result means that at small times the spanwise perturbation is essentially composed by packets having a spanwise wavelength smaller than the most amplified one, as shown in Figure 6.19 (a) by the iso-surfaces of the spanwise velocity component, for $t = 700$. These packets, localized in the spanwise and streamwise direction, slowly increase their size asymptotically in time (see Figure 6.19 (b) for $t = 1500$), approching the spanwise wavenumber $\beta_{S_{max}}$.

Figure 6.20 (a) shows the spanwise perturbation vorticity iso-surfaces at $t = 2500$ for the initial optimal perturbation of amplitude $A_0 = 10^{-8}$. It is possible to observe that some vorticity rolls are present in the separated region, together with elongated structures in the attached zone. The latter ones recall the streamwise vortices associated with the convective mode M_G (one can compare with Figure 6.11), although a small streamwise oscillation of the structures is observed. Such an oscillation is due to the vortex shedding induced by the high sensitivity of the flow to the noise generated by the numerical errors (see the discussion in Chapter 5), and it can be observed because of the low amplitude of the perturbation. In fact, at $t = 2500$, the perturbation has been only slightly amplified by the asymptotic mechanism, and the vorticity perturbation is of order 10^{-11}, just one order of magnitude greater than the numerical residual. Indeed, if the optimal perturbation is initialized with a larger amplitude, $A_0 = 10^{-6}$, the elongated structures recall exactly the structure of mode M_G, as shown in Figure 6.20 (b). Thus, it is likely that such a mode dominates the dynamics during the transient inducing in the frequency spectrum a dominating wavenumber close to 0.17. Indeed, although M_G is asymptotically stable, it could be excited during the transient by means of non-linear interactions of the modes developing and amplifying into the flow. Nevertheless, due to the asymptotical instability of mode M_S, at a larger time the structures having smaller wavelength begin to merge each other, resulting in rolls of spanwise vorticity alternated at the most amplified wavenumber $\beta_{S_{max}}$, so that mode M_S become the dominant one.
In order to verify such an hypothesis on the excitation of the Gortler mode by means of linear amplification of mode M_S and non-linear interactions among the perturbations, a DNS has been performed in which the spanwise domain length has been chosen equal to the most amplified wavelength for the onset of the Gortler mode ($L_z = 2\pi/\beta_{G_{max}} = 37$). In order to perform a comparison with the results shown in Figure 6.18, an initial perturbation identical in shape and amplitude to the one previously used has been superposed to the base flow. A Fourier transform in z of the streamwise velocity signal has been

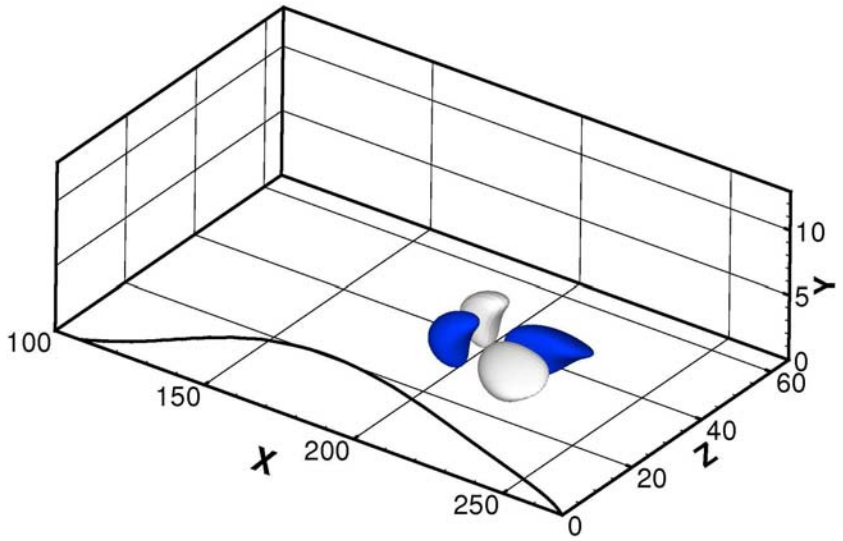

(a)

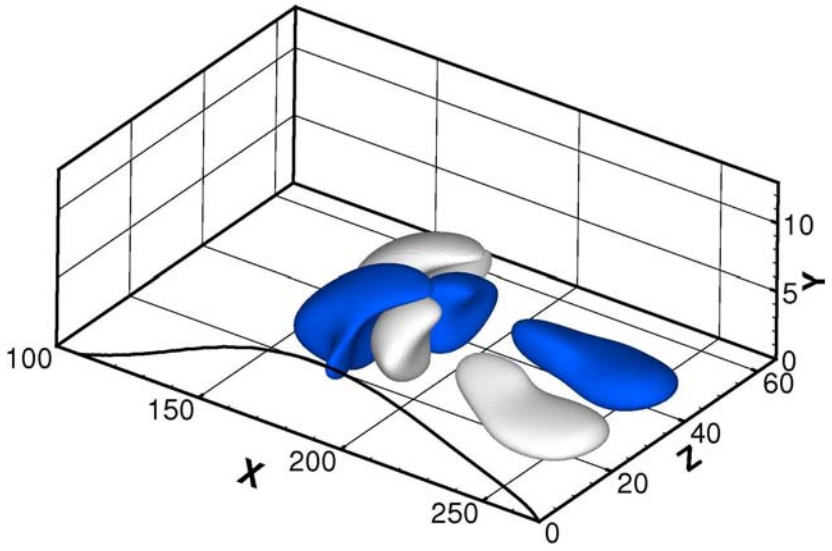

(b)

Figure 6.19: Blow up in the separated region of the iso-surfaces of the spanwise velocity at $t = 700$ (a), where the dark and light surfaces represent the $7 \cdot 10^{-11}$ and $-7 \cdot 10^{-11}$ value, respectively, and at $t = 1500$ (b), where the dark and light surfaces represent the $2 \cdot 10^{-11}$ and $-2 \cdot 10^{-11}$ value, respectively. The black line is the separation streamline.

performed at the point of greater amplification whithin the separated region at $t = 700$ and $t = 1700$. As shown in Figure 6.21, the dominant frequency is always coincident to the Gortler most amplified wavenumber ($\beta = \beta_{G_{max}} = 0.17$). It is worth to notice that, in the previous case (for $L_z = 2\pi/\beta_{S_{max}} = 62.8$) the dominant wavenumber was the double of the minimum one allowed in the flow ($\beta = 0.1$), whereas for $L_z = 2\pi/\beta_{G_{max}} = 37$ it is equal to such minimum, which is $\beta = 0.17$. Thus, in both cases the wavenumber that dominates the flow during the transient is very close to the most amplified wavenumber for the onset of the Gortler mode, corroborating the hypothesis that such mode has indeed a role in the transient process leading to the asymptotic self-sustained amplification of mode M_S.

6.3.2 Three-dimensional perturbations

The dynamics of the flow has been analysed with respect to a three-dimensional perturbation of small amplitude. The optimal spanwise-modulated perturbation computed by the global model for $\beta = \beta_{S_{max}}$ has been superposed to the base flow with an amplitude $A_0 = 10^{-8}$. The transient evolution of the perturbation does not present remarkable differences from the one observed in the previous simulations, except for the spanwise-modulation of the TS waves convected by the separation bubble, and the lower peak value of the energy gain curve. The Fourier transform in the spanwise direction of the streamwise component of the velocity at the point of maximum amplification within the bubble, is shown for $t = 700$ and $t = 4700$ in Figures 6.22 (a) and (b), respectively. In the early transient phase preceeding the onset of mode M_S, the dominant spanwise wavenumber remains the one at which the flow has been perturbed, which is equal to the most amplified wavenumber for mode M_S. Surprisingly, at sligthly larger times (approximately for $1000 < t < 6000$), the dominant wavenumber doubles, as shown in Figure 6.22 (b) for $t = 4700$. Such a behaviour could not be ascribed to non-linear effects or secondary instability of the growing waves, due to the very low amplitude of the perturbations at such time. In fact, considering that an initial perturbation of magnitude $A_0 = 10^{-8}$ has been used to initialize the DNS, and that at $t = 4700$ an amplification of about 6.8 has been reached, one could conclude that at such times non-linearity does not play any role. The same conclusion can be drawn about secondary instability, which is usually triggered when perturbations reach a finite amplitude. Thus, as in the previous case, this behaviour has to be ascribed to some linear mechanism. Indeed, the dominating wavenumber, although differing from the initial-perturbation one, is very close to the most amplified M_G one, and is found to dominate the transient dynamics finally leading to the formation of streamwise vortices recalling mode M_G, as in the previously discussed case. Such results confirm the important role of Gortler mode in the self-sustained process leading to asymptotical instability of the mode M_S, being able to arise in the flow even when the wavenumber of the initial perturbation is equal to $\beta_{S_{max}}$. The same dynamics is observed in simulations initialized by the same perturbation at a larger amplitude, $A_0 = 10^{-6}$, altough some differences due to non-linear effects are observed.
On the other hand, a different behaviour is recovered when the base flow is initialized with the optimal asymptotic initial condition estimated by the global model at a large time, namely, $T = 5000$ for $\beta = 0.1$, shown in Figure 6.23. It is known that the optimal

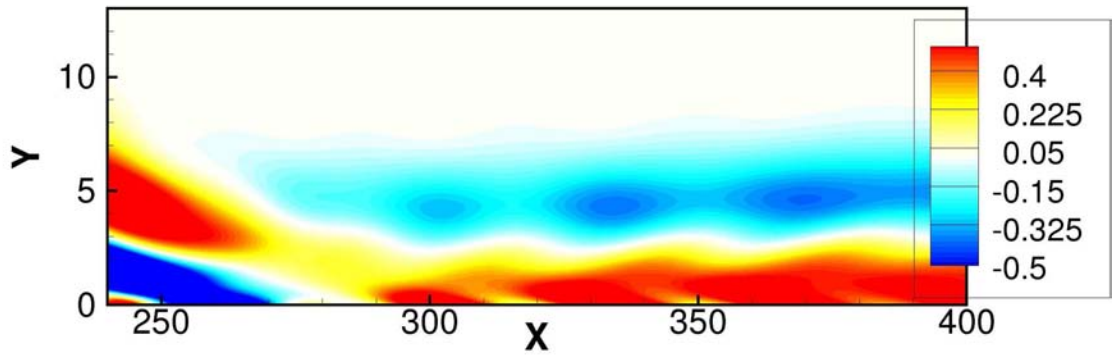

(a)

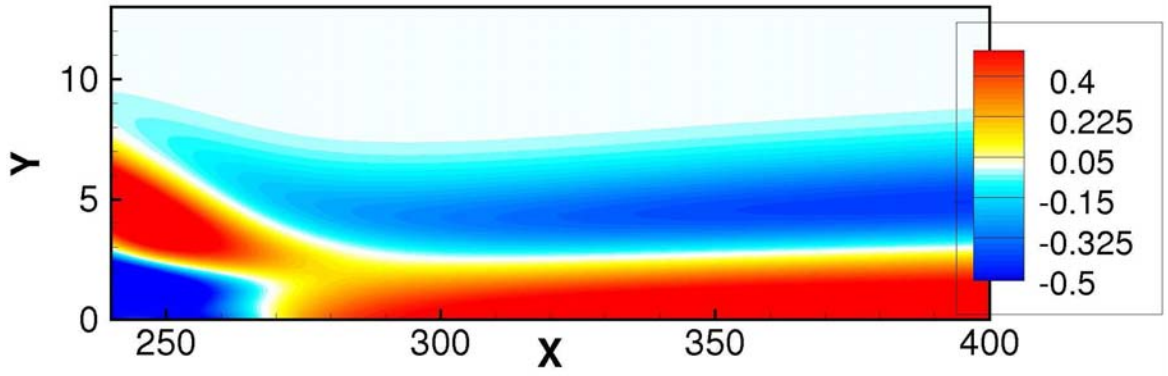

(b)

Figure 6.20: Blow-up of the shaded contours of the spanwise vorticity extracted from a three-dimensional DNS initialized by the optimal initial perturbation with amplitude $A_0 = 10^{-8}$ (a) and with amplitude $A_0 = 10^{-6}$ (b) at $z = 42$ and $t = 2500$. The perturbation has been normalized by its maximum value.

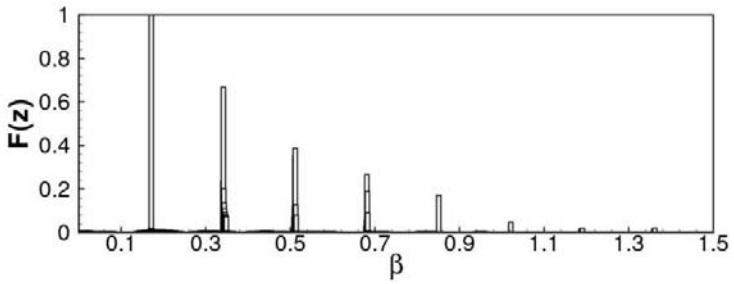

(a)

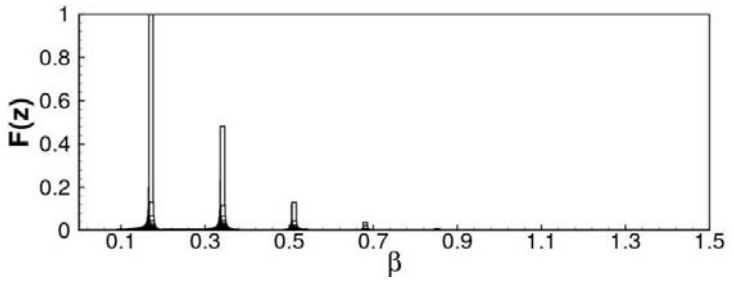

(b)

Figure 6.21: Fourier transform in z of the streamwise velocity extracted from a DNS initialized by the two-dimensional optimal initial perturbation at the point of greater amplification whithin the separated region for $L_z = 2\pi/\beta_{G_{max}} = 37$ at the time instants $t = 700$ (a), $t = 1700$ (b).

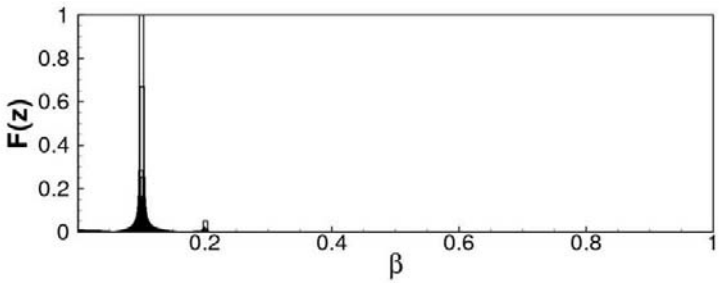

(a)

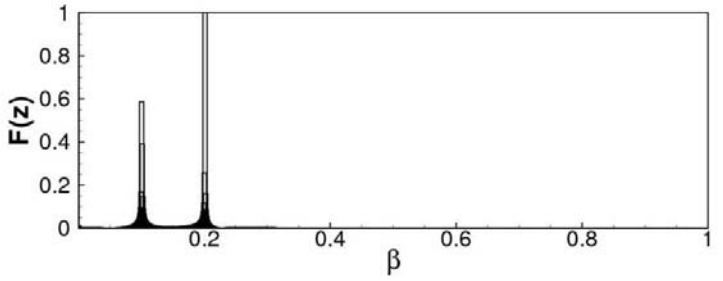

(b)

Figure 6.22: Fourier transform in z of the streamwise velocity extracted from a DNS initialized by the optimal initial perturbation for $\beta = 0.1$ at the point of greater amplification whithin the separated region for $L_z = 2\pi/\beta_{S_{max}} = 62.8$ at the time instants $t = 700$ (a), $t = 4700$ (b).

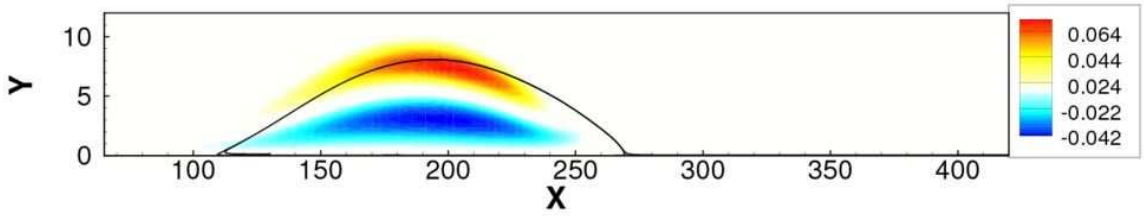

Figure 6.23: Contours of the spanwise velocity component of the optimal perturbation computed by the global model for $T = 5000$ and $\beta = 0.1$.

asymptotical initial condition leading an unstable mode to asymptotical growth, usually having the same form of its adjoint counterpart, is able to optimally induce its onset (for instance, see Marquet et al. (2009)). In fact, the Fourier spectra computed in the spanwise direction at different instants of time is always dominated only by the most amplified wavenumber $\beta = 0.1$. Thus, it could be inferred that the onset of the Gortler modes depends on the spatial structure of the perturbation.
In particular, the mechanism of selection of modes M_S and M_G could be linked to some intrinsic features of the flow, such as its structural sensitivity. Giannetti and Luchini (2007) have discussed how finite amplitude perturbations present into the flow could induce modifications of the Navier-Stokes operator; every mode could thus be differently affected by such modifications, depending on its zones of maximum structural sensitivity. The sensitivity of an eigenvalue ω to a perturbation of the operator $\delta\mathbf{A}$ is given by Giannetti and Luchini (2007):

$$\delta\omega = \varepsilon \frac{(\hat{\mathbf{q}}^+, \delta\mathbf{A} \cdot \hat{\mathbf{q}})}{(\hat{\mathbf{q}}^+, \mathbf{B} \cdot \hat{\mathbf{q}})}, \tag{6.10}$$

where $\hat{\mathbf{q}}$ is the eigenvector associated with ω, and $\hat{\mathbf{q}}^+$ is its adjoint counterpart. The authors demonstrate that $\delta\omega$ is always smaller than:

$$\lambda(x, y) = \frac{||\hat{\mathbf{q}}||\,||\hat{\mathbf{q}}^+||}{\int_{x_{in}}^{x_{out}} \int_0^{L_y} \hat{\mathbf{q}} \cdot \hat{\mathbf{q}}^+ dxdy}, \tag{6.11}$$

where $||\cdot||$ indicates the modulus of the vector. Thus, the sensitivity vanishes in regions where either the direct global mode or the adjoint global mode vanishes; whereas, the regions where λ is greater than zero may be identified as the wave-maker regions. Such regions have been identified for both modes M_S and M_G and are provided in Figures 6.24 (a) and (b), respectively. One could observe that the sensitivity region associated with mode M_S is localized mainly inside the recirculation bubble, whereas, for mode M_G it is localized in the shear layer. Thus, it is possible to conclude that KH waves being convected through the shear layer of the bubble, like the ones generated by the optimal initial perturbation, would excite the M_G mode. Instead, a perturbation whose energy is distributed over all the recirculation zone (like the optimal perturbation for $T = 5000$ and $\beta = 0.1$) would induce the onset of mode M_S. Such a result could mean that in the linear regime a mechanism exists for the onset of mode M_S which does not

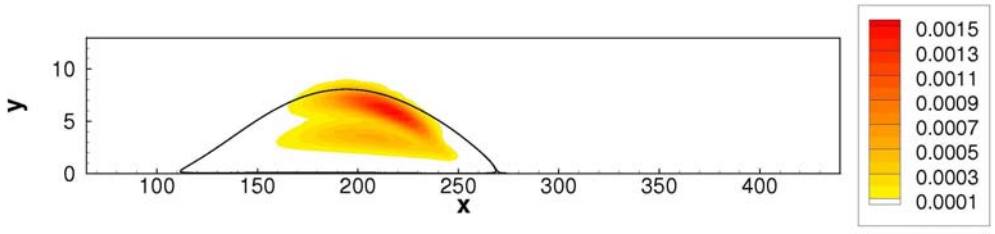

(a)

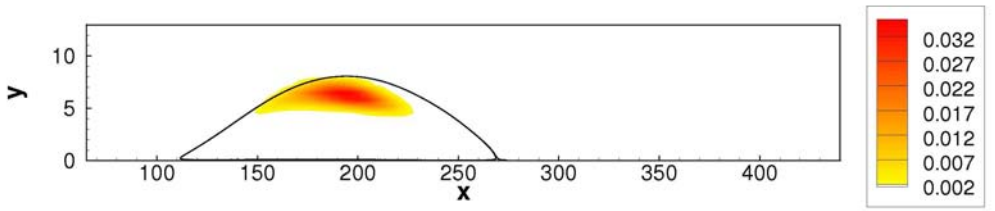

(b)

Figure 6.24: Contours of the λ parameter estimating the structural sensitivity of modes M_S (a) and M_G (b).

depend from the excitement of the Gortler mode, but that usually such a mechanism is skipped because it is not the one leading to the largest energy amplification, and mode M_G is often observed during the transient leading to mode M_S. Therefore, a perturbation placed at the upstream part of the bubble leads to an energy amplification through the KH mechanism; transiently evolves in the form of TS waves and unsteady wave packets recalling modes M_{US}; consequently excites the Gortler modes and finally takes the form of mode M_S.
The conjecture here discussed on the role of mode M_G will be analyzed in detail in the following section, dealing with the dynamics of large amplitude perturbations.

6.4 Dynamics of large amplitude perturbations: primary and secondary transition

Figure 6.25 shows the energy gain provided by a DNS initialized by the two-dimensional optimal disturbance with an amplitude $A_0 = 10^{-4}$. As one can observe, two zones of transition are identified (enclosed by the dashed lines, hereafter referred as primary and secondary transition). The first one, for $400 < t < 1000$, is transient, and is due to the strong spatial amplification of KH/TS waves. For $t > 1000$ a relaminarization occurs, followed by the onset of mode M_S. At $t > 8000$, a self-sustained cycle of transition occurs, which is due to the presence of the asymptotically unstable mode M_S, although at $t \approx 10000$, $t \approx 11500$, $t \approx 13500$, $t \approx 19500$ the perturbation is found to decrease temporary, affecting the energy gain curve with a low-frequency modulation. In the following, the dynamics of the perturbation for $400 < t < 1000$ and for $t > 8000$ will be analyzed in detail.

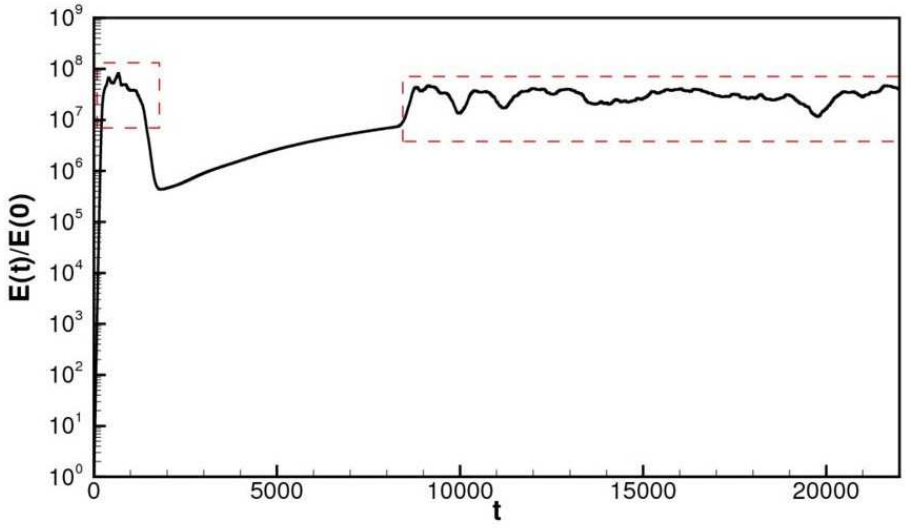

Figure 6.25: Energy gain obtained by DNS for the initial optimal perturbation with amplitude $A_0 = 10^{-4}$

6.4.1 K-type transition

Figures 6.26 (a), (b), (c) and (d) show the streamwise velocity contours at $t = 300$, $t = 400$, $t = 500$ and $t = 600$, respectively. At $t = 300$, the dynamics is similar to the one recovered by a two-dimensional computation in the case of a large-amplitude initial perturbations, shown in Chapter 4. A convectively amplified two-dimensional wave packet is identified in the attached zone, which is the result of the excitement, by means of the high sensitivity of the base flow, of a local spatial instability (see Chapter 4). As shown in Figure 6.26 (b), such a wave packet is convected downstream and is amplified until non-linear interactions kick in, introducing a modulation in the spanwise direction. Some subharmonics of the dominant wavelength are recovered also in the streamwise direction (see Figure 6.26 (c) at $x = 380$). At the same time, another wave packet is created and shed by the bubble, as shown in Figure 6.26 (d), which undergoes an irregular evolution. Therefore, an unsteady behaviour is established in the attached zone, which highly resembles the scenario of the K-type transition, which has been discussed in Chapter 2. In particular, regions of high wall-normal shear can be identified, which are associated with strong velocity *spikes*, shown in Figure 6.27 by the isolines of the spanwise-vorticity at $t = 1000$. Such results strongly recall the ones provided by Rist and Maucher (1994) and Rist and Fasel (1995) for the transition scenario via secondary instability of TS waves. Indeed, the TS packets convected by the separation bubble experience secondary instability and transition via the formation of Λ-vortices, which are often recovered in correspondence of the velocity spikes in the late stage of K-type transition. Such vortical structures have been identified

here using the iso-surfaces of the Q-criterion, i.e., the positive values of the quantity

$$Q = \frac{1}{2}(||\Omega||^2 - ||S||^2), \tag{6.12}$$

S being the rate-of-strain tensor and Ω the vorticity tensor (Hunt et al., 1988). In Figure 6.28, showing the Q-criterion iso-surfaces at $t = 600$, two pairs of Λ-vortices are recovered. They are followed by a second pair of Λ-vortices (not shown) aligned with the first one, confirming that the primary transition is a typical K-type transition. Finally, at such low Reynolds number, transition via TS waves is not sustained, so that, for $t > 1000$, the flow relaminarizes.

It is noteworthy that a similar scenario has also been recovered when the flow is perturbed by a time-continuous three-dimensional random white noise at the inlet points, as it may happen in real experiments, where the inlet flow may be affected by some noise. In such a case, the K-type transition is sustained also for disturbances of smaller amplitude. Figure 6.29 shows the energy gain curve provided by a three-dimensional computation continuously perturbed at the inlet with random disturbances of amplitude $A_0 = 10^{-6}$. One can observe that the flow does not relaminarize, differently from the case of an impulsively injected perturbation (see Figure 6.25), but directly transitions toward turbulence. Since such a transition scenario is induced by the production and convection of KH/TS waves, it is straightforward to investigate about the existence, in a three-dimensional framework, of a typical two-dimensional mechanism such as the flapping frequency. In order to shed light on such issue, a Fourier transform in time has been performed of the energy signal provided by the three-dimensional computation shown in Figure 6.29. As shown in Figure 6.30, several low frequencies are recovered, the lowest one being close to the value of the primary flapping frequency disscussed in Chapter 4. Thus, as anticipated by the global instability analysis (see Figure 6.13), it seems that also in a three-dimensional framework the interaction of backward-forward induced KH/TS waves induces a low-frequency beating, which represents a robust feature of separated boundary-layer flows.
In the case of a perturbation of lower amplitude , $A_0 = 10^{-7}$, a partial relaminarization is observed (the energy gain temporary decreases for $t \approx 1000$), although TS waves are found to be continously convected and amplifyed by the separated zone, due to the continous forcing at the inlet, and an unsteady mechanism of vortex shedding is established. Thus, it is possible to infer that the second type of transition arising at large times as a consequence of the onset of mode M_S, would not be recovered in an experimental framework in presence of high levels of noise, since transition would directly occurs via the K-type route. This could explain the difficulties arising in recovering the three-dimensional mode M_S in experiments, its onset being observed only in low-levels-of-noise environments (see Beaudoin et al. (2004), for instance).

6.4.2 Transition via Gortler modes breakdown

In this Section, the secondary transition at large times will be analyzed in detail. In Figure 6.25 one can observe the onset of mode M_S for $t > 2000$ and its successive saturation (the slope of the energy gain curve decreases with time for $2000 < t < 8000$), followed by an unsteady behaviour for $t > 8000$. Figures 6.31 (a) and (b) show two snapshots of the spanwise vorticity iso-surfaces at $t = 8500$ and $t = 9500$, respectively. At $t = 8500$, one

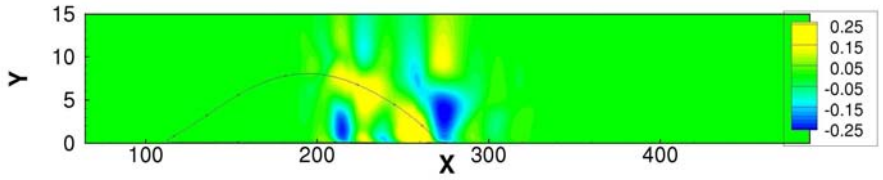

(a)

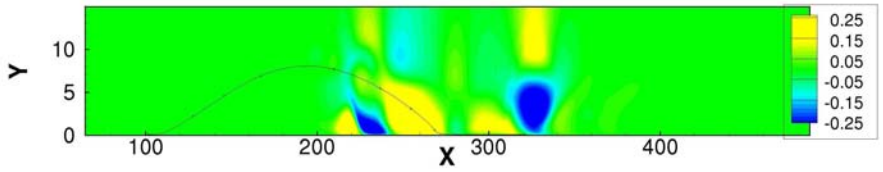

(b)

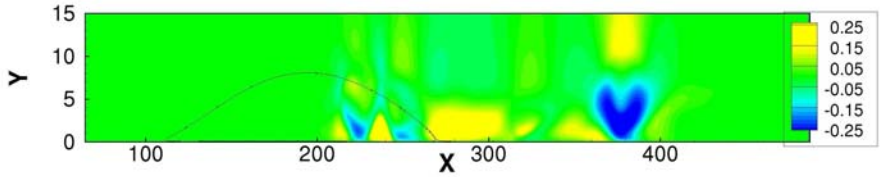

(c)

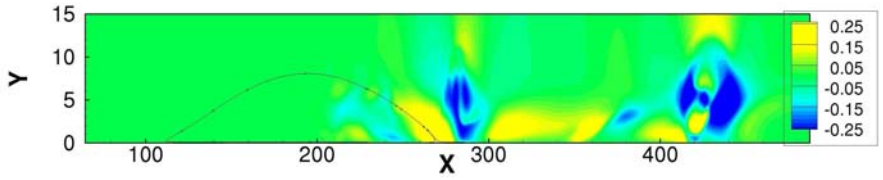

(d)

Figure 6.26: Streamwise velocity contours on the plane $z = 25$ extracted from a DNS initialized by the initial optimal perturbation with amplitude $A_0 = 10^{-4}$ at $t = 300$ (a), $t = 400$ (b), $t = 500$ (c), and $t = 600$ (d).

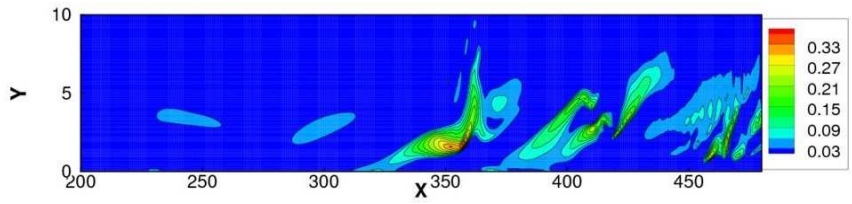

Figure 6.27: Contours of the spanwise vorticity extracted from a DNS initialized by the initial optimal perturbation with amplitude $A_0 = 10^{-4}$ at $t = 1000$ in the plane $z = 25$.

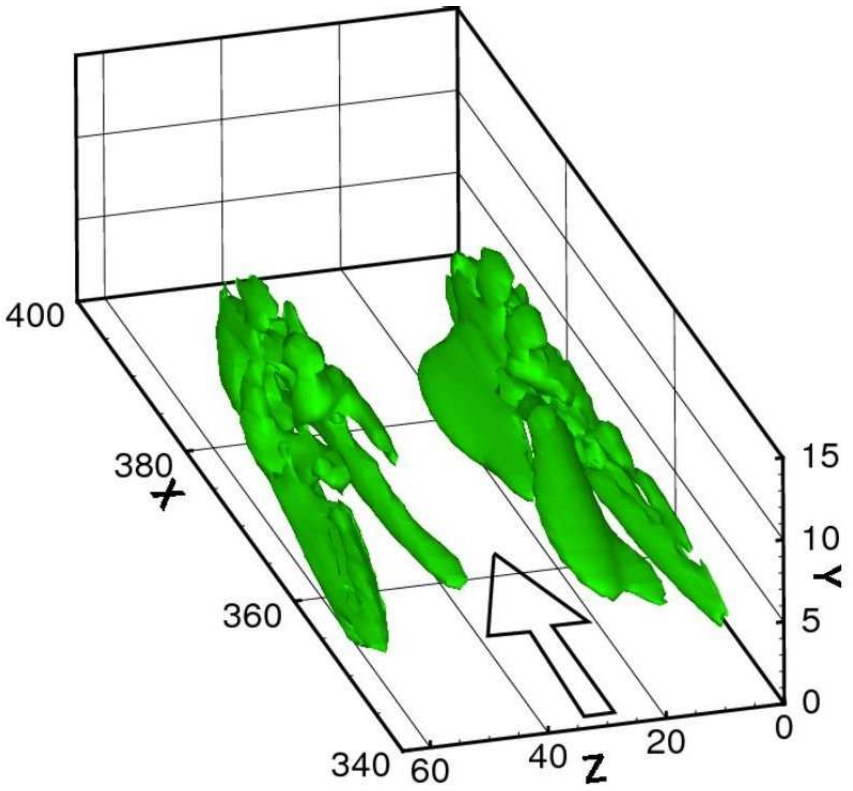

Figure 6.28: Iso-surfaces of the Q-criterion identifying vortical structures extracted from a DNS initialized by the initial optimal perturbation with amplitude $A_0 = 10^{-4}$ at $t = 600$

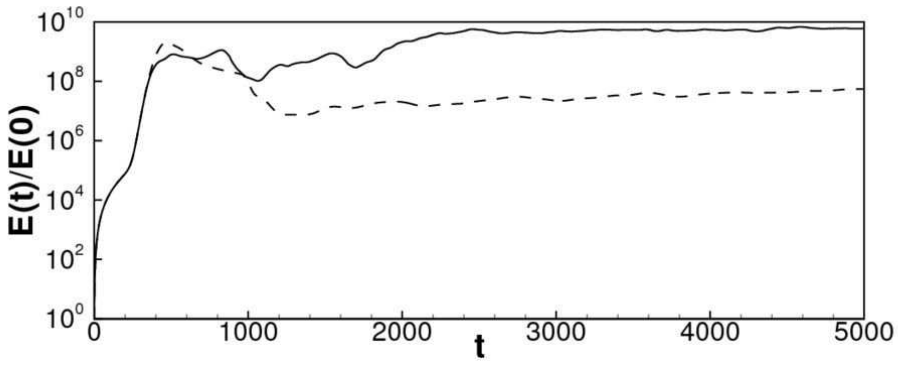

Figure 6.29: Evolution in time of the energy gain obtained perturbing the flow at the inlet points by a three-dimensional random white noise of amplitude $A_0 = 10^{-6}$ (solid line) and $A_0 = 10^{-7}$ (dashed line).

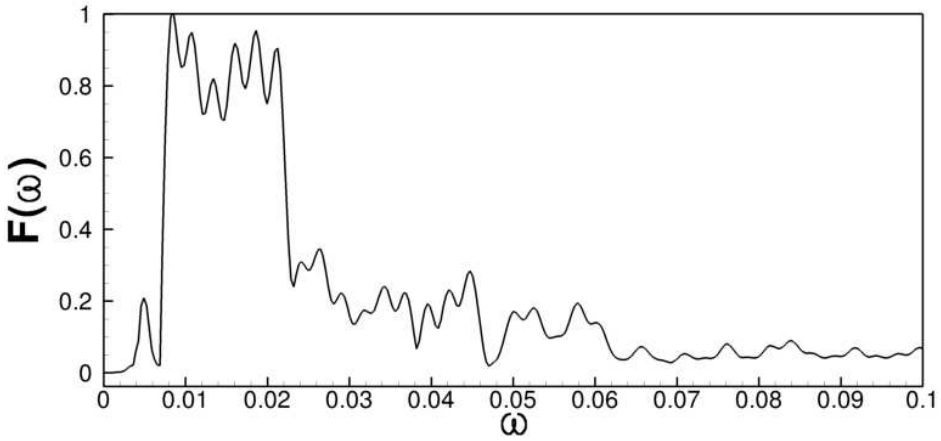

Figure 6.30: Fourier trasnform in time of the energy signal obtained perturbing the flow at the inlet points by a three-dimensional random white noise of amplitude $A_0 = 10^{-6}$.

can observe roll structures, spatially extended in the streamwise direction, which strongly recall mode M_G, shown in Figure 6.4 (b). Later, the flow is clearly transitioning toward turbulence, since an unsteady behaviour begins to be established. In particular, transition occurs in a narrow region localized in the spanwise direction, although extended in the streamwise direction from the reattachment point throughout the attached boundary layer. Figures 6.32 (a) and (b) provide the streamwise velocity perturbation contours at $t = 8500$ on the planes $z = 36$ and $z = 26$, respectively. The shaded contours have been obtained by the DNS, whereas, the solid-line contours have been obtained by the global eigenvalue analysis. Strong similarities can be observed between the two solutions; in Figure 6.32 (a) a great part of the energy is concentrated at the exterior of the recirculation bubble, indicating the presence of a structure very similar to mode M_G. Such a structure follows the high shear region along the separation streamline, and develops in a spatially extended streamwise vortex. The presence of mode M_G implies the selection of the most amplified Gortler spanwise wavenumber which is larger than the one associated with mode M_S, as previously demonstrated, explaining the concentration of the vorticity perturbation in a narrow zone in the spanwise direction. It is noteworthy that unsteadiness is recovered on a narrow spanwise region of similar extent, also when a larger spanwise dimension of the computational domain is chosen.
In Figure 6.32 (b) one can observe some structures recalling mode M_S, the perturbation being mostly located within the bubble. Thus, as shown by the contours of Figures 6.32 (a) and (b), both modes, M_S and M_G, are recovered within the flow, and play a role in the transition mechanism. In particular, it is possible to classify mode M_S as a *resonator* (see Marquet et al. (2008) and Chapter 2) placed within the separated zone, which is able to generate a self-sustained perturbation cycle; whereas, mode M_G can be considered the *amplifier* of the perturbations produced by the resonator, so that transition occurs via a convective mechanism resulting from the interaction of both modes. In particular, the Gortler mode, although asymptotically stable, is able to strongly spatially amplify the perturbations sustained within the separation bubble by M_S, so that disturbances reach

large amplitudes leading the flow to unsteadiness. Moreover, the cycle of interaction between the two modes appears to be promoted by non-linear effects, due energy saturation, which does not allow mode M_S to grow asymptotically. Indeed, for large-amplitude perturbations, $\beta_{G_{max}}$ remains among the dominating wavenumber at large times, although the spectrum is wider than in the case of small amplitude perturbations, as shown by Figure 6.33 providing the Fourier transform in the spanwise direction of the streamwise velocity at $t = 12000$. Such results stress the crucial role of mode M_G in the transition dynamics, and confirm the role of non-linear interactions in the onset of mode M_S via the excitation of the Gortler modes.
In order to investigate in which way the Gortler mode, feeded by the steady resonator M_S, experiences transition, the streamwise perturbation velocity is reported in Figure 6.34 on the plane $y = 1$ at several instants of time. Figure 6.34 (a) shows streamwise elongated structures at $t = 4500$ due to the onset of modes M_S and M_G. At $t = 8500$ (see Figure 6.34 (b)) the elongated structures having positive streamwise velocity (red contours) split into two parts in the spanwise direction, followed by an injection of negative streamwise velocity (blue contours) from the reattachment point along the region between the two high-speed elongated structures. Therefore, three pairs of streamwise vortices are created inside the attached zone. One could conjecture that this is due to non-linear effects which are able to produce subharmonics of the dominant wavenumber. Moreover, it could also be conjectured that, since modes M_S and M_G present a different wall-normal and spanwise distribution of the regions with positive and negative spanwise vorticity, the interaction of these modes could easily induce the generation of spanwise-alternated zones of positive and negative spanwise vorticity, as shown in Figure 6.31. At $t = 9500$, the elongated structures seem to experience secondary instability (Figure 6.34 (c)), due to the close interaction of low- and high-momentum regions in the spanwise and wall-normal direction. In particular, the low-velocity structure at the middle of the spanwise domain experiences symmetric streamwise oscillations. Secondary instability suddenly evolve into a more complex pattern, the unsteadiness spreading out through the attached boundary layer, as shown in Figure 6.34 (d). Structures of smaller scale are recovered into the flow, which are spread out in the spanwise direction. Eventually, such a pattern does not evolve into turbulence, but the perturbation temporarily decreases and the flow seems to partially relaminarize, as shown in Figure 6.34 (e). Such a phenomenon is associated with the temporary decrease of the energy already noticed in Figure 6.25. This phenomenon seems to be similar to the flapping phenomenon, which has been recovered in a linear three-dimensional framework by the global model in section 6.2.3. A power density FFT transform has been performed of the energy signal multiplied by a Hamming window-function on a sampling period from $t = 8500$ to $t = 26500$. The dominant wave number in time has been found rather close to the low-frequency one recovered by the global model ($\omega = 0.0045$ by FFT, $\omega = 0.006$ by the global model). Nevertheless, during the secondary transition here analysed, no evidence of TS/KH waves is found, so that the modulation on the energy gain could be due to a different mechanism.
Going back to the time evolution of the perturbation, at larger times, a further increase of the energy, associated with a strong unsteady behaviour of the flow is observed, as provided in Figure 6.34 (f) for $t = 12000$. In order to investigate the primary cause of the breakdown of such elongated structures, the iso-surfaces of the Q-criterion (defined in the previous section), have been analyzed at $t = 10000$, when the Gortler rolls are about

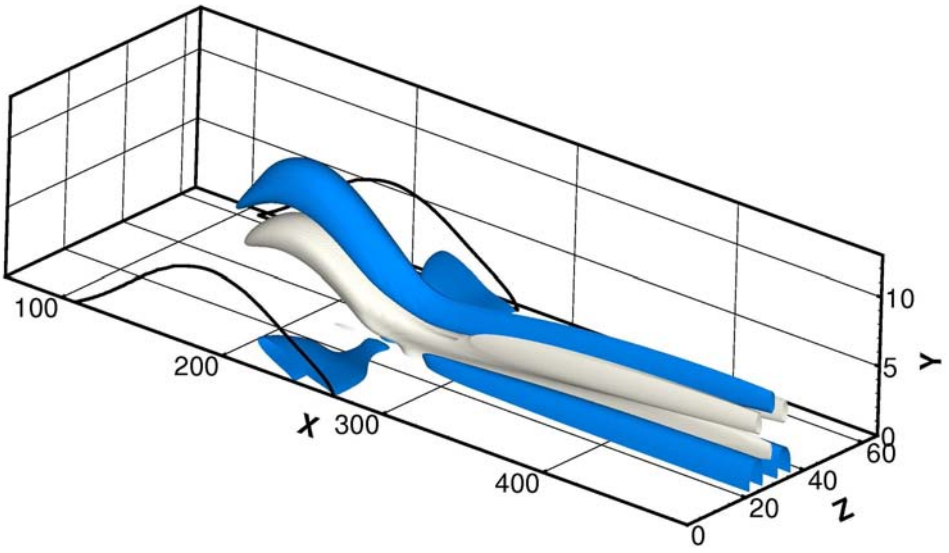

(a)

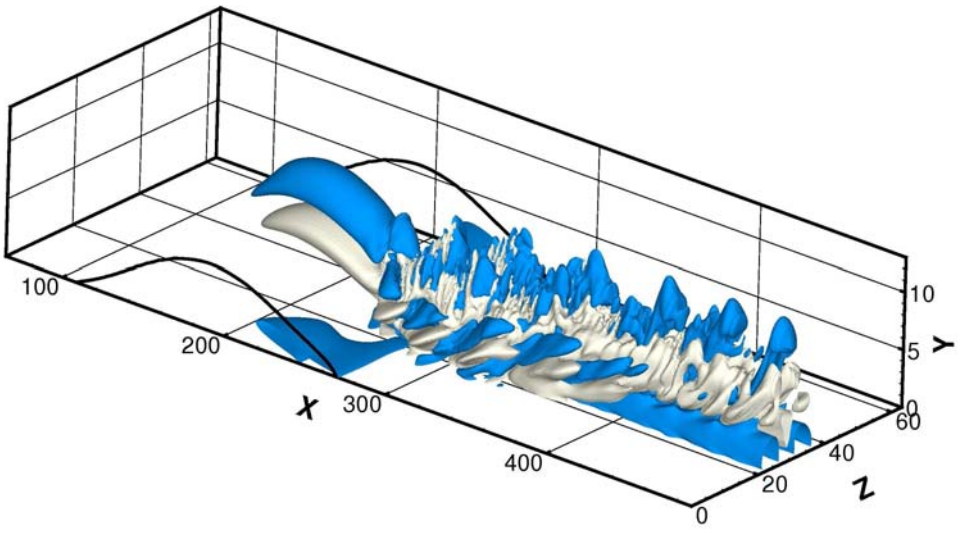

(b)

Figure 6.31: Iso-surfaces of spanwise vorticity at $t = 8500$ (a) and at $t = 9500$ (b), where the dark and ligth surfaces represent the -0.03 and 0.03 values. The solid line is the separation streamline

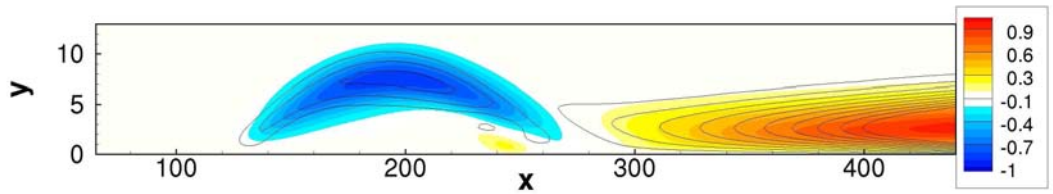

(a)

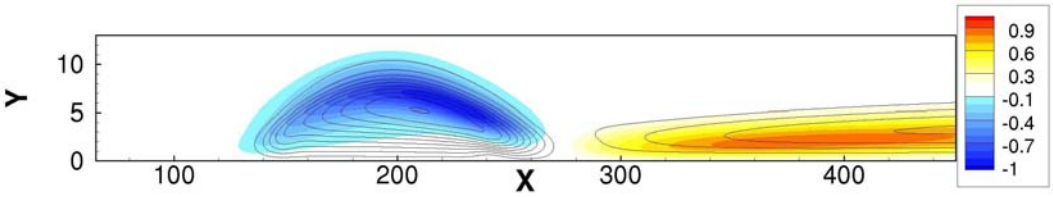

(b)

Figure 6.32: Contours of streamwise velocity of the perturbation extracted by the DNS at $t = 8500$ and $z = 36$ (shaded contours) and of the mode M_G (solid lines) (a); of the perturbation extracted from DNS at $t = 8500$ and $z = 26$ (shaded contours) and of mode M_S (solid lines) (b). In both cases the solid lines and the shaded contours represents 14 contours from -1 to 1, where the perturbations have been normalized with respect to their maximum value.

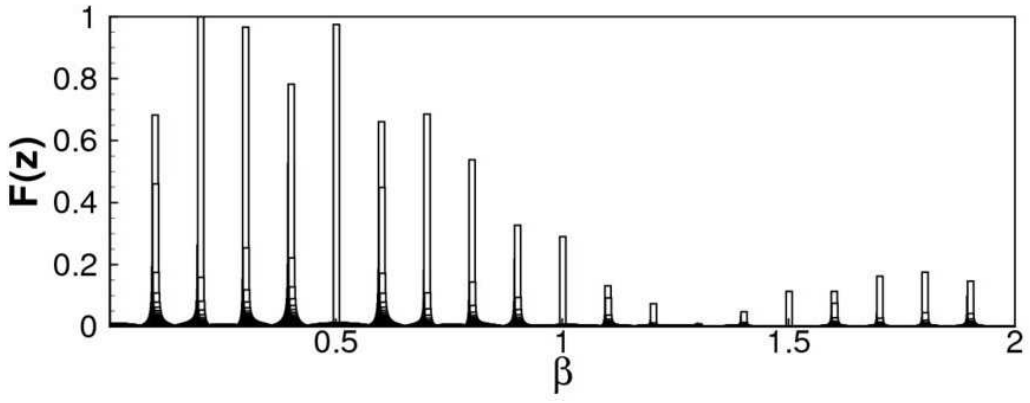

Figure 6.33: Fourier transform in the spanwise direction of the streamwise velocity extracted by a DNS initialized by the optimal initial perturbation with amplitude $A_0 = 10^{-4}$ at $t = 12000$, $x = 250$ and $y = 1$.

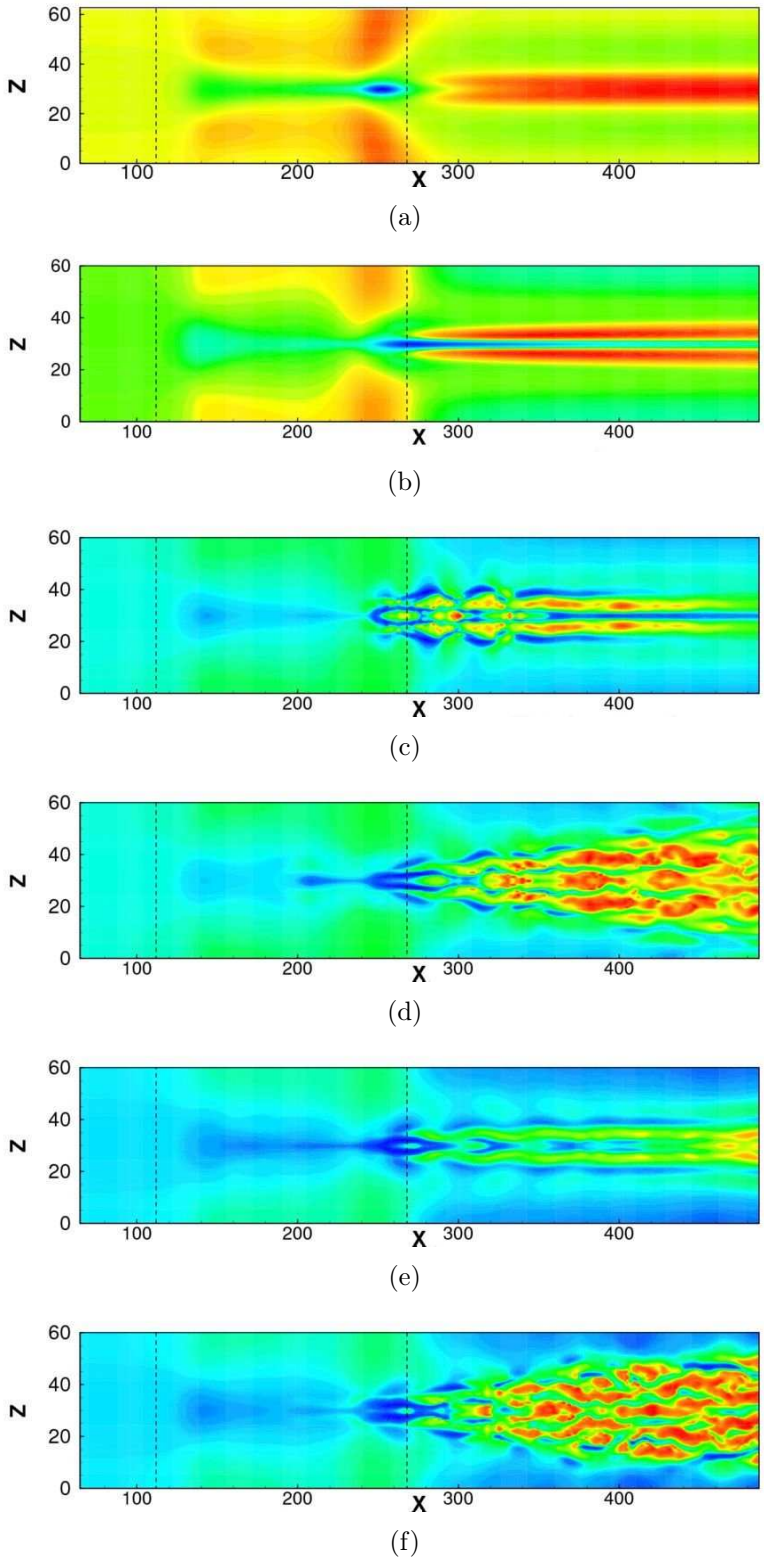

(a)

(b)

(c)

(d)

(e)

(f)

Figure 6.34: Streamwise component of velocity at $y = 1$ and $t = 4500$ (a), $t = 8500$ (b), $t = 9500$ (c), $t = 10500$ (d), $t = 11000$ (e), $t = 12000$ (f), extracted from a DNS initialized with the optimal perturbation of amplitude 10^{-4}. The dashed lines represents the separation and reattachment abscissae.

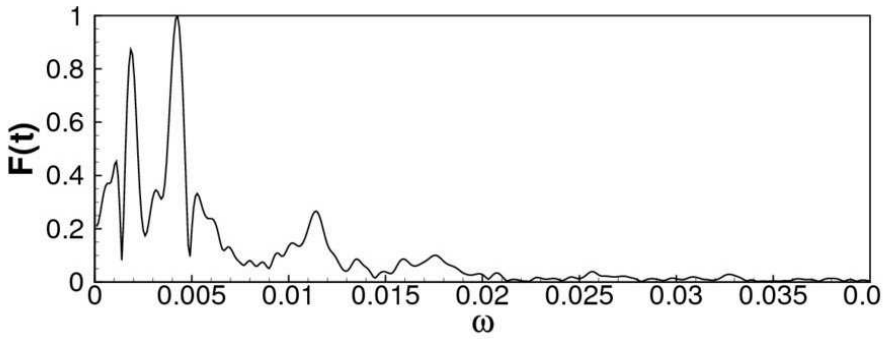

Figure 6.35: Power density FFT transform in time of the energy signal from $t = 8500$ to $t = 26500$.

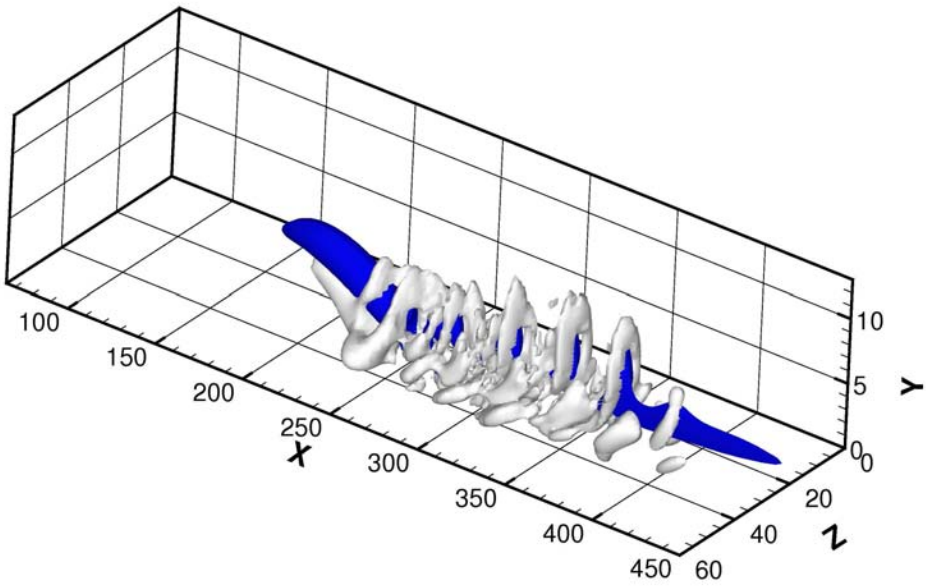

Figure 6.36: Iso-surfaces of the vortical structures identified by the Q-criterion (light surfaces) and of negative streamwise perturbation (dark surfaces) at $t = 10000$ (surfaces for $Q = 6$, $u = -0.2$).

to breakdown. As shown in Figure 6.36 (a) by the light iso-surfaces, a series of hairpin vortices are clearly identified at this stage, all of them presenting a low-momentum region between their legs (the blue surface represents a negative streamwise perturbation). Evidence of hairpin structures have been experimentally (Swearingen and Blackwelder, 1987, Peerhossaini and Wesfreid, 1988) and theoretically (see Yu and Liu (1994), for instance) found for a quasi-varicose secondary instability of Gortler vortices. Figure 6.37 shows the shaded contours of the streamwise component of perturbation at $t = 10000$ on the plane $x = 260$. One can observe the mushroom-like structure typical of non-linearly saturated Gortler vortices which is distorted on the peak of the low-speed region as well as on both sides of the stem region. Such regions correspond to the ones where the varicose secondary mode computed by Yu and Liu (1994) for a pair of non-linearly saturated Gortler vortices attains its maximum value. The authors found that the varicose secondary instability of Gortler vortices is mainly due to the Reynolds stress-conversion mechanism associated with the wall-normal rate of strain $\partial U/\partial y$ of the base flow, whereas sinuous modes are mostly associated with the spanwise rate of strain $\partial U/\partial z$. It is so likely that, in the considered case, the presence of alternated Gortler vortices in the wall-normal direction (a feature of both modes M_S and M_G) induces a strong wall-normal shear, generating varicose oscillations and the subsequent hairpin vortices which are the primary cause of the secondary transition in the considered flow.

Such an hypothesis has been verified by extracting snapshots of the perturbation velocity and vortical structures at different instants of time when the energy of perturbations is about to rapidly increase, namely for $t \geq 9000$ (see Figure 6.25). Figures 6.38 (a), (b) and (c) provide the low and high speed streaks (blue and light blue surfaces, respectively) and the vortical structures (yellow surfaces) for $t = 9000$, $t = 9100$ and $t = 9300$, respectively. The vectors are shown on the plane crossing the vortical structure between the high- and low-speed elongated structure ($z = 28.5$) for $t = 9000$, $t = 9100$, and on the plane crossing the low-speed streak and the head of the hairpin ($z = 32.5$) for $t = 9300$. The dashed line in Figure 6.38 (a) shows that a shear layer is created by the vertical interaction of the low- and high-speed regions, which is almost parallel to the wall. A streamwise vortex can be observed between the two elongated structures and in correspondence with such a shear layer. A second vortical structure is also present on the opposite flank of the low-momentum zone (not shown). At $t = 9100$, the elongated vortex is broken into smaller pieces by the wall-normal oscillations of the low-speed streak due to its secondary instability, as shown in Figure 6.38 (b). Thus, several inclined shear layers are created (only two of them are shown by the dashed lines in Figure 6.38 (b)), all of them generated by the interaction of the low- and high-momentum regions. At $t = 9300$, the inclined vortices at the two flanks of the low-speed region are found to connect through vortical regions called the 'heads' of the hairpin, which are represented by the black circles in Figure 6.38 (c). Finally, a train of hairpin vortices in streamwise succession is generated, leading the flow to unsteadiness.

Thus, the present computations have shown that a secondary scenario of transition exists in a separated boundary layer flow at a low level of noise, which involves the breakdown of Gortler vortices and the generation of hairpin-like structures. It has been observed that the hairpin vortices are induced by the wall-normal shear layer present between the positive and negative Gortler vortices, validating the hypothesis that unsteadiness in this configuration is due to the secondary varicose instability of such elongated structures.

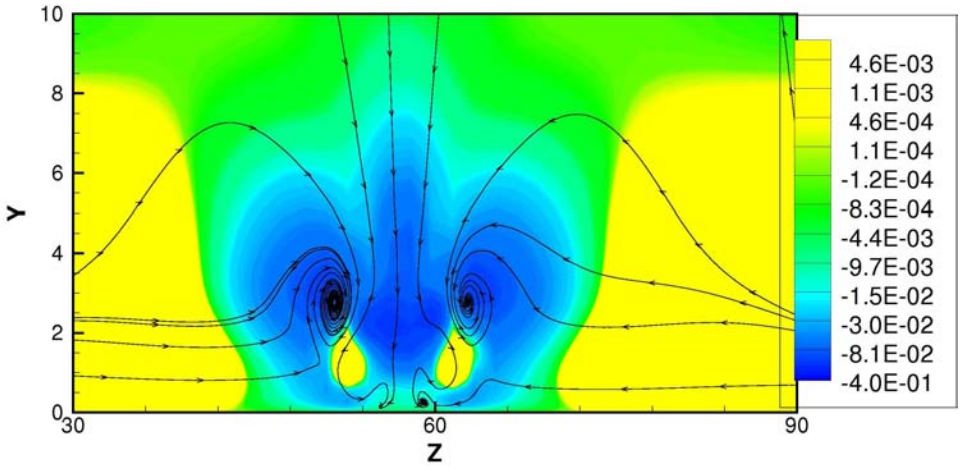

Figure 6.37: Shaded contours of the streamwise component of perturbation and streamlines extracted by DNS at $t = 10000$ on the plane at $x = 260$.

6.5 Discussion of the results

In this chapter the role of global centrifugal modes on the instability dynamics and the successive transition of a separated boundary layer flow has been investigated. The global eigenvalue analysis has been used in order to identify the three-dimensional centrifugal modes having the highest amplification rate. Among the others, two steady modes have been mostly analyzed, the unstable mode M_S and the stable one M_G. A Rayleigh criterion for M_S and a Gortler analysis for M_G have shown that these have both a centrifugal origin, the former due to an intrisic mechanism due to the curvature of the closed streamlines within the bubble, the latter due to a convective mechanism of Gortler type on the streamlines past the recirculation.
By means of DNS the onset of such centrifugal modes in the dynamics of the flow has been investigated, with respect to small or large amplitude perturbations. Both modes M_S and M_G have been recovered in the flow when it is perturbed with small amplitude perturbations. In particular, by means of a structural sensitivity analysis, it has been shown that the stable mode M_G could be excited by the convection of KH/TS waves along the shear layer, which a typical mechanism inducing a strong transient energy amplification in the considered separation bubble.
In the case of large amplitude initial perturbations, two different scenarios of transition are observed. The first scenario, which strongly recalls the K-type transition, is transient and due to the strong amplification and secondary instability of KH/TS waves. The second one, which is asymptotical and recovered for large times, is due to a convective mechanism resulting from the interaction of both modes M_S and M_G. In particular, it has been observed that a self-generation cycle of the perturbations is established; mode M_S has the

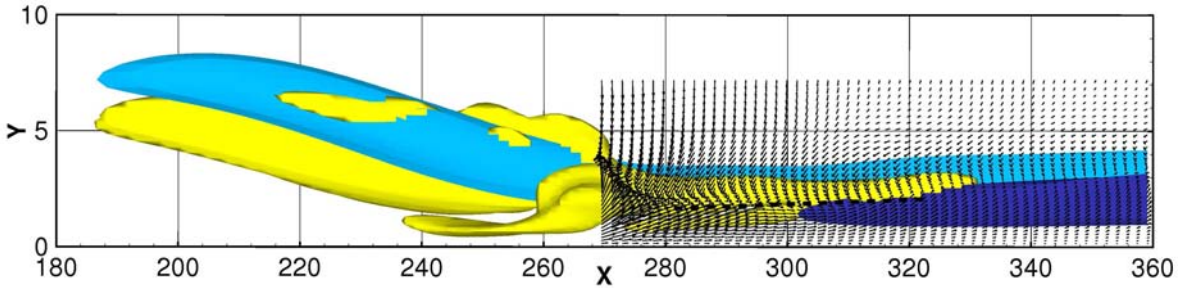

(a)

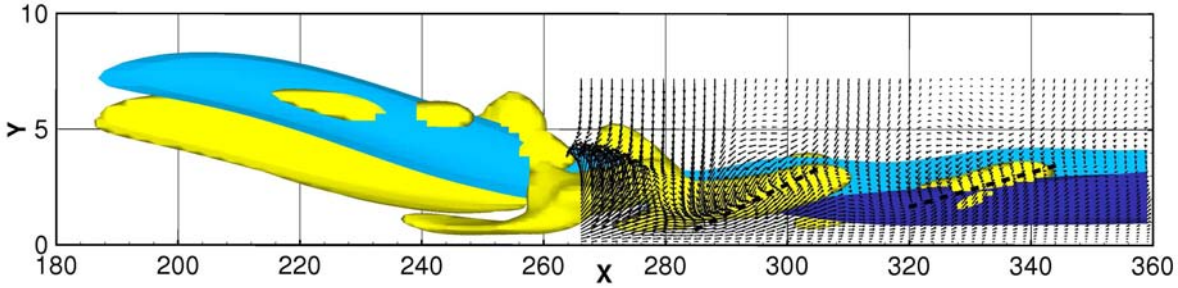

(b)

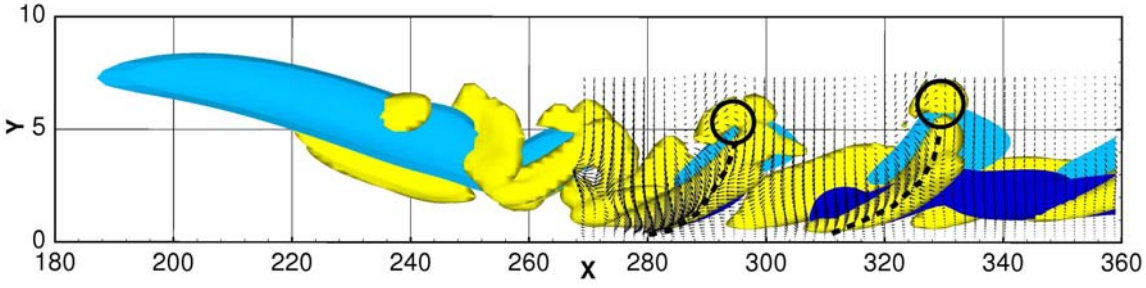

(c)

Figure 6.38: Surfaces of positive and negative streamwise velocity (dark and gray surfaces for $u = 0.1$ and $u = -0.1$, respectively) and of vortical structures represented by the Q-criterion at (a) $t = 9000$ (light surface for $Q = 5$), (b) $t = 9100$ (for $Q = 5$) and (c) $t = 9300$ (for $Q = 20$).

role of a *resonator*, placed within the separated zone, which is able to continuously sustain perturbations on the shear layer, exciting mode M_G which behaves as an *amplifier* of the perturbations produced by the resonator. Thus, Gortler rolls on the attached boundary layer are created and sustained, which undergo secondary varicose instability due to the wall-normal shear induced by the interaction of low- and high-momentum regions. Such mechanism induces the formation of a train of hairpin vortices in streamwise succession, which are often observed in the presence of Gortler vortices, leading the flow to transition. Thus, global and convective centrifugal modes have shown to play an important role in the destabilization and large-time transition of the separated flow under consideration. The scenario of transition via breakdown of Gortler rolls has been found to involve the formation of hairpin vortices in streamwise succession, which are a recurrent structure in transitional boundary layer flows (see Wu and Moin (2009)).

7

Three-dimensional optimal localized perturbations in an attached boundary layer

In the previous Chapters it has been investigated which kind of perturbation most easily brings a flat-plate separated boundary-layer flow on the verge of turbulence. It has been found that the most amplified disturbance in such a flow is a wave packet which transiently grows, while travelling downstream at the group velocity; for finite amplitudes, it could experience secondary instability inducing a K-type transition at small times.
For attached boundary layers, the perturbations inducing the maximum energy amplification have been computed in the eighties by means of local methods (see Corbett and Bottaro (2000), for instance); local optimal perturbations have been found to consist of pairs of counter-rotating streamwise vortices, capable to elicit streamwise streaks by the lift-up effect (Landahl (1980)). If growth is sufficient, such elongated structures could experience secondary instability and breakdown, due to the inflection of the velocity profiles in their interaction zone (Schoppa and Hussain (2002)).
Nevertheless, the local optimal perturbation concept has the limitation of focusing onto a single wavenumber/frequency at a time, plus that of neglecting non-linear effects. When a direct simulation is performed to assess the effectiveness of such perturbations in triggering transition, suboptimal disturbances are found to be much more efficient than optimals (Biau and Bottaro (2009)). Indeed, in practical cases boundary layers undergo transition by receptively selecting and amplifying exogenous disturbances, which are often localized and/or characterized by a wide spectrum of frequencies. Thus, it makes sense to inquire on the initial spatially localized flow patterns which most easily amplify and cause breakdown. However, nothing has been done so far to identify such initial localized states which are able to induce the formation of a turbulent spot.
In this Chapter the initial localized disturbances capable to provoke breakdown to turbulence effectively in a boundary layer are identified. The aim is to optimize not simply an initial state (at $x = 0$ or $t = 0$) characterized by a single wavenumber and/or frequency, but a wave packet, localized in the streamwise direction (and eventually also of limited spanwise extent). Direct-adjoint iterations have been used on a non-parallel boundary-layer flow in a localized domain, with no assumption on the shape and the frequency spectrum of the perturbation in all directions. To assess whether the optimal localized flow state is effective in provoking breakdown, direct numerical simulations are then performed, highlighting the importance of non-linear effects which lie at the heart of the origin of a turbulent spot.
This part of the thesis has been accepted for publication in the Journal of Fluid Mechanics

in January 2010.

7.1 Problem formulation

An attached boundary layer flow is here considered, evolving on a flat plate. Several rectangular computational domains are employed, the reference one having $L_x = 400$, $L_y = 20$ and $L_z = 2Z = 10.5$. The inlet is placed at $x_{in} = 200$ from the leading edge of the wall, whereas the outlet of the reference domain is placed at $x_{out} = 600$.
For the base flow computation and the DNS, at inlet points, a Blasius boundary–layer profile is imposed for the streamwise and wall-normal components of the velocity vector, and the spanwise component is set to zero. At outlet points, a standard convective condition is employed. At the bottom wall, the no-slip boundary condition is prescribed. At the upper boundary, the wall-normal velocity component of the Blasius profile is imposed, whereas the spanwise component and the vorticity are set to zero. Finally, in the spanwise direction, periodicity is imposed for the three velocity components. Most of the computations have been carried out at $Re = 610$.
For the direct-adjoint computations, a fringe region of length $L_f = 90$ is adopted for the computations on the reference domain, which has been described in Section 3.4. For the solution of the linearized Navier–Stokes equations, the reference computational domain is discretized by a $501 \times 150 \times 41$ Cartesian grid stretched in the wall-normal direction (the height of the first cell close to the wall is equal to 0.1, whereas the lengths of the cell in the x and z direction are 0.98 and 0.25, respectively). In order to ascertain that such a grid is sufficiently fine to accurately describe the linear dynamics of the considered flow, computations have been performed using a $801 \times 200 \times 61$ grid, and the results have been found essentially unchanged. Non-linear simulations have been performed using a finer grid ($801 \times 200 \times 121$) chosen in order to resolve also the small scales of turbulence. Moreover, the reference physical domain is increased to $L_x = 490$, to allow for a longer development of turbulent structures; this is achieved by replacing the fringe region with the convective boundary condition. A longer domain can thus be studied at a reduced computational cost.
Concerning the global model, the problem (3.27) is discretized employing $N = 1100$ modes. The modes are discretized using $n_x = 230$ collocation points in the x-direction and $n_y = 47$ collocation points in y-direction.

7.2 The linear optimal dynamics

Direct-adjoint computations are carried out at $Re = 610$, for a domain with dimensions $L_x = 400$, $L_y = 20$, $L_z = 10.5$, where the value of L_z is selected in order to obtain the largest amplification, as shown in Section 7.2.2. The optimal energy gain, $G(t)$, is found to reach, at the chosen convergence level $err = 10^{-5}$ (see the convergence study in Appendix B), a maximum of about 736, at time $T_{max} \approx 247$. Such a value is greater than that found by a local parallel approach at the same Reynolds number.

In order to get some insight onto the amplification mechanism, the evolution of the optimal perturbation in time is analyzed. In figure 7.1 the initial (at $t = 0$) optimal perturbation on the plane $z - y$ for a given streamwise position, $x = 450$, is depicted.

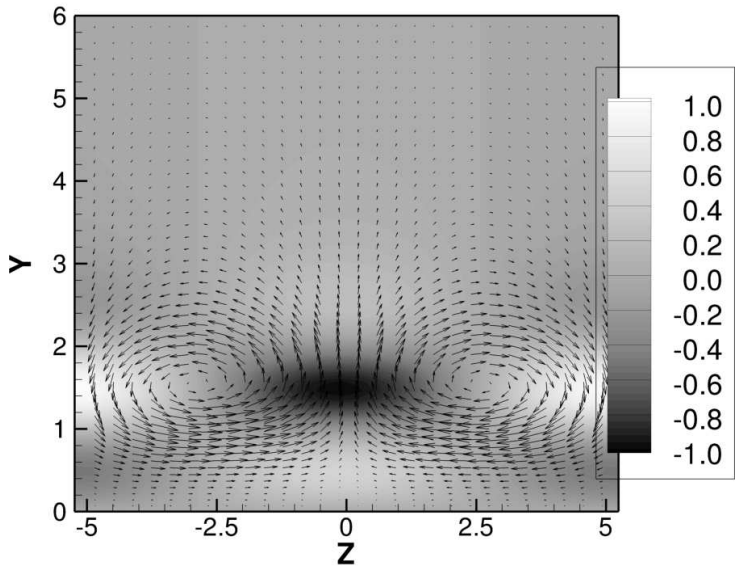

Figure 7.1: Optimal initial perturbation on the $x = 450$ plane for $Re = 610$. The vectors represent the v and w components whereas the shading is relative to the normalized streamwise velocity.

The optimal spatially localized initial disturbance is characterized by a counter-rotating vortex pair in the $z - y$ plane. In previous works, several authors (see Farrell, 1988, Butler and Farrell, 1992, Luchini, 2000, Schmid, 2000, Corbett and Bottaro, 2000) have optimized locally the time amplification in terms of the energy density of a perturbation characterized by a given wave number in both the streamwise and spanwise direction (denoted respectively by α and β). Those authors have found that the local optimal perturbation is characterized by a counter-rotating vortex pair in the $z - y$ plane, with no modulation in the streamwise direction ($\alpha = 0$), amplified in time by means of the *lift-up* mechanism (Landahl (1980)). In the present case, where the perturbation has no pre-assigned wavelength, a modulation is found in the x direction, the perturbation being composed by upstream-elongated structures with velocity components of alternating signs also in the $x - y$ plane, as shown by the iso-surfaces of the streamwise, wall-normal and spanwise velocity in figure 7.2. The time evolution of such an optimal solution shows that the perturbation tilts downstream via the Orr mechanism (Schmid and Henningson (2001)), while being amplified by the lift-up mechanism, resulting at the optimal time, T_{max}, in streaky structures with alternating-sign velocity components in the x direction, as displayed in figure 7.3. Indeed, the amplification of the initial perturbation is also due to the Orr mechanism and to the spatial growth related to the non-parallelism of the flow.

In order to estimate the importance of such effects, a direct-adjoint optimization is performed using a two-dimensional domain with $L_x = 400$ and $L_y = 20$, for which the lift-up mechanism is inhibited. In this case the energy gain reaches only a maximum value of 80 at time $t \approx 650$, which is very low with respect to the maximum amplification of the three-dimensional case, proving that both the Orr mechanism and the convective spatial

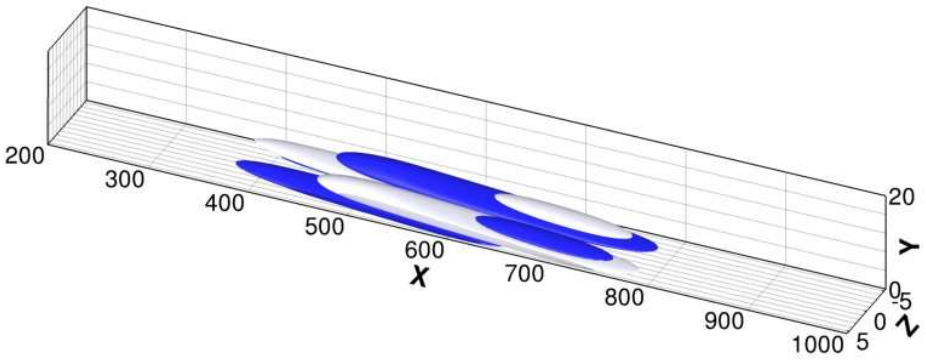

(a)

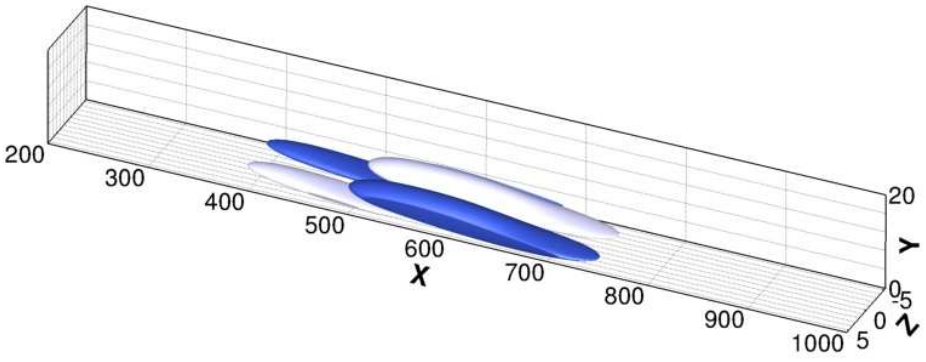

(b)

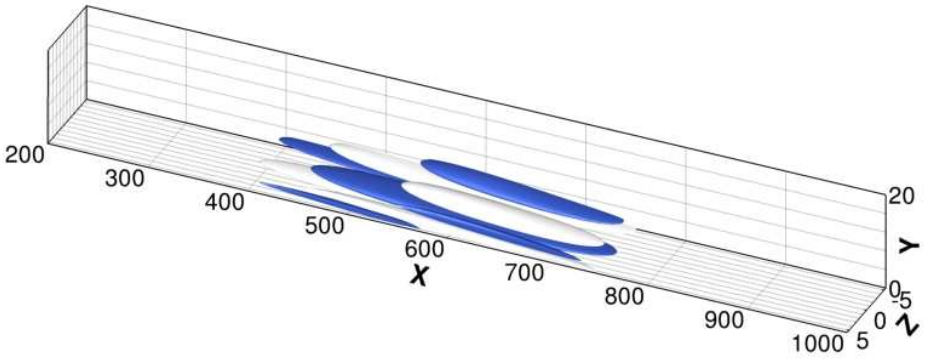

(c)

Figure 7.2: Iso-surfaces of the streamwise (a), wall-normal (b), and spanwise (c) velocity components of the optimal initial perturbation at $Re = 610$, for a longitudinal domain length $L_x = 800$. Light and dark surfaces indicate positive and negative values of the velocity components, respectively. The absolute values of their magnitude are 0.01 for the streamwise, 0.1 for the wall-normal, and 0.22 for the spanwise component. All the perturbations are normalized by the maximum value of the spanwise velocity component.

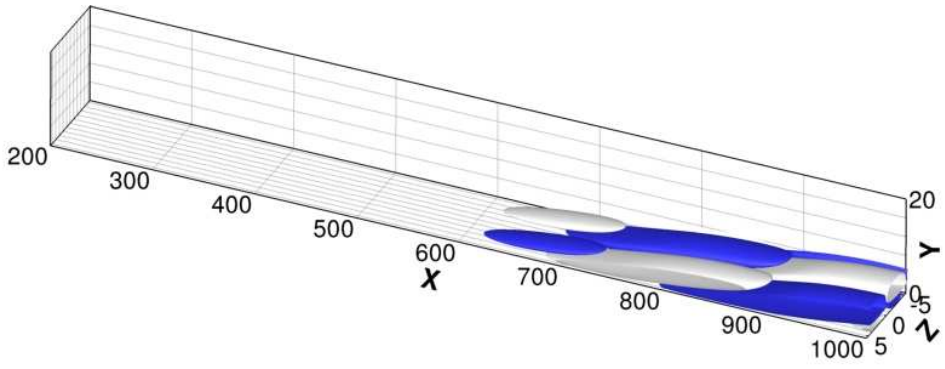

(a)

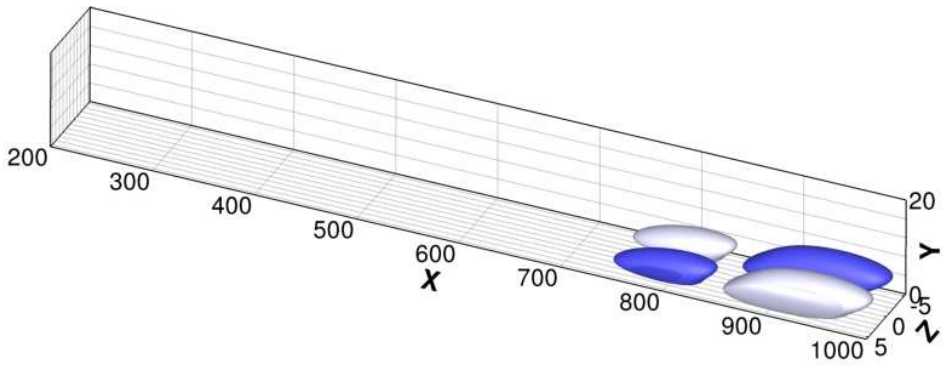

(b)

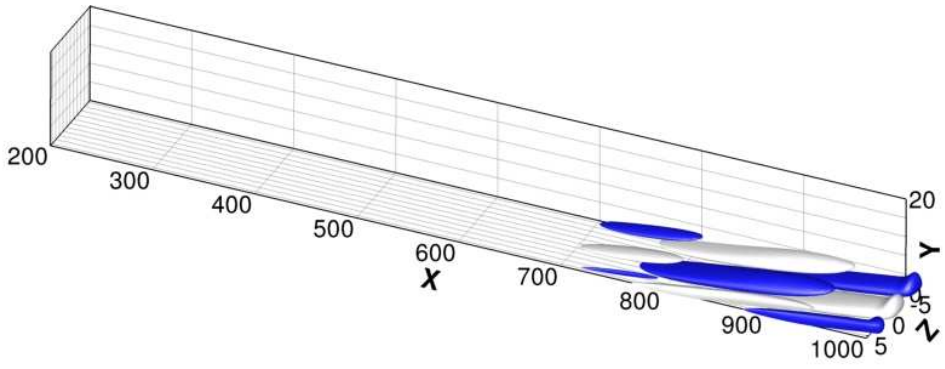

(c)

Figure 7.3: Iso-surfaces of the streamwise (a), wall-normal (b), and spanwise (c) velocity components of the optimal disturbance at $t = T_{max}$. Light and dark surfaces indicate positive and negative values of the velocity components, respectively. The absolute values of their magnitude are 1.8 for the streamwise, 0.1 for the wall-normal, and 0.5 for the spanwise component. All the perturbations are normalized by the maximum value of the spanwise velocity component at $t = 0$.

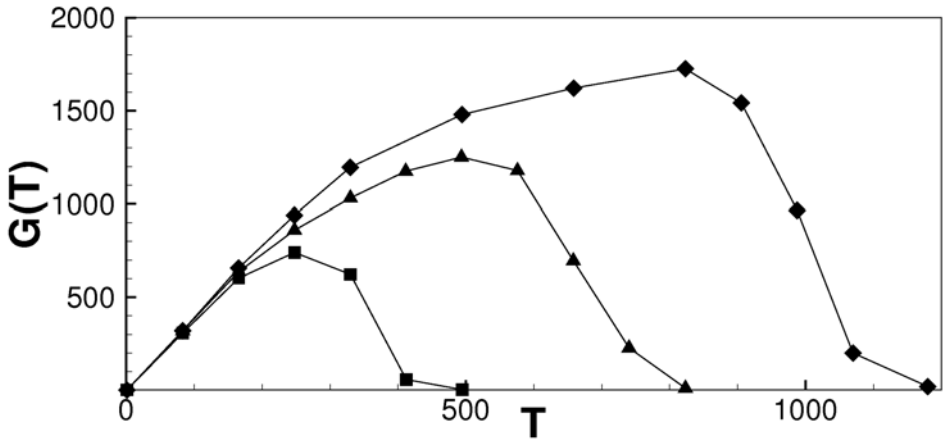

Figure 7.4: Envelope of the optimal energy gain computed by direct-adjoint method at $Re = 610$ for $L_{x1} = 400$ (squares), $L_{x2} = 800$ (triangles), $L_{x3} = 1200$ (diamonds).

growth have a secondary role in the three-dimensional optimal dynamics at $Re = 610$. In order to find how large is the contribution of the convective spatial growth mechanism, the two-dimensional optimization is also performed using the parallel flow obtained by reproducing at each abscissa the inlet base flow profile. The optimization gives an optimal value of the energy gain equal to 35, indicating that about one half of the two-dimensional energy growth is due to the convective amplification induced by the non-parallelism of the base flow.

7.2.1 Analysis of the streamwise modulation of the optimal perturbation

To investigate the influence of the longitudinal domain length on the transient amplification, two computations are performed with $L_{x2} = 800$ and $L_{x3} = 1200$, equal to two and three times the length of the reference domain. These two domains are discretized by 1001 and 1501 points in the streamwise direction, respectively. As shown in figure 7.4, the optimal energy gain reaches a peak of 1250 at $T \approx 490$ using L_{x2} and 1720 at $T \approx 821$ using L_{x3}, increasing of about 500 and 1000 units with respect to the value of G_{max} in the reference case. Such a strong increase of the energy gain with the longitudinal length of the domain is mostly due to a combined effect of the Orr mechanism and of the spatial amplification linked to the non-parallelism of the flow. Indeed, a two-dimensional direct-adjoint optimization performed using $L_{x2} = 800$ predicts again an increase of about 500 units for the $G(t)$ peak with respect to the value found for the reference domain with $L_{x1} = 400$. Moreover, the value of the optimal time increases linearly with the streamwise domain length. This could be expected by considering that the perturbation is convected by the base flow through the whole domain while amplifying itself, so that $t \propto L_x/U_\infty$. The effects of the variation of the domain length on the shape of the optimal perturbation are shown in figure 7.5, where the optimal initial solutions are provided, for L_{x1} and L_{x2} using dashed and solid lines, respectively. In order to allow a meaningful comparison, the

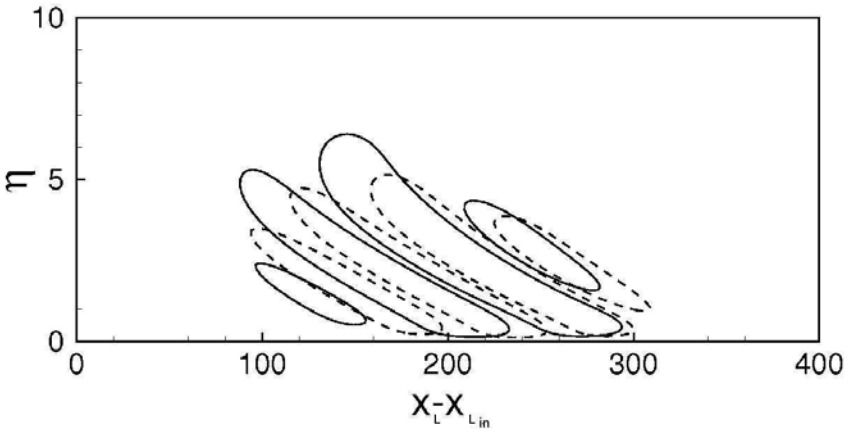

Figure 7.5: Contours of the streamwise component of the optimal initial perturbation for L_{x1} (dashed contours) and L_{x2} (solid contours) at $Re = 610$. The perturbations has been normalized by their maximum value; contours with absolute value equal to 0.15 are shown.

perturbation is plotted using normalized coordinates: the wall-normal self-similar coordinate $\eta = y\sqrt{Re/x}$, and the scaled abscissa $x_L = xL_{x_1}/L_x$. It can be noticed that the longitudinal extent, the inclination, and the modulation of the perturbations are approximately the same, meaning that, when observed in normalized coordinates, the result of the optimization depends mildly on the streamwise domain size considered to compute the objective function.

To verify such a result, the characteristic streamwise wavenumber (α_c), defined as the most amplified wave number recovered in the optimal initial perturbation by means of a spatial Fourier transform, is extracted from the optimal perturbation computed at different target times for the three domain lengths L_{x1}, L_{x2}, L_{x3} and scaled by L_x/L_{x_1}. The three normalized curves of α_c are plotted with respect to the scaled time $t_L = tL_{x_1}/L_x$. Figure 7.6 shows that the three curves collapse reasonably well onto one another, confirming the result that, using normalized coordinates, the shape of the optimal perturbation is approximately invariant with respect to the longitudinal length used in the optimization. Such a result allows us to reduce the number of independent parameters in the optimization, as the streamwise wavelength of the perturbation scales with L_x. It is noteworthy that the characteristic streamwise wave number, α_c, is rather high at small times and decreases with time towards an asymptotic value.

A similar analysis is carried out focusing on the influence of the Reynolds number on the optimal initial perturbation: the direct-adjoint optimization is performed for two smaller Reynolds numbers, $Re = 300$ and $Re = 150$. Both values of Re are chosen with the aim of keeping the entire flow, from the inlet to the outlet, locally stable with respect to Tollmien-Schlichting modes, in order to ensure that the x-modulation of the optimal perturbation is not due to the interaction of local optimals with such modes. Figure 7.7 provides the spanwise velocity component contours of the optimal initial perturbation computed at $Re = 610$ (solid line), $Re = 300$ (dashed line), $Re = 150$ (dotted line) and $L_x = L_{x1}$. At all values of Re the optimal perturbation displays a modulation in the x-direction. Moreover, the streamwise extent of the perturbation in normalized coordinates

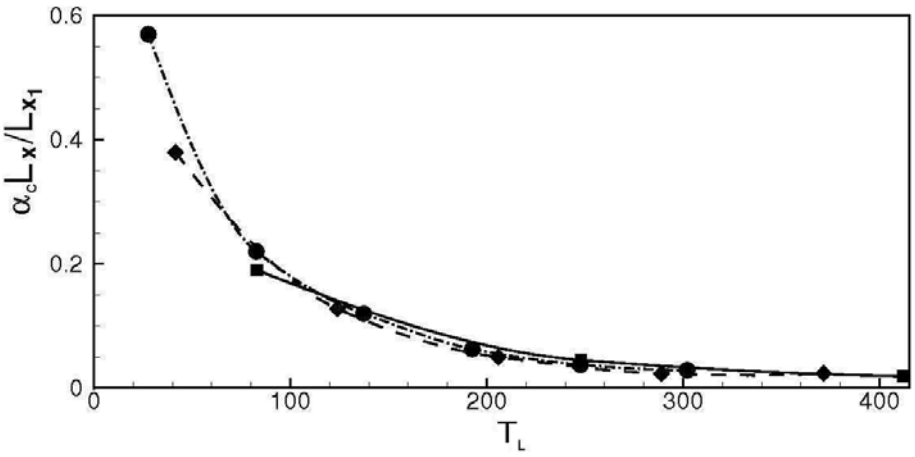

Figure 7.6: Normalized time versus the most amplified normalized longitudinal wave number at $Re = 610$, for $L_{x1} = 400$ (squares), $L_{x2} = 800$ (diamonds) and $L_{x3} = 1200$ (circles).

is found to vary, with an increase of the characteristic wavenumber with Re. To assess the variation of the streamwise modulation with the Reynolds number, the characteristic streamwise wave number, α_c, is extracted from the optimal initial perturbations computed at different target times for the three values of Re. The values of α_c, shown in Figure 7.8 (a) for each value of the target time ($T = 166, 247, 330, 420$, represented by squares, diamonds, circles and triangles, respectively) are found to scale well with the square root of the Reynolds number. Indeed, dividing the α_c values by the square root of the Reynolds number, the three curves collapse onto one for sufficiently large times (see Figure 7.8 (b)).

The results indicate that α_c behaves as

$$\alpha_c \propto \frac{\sqrt{Re}}{L_x}, \tag{7.1}$$

providing the variation of the optimal streamwise modulation with the domain length employed to integrate the objective function and with the Reynolds number. Using such a scaling law, one may recover the classical result on the optimal temporal growth in a parallel boundary layer flow, since it yields $\alpha_c \to 0$ for an infinitely long domain.

Once the dependence of the characteristic streamwise modulation on the independent parameters of the optimization, Re and L_x, is analyzed, the origin of such a modulation needs to be investigated. Since the global optimal perturbation is found to be characterized by more than one wavenumber in x, it is conjectured that it can originate from a superposition of local optimal single-wavenumber perturbations. Thus, following the method of Corbett and Bottaro (2000), a local optimization is performed using the inlet velocity profile as a base flow. Such an optimization is carried out for 160 values of α varying in the range $-0.4, 0.4$. To allow a meaningful comparison, the wave number of largest module, 0.4, is chosen larger than the largest streamwise wavenumber obtained by a spatial Fourier transform of the global optimal perturbation. Similar criterion is used to pick the wavenumber of smallest module, 0.005. A three-dimensional perturbation is

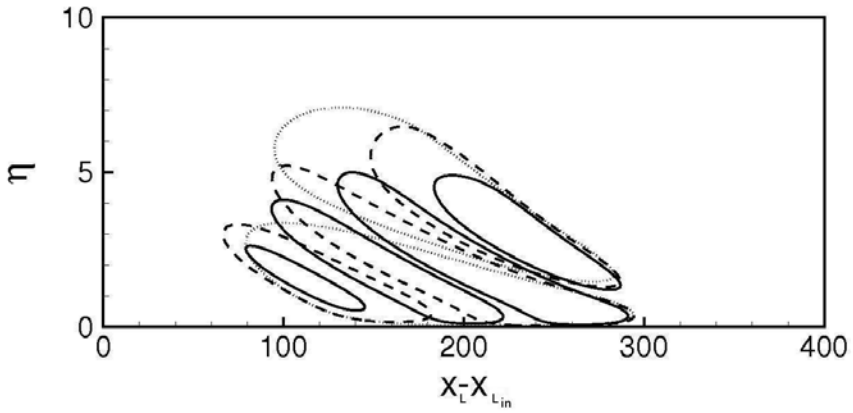

Figure 7.7: Contours of the spanwise component of the optimal initial perturbation for $Re = 610$ (solid contours), $Re = 300$ (dashed contours) and $Re = 150$ (dotted contours). The perturbations have been normalized by their maximum value; contours with absolute value equal to 0.15 are shown.

thus reconstructed as a superposition of the local optimal ($\alpha = 0$) and all the suboptimal ($\alpha \neq 0$) solutions computed at the target time T_{max}, namely:

$$\mathbf{q}(x, y, z) = \sum_{j=1}^{n} \kappa_j \, \bar{\mathbf{q}}_j(y) \exp\left(i\beta z - i\alpha_j x\right), \tag{7.2}$$

where $n = 160$, $\bar{q}_j(y)$ is the result of the local optimization at a given value of α (see Corbett and Bottaro (2000)), and κ_j is linked to the energy of each single-wavenumber perturbation. For the present analysis, a value of β equal to 0.6 is employed, corresponding to the optimal spanwise wavenumber (see section 7.2.2). At $t = 0$, all the locally optimized perturbations are superposed with initial energy equal to 1. Figure 7.9 shows for $t = T_{max}$ that such a reconstruction is able to qualitatively reproduce packets of counter-rotating vortices as well as the x-modulated streak-like structures, demonstrating that the three-dimensional dynamics of a boundary layer is characterized by the superposition of modes with zero and non-zero streamwise wave number. The analysis of the variation of α_c with time is also performed for the three-dimensional perturbation reconstructed as a superposition of local optimal and suboptimal perturbations. As shown in figure 7.10, the α_c curves obtained from the global optimal perturbation and the superposition of local optimal and suboptimal solutions, for $L_x = 800$, are found to be very close for all times but the smallest ($t = 41$), meaning that such a reconstruction is able to reproduce the streamwise wave number dominating the optimal dynamics.

7.2.2 Analysis of the spanwise modulation of the optimal perturbation

The effect of the spanwise domain length on the optimal dynamics is analyzed by performing the energy optimization for several lengths. Figure 7.11 (a) shows the behaviour of the

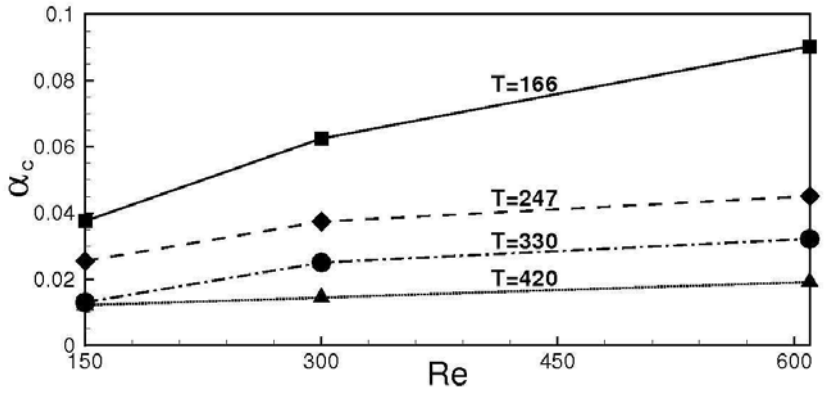

(a)

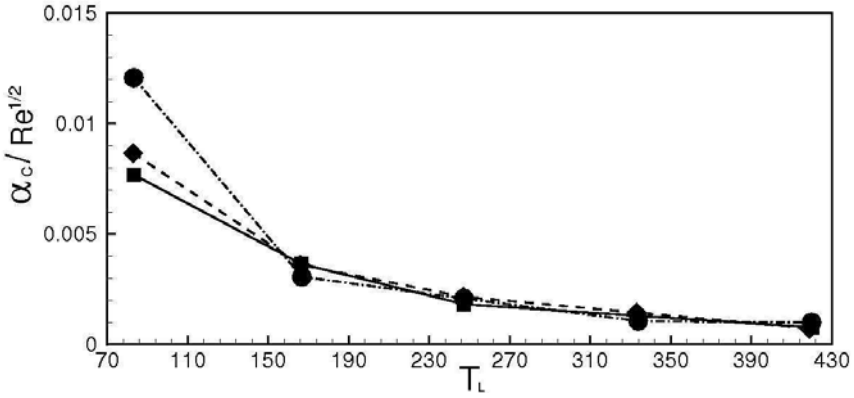

(b)

Figure 7.8: Most amplified longitudinal wave number versus the Reynolds number for $T = 166$ (solid line), $T = 250$ (dashed line), $T = 330$ (dashed-dotted line) and $T = 420$ (dotted line) (a). Most amplified longitudinal wavenumber normalized with respect to $\sqrt{Re}$ versus the normalized time for $Re = 610$ (squares), $Re = 300$ (diamonds) and $Re = 150$ (circles) (b).

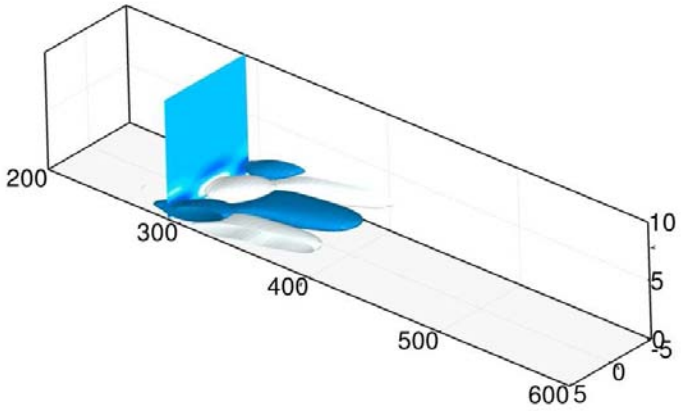

Figure 7.9: Iso-surfaces of the streamwise velocity component of the perturbation computed for $t = T_{max}$ by a superposition of local optimal and suboptimal perturbations for $\beta = 0.6$ and $Re = 610$. Light and dark surfaces indicate respectively positive and negative values of the velocity components of absolute value 0.75. The perturbation is normalized by its maximum value.

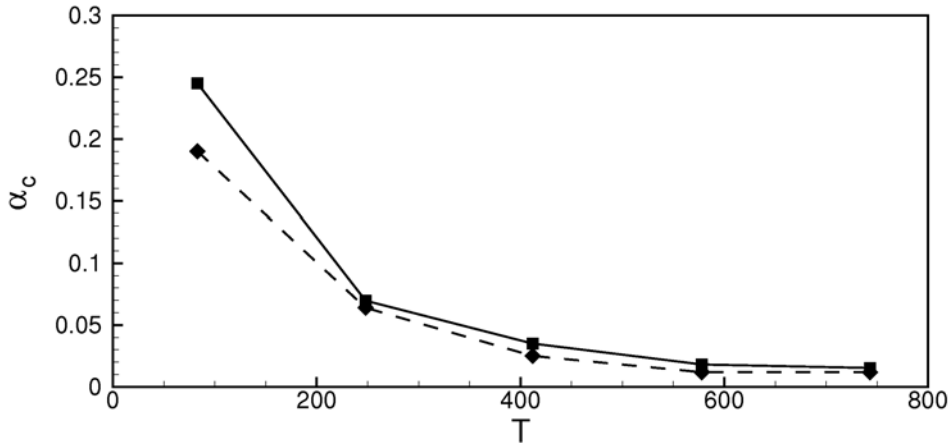

Figure 7.10: Most amplified longitudinal wave number versus time at $Re = 610$, obtained by the direct-adjoint method for $L_x = 800$ (diamonds) and by the superposition of local optimal and suboptimal perturbations (squares).

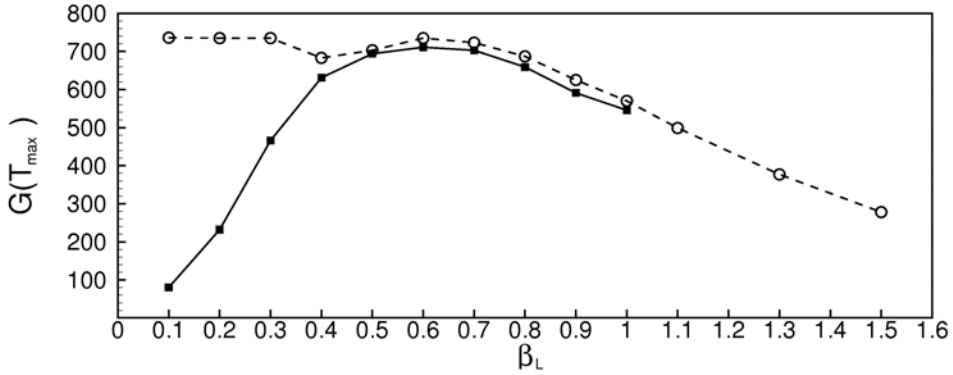

Figure 7.11: Peak value of the optimal energy gain versus the spanwise minimum wavenumber, β_L, obtained by the global model (squares) and by the direct-adjoint method (circles) with $\beta_L = (2\pi)/L_z$.

maximum optimal energy gain versus the spanwise minimum wave number, $\beta_L = (2\pi)/L_z$, computed by means of the global model (squares) and by the direct-adjoint procedure (circles). It is worth to point out that, concerning the global model, the wavenumber of the optimal perturbation is prescribed, $\beta = \beta_L$, whereas in the direct-adjoint computation β_L represents the minimum allowed value of the optimal perturbation wavenumber. Since the problem under consideration is homogeneous in the spanwise direction, it is anticipated that the result of the optimization would contain only one wavenumber in that direction, namely the one which is able to induce the largest amplification among the multiples of β_L. Thus, for small values of β_L, the two optimization methods would give different results, as one can notice in figure 7.11 (a). Indeed, the global model predicts a well defined peak for $\beta_L = 0.6$, hereafter called β_{opt}, corresponding to $L_z = 10.5$, which is very close to the optimal wave number computed locally by Corbett and Bottaro (2000). In the direct-adjoint optimization, for high values of β_L, the optimal amplification peaks match those computed by the global model, whereas a plateau is found for subharmonic values of β_{opt}, namely, $\beta_L = 0.1, 0.2, 0.3$. For such values, the wavenumber characterizing the perturbation is equal to β_{opt}, whereas for $\beta_L = 0.4$ one has $\beta = 0.8$. A similar behaviour is found for the optimal time (not shown): for subharmonic values of β_{opt}, the time of maximum growth in the direct-adjoint procedure matches the optimal time found when $\beta = 0.6$, whereas the global model predicts a large increase of the optimal time for low values of β_L.

The effect of the spanwise size of the domain onto the shape of the optimal perturbation is now analyzed. Figure 7.12 (a) shows the variation in time of the characteristic wavenumber, α_c, for several values of β_L larger than optimal. The values of α_c decrease for increasing β_L, showing a trend which is not far from that displayed for $\beta_L = \beta_{opt}$ (solid line). Indeed, they are found to slowly converge to a value different from zero, which is very close to that achieved asymptotically when $\beta_L = \beta_{opt}$. Figure 7.12 (b) shows the variation of α_c with time for two values of β_L smaller than optimal, more representative of realistic cases. The value $\beta_L = 0.035$ is chosen to be incommensurable with the optimal one. All the curves almost overlap the optimal one, indicating that, for a

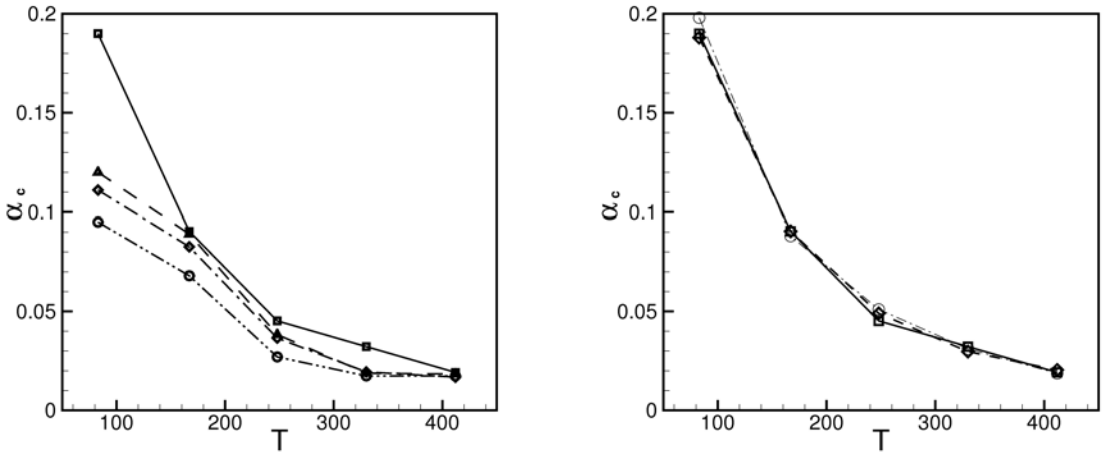

Figure 7.12: Most amplified longitudinal wave number versus time at $Re = 610$, obtained by direct-adjoint method for $\beta_L = 0.6$ (squares), $\beta_L = 0.8$ (triangles), $\beta_L = 1.0$ (diamonds), $\beta_L = 1.3$ (circles) (a), and for $\beta_L = 0.6$ (squares), $\beta_L = 0.1$ (diamonds), $\beta_L = 0.035$ (circles) (b).

sufficiently large domain, the streamwise shape of the optimal perturbation matches that obtained for $\beta = \beta_{opt}$. This is true even when the spanwise domain length is not an exact multiple of the optimal one. In conclusion, the three-dimensional optimal perturbation in a boundary layer is characterized, for large spanwise domain lengths (small β_L), by streamwise elongated structures alternated in the x and z directions with an angle $\Theta_{opt} = \arctan(\alpha_{opt}/\beta_{opt})$ ($\Theta_{opt} \approx 4.5°$).

7.3 The *near-optimal* linear dynamics

The results of the previous analysis show that the optimal three-dimensional perturbation is localized in x and characterized by a wide frequency spectrum in the streamwise direction. On the other hand, it is well known that such a perturbation has a spanwise sinusoidal shape since the problem under consideration is homogeneous in the spanwise direction. It could be argued that such a disturbance is not realistic; indeed, in a real framework, disturbances are most likely characterized by a range of frequencies, and not by a monochromatic signal, and are often localized in wave packets, for example when they are caused by a localized roughness element or a by gap on the wall. Thus, a *near-optimal* perturbation is now focused upon, characterized by the following features:

1. it must show a wide spectrum of spanwise frequencies,

2. it must be localized in both x and z,

3. it must amplify essentially as much as the "true" global optimal disturbance.

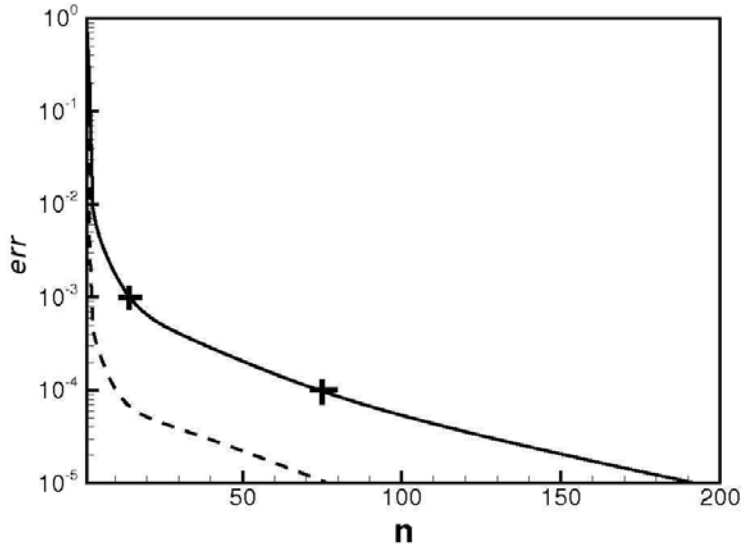

Figure 7.13: Normalized increment of the objective function versus the number of direct/adjoint iterations represented in a semi-logarithmic scale at $t = 247$ and $\beta_L = 0.1$ for a computation initialized by a wave packet (solid line) and a single-wavenumber initial guess (dashed line). The crosses indicates the convergence levels at which the *near-optimal* wave packets have been extracted.

In order to compute such a *near-optimal* perturbation, an artificial wave packet is built in the two domains of largest spanwise extent (corresponding to $\beta_L = 0.1$ and $\beta_L = 0.035$), by multiplying the optimal single-wavenumber perturbation times an envelope of the form $\exp -(z^2/L_z)$. Such a wave packet is then used as initial guess for the optimization procedure. Figure 7.13 provides the variation of the objective function versus the number of iterations for two computations with $\beta_L = 0.1$: the first one, initialized by the artificial wave packet (solid line); the second one, initialized by a single-spanwise-wavenumber perturbation (dashed line). One could observe that both curves experience a marked change in slope and that, in the first case, the convergence is slower. The partially optimized perturbation is extracted at two levels of convergence, *err* (defined in the appendix). Figure 7.14 shows such intermediate solutions at $err_1 = 10^{-3}$ and $err_2 = 10^{-4}$ (indicated with crosses in Figure 7.13), as well as the wave packet used as the initial guess. It is possible to notice that at err_1 the perturbation is still spanwise localized, although its shape has changed. In particular, the streak-like structures at the edge of the wave packet are inclined with respect to the z axis, resulting in oblique waves bordering the wave packet. Such a tilting is linked to the superposition of different modes in the spanwise direction. Indeed, Fourier transforms in z of the perturbation at different streamwise locations show that it is composed by many different modes, the spectrum being centered around the optimal wave number, as displayed in figure 7.15 (a). On the other hand, at the convergence level err_2 the disturbance is spread out in the whole domain, although a single-spanwise-wavenumber signal is not yet recovered. Most importantly, both solutions, although strongly different in the spanwise direction, are

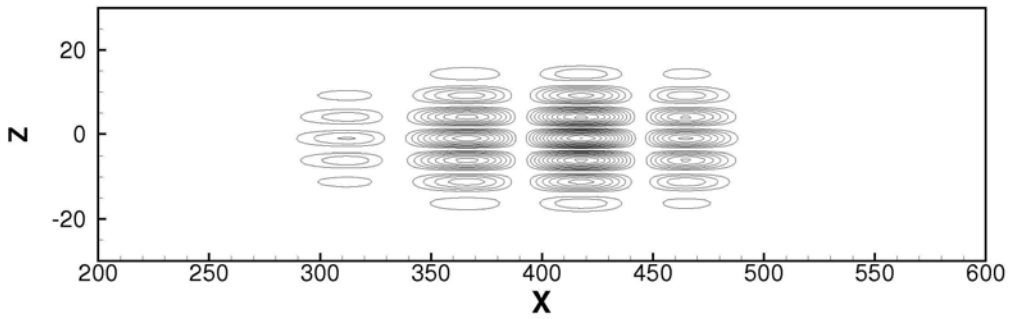

(a)

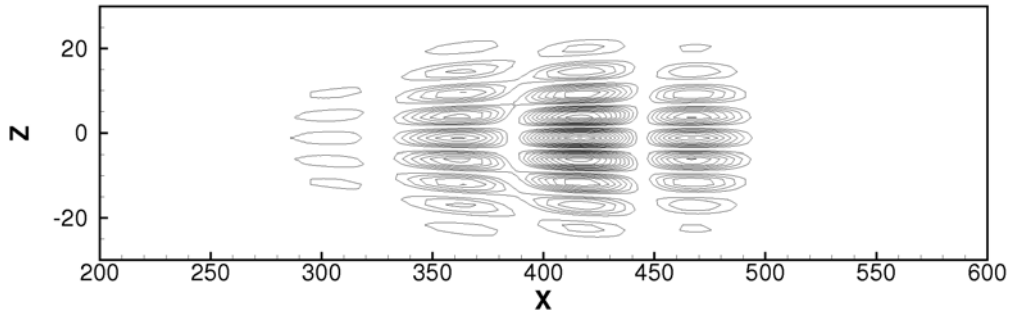

(b)

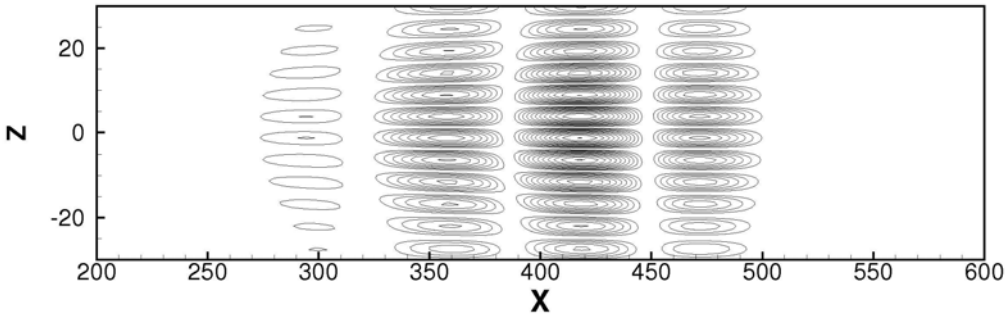

(c)

Figure 7.14: Contours of the perturbation streamwise velocity component for the initial guess (a), for the intermediate solution at $err_1 = 10^{-3}$ (b), and at $err_2 = 10^{-4}$ (c).

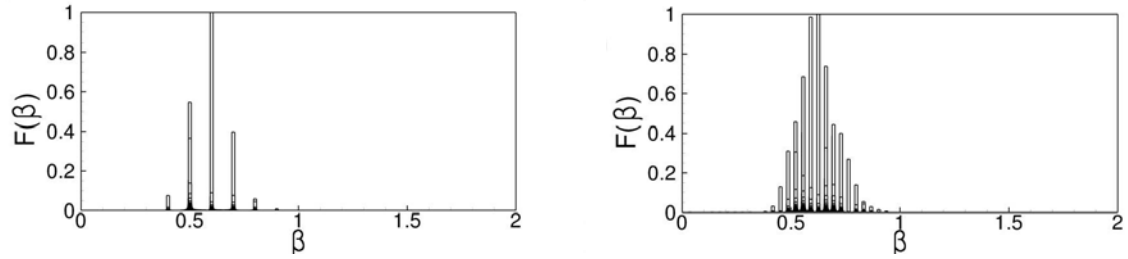

(a) (b)

Figure 7.15: Fourier transform in z at $y = 1$ and $x = 400$ of the streamwise velocity component of the solution at the convergence level $err_1 = 10^{-3}$ for $\beta_L = 0.1$ (a) and $\beta_L = 0.035$ (b). F(β) is the normalized Fourier coefficient.

very much amplified, reaching a value of G which differs by less than 1% from the optimal one ($G(t)_{opt} = 736$, $G(t)_{err_1} = 728$, $G(t)_{err_2} = 734$). Thus, it is possible to conclude that several near-optimal perturbations exist, intermediate solutions of the optimization process, characterized by different shapes in the spanwise direction, and producing very large growth in disturbance energy. It is worth to point out that such a result could have been anticipated, since the linearized Navier-Stokes operator is self-adjoint in the spanwise direction for the considered flow. Indeed, no transient energy growth can be produced in the spanwise direction, so that the influence of the spanwise shape of the perturbation on the energy gain is weak with respect to the streamwise and wall-normal ones. Therefore, a perturbation composed by a superposition of wavenumbers in the range $0.5 \leq \beta_L \leq 0.8$ (like the near-optimal wave packets at err_1 for $\beta_L = 0.1$ and $\beta_L = 0.035$ whose spectra are shown in figure 7.15 (a) and (b)) induce a quasi-optimal energy gain. Finally, it should be pointed out that the self-adjoint character of the Navier-Stokes operator in the spanwise direction may also explain the reduction of the convergence rate observed in figure 7.13 after level err_1, when the largest residual adjustments of the solution occur in the spanwise direction. In the following section the non-linear evolution of a *near-optimal* wave packet is studied, using the intermediate solution extracted at $err_1 = 10^{-3}$. Figure 7.16 (a) and (b) show such a state at $t = 0$ and $t = T_{max}$, respectively, for $\beta_L = 0.035$.

7.4 The non-linear dynamics

Although the optimal perturbation computed in the previous section is able to induce a very significant growth of the disturbance energy density in a linearized framework, it is not straightforward that it should effectively provoke transition. Therefore, the investigation of the non-linear evolution of such a global optimal state is worthwhile. Simulations of the Navier-Stokes equations are thus performed after superposing the initial optimal disturbance (with a given amplitude) to the base flow. The optimal transversal domain length $L_z = 10.5$ and a streamwise length of $L_x = 490$ are chosen. To allow a comparison with some of the most probable transition mechanisms already known in the literature, a direct numerical simulation is carried out also for the evolution of the local optimal (with $\alpha = 0$) and suboptimal (with $\alpha = \beta_{L_{opt}}$) perturbation superposed to the

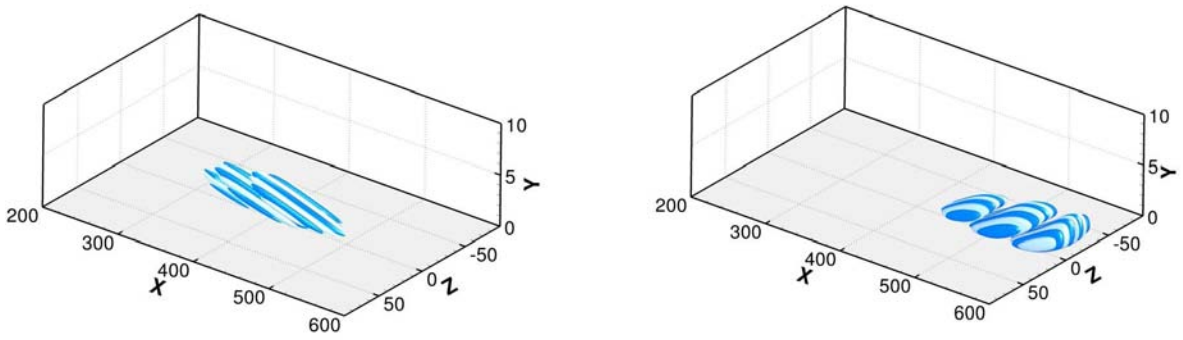

(a) (b)

Figure 7.16: Iso-surfaces of the streamwise component of the near-optimal perturbation at the convergence level $err_1 = 10^{-3}$ for $L_z = 180$ at the time instants $t = 0$ (a) and $t = T_{max}$ (b). Light and dark surfaces indicate respectively positive and negative values of the velocity component of absolute value 0.03 (a) and 3 (b), the perturbation being normalized by the maximum value of the spanwise velocity component at $t = 0$.

base flow, using the same initial energy as for the global optimal case. Figure 7.17 shows the mean skin friction coefficient obtained in the simulations initialized with three different initial energies: $E_{0(a)} = 0.5$, $E_{0(b)} = 2$ and $E_{0(c)} = 10$. The lowest and highest thin lines in figures 7.17 represent the theoretical distributions of the laminar and turbulent skin friction coefficient in a boundary layer, whereas the solid, dashed and dash-dotted lines are the mean skin friction coefficients obtained in the simulations initialized using the global optimal, the local optimal and the local suboptimal perturbation, respectively. The value of the energy $E_{0(a)}$ is found to be the lowest able to cause transition in the flow perturbed by the global optimal disturbance. Indeed, figure 7.17 (a) shows that in such a case the mean skin friction (solid line), which initially follows the theoretical laminar value, rises up towards the turbulent value. On the other hand, the skin friction coefficient curves relative to the local optimal and suboptimal cases lay on the theoretical laminar curve for $E_{0(a)} = 0.5$. Figure 7.17 (frames b and c) shows that the suboptimal x-modulated perturbation begins to induce transition for the energy value $E_{0(b)}$, whereas the zero-streamwise wave number perturbed flow experiences transition only for a rather large initial disturbance energy, $E_{0(c)}$. It is worth observing that such an initial energy value results in a streak amplitude prior to transition of 28% of the freestream velocity value, which is close to the threshold amplitude identified by Andersson et al. (2001) for sinuous breakdown of streaks. Moreover, such results point out the effectiveness of suboptimal perturbations in inducing transition, confirming those by Biau et al. (2008) for a square duct flow. It is interesting to observe that, when initialized by the global optimal disturbance, transition always starts around $x = 400$, almost irrespective of the initial energy level. This could be the signal of the emergence of a *global mode* (Huerre and Monkewitz (1990)).

To generalize the result to larger spanwise domain lengths, the non-linear evolution

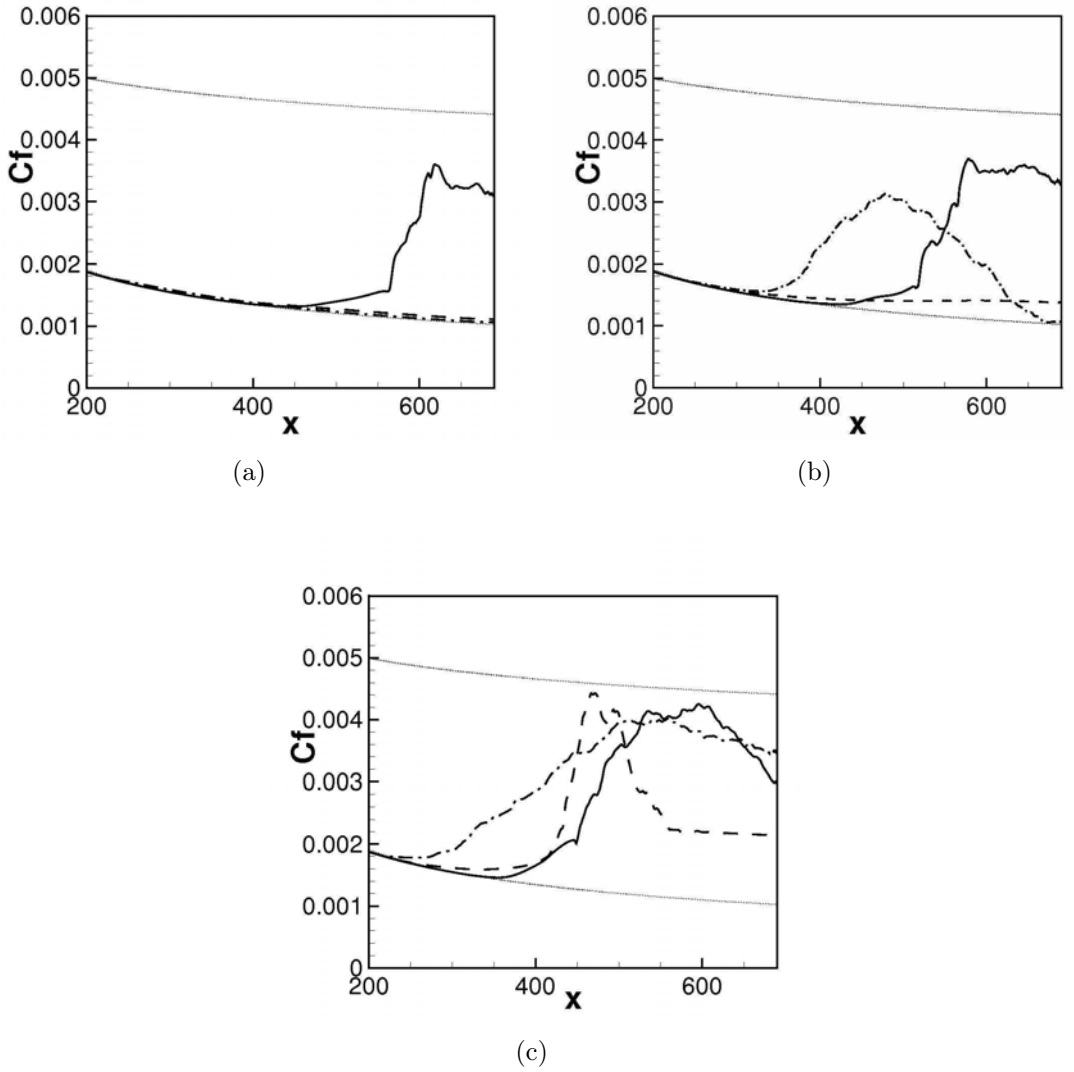

(a) (b)

(c)

Figure 7.17: Distribution of the mean skin friction coefficient at $t = 700$ for the base flow initially perturbed by: the global three-dimensional optimal (solid line); the local optimal with $\alpha = 0$ (dashed line); the suboptimal with $\alpha = \beta_{opt}$ (dash-dotted line). Three initial energy levels are considered: $E_0 = 0.5$ (a); $E_0 = 2$ (b); and $E_0 = 10$ (c). The lowest and highest thin lines represent the theoretical distributions of the mean skin friction coefficient for a laminar and a turbulent boundary layer, respectively.

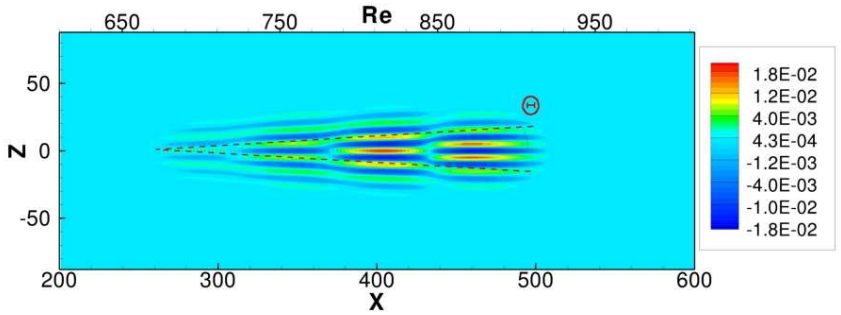

(a)

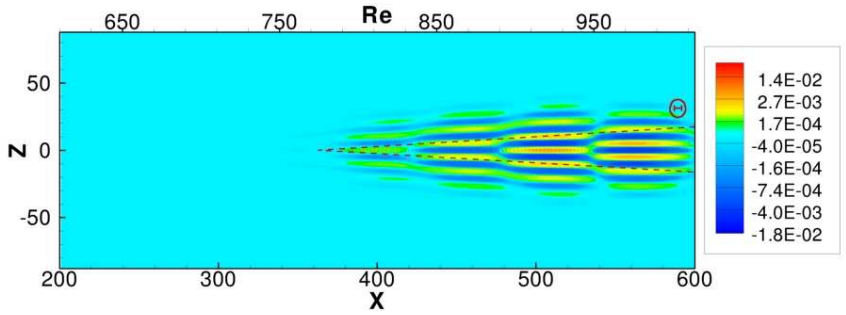

(b)

Figure 7.18: Contours of the streamwise component of the near-optimal perturbation for $\beta_L = 0.035$ on the $y = 1$ plane at $t = 0$ (a) and its linear evolution at $t = T_{max}$ (b).

of the *near-optimal* wave packet, discussed in the previous section, is simulated using a computational domain with $L_z = 180$. The initial energy is $E_0 = 0.5$ so that the flow is found to experience transition. Figure 7.18 (a) shows the perturbation on an $x - z$ plane at $t = 0$, and the angle Θ in the figure is equal to that obtained in the optimal case ($\Theta_{opt} \approx 4.5°$). Figure 7.18 (b) displays a snapshot of the state at the target time, $T_{max} = 247$, obtained by solving the linearized Navier–Stokes equations, for later comparison. The wave packet is convected downstream without remarkable structural changes and the angle Θ is unchanged with respect to 7.18 (a). Figure 7.19 (a) provides an instantaneous image of the non-linear evolution of the *near-optimal* packet at $t = 160$. The perturbation is mostly convected downstream, while being amplified. Whereas the streamwise modulation of the packet is almost unaffected compared to the initial solution, the flow structure experiences spanwise diffusion. At $t = 220$ (figure 7.19 (b)), the streaks partially merge, and two *kinks* appear near the leading edge of the most amplified streak, affecting the streamwise modulation of the wave packet. To better analyze such a stage of breakdown, local views of the contours of the wall-normal, spanwise, and streamwise perturbation velocity components are shown in figures 7.20 (a), (b), and (c), respectively. Two kinks are visible in the wall-normal and streamwise perturbation velocity components, alternated in the streamwise direction and symmetric with respect to the $z = 0$ axis. On the other hand, an array of spanwise-antisymmetric transversal velocity packets alternated in the longitudinal direction are observed in figure 7.20 (b). Such patterns are similar to those observed in the case of quasi-varicose streak breakdown (see Brandt et al. (2004)), likely to occur when a low-speed streak interacts with a high velocity one incoming in its

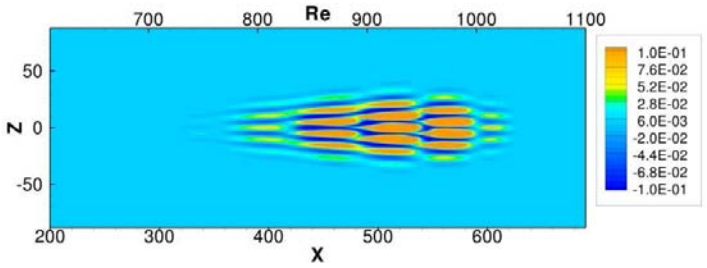

(a)

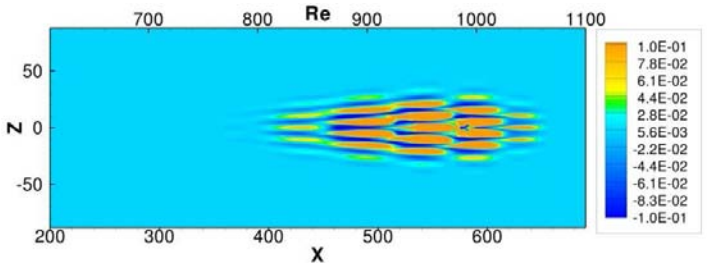

(b)

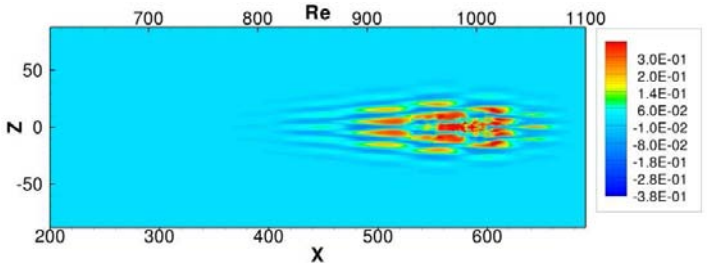

(c)

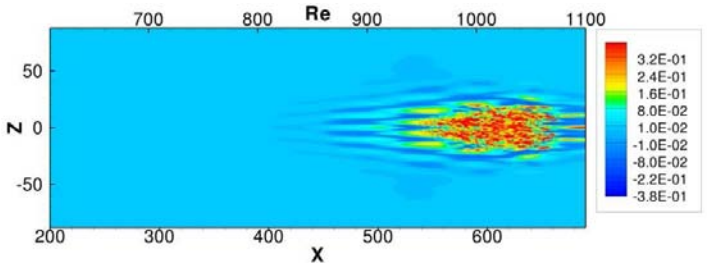

(d)

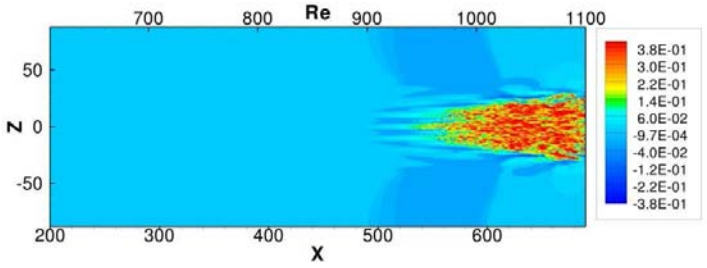

(e)

Figure 7.19: Contours of the streamwise component of the perturbation for $\beta_L = 0.035$ and $y = 1$, obtained by the DNS at $t = 160$ (a), $t = 220$ (b), $t = 250$ (c), $t = 330$ (d) and $t = 420$ (e).

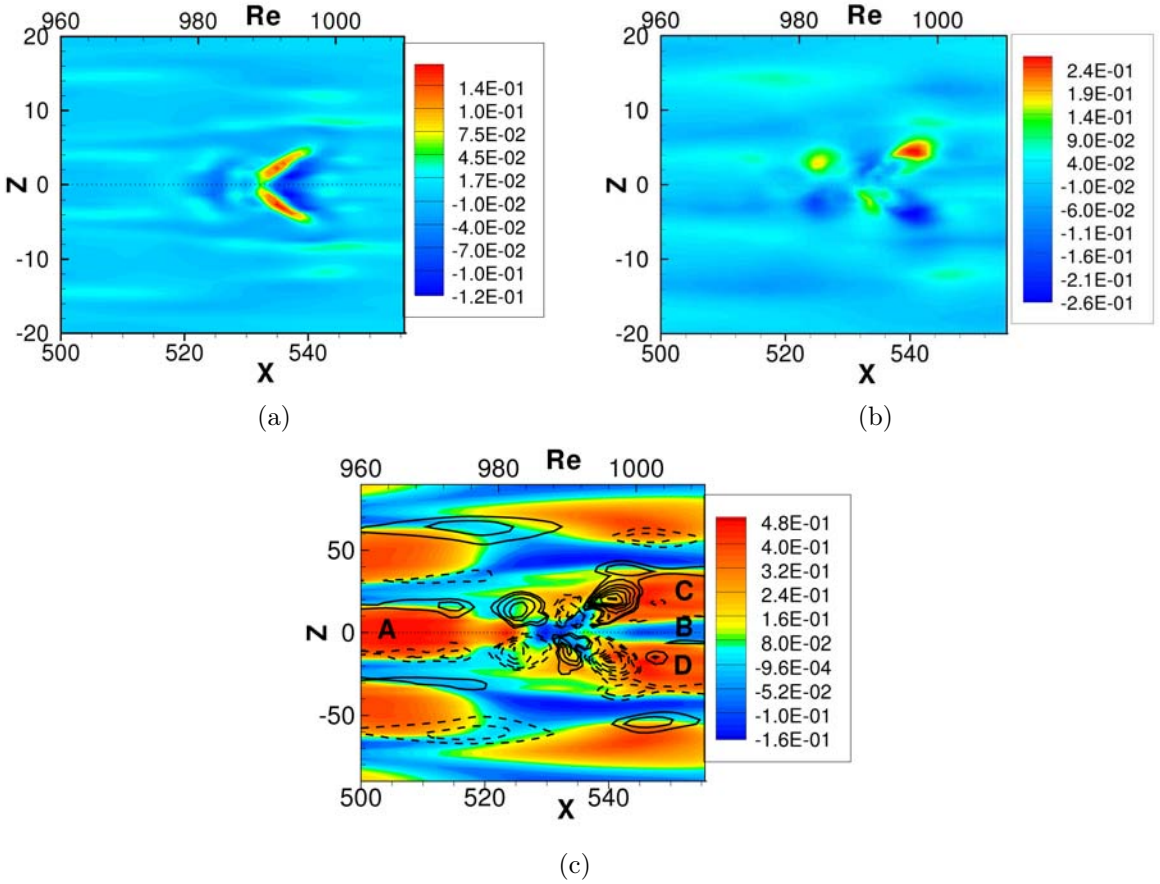

Figure 7.20: Contours of the wall-normal (a), spanwise (b) and streamwise (c) perturbation velocity components for $\beta_L = 0.035$ and $y = 1$ at $t = 220$. The dotted line is the $z = 0$ axis, whereas solid and dashed lines in (c) represent respectively positive and negative spanwise velocity contours.

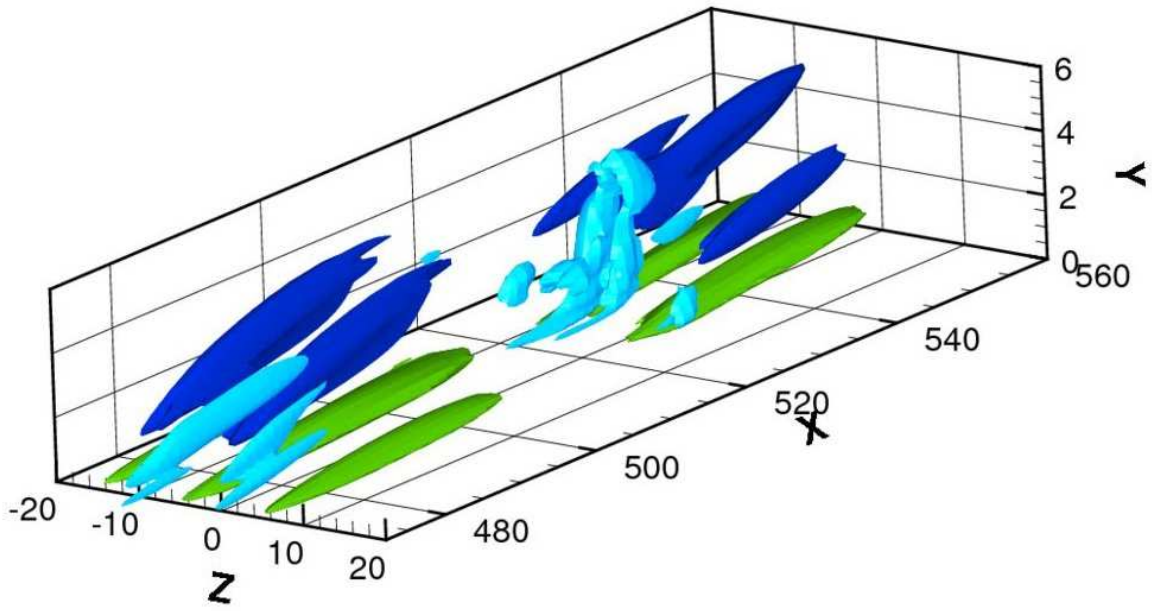

Figure 7.21: Iso-surfaces of the streamwise velocity, (blue represents negative perturbations whereas green indicates positive perturbations of absolute value equal to 0.5) and of the vortical structures identified by the Q-criterion (the light blue surfaces represents the positive value $Q = 660$) at $t = 180$.

front. In figure 7.20 (c) it can observed that the spanwise perturbations affect not only the streaks A and B on the $z = 0$ axis, but also the high-speed ones on the two sides of the $z = 0$ axis (labelled C and D). Indeed, the spanwise perturbations, although anti-symmetric about the $z = 0$ axis, are almost symmetric with respect to the middle axis of C and D. As a consequence, they induce spanwise oscillations on such streaks, resulting in a pattern which is typical of quasi-sinuous streak breakdown (*cf.* Brandt et al. (2004)). Thus, it can be concluded that both the scenarios of quasi-sinuous and quasi-varicose breakdown can be identified in the present case because of the staggered arrangement of the streaks, so that both front and side interactions between fast and slow velocity regions take place simultaneously. Therefore, in the highly symmetric configuration examined here, four streaks break down simultaneously, explaining the effectiveness of the global optimal and near-optimal perturbations in inducing transition.

To better study the vortical structure in the interaction zone, the Q-criterion (Hunt et al. (1988)) is adopted, which has been defined in Chapter 6. Figure 7.21 shows that, before breakdown, a hairpin vortex is present in the interaction zone of the streaks labeled as A, B, C, and D, preceded upstream by a pair of quasi-streamwise vortices. At the interior of the hairpin, a low-momentum region is found, corresponding to the low-speed streak B. This region tilts downstream, as also observed in the experiments by Lundell and Alfredsson (2004). To illustrate the mechanism of creation and breakdown of the hairpin vortex, the Q-contours identifying the hairpin vortex are plotted at four different times, together with the velocity perturbation vectors on the $x - y$ plane through its head. Figure 7.22 (a) shows the incipient hairpin at $t = 145$: two quasi-streamwise vortices,

which are placed on the flanks of the low-speed streak, begin to increase their size in the wall-normal direction, due to the increasing downstream tilting of the low-momentum streamwise fluctuations. Ahead of such streamwise vortices, an inclined shear layer is produced, induced by the front interaction of the upstream high-speed streak with the downstream low-speed one. At time $t = 165$, due to the further increase (because of lift-up) of the low- and high-momentum perturbations, non-linear effects allow the formation of a vortical region at the edge of the inclined shear layer, as shown in Figure 7.22 (b) by the black circle. Such a region of high spanwise vorticity generates an arch vortex connecting the two quasi-streamwise vortices, thus forming the head of the hairpin. At $t = 180$ (see figure 7.22 (c)), this head is lifted from the wall, and a second arch vortex appears upstream of the first, along the inclined zone of interaction of the low and high-speed streaks (shown by the second black circle in the figure). Finally, at $t = 190$, the first hairpin vortex further increases in size, while breaking up into smaller coherent patches of vorticity, although remnants of the original structure are still visible, *cf.* figure 7.22 (d).

A similar mechanism of generation of packets of hairpins has been discussed by Adrian (2007) for the case of fully developed turbulent boundary layers; in particular, the self-generation of packets of hairpins in streamwise succession, with size increasing downstream, was reported. Evidence for the presence of hairpin vortices in transitional flows has been recently given by Wu and Moin (2009), which have attributed the generation of such structures to the presence of Λ-vortices excited by receptivity to free-stream turbulence. In the present computation, it appears that the front interaction of the low and high momentum streaks is the primary cause of the hairpin formation in the early stages of transitions, whereas the subsequent induction of new hairpins is probably linked to the oscillations of the low-momentum fluid comprised between the legs of the hairpin.

Such a transition scenario is interesting because it somehow connects two opposite views of transition, namely that grounded on transient growth and secondary instability of the streaks (Brandt et al. (2004), Schoppa and Hussain (2002)), and the other based on vortex regeneration (Adrian (2007)). In fact, in previous studies of transitional boundary layer flows under free-stream turbulence (Brandt et al. (2004)), the presence of hairpin vortices was not observed, and the breakdown of the streaks was attributed to an instability of the inflectional velocity profiles due to the interaction of low and high-speed streaks.

Going back to the evolution in time of the perturbation, figure 7.19 (c) shows the presence of several subharmonics in both the streamwise and spanwise direction. Indeed, due to streak breakdown, close to the linearly optimal time (at $t = 250$) the most amplified elongated structures in the middle of the wave packet have already experienced transition. Later, as shown in figure 7.19 (d), the turbulent region spreads out in the spanwise and streamwise direction leading the nearest streaky structures to break up. Finally, at $t = 420$ (figure 7.19 (e)), the linear wave packet has totally disappeared and the disturbance takes the form of a localized *turbulent spot*. The spanwise rate of spread of the spot, defined as the angle at its virtual origin between its plane of symmetry and its mean boundary, is measured by using the criterion of the 2% freestream velocity contours proposed by Wygnanski et al. (1976). Such an angle is very close to that measured by Wygnanski et al. (1976) for a boundary layer flow, namely about 9°. It is about twice the optimal inclination of the initial wave packet ($\Theta_{opt} = 4.5°$), showing that turbulence spreads out

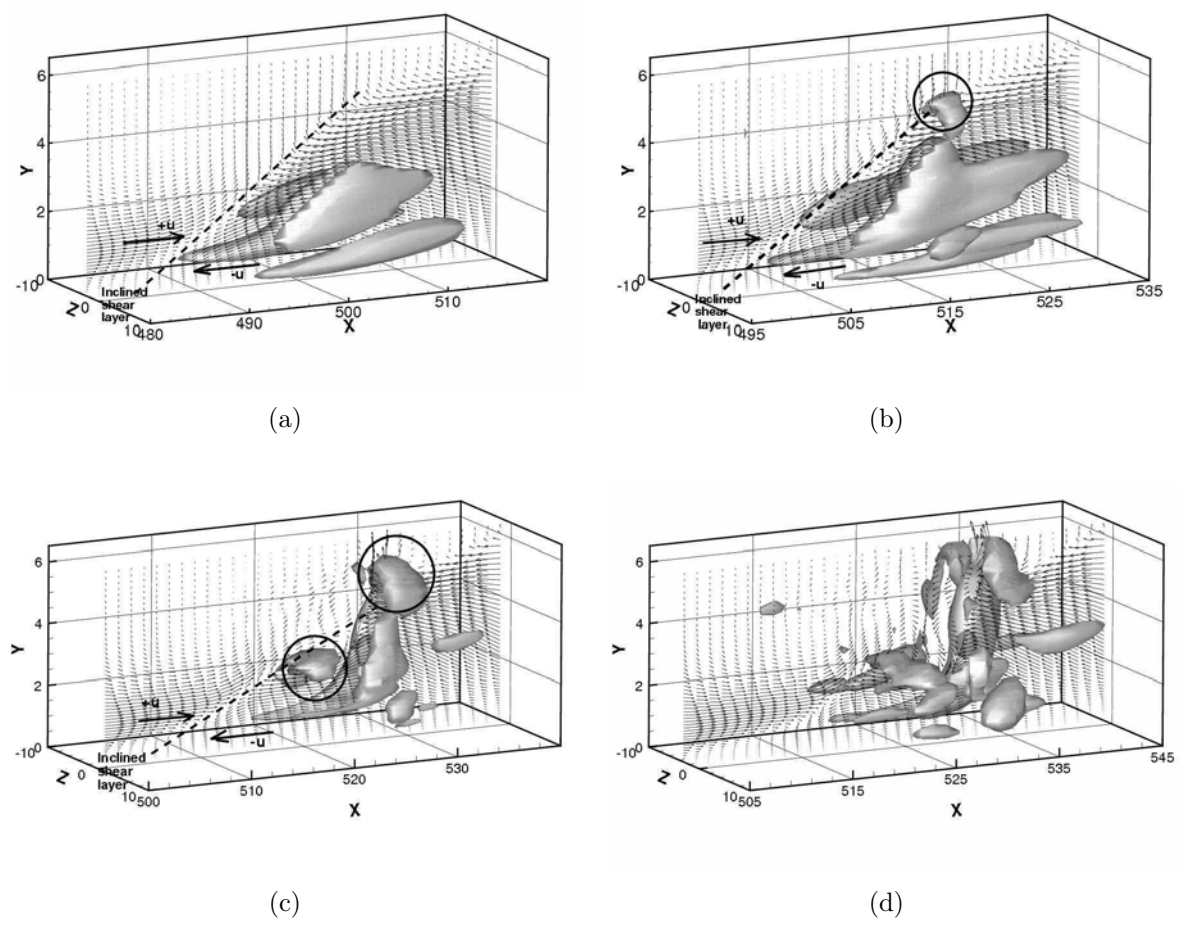

Figure 7.22: Iso-surfaces of the Q parameter and perturbation velocity vectors on the $z = 0$ plane at $t = 145$ (a), $t = 165$ (b), $t = 180$ (c), and $t = 190$ (d). The surfaces represent the positive values $Q = 370$ for (a) and (b), and $Q = 700$ for (c) and (d).

more quickly in the spanwise direction than in the streamwise one. Moreover, figure 7.19 (e) shows the presence of a *calmed region* trailing behind the chaotic zone, which is a typical feature of a turbulent spot (Schubauer and Klebanoff (1955)). Thus, the near-optimal wave packet computed by means of the three-dimensional direct-adjoint optimization represents a linear precursor of a *turbulent spot*. The size and position of a turbulent spot are usually chosen by receptivity, a process which in the present computations is bypassed by injecting on the base flow a localized disturbance of given energy resulting from an incomplete optimization procedure. For such a reason, no general conclusion about the streamwise position of turbulent spots in a real boundary layer flow can be drawn from here. Nonetheless, it can be concluded that the transition mechanism investigated here represents one – among many – viable path of transition via localized disturbances.

7.5 Discussion of the results

In this Chapter it has been investigated which initial disturbances are capable to provoke breakdown to turbulence effectively in a boundary layer. The aim has been to optimize not simply an initial state (at $x = 0$ or $t = 0$) characterized by a single wavenumber (in space) and/or frequency (in time), but a wave packet, localized in the streamwise and spanwise direction.

A direct-adjoint three-dimensional optimization procedure and a global eigenvalue analysis have been employed to compute the spatially localized perturbation capable to cause the largest growth of the disturbance energy in a finite non-parallel flat-plate boundary layer. The optimal initial perturbation is characterized by a pair of streamwise-modulated counter-rotating vortices, tilted upstream, resulting at optimal time in streak-like structures alternated in the streamwise direction. This indicates that perturbations with non-zero streamwise wavenumber have a role in the transient dynamics of a boundary layer. A scaling law has been provided describing the variation of the streamwise modulation of the optimal initial perturbation with the streamwise domain length and the Reynolds number.

Since the domain is homogeneous in the spanwise direction, the optimal initial perturbation is always characterized by a single wavenumber in this direction. Nevertheless, since for sufficiently large domains it is unlikely that a single-spanwise wavenumber disturbance emerges in a boundary layer as a result of exogenous forcing, a near-optimal localized perturbation characterized by a large spectrum of frequencies has been extracted during the optimization process. Such near-optimal initial disturbance is a wave packet of elongated disturbances modulated in the spanwise and streamwise direction, attaining a gain which is less than 1% smaller than the true optimal disturbance.

The capability of the localized optimal perturbations to induce transition has been investigated by means of direct numerical simulations. It is shown that the global optimal disturbance is able to induce transition for lower levels of the initial energy than local optimal and suboptimal perturbations. Interestingly, the local Reynolds number at which transition is initiated does not vary much with the initial energy level of the global optimal disturbance. Simulations are also carried out for the non-linear evolution of the near-optimal wave packet, which is found to evolve in a *turbulent spot* spreading out in

the boundary layer.
Transition is initiated in a region of the flow close to the center of the packet, by means of a mechanism including features of both quasi-sinuous and quasi-varicose breakdown. In fact, it is found that in this zone the streaks are able to interact on their sides as well as on their fronts, due to their alternated arrangement, so that more than one streak undergoes transition at the same time, explaining the efficiency of the optimal perturbation (as well as the near-optimal one) in yielding a chaotic behaviour. A hairpin vortex emerges in the region of interaction of the streaks prior to transition, generated by the inclined shear layer resulting from the front interaction of a low and a high-speed streak. Such an intense primary hairpin induces secondary hairpins and late stages of the breakdown see the continuous re-generation of such coherent structures.
The transition scenario presented here appears to connect two different views of transition, that based on transient growth and secondary instability of the streaks (Schoppa and Hussain (2002), Brandt et al. (2004)), and that which describes breakdown via the continuous regeneration of vortices (Adrian (2007), Wu and Moin (2009)). Although the present optimization is not capable to determine uniquely the x-position of a turbulent spot, an occurrence which depends on both receptivity and nonlinearity, the optimal and near-optimal wave packets computed by means of the three-dimensional direct-adjoint optimization represent a linear precursor of the spot, and the mechanism investigated here is a viable path to transition.

8

Conclusions and Outlook

The research presented in this thesis contributes to the study of the global instability dynamics in boundary-layer flows over a flat plate in a linear and non-linear framework. The goal has been to study in detail the different mechanisms inducing unsteadiness and transition in separated and attached flows over a flat plate, and to identify the disturbances which most effectively lead the flow to turbulence.

In Chapters 4, 5, and 6, several separated boundary layer flows are considered, obtained for different suction-and-blowing profiles at the upper boundary of the domain and for different values of the Reynolds number, all of them being highly non-parallel. In order to take into account the non-parallelism of the flows, a global eigenvalue analysis has been used in both a two- and three-dimensional framework, together with direct numerical simulations aimed at identifying the effects of non-linearity on the instability dynamics.

A study of the two-dimensional dynamics of the considered separated flows in Chapter 4 has clarified the role of non-normality and non-linearity of the differential Navier–Stokes operator on their instability. Linear eigenvalue analysis as well as numerical simulations with weakly non-linear perturbations have shown that the non-orthogonality of the convective Tollmien–Schlichting modes allows the bubble to act as a strong amplifier of small disturbances, due to a Kelvin-Helmholtz mechanism acting over the separation streamline. For finite amplitude initial perturbations, the energy exchange between modes due to non-linear effects induces the bubble to establish a wave packet cycle, similar to the one occurring at supercritical Reynolds numbers. Non-linear interactions contribute also to the excitation of a convectively unstable mode in the attached-flow region due to the high sensitivity of the boundary layer, inducing a further transient amplification of finite amplitude perturbations as well as an asymptotical instability at slightly subcritical Reynolds numbers.

Topological flow changes of the base flow have been found to occur close to transition, supporting the hypothesis of some authors (Dallmann et al., 1995, Theofilis et al., 2000) that the unsteadiness of separated flows could be due to structural changes within the bubble. Furthermore, non-normality effects have shown to play an active role also at large times, inducing a low-frequency oscillation, known as flapping frequency, due to the superposition of two convective non-normal modes. The onset of such a flapping frequency has been linked with the presence of topological flow changes of the base flow, and a possible explanation of such a behavior has been provided, in which it is conjectured that the oscillations are due to the interaction of the main wave packet with the perturbations carried upstream by the backflow inside the bubble. A scaling law based on the previous assumption is able to predict accurately the dependence of the flapping frequency on the

Reynolds number and the onset of a secondary frequency close to transition.
The amplifier dynamics and the flapping phenomenon could yield a possible scenario explaining the onset of unsteadiness in separated flows under the influence of localized disturbances, at subcritical and supercritical Reynolds numbers. However, the high non-normality of the considered separated flows has suggested that they may also act as a selective noise amplifier (Trefethen and Embree (2005)). Thus, in order to investigate whether and how the flow may select and amplify certain frequencies from the background noise, leading asymptotically the flow to unsteadiness, the sensitivity of the flow and its optimal response to an external forcing have been studied in Chapter 5 for several separated base flows.
It has been found that the most responsive disturbance takes the form of Kelvin-Helmholtz-like vortices, which roll up and amplify themselves along the shear layer, until being advected and die away in the attached boundary layer. An analysis of the value of the maximum response with respect to the size of the bubble has pointed out the crucial role of the shear layer in the response mechanism. Randomly perturbed direct numerical simulations have shown that the selected frequencies recovered by Fourier transform of the velocity signal in the asymptotic regime are in agreement with the most amplified frequencies derived from the optimal response analysis. For each flow a Strouhal number has been computed based on such frequencies, which has been found consistent with the ones based on the shedding frequencies measured by Pauley et al. (1990), Ripley and Pauley (1993), Lin and Pauley (1996) and Wasistho et al. (1997).
Thus, a connection has been established between the optimal response to external forcing and the asymptotical sustainement of vortex shedding at subscritical Reynolds numbers in separated flat-plate boundary-layer flows. However, it is known that in certain separated flows, a resonator dynamics associated with a three-dimensional global steady unstable mode may occur, which could dominate its asymptotic space-time dynamics.
In Chapter 6, by means of three-dimensional global eigenvalue analysis, a steady unstable mode has been recovered, together with a number of stable three-dimensional ones affecting the dynamics of the flow. The unstable and the less stable steady modes have been analyzed by means of a Rayleigh criterion and a Gortler analysis, demonstrating that such modes are originated by an intrinsic and convective (of Gortler type) centrifugal mechanism, respectively. By means of DNS, the onset and evolution of such centrifugal modes have been studied in a weakly non-linear framework. In particular, by means of a structural sensitivity analysis, it has been shown that the stable Gortler mode could be excited by the convection of KH/TS waves along the shear layer, which is a typical mechanism inducing a strong transient energy amplification in the considered separation bubble.
In the case of large amplitude initial perturbations, two different scenarios of transition are observed. The first scenario, which strongly recalls the K-type transition, is transient and due to the strong amplification and secondary instability of two-dimensional KH/TS waves. The second one, which is asymptotic and purely three-dimensional, is due to the interaction of the stable and unstable centrifugal modes. In particular, it has been observed that a self-generation cycle of the perturbations is established; the intrinsic mode has the role of a *resonator*, placed within the separated zone, which is able to continuously sustain perturbations on the shear layer, exciting the Gortler mode which behaves as an *amplifier* of the perturbations produced by the resonator. Thus, Gortler rolls on the

attached boundary layer are created and sustained, until they undergo secondary varicose instability due to the wall-normal shear induced by the interaction of low- and high-momentum regions. Such mechanism induces the formation of a train of hairpin vortices in streamwise succession, which are often observed in the presence of Gortler vortices, and which leads the flow to transition. Thus, global and convective centrifugal modes have shown to play an important role in the destabilization and large-time transition of the separated flow under consideration.

For the attached boundary layer, the aim has been to identify the initial localized states which most easily bring the flow to turbulence. In fact, local optimization (Corbett and Bottaro, 2000) could only focus onto a single wavenumber/frequency at a time, whereas in most practical cases boundary layers undergo transition by receptively selecting and amplifying exogenous localized disturbances characterized by a large spectrum of frequencies.

In Chapter 7 the initial wave packet capable to provoke breakdown to turbulence effectively in a boundary layer has been computed by means of a direct-adjoint method, with no assumption on the shape and the frequency spectrum of the perturbation in all directions. The global optimal initial perturbation is characterized by a pair of streamwise-modulated counter-rotating vortices, tilted upstream, resulting at optimal time in streak-like structures alternated in the streamwise direction; this indicates that perturbations with non-zero streamwise wavenumber have a crucial role in the transient dynamics of a boundary layer. A scaling law has been provided describing the variation of the streamwise modulation of the optimal initial perturbation with the streamwise domain length and the Reynolds number. In order to obtain a wave packet localized also in the spanwise direction, for sufficiently large domains a spanwise localized perturbation characterized by a large spectrum of frequencies has been extracted during the optimization process. Such near-optimal initial disturbance is a wave packet of elongated disturbances modulated in the spanwise and streamwise direction, attaining an energy gain which is less than 1% smaller than the true optimal disturbance.

The capability of the localized optimal perturbations to induce transition has been investigated by means of direct numerical simulations. It has been shown that the global optimal disturbance is able to induce transition for lower levels of the initial energy than local optimal and suboptimal perturbations. Moreover, the near-optimal wave packet has been found to evolve in a *turbulent spot* spreading out in the boundary layer. Transition is initiated in a region of the flow close to the center of the packet, by means of a mechanism including features of both quasi-sinuous and quasi-varicose breakdown. In fact, it is found that in this zone the streaks are able to interact on their sides as well as on their fronts, due to their alternated arrangement, so that more than one streak undergoes transition at the same time, explaining the efficiency of the optimal perturbation (as well as the near-optimal one) in yielding a chaotic behaviour. A hairpin vortex emerges in the region of interaction of the streaks prior to transition, generated by the inclined shear layer resulting from the front interaction of a low and a high-speed streak. Such an intense primary hairpin induces secondary hairpins and late stages of the breakdown see the continuous re-generation of such coherent structures.

The transition scenario presented here appears to connect two different views of transition, that based on transient growth and secondary instability of the streaks (Schoppa and Hussain (2002), Brandt et al. (2004)), and that which describes breakdown via the

continuous regeneration of vortices (Adrian (2007), Wu and Moin (2009)). The optimal and near-optimal wave packets computed by means of the three-dimensional direct-adjoint optimization could thus represent a linear precursor of the spot, and the mechanism investigated here is a viable path to transition.

8.1 Future works

In this thesis we studied the mechanisms which most effectively lead a flat plate boundary-layer flow to transition. An optimization of the energy based on the linearized Navier–Stokes equations is performed for both the separated or attached flows, aimed at identifying the perturbations inducing an optimal energy amplification at a finite time. For separated boundary-layer flows, only perturbations having a single spanwise wavenumber are considered, whereas, for the attached boundary layer, spanwise-localized perturbations are taken into account. It has been shown that such perturbations induce an energy gain close to optimal, and are able to effectively induce a turbulent spot. Thus, a similar analysis on spanwise-localized near-optimal disturbances could be performed on separated boundary-layer flows, in order to investigate which is the role of the spanwise direction in the amplification process, and whether spanwise-localized disturbances could induce turbulence effectively in such flows.
In this thesis, an optimization based on the linearized Navier–Stokes equations is used, and the effects of non-linearity are studied by performing direct numerical simulations following the evolution of the perturbations computed by means of the optimization. However, non-linear effects are not taken into account during the optimization process, so that some purely non-linear mechanisms might be neglected by such analysis. In fact, recent studies by Nagata (1990, 1997), Waleffe (1998), Faisst and Eckhardt (2003), Wedin and Kerswell (2004), Eckhardt et al. (2007) have outlined the possibility that transition could be related to some non-linear equilibrium solutions of the Navier–Stokes equations. The recent theory of Exact Coherent Structures (ECS) (Waleffe (1998, 2003)) has demonstrated some effectiveness in describing late stages of transition. The more convincing evidence for this has come from the circular pipe flow: ECS in the form of streamwise travelling waves have been identified in a pipe (Faisst and Eckhardt (2003), Wedin and Kerswell (2004)) which have close qualitative and quantitative similarities to the transient flow structures within a *puff* (Hof et al. (2004)).
Nevertheless, it is still unclear which type of perturbation is the most suited to excite such unstable states, taking the flow on the edge of chaos. Indeed, a weak connection has been found between the local linear optimal perturbations and the occurrence of travelling waves in a flow. Thus, a non-linear optimization could be carried out, aimed at investigating the existence of purely non-linear optimals, and of the non-linear mechanisms inducing energy growth and transition. Towards this end, an extension of the direct-adjoint optimization described here to non-linear Navier–Stokes equations is currently being pursued, and will be the object of future works aimed at clarifying which perturbations could optimally induce transition in flat-plate boundary-layer flows.

A

Suction velocity profiles: $V_{top}(x)$

The following tables define the values taken by V_{top} along the streamwise position $x - x_{in}$ for base flows bf1, bf2, bf3.

$x - x_{in}$	0	10	20	30	40	50	60
bf1	0.0227	0.0249	0.0308	0.0418	0.0614	0.0900	0.1155
bf2	0.0253	0.0277	0.0343	0.0467	0.0688	0.0983	0.1254
bf3	0.0295	0.0323	0.0401	0.0544	0.0780	0.1110	0.1406

$x - x_{in}$	70	80	90	100	111	120	130
bf1	0.1241	0.0097	0.0068	0.0445	0.0233	0.0029	-0.0164
bf2	0.1352	0.1083	0.0789	0.0547	0.0315	0.0084	-0.0142
bf3	0.1523	0.1266	0.0974	0.0722	0.0470	0.0206	-0.0066

$x - x_{in}$	140	150	160	170	180	190	200
bf1	-0.0329	-0.0448	-0.0532	-0.0529	-0.0411	-0.0263	-0.0149
bf2	-0.0357	-0.0546	-0.0685	-0.0734	-0.0670	-0.0523	-0.0355
bf3	-0.0335	-0.0597	-0.0862	-0.1041	-0.1014	-0.0813	-0.0557

$x - x_{in}$	210	220	230	240	250	260	270
bf1	-0.0077	-0.0043	-0.0030	-0.0013	0.0014	0.0036	0.0042
bf2	-0.0212	-0.0108	-0.0039	0.0003	0.0028	0.0041	0.0048
bf3	-0.0337	-0.0187	-0.0096	-0.0034	-0.0012	0.0041	0.0053

$x - x_{in}$	280	290	300	310	320	330	340
bf1	0.0038	0.0032	0.0028	0.0027	0.0027	0.0027	0.0026
bf2	0.0050	0.0050	0.0049	0.0047	0.0045	0.0042	0.0040
bf3	0.0054	0.0051	0.0048	0.0047	0.0046	0.0045	0.0043

$x - x_{in}$	350	360	370	380	390
bf1	0.0025	0.0024	0.0024	0.0023	0.0023
bf2	0.0038	0.0037	0.0035	0.0034	0.0033
bf3	0.0041	0.0039	0.0037	0.0036	0.0035

B

Convergence analysis of the optimization methods

B.1 The direct-adjoint method

The convergence properties of the algorithms are analyzed for the case of the attached boundary layer at $Re = 610$, using a domain with dimensions $L_x = 400$, $L_y = 20$, $L_z = 10.5$. The direct-adjoint optimization reaches a maximum value of the optimal energy gain, $G(t)$, of about 736 approximately at time $T_{max} \approx 247$ as shown in Figure B.1 (a). Figure B.1 (b) provides the normalized increment of the objective function, $err = (E(T)^{(n)} - E(T)^{(n-1)})/E(T)^{(n)}$, versus the number of iterations, n, for a direct-adjoint computation performed at the optimal time. The algorithm is able to reach very quickly a level of convergence of about 10^{-4}; then, the convergence rate decreases, so that about 80 iterations are needed to reach a level of convergence of 10^{-5}. Provided that only minor differences are observed between the solutions corresponding to the two convergence levels 10^{-4} and 10^{-5}, the convergence level 10^{-4} can be considered satisfactory.

It is worth to point out that the iterative optimization technique is equivalent to perform power iterations for the maximization of a Rayleigh quotient, a procedure which is mathematically guaranteed to converge to the global optimum. The convergence history depends slightly on the initial guess, as shown in figure B.2 (a) which provides the normalized increment of the objective function, err, versus the number of iterations for an initial guess resulting from: 1) the direct-adjoint optimization stopped at the level of convergence $err = 10^{-3}$ (diamonds); 2) the global model optimization (squares); 3) the global model optimization with a random noise of amplitude 10^{-8} superposed at the inlet points (triangles). It is observed that, although the convergence is accelerated for an initial guess extracted from a previous direct-adjoint optimization, the slope of the convergence curve slightly varies. Moreover, when the initial guess is perturbed with some noise, although the normalized increment, err, temporarily increases, a rapidly decreasing curve is quickly re-established. A study of the convergence history is carried out also with respect to the time step chosen for the computation: the convergence curves are found to be independent of such a parameter.

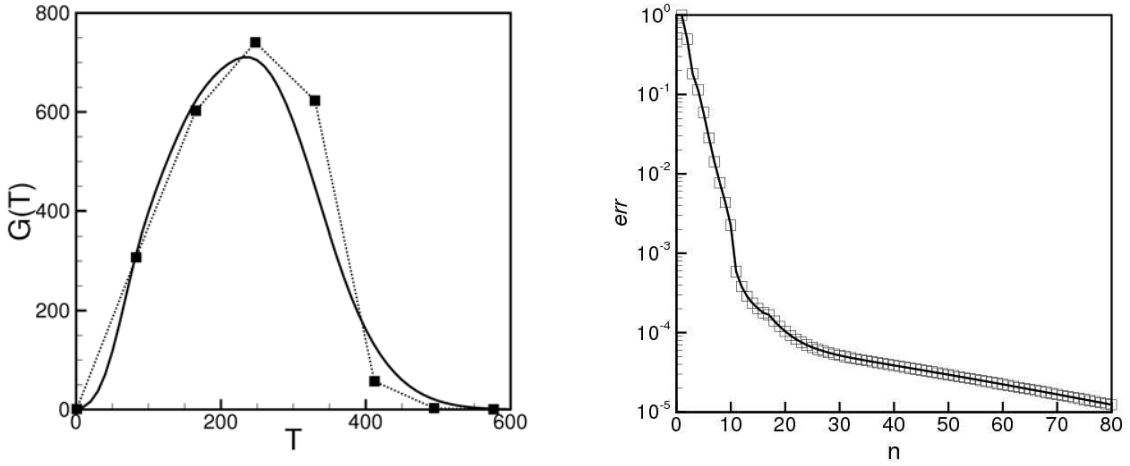

(a) (b)

Figure B.1: Envelope of the optimal energy gain obtained by the direct-adjoint method (black squares) and the global model (solid line) (a); normalized increment *err* of the objective function versus the number of iterations at $T = 247$ represented in a semi-logarithmic scale.

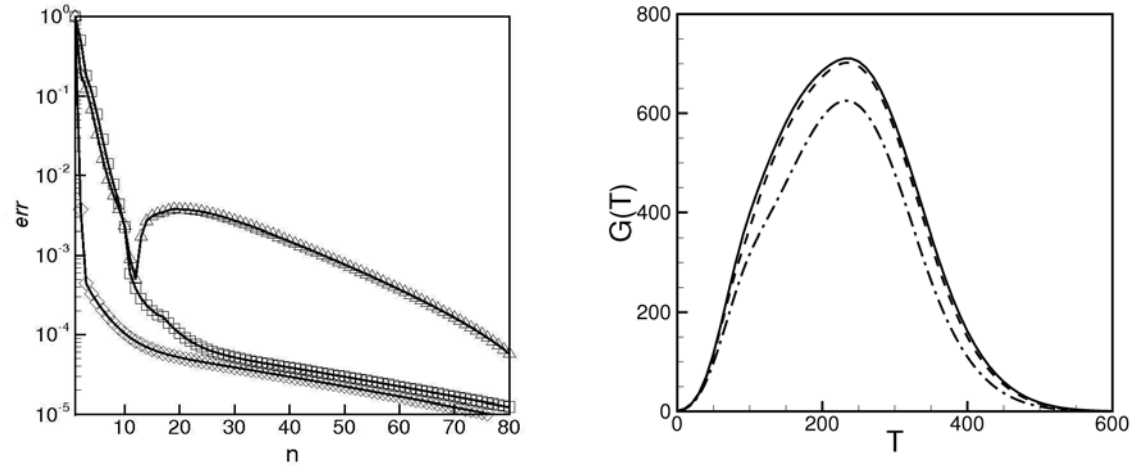

(a) (b)

Figure B.2: Normalized increment *err* of the objective function versus the number of iterations at $T = 247$ represented in a semi-logarithmic scale for an initial guess resulting from a direct-adjoint optimization stopped at the level of convergence $err = 10^{-3}$ (diamonds), from the global model optimization (squares), and from the global model optimization with a random noise of amplitude 10^{-8} superposed at the inlet points (triangles) (a). Envelope of the optimal energy gain computed by the global model for 1100 modes (solid line), 1000 modes (dashed line) and 900 modes (dashed-dotted line) at $Re = 610$ and $L_x = 400$ (b).

B.2 The global eigenvalue analysis

The optimal energy gain is computed also by the global model of section 3.5. The resulting curve follows qualitatively the data obtained by the direct-adjoint method, although the maximum $G(t)$ is lower than that previously computed, and is equal to 710 at $t = 235$, as shown in figure B.1 (a) (solid line). A possible reason for this mild discrepancy is that the continuous spectrum is captured only in a discrete sense by the present procedure. Hence it becomes important to employ both a large value of L_y (together with acceptable resolution along y) while capturing the largest possible number N of modes. In the solution of equation (3.34) we have used up to $N = 1100$ modes, which is the maximum allowed by our computing systems for the storage of the matrices in (3.27). To verify that $N = 1100$ is sufficient, the convergence of the global model optimization has been studied by varying the number of modes chosen for the optimization. Figure B.2 (b) shows the optimal energy gain curves computed with $N = 900$ (dashed-dotted line), $N = 1000$ (dashed line) and $N = 1100$ modes (solid line). Although for the two better resolved computations the energy gain curves change only slightly, the convergence is not yet perfect.

B.3 Computational costs

Concerning the computational cost, the direct-adjoint optimization is able to reach in about 8 hours of CPU time on a single processor Intel(R) Core(TM) @ 2.67-GHz, a convergence level of 10^{-4} at the optimal target time. Concerning the global model, with $N = 1100$ modes, about 70 hours are needed to compute the global spectrum using the eight cores of two Intel Itanium 2 Quad core @ 667-MHz processors. Once the spectrum is computed, such a method can quickly determine the energy gain curve with a high resolution in time; for example, three hours of computation on a single core of an Intel Itanium 2 @ 667 MHz processor are necessary to compute the energy gain curve with a time resolution of 10 (the $G(t)$ values are computed for $t = 10n$ with $n = 1, 2, ..., 60$). The same task takes about 500 hours when using the direct-adjoint optimization. Thus, it is possible to conclude that the global model yields an acceptable estimate of the time at which the energy peaks; from this point on it is best to adopt the direct-adjoint procedure to accurately evaluate the maximum gain by optimizing in a small window of the optimal time provided by the global model.

Bibliography

Acarlar, M. S. and Smith, C. R. (1987). A study of hairpin vortices in a laminar boundary layer Part 2 Hairpin vortices generated by fluid injection . *J. Fluid Mech.*, 175:43–48.

Adrian, R. J. (2007). Hairpin vortex organization in wall turbulence . *Phys. Fluids*, 19:041301.

Åkervik, E., Brandt, L., Henningson, D. S., Hoepffner, J., Marxen, O., and Schlatter, P. (2006). Steady solutions of the Navier–Stokes equations by selective frequency damping . *Phys. of Fluids*, 18(068102).

Åkervik, E., Ehrenstein, U., Gallaire, F., and Henningson, D. S. (2008). Global two-dimensional stability measures of the flat plate boundary-layer flow . *Eur. J. Mech. B/Fluids*, 27(5):501–642.

Åkervik, E., Hoepffner, J., Ehrenstein, U., and Henningson, U. (2007). Optimal growth, model reduction and control in a separated boundary layer flow using global eigenmodes. *J. Fluid Mech.*, 579:305–314.

Alam, M. and Sandham, N. D. (1999). Direct numerical simulation of "short" laminar separation bubbleswith turbulent reattachment. *J. Fluid Mech.*, 403:223–250.

Alizard, F. (2007). Etude de stabilité linéaire globale d'écoulement fortement décollé de couche limite de plaque plane. *PhD thesis, ENSAM*.

Alizard, F. and Robinet, J.-C. (2007). Spatially convective global modes in a boundary layer . *Phys. Fluids*, 19(114105).

Andersson, P., Berggren, M., and Henningson, D. S. (1999). Optimal disturbances and bypass transition in boundary layers . *Phys. Fluids*, 11:134–150.

Andersson, P., Brandt, L., Bottaro, A., and Henningson, D. S. (2001). On the breakdown of boundary layer streaks . *J. Fluid Mech.*, 428:29–60.

Armaly, B., Durst, F., Pereira, J., and Schonung, B. (1983). Experimental and theoretical investigation of backward-facing step flow. *J. Fluid Mech.*, 127:473–496.

Asai, M., Minagawa, M., and Nishioka, M. (2002). The instability and breakdown of a near-wall low-speed streak . *J. Fluid Mech.*, 455:289–314.

Bakchinov, A. A., Grek, G. R., and Kozlov, V. (1992). A mechanism of turbulent spot formation . *Sibirskii Fiziko-Tekhnicheskii Zhurnal*, 4:39–45.

Barkley, D., Blackburn, H. M., and Sherwin, S. J. (2008). Direct optimal growth analysis for timesteppers . *Int. J. Numer. Meth. Fluids*, 57(1435–1458).

Barkley, D., Gomes, G. M., and Henderson, R. D. (2002). Three-dimensional instability in flow over a backward-facing step. *J. Fluid Mech.*, 473:167–190.

Barkley, D. and Henderson, R. D. (1996). Three-dimensional floquet analysis of the wake of a circular cylinder . *J. Fluid Mech.*, 322:215–241.

Barrow, J., Barnes, F., Ross, M., and Hayes, S. (1984). The structure of a turbulent spot in a Blasius flow . *J. Fluid Mech.*, 149:319–337.

Bayly, B. J. (1987). Three-dimensional centrifugal-type instabilities in inviscid two-dimensional flows. *Physics of Fluids*, 31:56–64.

Beaudoin, J.-F., Cadot, O., Aider, J.-L., and Wesfreid, J. E. (2004). Three-dimensional stationary flow over a backward-facing step . *Eur. J. Mech. B/Fluids*, 23:147–155.

Bers, A. (1983). Handbook of Plasma Physics . *M.N. Rosenbluth and R.Z. Sagdeev eds.*, 1:3.2.

Biau, D. and Bottaro, A. (2009). An optimal path to transition in a duct . *Phil. Transact. Royal Soc. A*, 367:529–544.

Biau, D., Soueid, H., and Bottaro, A. (2008). Transition to turbulence in duct flow . *J. Fluid Mech.*, 596:133–142.

Blackburn, H. M., Barkley, D., and Sherwin, S. J. (2008). Convective instability and transient growth in flow over a backward-facing step. *J. Fluid Mech.*, 603:271–304.

Brandt, L., Schlatter, P., and Henningson, D. S. (2004). Transition in a boundary layers subject to free-stream turbulence . *J. Fluid Mech.*, 517:167–198.

Briggs, R. J. (1964). Electron-Stream Interaction with Plasma . *MIT Press, Cambridge.*

Briley, W. (1971). A numerical study of laminar separation bubbles using the Navier-Stokes equations. *J. Fluid Mech.*, 47:713–736.

Butler, K. M. and Farrell, B. F. (1992). Three-dimensional optimal perturbations in viscous shear flow . *Phys. Fluids A*, 4:1637–1650.

Chambers, F. and Thomas, S. (1983). Turbulent spots, wave packets, and growth . *Phys. Fluids*, 26:1160–1162.

Cherry, N., Hillier, R., and Latour, M. (1984). Unsteady measurements in a separated and reattaching flow . *J. Fluid Mech.*, 144:13–46.

Chomaz, J. M. (2005). Global instabilities in spatially developing flows: non-normality and non linearity. *Annu. Rev. Fluid Mech*, 37:357–392.

Chomaz, J. M., Huerre, P., and Redekopp, L. G. (1991). A frequency selection criterion in spatially developing flows. *Studies in applied mathematics*, 84:119–144.

Chu, P. and Fan, C. (1999). A three point sixth-order non uniform combined compact difference scheme. *J. Comp. Phys.*, 148(2):663–674.

Corbett, P. and Bottaro, A. (2000). Optimal perturbations for boundary layers subject to stream-wise pressure gradient . *Phys. Fluids*, 12:120–130.

Cossu, C. and Chomaz, J. M. (1997). Global measure of local convective instabilities . *Physical Rewiew Letters*, 78(4387–4390).

Couairon, A. and Chomaz, J. M. (1997). Absolute and convective instabilities, front velocities and global modes in nonlinear systems. *Physica D*, 108:236–276.

Dallmann, U., Herberg, T., Gebing, H., Su, W.-H., and Zhang, H.-Q. (1995). Flow field diagnostics- Topological flow changes and spatio-temporal flow structure. *AIAA Paper*, 220(95-0791).

Dovgal, A. and Sorokin, A. (2009). Wave packets of controlled velocity perturbations at laminar flow separation. *VII IUTAM Symposium*.

Dovgal, A. V., Kozlov, V. V., and Michalke, A. (1994). Laminar boundary layer separation: instability and associated phenomena. *Prog. Aerospace Sci.*, 30(1):61–94.

Drazin, P. G. and Reid, W. H. (1981). Hydrodynamic Stability . *Cambridge University Press*.

Eckhardt, B., Schneider, T. M., Hof, B., and Westerweel, J. (2007). Turbulence transition of pipe flow . *AnnU. Rev. Fluid Mech.*, 39:447–468.

Ehrenstein, U. (1996). On the linear stability of channel flows over riblets . *Phys. Fluids*, 8:3194–3196.

Ehrenstein, U. and Gallaire, F. (2005). On two dimensional temporal modes in spatially evolving open flows: the flat-plate boundary layer. *J. Fluid Mech.*, 536:209–218.

Ehrenstein, U. and Gallaire, F. (2008). Global low-frequency oscillations in a separating boundary-layer flow . *J. Fluid Mech.*, 614:315–327.

Ellingsen, T. and Palm, E. (1975). Stability of linear flow . *Phys. Fluids*, 18:487–488.

Elofsson, P. A. and Alfredsson, P. H. (1998). An experimental study of oblique transition in plane Poiseuille flows . *J. Fluid Mech.*, 358:177–202.

Emmons, H. (1951). The laminar-turbulent transition in a boundary layer. Part I . *Journal of Aeronautical Science*, 18:490–498.

Faisst, H. and Eckhardt, B. (2003). Travelling waves in pipe flow . *Phys. Rev. Lett.*, 91:224502.

Farrell, B. F. (1988). Optimal excitation of perturbations in viscous shear flow. *Physics of Fluids*, 31:2093–2102.

Fasel, H. (1976). Investigation of the stability of boundary layers by a finite-difference model of the navier-stokes equations. *J. Fluid Mech.*, 78:355 – 383.

Fasel, H. and Konzelmann, U. (1990). Non-parallel stability of a flat-plate boundary layer using the complete navier-stokes equations. *J. Fluid Mech.*, 221:311–347.

Gad-el Hak, M., Blackwelder, R., and Riley, J. (1981). On the growth of turbulent regions in laminar boundary layers . *Journal of Aeronautical Science*, 110:73–95.

Gallaire, F., Marquillie, M., and Ehrenstein, U. (2007). Three-dimensional transverse instabilities in detached boundary layers. *J. Fluid Mech.*, 571:221–233.

Gaster, M. (1965). On the generation of spatially growing waves in a boundary layer. *J. Fluid Mech.*, 22:433–441.

Gaster, M. (1969). The structure and behaviour of laminar separation bubbles. Technical report, Ministery of technology, Aeronautical research council.

Gaster, M. (1974). On the effect of boundary layer growth on flow stability. *J. Fluid Mech*, 102:127–140.

Giannetti, F. and Luchini, P. (2007). Structural sensitivity of the first instability of the cylinder wake. *J. Fluid Mech.*, 581:167–197.

Goulpié, P., Klingmann, B. G. B., and Bottaro, A. (1996). Gortler vortices in boundary layers with streamwise pressure gradient: Linear theory . *Phys. Fluids.*, 8:451–459.

Gustavsson, L. H. (1991). Energy growth of three-dimensional disturbances in plane poiseuille flow. *J. Fluid Mech.*, 224:241 – 260.

Haggmark, C. P., Bakchinov, A. A., and Alfreddson, P. H. (2000). Experiments on a two-dimensional laminar separation bubble . *Phil. Trans. R. Soc. Lond. A.*, 358:3193–3205.

Hall, P. (1982). The linear development of görtler vortices in growing boundary layers. *J. Fluid Mech.*, 130:41–58.

Hamilton, J. M., Kim, J., and Waleffe, F. (1995). Regeneration mechanisms of near-wall turbulent structures . *J. Fluid Mech.*, 287:317–348.

Hammond, D. and Redekopp, L. (1998). Local and global instability properties of separation bubbles. *Eur. J. Mech. B/Fluids*, 17:145–164.

Head, M. R. and Bandyopadhyay, P. (1981). New aspects of turbulent structure . *J. Fluid Mech.*, 107:297–337.

Henningson, D., Lundbladh, A., and Johansson, A. (1993). A mechanism for bypass transition from localized disturbances in wall-bounded shear flows . *J. Fluid Mech.*, 250:169–207.

Henningson, D., Spalart, P., and Kim, J. (1987). Numerical simulations of turbulent spots in plane Poiseuille and boundary-layer flows . *Phys. Fluids*, 30:2914–2917.

Henningson, D. S. and Åkervik, E. (2008). The use of global modes to understand transition and perform flow control. *Physics of Fluids*, 031302.

Herbert, T. (1988). Secondary instability of boundary layers . *Annu. Rev. Fluid Mech.*, 20:487–526.

Herbert, T. (1997). Parabolized stability equations. *Annu. Rev. Fluid. Mech.*, 29:245–83.

Hof, B., van Doorne, C., Westerweel, J., Nieuwstadt, F., Faisst, H., Eckhardt, B., Wedin, H., Kerswell, R., and Waleffe, F. (2004). Experimental Observation of Nonlinear Traveling Waves in Turbulent Pipe Flow . *Science*, 305:1594–1598.

Huerre, P. and Monkewitz, P. A. (1985). Absolute and convective instabilities in free shear layers. *J. Fluid Mech.*, 159:151–168.

Huerre, P. and Monkewitz, P. A. (1990). Local and global intabilities in spatially developing flows . *Annu. Rev. Fluid Mech.*, 22:473–537.

Hunt, J. C. R., Wray, A., and Moin, P. (1988). Eddies, stream, and convergence zones in turbulent flows. *Center for Turbulence Research Report*, CTR-S88.

Inger, G. R. (1987). Spanwise-periodic three-dimensional disturbances in the wake of a slightly stalled wing. *AIAA paper*, 87:0456.

Jackson, C. P. (1987). A finite-element study of the onset of vortex shedding in flow past variously shaped bodies . *J. Fluid Mech.*, 182:23–45.

Jacobs, R. G. and Henningson, D. S. (1999). Evaluation of data form direct numerical simulations of transition due to freestream turbulence . *Annual Reasearch Briefs*.

Jimenez, J. (1994). On the structure and control of near wall turbulence . *Phys. Fluids*, 6:1944–953.

Jones, B. M. (1934). Stalling. *J. R. Aero. Soc*, 38:753–770.

Joseph, D. (1976). *Stability of fluid motions I* . Springer-Verlag.

Kachanov, Y. S., Kozlov, V. V., and Levchenko, V. Y. (1977). Nonlinear development of a wave in a boundary layer . *Proc. USSR Acad. Sci., Fluid Mech.*, 3:49–53.

Kachanov, Y. S. and Levchenko, V. Y. (1984). The resonant interaction of disturbances at laminar turbulent transition in a boundary layer . *J. Fluid Mech.*, 138:209–247.

Kaiktsis, L., Karniadakis, G., and Orszag, A. (1996). Unsteadiness and convective instabilities in two-dimensional flow over a backward-facing step. *J. Fluid Mech.*, 321:157–187.

Kendall, J. (1985). Experimental study of disturbances produced in a pre-transitional laminar boundary layer by weak freestream turbulence . *AIAA paper*, 85-1695.

Klebanoff, P., Tidstrom, K., and Sargent, L. (1962). The three-dimensional nature of boundary layer instability . *J. Fluid Mech.*, 12:1–34.

Klebanoff, P. S. (1971). Effects of freestream turbulence on the laminar boundary layer . *Bull Am. Phys. Soc.*, 10(1323).

Klingmann, B. G. B. (1992). On transition due to three-dimensional disturbances in plane poiseiulle flow . *J. Fluid Mech.*, 240:167–.

Landahl, M. (1990). On sublayer streaks . *J. Fluid Mech.*, 212:593–614.

Landahl, M. T. (1980). A note on an algebraic instability of inviscid parallel shear flows . *J. Fluid Mech.*, 98:243–251.

Lehoucq, R., Sorensen, D., and Yang, C. (1997). *ARPACK Users' Guide: Solution of Large Scale Eigenvalue Problems with Implicitly Restarted Arnoldi Methods*.

Lin, J. M. and Pauley, L. L. (1996). Low-Reynolds-Number Separation on an Airfoil. *AIAA J.*, 34:1570–1576.

Lin, R. S. and Malik, M. R. (1996). On the stability of attachment-line boundary layers. Part 2. the effect of leading-edge curvature. . *J. Fluid Mech.*, 333:125–137.

Luchini, P. (2000). Reynolds number indipendent instability of the Blasius boundary layer over a flat surface: optimal perturbations . *J. Fluid Mech.*, 404:289–309.

Lundbladh, A. and Henningson (1994). Spatial simulations of oblique transition . *Phys. Fluids*, 6:1949–1951.

Lundbladh, A. and Johansson, A. (1991). Direct simulation of turbulent spots in plane Couette flow . *J. Fluid Mech.*, 229:499–516.

Lundell, F. and Alfredsson, P. H. (2004). Streamwise scaling of streaks in laminar boundary layers subjected to free-stream turbulence . *Phys. Fluids*, 16:1814–1817.

Marino, L. and Luchini, P. (2009). Adjoint analysis of the flow over a forward-facing step . *Theoretical and Computational Fluid Dynamics*, 23(1):37–54.

Marquet, O., Lombardi, M., Chomaz, J. M., Sipp, D., and Jacquin, L. (2009). Direct and Adjoint Global Modes of a Recirculation Bubble: Lift-up and Convective Non-ormalities . *J. Fluid Mech.*, 622:1–21.

Marquet, O., Sipp, D., Chomaz, J. M., and Jacquin, L. (2008). Amplifier and resonator dynamics of a low-Reynolds-number recirculation bubble in a global framework. *J. Fluid Mech.*, 605:429–449.

Marquillie, M. and Ehrenstein, U. (2003). On the onset of nonlinear oscillations in a separating boundary-layer flow. *J. Fluid Mech.*, 490:166–188.

Marusic, I. (2009). Unravelling turbulence near walls . *J. Fluid Mech.*, 630:1–4.

Marxen, O., Lang, M., Rist, U., and A., W. S. (2003). Combined experimental/numerical study of unsteady phenomena in a laminar separation bubble . *Flow, Turbulence and Combustion*, 71:133–146.

Mathew, J. and Das, A. (2000). Direct numerical simulations of spots . *Current science*, 76:816–820.

Matsubara, M. and Alfredsson, P. (2001). Disturbance growth in boundary layers subjected to free-stream turbulence . *J. Fluid Mech.*, 430:149–168.

Morkovin, M. V. (1984). Bypass transition to turbulence and research desiderata . *Transition in Turbines*, pages 161–204.

Na, Y. and Moin, P. (1998). The structure of wall-pressure fluctuations in turbulent boundary layers with adverse pressure gradient and separation. *J. Fluid Mech.*, 377:347–373.

Nagata, M. (1990). Three-dimensional finite amplitude solutions in plane Couette flow . *J. Fluid Mech.*, 217:519–527.

Nagata, M. (1997). Three-dimensional traveling-wave solutions in plane Couette flow . *Phys. Rev. Lett.*, 55:2023.

Orr, W. (1907). The stability or instability of the steady motions of a perfect liquid and of a viscous liquid . *Proc. R. Irish Acad. A*, 27:9–138.

Orszag, S. A. (1971). Accurate solution of the Orr-Sommerfeld stability equation . *J. Fluid Mech.*, 50:689–703.

Panton, R. L. (1997). *Self-Sustaining Mechanisms Of Wall Turbulence* . Computational Mechanics Publications, Southhampton.

Panton, R. L. (2001). Overview of the self-sustaining mechanisms of wall turbulence . *Progress in Aerospace Sciences*, 37:341–383.

Patel, V. and Head, M. R. (1969). Some observations on skin friction and velocity profiles in fully developed pipe and channel flows . *J. Fluid Mech.*, 38:181–201.

Pauley, L. L. (1994a). Response of two-dimensional separation to three-dimensional disturbances. *J. Fluids Engineering*, 116:433–438.

Pauley, L. L. (1994b). Structure of Local Pressure-Driven Tree-Dimensional Transient Boundary-Layer Separation. *AIAA J.*, 32:997–1005.

Pauley, L. L., Moin, P., and Reynolds, W. (1990). The structure of two dimensional separation. *J. Fluid Mech.*, 220:397–411.

Peerhossaini, H. and Wesfreid, J. E. (1988). On the inner structure of streamwise Gortler rolls . *Intl. J. Heat Fluid Flow*, 9:12.

Perry, A., Lim, T., and Teh, E. (1981). A visual study of turbulent spots . *J. Fluid Mech.*, 104:387–405.

Pier, B. (2002). On the frequency selection of finite-amplitude vortex shedding in the cylinder wake. *J. Fluid Mech.*, 458:407–417.

Pierrehumbert, R. (1986). A universal shortwave instability of two-dimensional eddies in an inviscid fluid . *Phys. Rev. Lett.*, 57:2157–2159.

Prandtl, L. (1935). *The Mechanics of Viscous Fluids* . Springer.

Rayleigh, L. (1880). On the stability of certain fluid motions . *Proc. Math. Soc. Londo*, 11:57–70.

Reddy, S. and Henningson, D. (1993). Energy growth in viscous channel flows. *J. Fluid Mech.*, 252:209 – 238.

Reynolds, O. (1883). An experimental investigation of the circumstances which determine whether the motion of water shall be direct or sinuous, and the law of resistance in parallel channels . *Philos. Trans. R. Soc. London Ser. A*, 173:935.

Ripley, M. D. and Pauley, L. L. (1993). The unsteady structure of two-dimensional steady laminar separation. *Physics of Fluids*, 12:3099–3106.

Rist, U. and Fasel, H. (1995). Direct numerical simulation of controlled transition in a flat plate boundary layer. *J. Fluid Mech.*, 298:211–248.

Rist, U. and Maucher, U. (1994). Direct numerical simulation of 2-D and 3-D instability waves in a laminar separation bubble . *AGARD-CP-551*.

Rist, U. and Maucher, U. (2002). Investigations of time-growing instabilities in laminar separation bubbles. *Eur. J. Mech. B/Fluids.*, 21:495–509.

Sankaran, R., Sokolov, M., and Antonia, R. (1988). Substructures in a turbulent spot . *J. Fluid Mech.*, 197:389–414.

Saric, W. S. (1994). Gortler vortices . *Ann. Rev. of Fluid Mech.*, 26:379–409.

Schlichting, H. (1933). Berechnung der Anfachung kleiner Störungen bei der Plattenströmung . *ZAMM*, 13:171–174.

Schmid, P. and Henningson, D. (1992). A new mechanism for rapid transition involving a pair of oblique waves . *Phys. Fluids*, 4:1986–1989.

Schmid, P. and Henningson, D. (2001). *Stability and transition in shear fows*. Springer.

Schmid, P. J. (2000). Linear stability theory and by pass transition in shear flows . *Phys. Plasmas*, 7:1788–1794.

Schmid, P. J. (2007). Nonmodal stability theory. *Annu. Rev. Fluid Mech.*, 39:129–162.

Schmid, P. J. and Henningson, D. (2002). On the stability of a falling liquid curtain. *J. Fluid Mech.*, 463:163–171.

Schoppa, W. and Hussain, F. (2002). Coherent structure generation in near-wall turbulence . *J. Fluid Mech.*, 453:57–108.

Schubauer, G. B. and Klebanoff, P. S. (1955). Contributions on the mechanics of boundary layer transition. *NACA*, TN 3498.

Schubauer, G. B. and Skramstad, H. K. (1948). Laminar-boundary layer oscillations and transition on flat plate . *NACA*, Rapport technique 909.

Singer, B. (1996). Characteristics of a young turbulent spot . *Phys. Fluids*, 8:509–512.

Singer, B. and Joslin, R. (1994). Metamorphosis of a hairpin vortex into a young turbulent spot . *Phys. Fluids*, 6:3724–3736.

Sipp, D. and Jacquin, L. (2000). Three-dimensional centrifugal-type instabilities of two-dimensional flows in rotating systems. *Physics of Fluids*, 12:1740–1748.

Skote, M., Haritonidis, J. H., and Henningson, D. S. (2002). Varicose instabilities in turbulent boundary layers . *Phys. Fluids*, 14:2309–2323.

Sommerfeld, A. (1908). Ein Beitrag zur hydrodynamische Erklärung der turbulenten Flüssigkeitsbewegungen . *Proceedings of the 4th International Congress of Mathematicians, III*, pages 116–124.

Squire, H. (1933). On the stability for three-dimensional disturbances of viscous fluid flow between parallel walls . *Proc. Roy. Soc Lond Ser A*, 142:621–628.

Swearingen, J. and Blackwelder, R. F. (1987). The growth and breakdown of streamwise vortices in the presence of a wall . *J. Fluid Mech.*, 182:255–.

Sychev, V., Ruban, A., Sychev, V., and Korolev, G. (2005). *Asymptotic theory of separated flows.* Springer.

Tatsumi, T. and Yoshimura, T. (1990). Stability of the laminar flow in a rectangular duct . *J. Fluid Mech.*, 212:437–449.

Theodorsen, T. (1952). Mechanism of turbulence . *Proceedings of the Midwestern Conference on Fluid Mechanics Ohio State University, Columbus.*

Theofilis, V. (1997). On the verification and extension of the Gortler-Hammerlin assumption in three-dimensional incompressible swept attachment-line boundary layer flow. . *Tech. Rep. IB A*, 44:223–297.

Theofilis, V. (2003). Advances in global linear instability of nonparallel and three-dimensional flows. *Prog. in Aerospace Sciences*, 39:249–315.

Theofilis, V., Hein, S., and Dallmann, U. (2000). On the origins of unsteadiness and three dimensionality in a laminar separation bubble. *Proc. R. Soc. London.*, 358:3229–3246.

Tillmark, N. and Alfredsson, P. H. (1992). Experiments on transition in plane couette flow . *J. Fluid Mech.*, 235:89–102.

Tollmien, W. (1929). Über die Entstehung der Turbulenz . *Nachr. Ges. Wiss. Göttingen*, pages 21–44.

Trefethen, L., Trefethen, A., Reddy, S., and Driscoll, T. (1993). Hydrodynamic stability without eigenvalues. *Science*, 261:578–584.

Trefethen, L. N. and Embree, M. (2005). *Spectra and Pseudospectra; the behaviour of nonnormal matrices and operators* . Princeton University Press.

Tuckerman, L. S. and Barkley, D. (2000). Bifurcation analysis for timesteppers . *Numerical Methods for Bifurcation Problems and Large-Scale Dynamical Systems*, 119(543–466).

Verzicco, R. and Orlandi, P. (1996). A finite-difference scheme for the three-dimensional incompressible flows in cylindrical coordinates . *J. Comp. Phys.*, 123(2):402–414.

Waleffe, F. (1995). Hydrodynamic stability and turbulence: beyond transients to a self-sustaining process . *Stud. in App. Math.*, 95:319–343.

Waleffe, F. (1998). Three-dimensional states in plane shear flow . *Phys. Rev. Lett.*, 81:4140–4143.

Waleffe, F. (2003). Homotopy of exact coherent structures in plane shear flows . *Phys. Fluids*, 15:1517–1534.

Wasistho, B., Geurts, B., and Kuerten, J. (1997). Numerical simulation of separated boundary-layer flow. *J. Engineering Mathematics.*, 32:177–194.

Watmuff, J. H. (1999). Evolution of a wave packet into vortex loops in a laminar separation bubble . *J. Fluid. Mech.*, 397:119–169.

Wedin, H. and Kerswell, R. (2004). Exact coherent structures in pipe flow: travelling wave solutions . *J. Fluid Mech.*, 508:333–371.

Westin, K., Boiko, A.V. Klingmann, K., Kozlov, V., and Alfredsson, P. (1994). Experiments in a boundary layer subjected to free-stream turbulence. Part 1. Boundary layer structure and receptivity . *J. Fluid Mech.*, 281:193–218.

Williams, P. T. and Baker, A. J. (1997). Numerical simulations of laminar flow over a 3D backward-facing step . *Int. J. Numer. Methods Fluids*, 24:1159–1183.

Wilson, P. and Pauley, L. L. (1998). Two and three dimensional large-eddy simulations of a transitional separation bubble. *Physics of Fluids*, 10 (11):2932–2940.

Wu, X. and Moin, P. (2009). Direct numerical simulation of turbulence in a nominally-zero-pressure-gradient flat-plate boundary layer . *J. Fluid Mech.*, 630:5–41.

Wygnanski, I., Sokolov, M., and Friedman, D. (1976). On a turbulent spot in a laminar boundary layer . *J. Fluid Mech.*, 78:785–819.

Yu, X. and Liu, J. T. C. (1994). On the mechanism of sinuous and varicose modes in three-dimensional viscous secondary instability of nonlinear Gortler rolls . *Phys. Fluids*, 6:736–750.

Zebib, A. (1987). Stability of viscous flow past a circular cylinder . *J. Eng. Math.*, 21:155–165.

Instabilité globale linéaire et non linéaire d'écoulements de couche limite attachées ou decollées sur une plaque plane

Résumé : Le but de cette thèse est de décrire en détail la dynamique linéaire et non linéaire d'une couche limite attachée ou décollée sur une plaque plane à bas nombre de Reynolds. La dynamique linéaire, pilotée par les interactions entre les vecteurs propres non-orthogonaux, est étudiée à travers deux méthodes différentes de instabilité globale : une analyse globale aux vecteurs propres et une optimisation directe-adjointe. Dans ces analyses globales, aucune structure spatiale est imposée a priori pour la perturbation, les effets convectifs dus au fort non-parallélisme de l'écoulement sont pris en compte. Pour le cas de la couche limite décollée, le déclenchement des instationnarités a été clarifié : i) pour une forte amplification des perturbations de nature convective et bidimensionnelle; ii) pour des effets de non normalité longitudinale engendrant le phenomène du *flapping*; iii) pour une forte sensibilité vis-à-vis d'un forçage harmonique; iv) pour un mode tridimensionnel globalement instable. Pour une couche limite attachée, le but a été d'identifier les perturbations localisées caracterisées par des fréquences multiples dans les directions longitudinale et transversale de l'écoulement, induisant une amplification de l'énergie des perturbations. Pour évaluer les effets de la non linéarité dans les mécanismes d'instabilité identifiés par les analyses de stabilité globale, des simulations numériques directes ont été réalisées pour les écoulements de couche limite attachées ou décollées, bidimensionnelles et tridimensionnelles. La dynamique des perturbations permettant une transition plus rapide vers la turbulence a été étudiée. Différents scénarios de transition ont été observés, les différents mécanismes de transition ont été analysés.

Mots clés : Instabilités globales, couche limite attachée et decollée, transition vers la turbulence, simulations numériques directes

Linear and non-linear global instability of attached and separated boundary-layer flows over a flat plate

Abstract : The aim of this thesis is to describe the linear and non-linear dynamics of both attached and separated boundary-layer flows over a flat plate at low Reynolds numbers. The linear dynamics, driven by the interactions among the non-orthogonal eigenvectors, is studied using two global instability approaches: the global eigenvalue analysis and the direct-adjoint optimization. In these global instability analysis no spatial structure is assumed a-priori for the perturbation, and the convective effects due to the high non-parallelism of the flow are taken into account. In the case of the separated boundary-layer flows, it has been clarified the role of the following features in the onset of unsteadiness: i) the strong two-dimensional convective amplification; ii) the non-normality effects such as the 'flapping' phenomenon; iii) the high sensitivity to external forcing; iv) the globally unstable three-dimensional mode. Concerning the attached boundary layer, the aim has been to identify localized perturbations characterized by more than one frequency in the streamwise and/or spanwise direction, inducing a strong energy amplification. In order to assess the effects of non-linearity on the instability mechanisms identified by the global linear stability analysis, direct numerical simulations have been performed in a two- and three-dimensional framework for both the attached and separated boundary-layer flows. The dynamics of the perturbations which most easily brings the flows on the verge of turbulence have been studied. Different scenarios of transition have been observed, and the mechanisms leading the flow to turbulence have been analyzed in detail.

Keywords : Global instability, attached and separated boundary-layer flows, transition to turbulence, direct numerical simulations

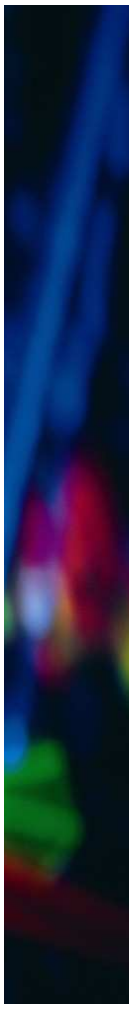

ARTS ET MÉTIERS ParisTech

ParisTech INSTITUT DES SCIENCES ET TECHNOLOGIES PARIS INSTITUTE OF TECHNOLOGY